The Electrodeposition and Electrochemical Properties of Nanostructured (H_1-e) Metal Films

By Jan Marwan

A thesis submitted for the degree of
Doctor of Philosophy

December 2002

Department of Chemistry
University of Southampton
Southampton, UK

University of Southampton
Abstract
Faculty of Science
Chemistry

Doctor of Philosophy

The electrodeposition and electrochemical properties of nanostructured (H_1-e) metal films

By Jan Marwan

Electrochemical deposition of metals from hexagonal lyotropic liquid crystalline phases produces metal films with a unique ordered nanostructure in which the cylindrical pores of 1.7 to 3.5 nm running through the film are arranged in hexagonal arrays.

Nanostructured Pd and Rh films were deposited electrochemically from the template mixture of either $C_{16}EO_8$ or Brij®56. Electrochemical studies showed that both metal films have a high electroactive surface area with the specific surface area of the order of 91 and 32 m^2/g, respectively. These values together with the TEM and X-ray data are consistent with the expected H_1 nanostructure.

The hydrogen region of nanostructured Pd in the cyclic voltammetry in 1 M H_2SO_4 was more resolved than that of plain Pd because of the thin walls of the nanostructure and the high surface area. We could distinguish the hydrogen adsorption and absorption processes. The permeation of hydrogen into the Pd metal lattice occurs with fast kinetics when the Pd surface is blocked by either crystal violet or Pt. We believe that the hydrogen absorption process takes place without passing through the adsorbed state so that hydrogen diffuses directly into the Pd bulk. This process speeds up when the formation of adsorbed hydrogen is suppressed by the coverage of poisons.

Nanostructured Pd was used as catalyst for methane oxidation in gas sensors. Pluronic F127 was found to be a suitable surfactant in the template mixture giving a far less viscous phase.

Electrochemical studies of nanostructured Rh films showed the surface oxide stripping peak on the cathodic scan moving towards positive potentials on potential-cycling attributable to changes in the surface oxide states. The peaks in the hydrogen region became better resolved on increasing the number of voltammetric cyles. Nanostructured Rh films were used for the electroreduction of nitrate and showed greater sensitivity compared to Rh electrodes deposited from the aqueous solution and compared to nanostructured Pd and Pt films.

Finally, we showed that we can deposit nanostructured metal films one on top of the other with pores running continuously through the final metal film. We have chosen for our studies Rh and Pd for which the surface oxide stripping peaks occur at well-separated potentials. We showed that increasing the thickness of the outer layer does not block the access to the pores of the inner metal electrode. By running successive voltammograms the surfactant were removed from the pores and we could see the increase in the oxide stripping of the outer layer followed by that of the inner metal layer. This finally was conclusive evidence that the pores are continuously accessible by the electrolyte solution through the final film.

Acknowledgement

Special thanks to Prof. Phil Bartlett for having given me the opportunity to come to Southampton to do my PhD. It has been a great experience for me to work under his encouraging supervision. He spent many hours with me to give me hints for my research and to teach me how to do professional science.

I would also like to thank Sergio Martinez Montequin for helping me out with the Word Document and to Stuart Evans for the tough discussion of special topics in my thesis. I would also like to acknowledge Mamdhou Abdelsalam and Mohammed Ghanem for their encouraging support. Thanks goes to Toru, Rob, David, Alex and Maciek. I'm very pleased that I have had the chance to work with all of them.

Thanks must also go to those who provided me with technical help in their specialist areas. These include Alistair Clarke (SEM) and Barbara Cressey (TEM).

The funding of this work provided by City Technology is gratefully acknowledged. Special thanks go to Dr. Martin Willett for his support.

Thanks and gratitude must also go to our collaborators at the University at Warwick: Prof Julian Gardner and Siu Man Lee.

The biggest thank you is for my parents and especially for my mother to whom this thesis is dedicated; for her encouragement, help, understanding and the fact that she strongly believes in me.

Index

Chapter 1 Introduction *1*

1.1 Liquid crystal phases and nanostructured metals **2**

1.1.1 Liquid crystals 2

1.1.2 The liquid crystal templating mechanism with the outline of two possible pathways 7

1.1.3 True liquid crystal templating 9

1.1.3.a Advantages 10

1.1.4 Mesoporous metals templated by liquid crystals from block copolymer-co surfactant-water systems 11

1.1.5 Electrochemical deposition of mesoporous metal films from lyotropic crystalline phases 12

1.1.5.a Application 15

1.1.5.b Properties of a nanostructured metal film 15

1.2 Electrochemistry of noble metals **16**

1.3 Gas sensors **18**

1.3.1 Solid – state - gas sensors 19

1.3.2 New technologies and improvements for gas sensors 21

1.4 Plan **22**

Chapter 2 Experimental *23*

2.1 Chemicals and Materials **24**

2.2 Instrumentation **24**

2.3 Preparation of the liquid crystal template mixtures **26**

2.4 Electrochemical deposition of nanostructured metal films **26**

2.4.1 Deposition onto gold electrodes of 1 mm and 25 μm diameter sealed in glass 26

2.4.2 Deposition onto the gold electrode area of SRL devices 27

2.5 Electrochemical measurements on nanostructured metal films **28**

2.6 Gas-testing measurements of nanostructured metal layers deposited onto SRL devices 29

Chapter 3 The preparation and characterizaton of H_I-e Pd films 30

3.1 Introduction 31

3.2 Phase behaviour 32

3.3 Electrodeposition of mesoporous Pd onto gold electrodes 36

3.4 Characterization of nanostructured palladium 38

3.5 Electrochemical characterization of the electroactive surface area 44

3.6 The oxide region in the voltammetry of H_I-e Pd 48

3.6.1 Mass loss of H_I-e Pd by repeatedly cycling into the oxide formation region 48

3.6.2 Surface modifications of H_I-e Pd films 54

3.7 Hydrogen electrode reaction on nanostructured palladium 56

3.7.1 Introduction 56

3.7.2 Electrochemical measurements 57

3.7.3 Absorption of hydrogen into H_I-e Pd 63

3.8 Conclusion 73

Chapter 4 The effect of poisons on promoting the H sorption into the Pd metal lattice 74

4.1 Introduction 75

4.2 The hydrogen absorption process 76

4.3 Conclusion 93

Chapter 5 Preparation and characterization of H_I-e Rhodium films 94

5.1 Introduction 95

5.2 Phase behaviour 95

5.3 The electrodeposition of mesoporous H_I-e Rh films onto gold electrodes. 98

5.4 Characterization of H_I-e Rh films 100

5.5 Electrochemical characterization of H_I-e Rh films 104

5.6 The catalytic use of H_I-e Rh as high surface area metal for the electroreduction of nitrate 113

5.6.1 Introduction 113

5.6.2 Electroreduction of nitrate on rhodium electrodes 115

5.7 Conclusion 126

Chapter 6 The electrochemical deposition of (H_I–e) layers of two metals in which the pores interconnect 127

6.1 Introduction 128

6.2 Electrochemistry of noble metals 130

6.3 Increasing the thickness of one layer deposited on top of the other 133

6.4 Increase of the surface oxide with the removal of the surfactant 139

6.5 Conclusions 145

Chapter 7 Pellistors 146

7.1 Introduction 147

7.2 Characterization of devices 150

7.3 Deposition from the template mixture 155

7.3.1 Deposition from the Brij®56 system 155

7.3.2 Mass spectroscopic measurements of Brij®56 158

7.3.3 Deposition of Pd from the Pluronic (F 127) template mixture onto the SRL 162g device 167

7.3.3.a The deposition behaviour 167

7.3.3.b Proof of a successful deposition of Pd on the gold electrode of the SRL device from the Pluronic(F127) template mixture with high surface area... 170

7.4 Manufacturing defects 172

7.5 Methane response on H_I-e metal catalyst layers 174

7.6 Multideposition process 186

7.7 Conclusion 189

Chapter 8 Conclusions and Future work *191*

8.1 Conclusions 192

Chapter 1 Introduction

1.1 Liquid crystal phases and nanostructured metals

The engineering of porosity in materials is emerging as a new area of great technological and scientific interest [1-4]. Materials with tailor made pore sizes of nanometer-sized dimensions and shapes are particularly important in applications where molecular recognition is needed, such as shape-selective catalysis, molecular sieving, selective adsorption and chemical sensing [5]. Several methods have been mentioned in the literature to produce materials punctured by pores of nanometer-sized dimensions.

One approach has been reported by Kolb et al. [3, 6] who can build large arrays of metal clusters using tip-induced deposition on gold substrates. The other main approach which we want to mention here is the work of Attard et al. [1] who report the use of lyotropic liquid crystals to create a structure on a nanoscale. The lattice periodicity of the nanstructured material is a few nanometers. These two types of nanostructured materials are quite different. One is built by assembling cluster by cluster whereas the second one is obtained by exploiting the properties of the surfactant, which works as a templating agent to obtain the nanostructure.

Nanostructured materials that are used extensively as heterogeneous catalyst and adsorption media can be found in a range of microporous (pore diameter ≤ ≈ 20 Å) and mesoporous (≈ 20-500 Å) dimensions. The demand for micro- and mesoporous structures has lead to the development and tailoring of inorganic mesoporous materials synthesized by employing structure directing agents using liquid crystalline phases.

In the next section, we introduce liquid crystals and outline the structure and physical properties of liquid crystalline phases from which porous materials in micro- and meso dimensions can be synthesized.

1.1.1 Liquid crystals

The fundamental difference between crystals and liquids is the fact that ordered arrays of molecules are found in crystals in contrast to the random arrangement of molecules in liquids. The order in a crystal is normally positional and orientational. On the other hand the molecules in liquids diffuse randomly throughout the sample container.

Astonishingly, phases can be encountered in which the order of the molecules is less than in crystals and more pronounced than in liquids. These phases are grouped together and called liquid crystals (LC), since they share properties which are normally associated to both liquids and crystals. Molecules, forming liquid crystals, self-assemble into organized mesophases as intermediate between the crystalline solids and the isotropic liquids depending on the ambient conditions such as temperature (thermotropic liquid crystals) and concentration of the molecules in a solvent such as water (lyotropic liquid crystals) [7]. The molecules in these mesophases aggregate dynamically and collectively to a viscous phase with a high degree of organization.

Lyotropic liquid crystals can be formed by amphiphile molecules containing a water insoluble (hydrophobic) organic tail section and a water-soluble (hydrophilic) head group. The amphiphile character of these molecules causes the self-assembly into highly ordered matrices in the presence of a polar medium such as water.

Amphiphile molecules are known as surfactants. Generally two types of surfactant molecules can be encountered, ionic surfactant and non-ionic surfactant. One example of an ionic surfactant is shown below, sodium dodecyl sulfate consisting of a polar head group (sulfate salt) and a long non-polar hydrocarbon chain.

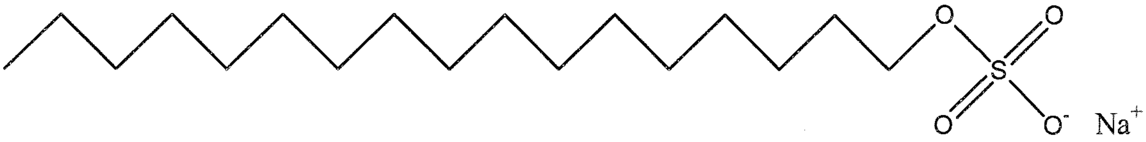

Sodium dodecyl sulfate molecule

The other type, the non-ionic surfactant is shown with a long alkyl chain as hydrophobic section and a hydrophilic polar head group built up of ethylene glycol groups [8].

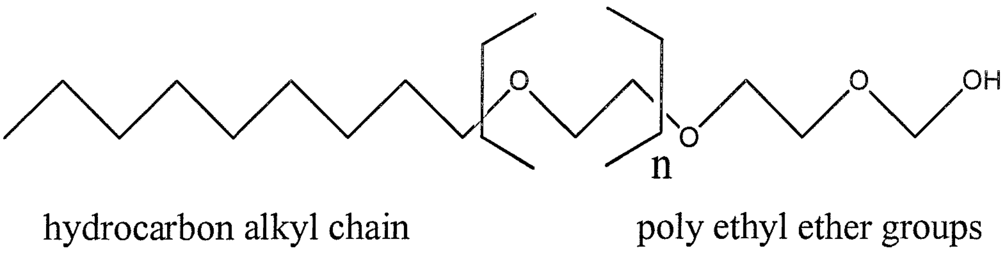

When mixing the amphiphile surfactant with water at concentrations below the critical micelle concentration (CMC) it dissolves in water and behaves like an electrolyte solution, if it is an ionic surfactant. As the concentration of the surfactant increases above the CMC, the amphiphilic molecules self-assemble to create aggregates in which the hydrocarbon chains are packed inside and the polar head groups form the surface surrounded by the aqueous medium. These structures are called micelles and they are stable as long as the surfactant concentration is above the CMC. Typically the value of the CMC is less than 1 wt% of surfactant concentration with respect to the amount of water [4, 8].

Different phases of lyotropic liquid crystals can be encountered depending on the ratio of surfactant to water in the liquid crystalline media and the temperature chosen. The most common phases are micellar, hexagonal, cubic and lamellar [4, 8, 9]. It is possible to extend this range to the inverse phases such as the inverse hexagonal and inverse cubic phase. These phases correspond to the most stable equilibrium existing at a certain concentration between all the chemicals present.

Figure 1 presents various supramolecular building blocks obtained when the ratio surfactant to water was increased from a) to e).

With the further increase of the surfactant concentration, more micelles are formed so that a concentration is reached at which the micelles combine to form larger structures. Figure 1 b) corresponds to an arrangement in which the ratio of surfactant to water was increased. The surfactant is ordered in cylinders of indefinite length. The head groups of the molecules form the surface and the hydrocarbon chains are packed inside. The cylinders are surrounded by the aqueous media. This arrangement exhibits the 2-dimensional hexagonal and the 3-dimensional cubic phase.

In c) the ratio surfactant to water was further increased to a large extent. The surfactant molecules are arranged in bilayers separated by the aqueous medium. From such an arrangement the lamellar phase can be obtained.

In d) the amount of surfactant is large. The surfactant molecules are arranged in cylinders as in b). However unlike the arrangement given in b) the surface of the cylinders is formed by surfactant molecule head groups packed inside and surrounded by the aqueous solution which is now trapped inside the cylinders. From such an arrangement the inverse hexagonal and inverse cubic phases can be obtained.

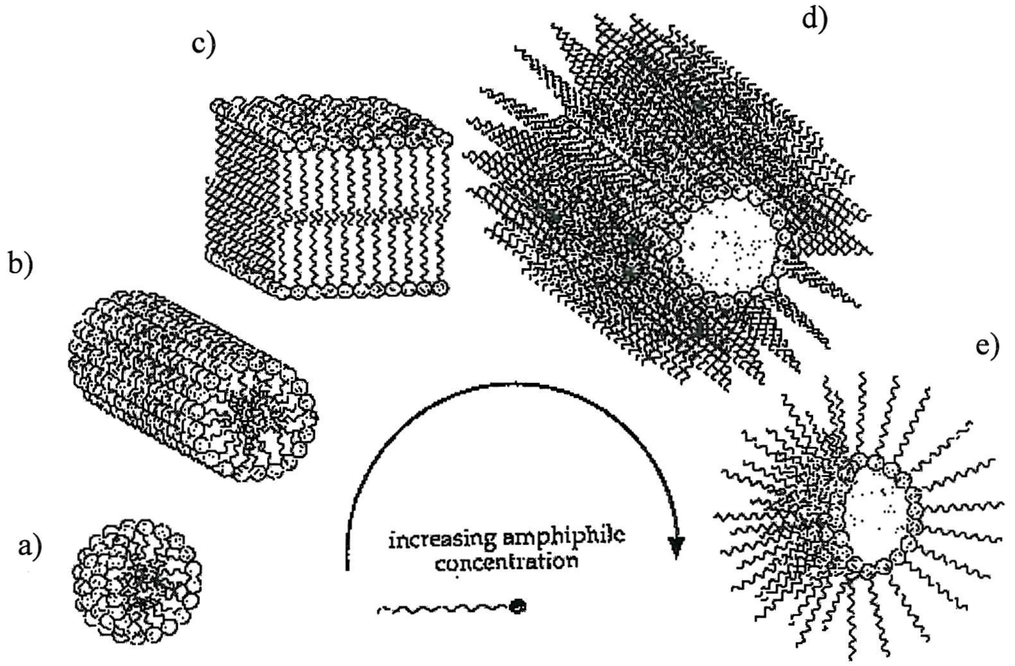

Figure 1: Various supramolecular building blocks of lyotropic liquid crystals obtained by increasing the concentration of surfactant in water. From left to right the phases obtainable from each arrangement are: a) micellar, b) hexagonal and cubic, c) lamellar, d) inverse hexagonal and inverse cubic, and e) inverse micellar [10].

In Figure 1 e) the concentration of surfactant in water is high so that the aqueous medium is trapped inside the spheres formed by the surfactant molecule head group. This arrangement gives the inverse micellar phase.

It is of interest to note when comparing all the supramolecular building blocks that the arrangement given in a) and b) is the opposite of d) and e) considering the position of the surfactant molecule head groups.

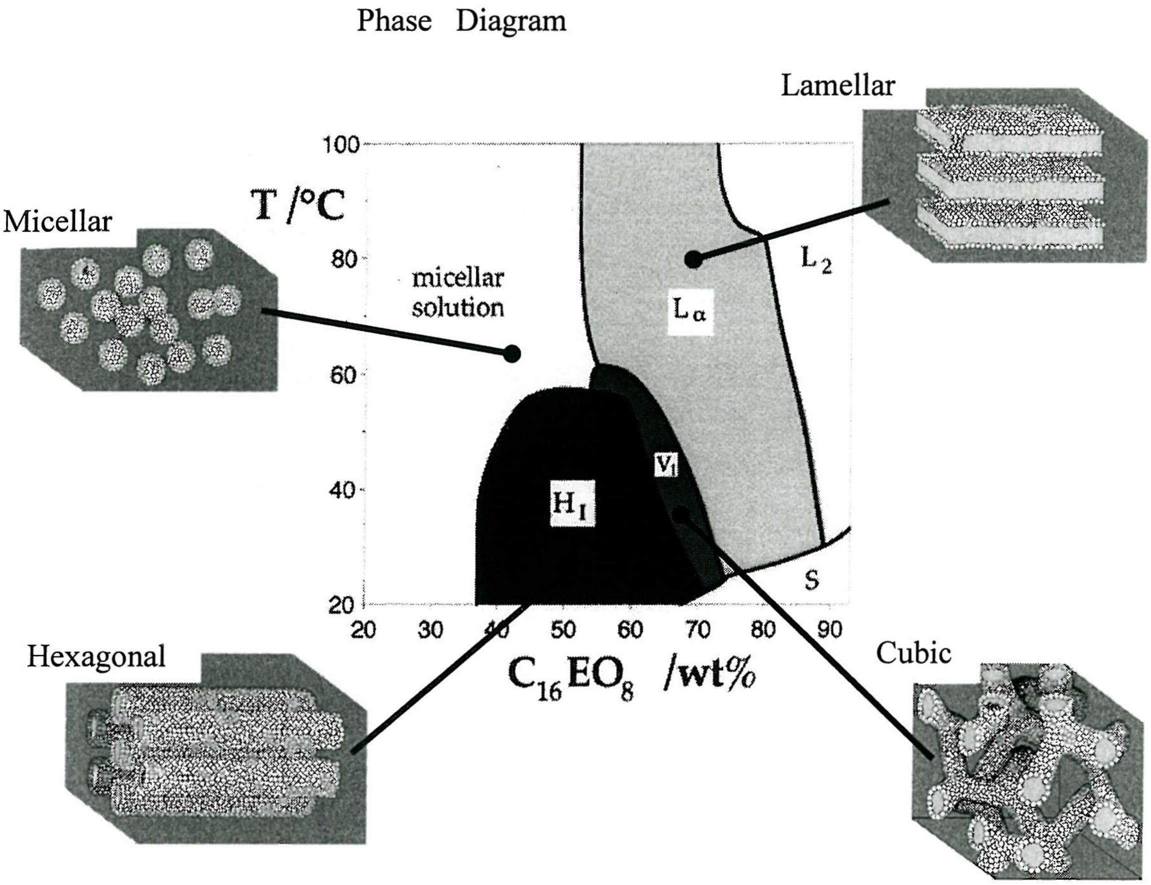

Figure 2: $C_{16}EO_8$ as surfactant mixed with water at different ratios to obtain the phase diagram for the most common phases in the lyotropic liquid crystalline media [11].

Considering the characteristics of lyotropic liquid crystals, we can build up a phase diagram for the most common phases to be encountered in the liquid crystalline media. The phase diagram shown in Figure 2 using $C_{16}EO_8$ as surfactant mixed with water demonstrates that the existence of each liquid crystalline phase is based on the ratio of surfactant to water and on the temperature chosen. The most common phases such as hexagonal, cubic and lamellar can be obtained. We note that at room temperature the hexagonal phase covers a large range of surfactant concentration.

The factor that could be responsible for the sequence of the mesophases observed with increasing temperature is claimed to be a decrease in intermicellar repulsions [11]. The transformation of hexagonal via cubic to lamellar phases is due to a decrease in the repulsions between adjacent head groups in the interface. According to the reference mentioned above it probably arises from a decrease in the hydration of the EO groups with increasing temperature. The maximum temperatures for the existence of the different mesophases represent the point at which the surface area reaches the packing limit.

According to the reference [11] in addition it is interesting to note that with increasing m in C_nEO_m the stability of the hexagonal phase increases whereas the stability of the lamellar phase decreases. Extensive lamellar regions occur only with small EO_m surfactant ($m < 5$). The cubic phases occur only with EO_m surfactant where $m > 8$. The authors reported that at low values of n the melting point of the hexagonal phase (H_1) is at a lower temperature limit than the cloud point. The cloud point approaches the H_1 melting point with increasing n.

1.1.2 The liquid crystal templating mechanism with the outline of two possible pathways

In 1992 Beck and co-workers [12, 13] synthesized a range of mesoporus silicate materials (denoted as the M41S family) using low concentrations (1 – 10 wt%) of cationic surfactant. The researchers at Mobil R & D corp. introduced a new family of mesoporous molecular sieves, M41S, which exhibit narrow pore size distribution whose dimensions can be tailored from 15 to 100 Å. The M41S family consists of three structure types. The first of these, MCM41 (Mobil Corporation Material 41), contains a hexagonal arrangement of channels. A second material, MCM-48, has a complex interconnecting, 3-dimensional channel system and MCM-50 is characterized by a lamellar system.

Partial exchange of silica to alumina in M41S materials results in mesoporous aluminosilicates. Similarly, it is possible to incorporate transition metals, such as vanadium into the MCM-41 structure [14].

It is generally accepted that to synthesize silica / surfactant mesophases it needs the assembly of dissolved silica sources around surfactant arrays.

Mobil researchers [15] observed that the resulting silica / surfactant mesophases strongly resemble mesophases seen in surfactant / water systems. They suggested that surfactant molecules act as structure-directing agents in the synthesis of MCM-41.

They postulated the so called "liquid-crystal templating mechanism" and proposed two possible pathways.

The proposed mechanistic pathways suggest either 1) the presence of the liquid-crystal phase prior to the addition of the reagent or 2) that the silicate species generated in the reaction mixture influences the ordering of surfactant micelles to the organized liquid-crystal phase. For either pathway, the resultant composition produces an inorganic material that mimics known liquid-crystal phases.

The case where the surfactant concentration is in the range of the hexagonal phase corresponds to using a preformed liquid-crystalline array as the template for the inorganic phase, as described in pathway 1 in Figure 3. However, as shown in the following, this is not the formation pathway in the initial Mobil work.

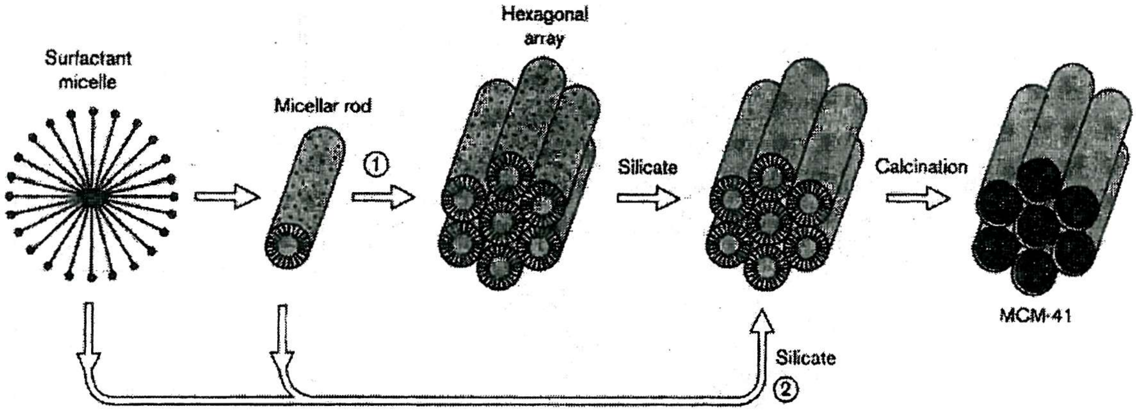

Figure 3: Schematic representation of the reaction pathway for the formation of MCM 41: 1) liquid crystal phase initiated and 2) silicate anion initiated to form the ordering of surfactant micelles to the liquid crystal phase [9].

According to ^{14}N NMR investigations Chen et al. [16] showed that under the conditions used by Mobil scientists preformed H_1 liquid-crystalline phases are not present in the synthesis medium and therefore are not the structure-directing agent. In the course of further research [4] the Mobil scientists also concluded that for the synthesis and the conditions chosen preformed H_1 liquid crystal were not formed initially. These investigations seemed to be in contradiction with the reaction pathway 1 and thus favouring the idea that MCM 41 can only be formed by adding silica to the micellar solution. This would imply that the silicate species significantly change the thermodynamics of the phase system.

A great deal of attention has been paid to the synthesis of MCM-41 with surfactant concentrations in the range of the micellar phase [17-19].

It is generally accepted that some sort of self-assembly of the micelles in the synthesis mixture is responsible for the porous structure. With the addition of silica to the surfactant mixture the interfacial interactions become increasingly important. The presence of a silicate anion species not only serves to charge balance the surfactant cations but also participate in the formation and ordering of the liquid-crystal phase. This implies that silica and surfactant cooperatively organize into an organic-inorganic liquid-crystalline phase during the course of their reaction. The details of the mechanism are still uncertain. Mainly two models have been proposed.

The first model is based on ^{14}N NMR spectroscopy and X-ray powder diffraction data where it is assumed [20] that hexagonal mesophases are present and that the silica source dissolves into the aqueous regions around the surfactant arrays. The silicates becomes ordered into layers between which the hexagonal mesophases are sandwiched. These silicate sheets and hexagonal surfactant phases then give rise to hexagonal silca-surfactant mesophases via puckering of the silicate sheets.

The second model [16] is based on X-ray powder diffraction, thermogravimetric analysis, ^{29}Si NMR and in situ ^{14}N NMR spectroscopy of precursor solutions. It was suggested that randomly ordered rodlike micelles were formed initially and that they interact with silicate species to form surfactant rods encapsulated by 2-3 monolayers of silica. These species then spontaneously assemble into a hexagonal structure that has long range order.

1.1.3 True liquid crystal templating

The success in fabrication of nanostructured silicas and modified silicas has been a stimulus to work in the use of template approaches to the fabrication of nanostructured materials and in the last few years there has been much effort to extend this approach to the fabrication of non-siliceous materials [21]. Attard et al. successfully synthesized nanstructured silica [1] from synthesis gels containing non-ionic polyoxyethylene surfactant at concentrations required to form liquid crystal phases. This method, which is not restricted to the formation of silica, employs much higher concentration of the surfactant (typically of the order of 50 wt%) so that the fabrication of the nanostructured material takes place from a lyotropic liquid crystalline phase in a process which can be described as true liquid crystal templating. It was shown that mesoporous silica, with pore morphologies identical to the M41S material, could be produced in the lyotropic liquid crystal phases of non-ionic polyoxyethylene surfactant.

The synthesis was carried out at room temperature under mildly acidic conditions. In this direct templating method, a source of silica used as precursor is provided by tetramethyl orthosilicate (TMOS) which hydrolysed in the aqueous domains of the regions of the liquid crystalline phases and then polymerized to solid silica. The methanol produced during the hydrolysis of the TMOS was removed throughout the synthesis procedure by keeping the synthesis gel under constant vacuum. Liquid crystalline phases such as hexagonal, cubic and lamellar were obtained as products and the former also showed stability to calcination.

Calcination of the silica removed the template leaving an organised porous structure.

1.1.3.a Advantages

We want to outline briefly the significant advantages of the true liquid crystalline templating approach.

The nanostructure of the final material is determined by the structure of the allotropic liquid crystalline phase, consequently the dimensions and topology of the structure can be varied in a predictable fashion by the choice of the surfactant and by the addition of co-solvent, based upon the knowledge of the phase behaviour of the system. The direct templating method is not limited to hexagonal, lamellar and cubic phases but has the possibility of being extended to inverse phases. This wide range of different lyotropic phases with varying topologies can be exploited.

The method is not limited to inorganic oxides such as silica as there is no need for headgroup-precursor interactions. The use of non-ionic surfactant, in the direct templating method emphasizes the fact that charge interactions are not important.

Hence this approach covers the formation of a wide range of mesoporous materials, from polymers to metals, by a suitable choice of a surfactant.

1.1.4 Mesoporous metals templated by liquid crystals from block copolymer-co surfactant-water systems

A potentially predictable approach for the synthesis of mesoporous materials is the direct templating by the use of liquid crystalline phases. Such an approach allowed us to design structural features of mesophases by controlling in advance the templating of liquid crystalline phases. Until now the templating of mesoporous materials has been restricted to only a few surfactants in the surfactant/water binary system [1, 2, 22, 23]. Attention has been directed towards the templating synthesis of periodic mesoporous metals by templating with liquid crystalline phases prepared from ternary systems consisting of amphiphilic triblock copolymers such as Pluronic F127, cosurfactant such as butanol, and water [24, 25]. Amphiphilic poly(ethylene oxide)-poly(propylene-oxide)-poly(ethylene oxide) (PEO-PPO-PEO) block copolymers, known as Poloxamers and Pluronics, are commercially cheaply available and have the ability to form lyotropic liquid crystalline structures in water [26]. The PEO-PPO-PEO block copolymer, Pluronic F127 (Poloxamer 407), can be represented as $EO_{100}PO_{70}EO_{100}$ on the basis of its 12 600 molecular weight and 70 wt% PEO content [27]. Pluronic F127 (formula shown below) is a unique surfactant because of its high molecular weight with a large hydrophilic volume. The long hydrophilic chain offers the possibility to synthesize mesoporous materials with thick walls that may lead to an increased hydrothermal stability [28]. The triblock-copolymer-alcohol-water system exhibits a rich phase behaviour. Phases such as micellar, reverse micellar, cubic, hexagonal and lamellar lyotropic liquid crystalline phases can be obtained by varying the content of the selective solvent, water and butanol. The cosurfactant chain length and the cosurfactant/surfactant mass ratio can be used to have the control over the pore size.

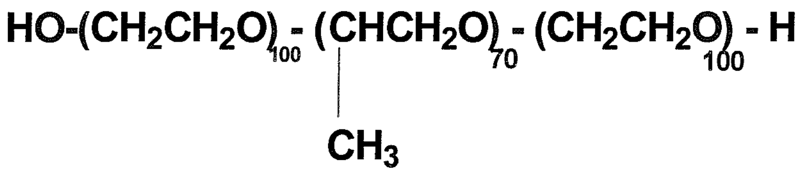

$$HO\text{-}(CH_2CH_2O)_{100}\text{-}(\underset{CH_3}{\underset{|}{C}}HCH_2O)_{70}\text{-}(CH_2CH_2O)_{100}\text{-}H$$

Pluronic F127

When mixed with water the Pluronic F127 surfactant molecules assemble spontaneously in regular structures of nanometer-sized dimensions and gives rise to a large range of pore size diameters with high hydrothermal stability.

Based upon the knowledge obtained from the studies of lyotropic liquid crystalline phases, we direct our attention in the next section towards the fabrication of mesoporous materials.

1.1.5 Electrochemical deposition of mesoporous metal films from lyotropic crystalline phases

To show the procedure of how to make nanostructured materials, we found it more convenient to get the reader first acquainted with the structure and properties of the lyotropic phases. Using this background knowledge, we can focus on the electrochemical deposition of mesoporous materials exploiting the physical properties of lyotropic liquid crystalline media.

Particular interest exists and much effort has been put to study the electrochemical deposition of nanostructured metals from lyotropic liquid crystalline media of non-ionic surfactant, preferably from the hexagonal H_1 phase. Using this approach nanostructured metal films of Pt [22, 23, 29-32], Co [33], Sn [34, 35], Ni [36], metal alloys [37, 38], semiconductors [39] and polymers [40] have been deposited.

As one example for the templated electrodeposition process we outline the fabrication of mesoporous Pt films. Attard et al. [2] developed a method to produce Pt thin films on nanoscale. These films were obtained by electrochemical deposition of the Pt metal on a gold electrode from a hexagonal lyotropic liquid crystalline phase used as the template mixture. This mixture contains a non-ionic surfactant surrounded by the aqueous medium in which Pt, present in the form of Pt salt, is dissolved.

The reduction of Pt (IV) dissolved within the aqueous domains of the hexagonal liquid crystal structure leads to the electrodeposition of nanostructured Pt films. The surfactant molecules, arranged in cylinders of indefinite length with hexagonal geometry, were removed after deposition to leave a thin film with hexagonally arranged ordered nanostructure as a cast of the liquid crystalline architecture. Figure 4 pictures the templated electrodeposition process.

Templated Electrodeposition:

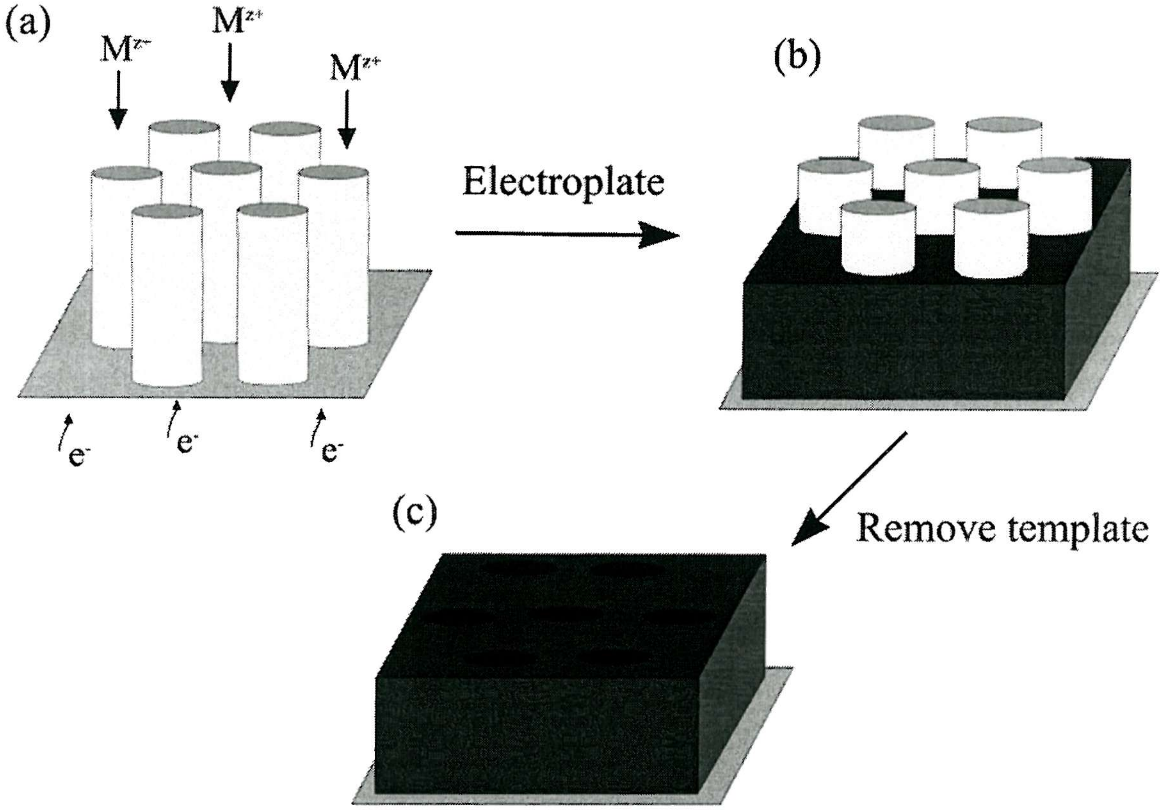

Figure 4: Schematic representation of the templating process used to deposit the nanostructured metal films. The cylinders represent the micellar rods in the lyotropic liquid crystalline phase. Within the aqueous domains of this phase the metal is dissolved and after electrochemical deposition of the metal and removal of surfactant the nanostructured metal is produced with hexagonally arranged pores continuously running through the film.

These films exhibit a very high surface area of the order of 5×10^6 cm^2/cm^3 corresponding to a specific surface area of the order of 22 m^2/g [22]. It was shown that Pt films can also be prepared with different topologies from other lyotropic liquid phases (in addition the cubic phase). Figure 5 shows the Transmission electron micrographs (TEM) of Pt films deposited from the hexagonal and cubic phase.
Separately, it was also shown that the diameter of the pores and the wall thickness depends on the surfactant used. The authors claimed that the size of the pore diameter can be controlled by the choice of surfactant [22].

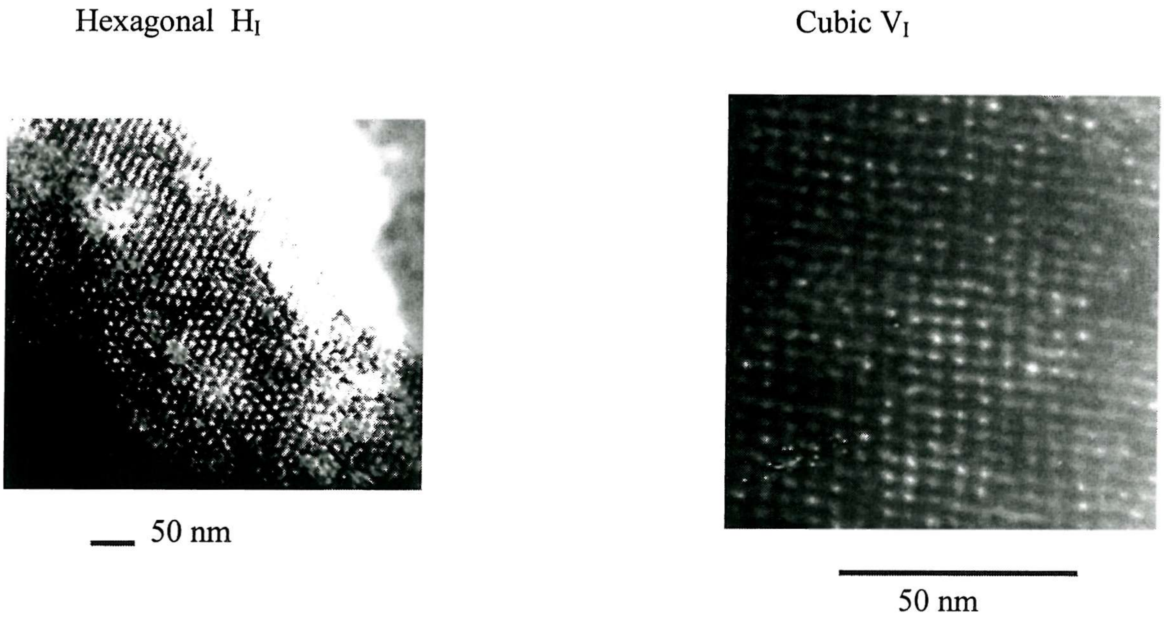

Figure 5: Transmission electron micrograph of a sample scraped from a nanostructured Pt film deposited from the $C_{16}EO_8$ plating bath. The figure shows an hexagonal and cubic arrangement of the pores [22].

The true liquid crystal templating can be extended to a wide range of metals [33, 39]. In principle any metal can be used in the template mixture. Limitation for the electrodeposition of the metal is given if the potential for the deposition occurs in a region where hydrogen or oxygen evolves. The electrodeposition is also restricted when the faradaic efficiency is decreased. Another sort of limitation is given by the metal salt destabilizing the boundaries of lyotropic liquid crystalline phases. An example for that is $CuSO_4$ which destabilizes the phase boundary of the H_I hexagonal phase so that H_I cannot be obtained by electrodeposition of Cu from this phase. In order to avoid this problem $CuSO_4$ can be replaced by $CuCl_2$ or $CuNO_3$.

1.1.5.a Application

There is a range of applications available for which one can use mesoporous metals.

Pt is a metal which can be used in a variety of catalytic processes. These include the oxidation of ammonia for the production of nitric acid [41], hydrogenation of olefins [42, 43] and reduction of NO_x in the control of car-exhaust emissions [44]. Pt also plays an important role in a variety of electronic and electrical devices [42, 43, 45]. Using the approach to the deposition of nanostructured materials from lyotropic liquid crystalline phases high surface area Pt microelectrodes are shown to be excellent amperometric sensors for the detection of hydrogen peroxide over a wide range of concentration [31]. In addition, nanostructured Pt can be used as electrode material for oxygen measurements [30] or in electroanalysis [32].

With the emergence of the fabrication of nanostructured metal films from lyotropic liquid crystalline media, investigations were reported on the electrochemical deposition of cobalt films with ordered arrays of uniform pore distribution on a hexagonal lattice with long range of periodicity. These nanostructured Co films exhibit in magnetic measurements magnetic properties unlike those of bulk polycrystalline cobalt. This fabrication technique might be of advantage for the development of new magnetic materials [33].

The electrochemical deposition of Pd as high surface area metal with regular, controlled nanostructure is of potential application as a catalyst for methane oxidation in gas-sensors. This will be described in detail in Chapter 7.

1.1.5.b Properties of a nanostructured metal film

With the deposition of H_I-e metal films from lyotropic liquid crystalline media, we obtain a regular porous structure. The pores in regular arrangement run through the film so that the controlled nanostructure is obtained. Using this approach it has become possible to deposit electrochemically high surface area metal films with the geometrical area of the same value as used for the deposition of planar metal films. Comparing this to planar metal films the research has made a significant step forward [22]. Electrochemical measurements in the porous structure also imply disadvantages which we have to consider in our studies. Especially we want to address the electric double layer near the electrode surface and the diffusion of electroactive species in the pores.

At equilibrium potentials a charged metal surface is balanced by species of opposite charge. According to the Gouy-Chapman model these species are forming the excess charge near the electrode surface and decay exponentially with the increase of the Debye length. This double layer formed at the electrode surface is of a few nanometer thick. In nanometer-sized pores the behaviour therefore can be much different from that at planar electrodes.

We also want to consider the diffusion of electroactive species in narrow pores. The flux of these species to the electrode surface will cause the existence of a diffusion layer. At planar electrodes this diffusion layer thickness can be made thinner by applying convection to the system. This would not be the case for nanometer-sized pores. A diffusion layer of electroactive species determines the solution behaviour within these pores.

In terms of the disadvantages of using H_I-e metal films with narrow pores we also want to stress probable defects on the Pd surface in the pores. These defects possibly can be seen in additional features in the cyclic voltammetry of H_I-e metal films compared with the voltammetry of a planar electrode.

1.2 Electrochemistry of noble metals

Constant interest exists in the study of the electrochemical properties of noble metals. The references mentioned here cover only a selected sample of the published material [46-50]. The most widely studied noble metal is platinum. Platinum electrodes were studied by carrying out cyclic voltammetric measurements over the full range of potentials covering the adsorption and desorption of hydrogen and oxygen [47]. The approach to the deposition of mesoporous metals such as platinum from lyotropic liquid crystalline phases, preferably the hexagonal phase, enabled the researchers in Southampton to study the electrochemical properties of mesoporous Pt [22, 23].

However, a lot of research has also been done on the electrochemistry of bulk palladium. Its electrochemical properties differ significantly from those of Pt. The Pd metal has the special ability for hydrogen to enter and permeate rapidly through the lattice in large quantities [51]. Therefore the palladium-hydrogen system has been the focus of several studies [47-50, 52].

There has not been a great deal reported on the electrochemistry of mesoporous Pd. Cioffi et al. [53] reported about the electrochemical synthesis of Pd nanoparticles that are subsequently potentiostatically deposited or embedded into the electrochemically produced polymer matrix (polypyrrole film). They carried out cyclic voltammetric measurements of the Pd nanocomosites and realized that nanostructured and bulk-Pd exhibit different response on the anodic scan. The peak for the formation of PdO at the anodic scan is more pronounced for Pd nanocomposites than for bulk Pd. In addition, the oxidation peak at the anodic scan using Pd nanocomposites electrodes involves more charge than using bulk Pd. This is clearly in contrast to the reduction at the cathodic scan. The oxide stripping peaks for both electrodes are well-pronounced not showing any difference in the charge passed in the stripping reaction. However, the authors are not able to give a reasonable explanation for this inconsistent behaviour.

Guerin and Attard [37] analyzed the electrochemical properties of mesoporous Pd + Pt films. These alloys were deposited from the aqueous binary mixture that contained a non-ionic surfactant to produce the liquid crystalline phase. The main focus lay in the hydrogen region and the unusual electrochemical phenomenon which the authors observed in their studies. The cyclic voltammetry of nanostructured Pt-Pd alloys differs markedly from that of bulk Pd. For bulk Pd the hydrogen region only shows features which are associated with hydrogen absorption into the bulk. In the case of nanstructured Pd-Pt alloys some differences, when comparing to bulk Pd can be noticed. 3 peaks in total can be observed. Two of them are attributable to hydrogen adsorption and absorption. The appearance of the last peak was associated with the dissolution and replating effect. During cyclic voltammetry some Pd will be stripped from the electrode surface and replated leading to the formation, after several cycles, of islands or layers of Pd. The authors claimed that these islands or layers, as they grow, will also finally start to show adsorption and absorption characteristics.

1.3 Gas sensors

There is a growing need for gas detection in both domestic and industrial areas for the purpose of control and safety applications.

The specific needs for gas detection and monitoring have emerged particularly as technology and industrialization appeared with the outcome that organic fuels and other chemicals have become an essential part of domestic as well as industrial life. The concern about the protection of the environment has raised much attention due to the increased consumption of natural gases in domestic and industrial appliances. The detection of gases has become an increasing problem. For example, people working in coal mines needed to detect the presence of combustible gases.

Because of the potential danger from the exposure to gases, sensors appeared in industries and in homes. This emerged from the concern to protect the environment. Nowadays sensors are used in everyday life placed in houses, offices, shops etc.

There are currently needs for three broad categories of gas monitoring: toxic gases, flammable gases and oxygen concentration. The first two prevent the risk of contamination or explosion while the third is important for the control of concentration of oxygen in combustion processes as well as the control of breathable gas in atmospheres.

One of the first needs for gas sensors was to protect the environment against the unwanted occurrence of fire and explosion. In this case the concentration to be measured is in the range up to the lower exposure limit which, for flammable gases, is up to a few per cent. For people working in coal mines, combustible gases such as methane were often present and could not be detected by human senses. 5% of methane in air is sufficient to reach the lower exposure limit.

1.3.1 Solid – state - gas sensors

Solid – state – gas sensors, with sufficiently low purchase cost are widely used. In addition, there is a significant sector of the gas sensor market that is served by liquid electrolyte electrochemical cells.

Solid – state – gas sensors can be grouped into solid-electrolyte, semiconductor and catalytic gas sensors. The first two are of minor interest in our research and are described in more detail by P. T. Moseley [54].

The catalytic gas sensor is the one of interest for the present work. Potentially explosive mixtures of methane or other flammable gases can be monitored by means of catalytically active solid state gas sensors. They consist of catalytically active material, a thermometer and a heater to ensure a sufficient temperature of the catalyst for a rapid combustion of the gas. Those devices, referred to as pellistors, are essentially catalytic micro-calorimeters.

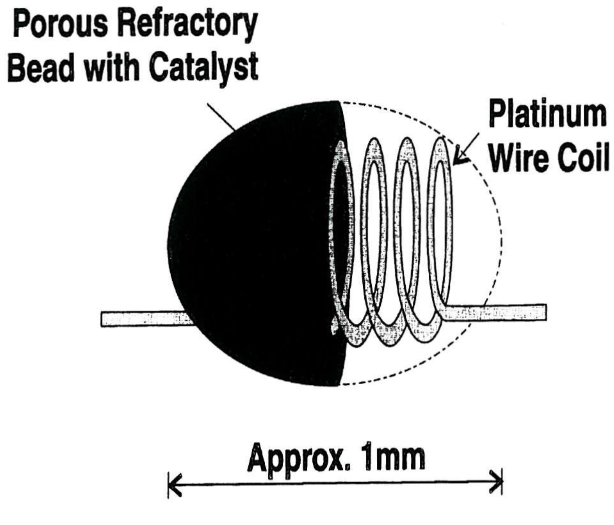

Figure 6: Representation of a pellistor, showing the platinum wire used as a heater and the bead loaded with the catalyst

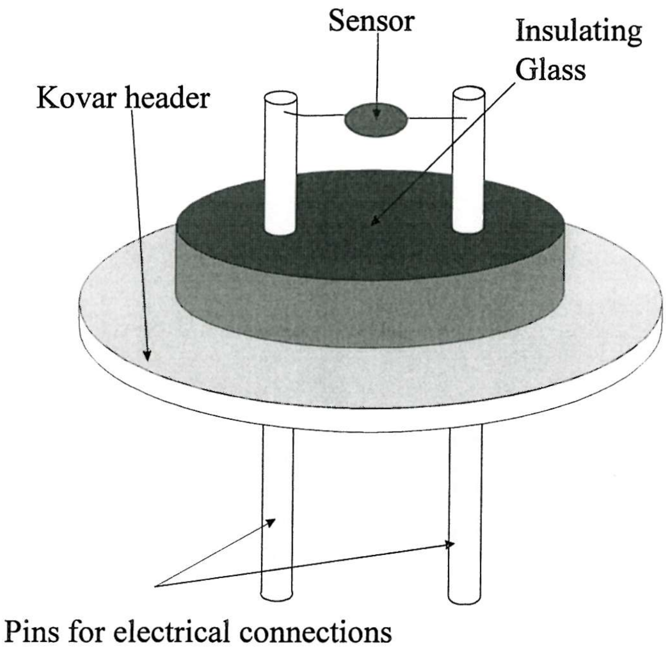

Figure 7: Schematic representation of a commercial pellistor mounted on a header

Commecial pellistors, Figure 6 and Figure 7, consist of a platinum coil embedded in a porous refractory bead. The bead is loaded with the catalyst. The platinum coil serves two purposes: heating the bead to its operating temperature (500 to 550 °C) and measuring, by changing its resistance, any heat change of the bead. In the absence of methane, the platinum wire has a certain resistance which is taken as the reference resistance for the measurement. In the presence of some methane in the atmosphere surrounding the sensor, the catalyst starts to oxidize methane which reacts to produce water and carbon dioxide. Consequently heat will be produced which brings the sensor bead to a higher temperature. Since the platinum wire is embedded in the bead it is also affected by any temperature changes and as a metal its resistance increases proportionally with the temperature. The Wheatstone bridge, described in detail in Chapter 7, is used to measure the resistance changes and with the use of a calibration curve it can be related to the concentration of methane in air.

1.3.2 New technologies and improvements for gas sensors

The successful fabrication of pellistors is a labour intensive process. It requires a technician to have some experience in making the platinum coil and depositing the droplet of solution to make the bead. The amount of catalyst deposited are controlled by eye. The pellistors can only be made one by one. This process is time-consuming and requires labour intensive costs to produce large batches of pellistors.

There has been a growing need for the fabrication of a new type of pellistor manufactured in large numbers without interference of a technician. This could reduce the cost required for the manufacturing process.

With the emergence of silicon and micromachined technologies sensors can be produced in large numbers at lower cost with a high degree of precision in the pattern and with the thickness of the different layers of only a few tens of nanometers. This miniaturization can reach a very low size of the sensor so that the ability to design and to make a sensor requires smaller amounts of catalyst and less power to operate.

The fabrication of nanostructured materials of high surface area from the lyotropic liquid crystalline media combined with the very fact that palladium is known to be as one of the best catalyst for the methane oxidation [55, 56] offers unique opportunity as catalytic active material in sensors.

One of the main problems arising from the work with pellistors is their lack of selectivity. Any combustible gas will in principle lead to a response of the sensor. The detection of methane as the gas of interest results also to the detection of other hydrocarbons such as propane or butane as well as organic vapours such as ethanol or acetone. These gases are likely to interfere. A certain degree of selectivity can be achieved either by mixing the metal oxide semiconductor catalyst and pellistor type catalyst [57-59] or by operating the sensor at different temperature [60]. Another attractive way to achieve this selectivity is the use of an array of sensing elements, each with different catalysts. Each catalyst can then detect gases differently. This combination results in a network from which it is possible to obtain precise distinction between several combustible gases [61-65].

The catalytic activity of pellistors can be largely affected by gas-phase species as part of the gaseous reactants. In addition to coke formation which results from the hydrocarbon catalyst interaction [66-68], poisoning have been reported for various chemical products such as molecules containing sulphur, halogen, silicon etc. [69-72]. It has been the focus in the course of the research of many scientists to understand the mechanism of the process of poisoning.

1.4 Plan

In the course of our research we have been particularly interested in the electrochemical deposition of nanostructured materials from the lyotropic liquid crystalline phases of non-ionic surfactant. We report about the deposition of nanostructured Pd and Rh metals by electrochemical reduction of the metal ions dissolved in the aqueous domains of a hexagonal lyotropic liquid crystalline phase. In Chapter 3 and Chapter 5 we describe in the first part the surface morphology using scanning electron microscopy and prove the existence for the hexagonal arrangement and regular pore distribution by TEM and XRD. In the next part we describe the electrochemical behaviour of the nanostructured Pd and Rh metal films covering the full range of potentials including the adsorption and desorption of hydrogen and oxygen. We focus our attention on the palladium - hydrogen system in Chapter 3 and in Chapter 4 we investigate in detail the effect of poisons on the process of the hydrogen absorption into Pd bulk.

Using the approach to the deposition of nanostructured Pd and Rh, in Chapter 6 we describe the deposition of two nanostructured metal films one on top of the other. In using cyclic voltammetric measurements we demonstrate the epitaxial deposition and show that the pores within the layers continuously interconnect.

The electrochemical deposition of Pd as high surface area metal with regular, controlled nanostructure is of potential application as a catalyst for methane oxidation in gas sensors. This is the subject of Chapter 7.

Chapter 2 Experimental

2.1 Chemicals and Materials

All aqueous solutions were freshly prepared using purified water (18 MΩ cm^{-1} resistance) from a Whatman "STILLplus" system coupled to a Whatman RO 50. Hydrochloric acid 37% (AnalaR BDH), sulfuric acid 98% (AnalaR BDH), ammonium tetrachloropalladate (premion-99.998% Alfa Aesar), rhodium (III) chloride (Alfa Aesar), hexachloroplatinic acid (Aldrich), Brij® 56 (Aldrich), octaethylene glycol monohexadecyl ether ($C_{16}EO_8$, Fluka), perchloric acid 60% (Fluka), crystal violet (Aldrich), sodium nitrate (Aldrich), sodium nitrite (Aldrich), sodium hydroxide (AnalaR BDH), ammonium chloride (Fisons plc.), methanol 99.8% (Alfa Aesar), and heptane 99% (Lancaster) were all used as received. To prepare the reference electrodes the following reagents were used: potassium chloride (AnalaR BDH), mercury (II) chloride (AnalaR BDH), mercury (electronic grade-99.9998% Alfa Aesar), sodium sulfate (AnalaR BDH), mercurous sulfate (Fluka). All glassware used was soaked overnight in a 3 % Decon/deionised water solution and washed thoroughly at least 3 times with deionised water prior to use.

2.2 Instrumentation

Experiments were carried out using an EG&G Potentiostat/Galvanostat Model 263 A. For the electrochemical studies the gold electrodes (1 mm and 25 μm diameter gold wires sealed in glass) were polished to a mirror finish using sand paper and then alumina (Buehler) slurries with successively smaller particle sizes ranging from 25 μm to 0.3 μm. For the purpose of structural characterization of the produced metal films the working electrode was a 1 cm^2 area flat electrode (made by evaporating of a 10 nm chromium adhesion layer followed by 200 nm thick gold layer onto thin glass microscopic slides). Large area (1 cm^2) platinum gauze was used as counter electrode. As reference electrode a home made saturated calomel electrode (SCE) as well as a saturated mercurous sulphate electrode (SMSE) were used. The 1 cm^2 flat gold working electrode was cleaned by sonication using an ultrasonic bath (Decon FS1006) in isopropanol for 15 minutes, then kept in deionized water until use.

The phase transitions were identified on the basis of the optical textures which are characteristic for each lyotropic liquid crystalline phase in a defined range of temperature and surfactant concentration. The presence of these phases was observed by using an Olympus BH-2 polarised light microscope equipped with a Linkam TMS90 heating stage and temperature control unit. The heating and cooling rates were varied between 30°C / min and 5°C / min. The temperature of the phase transition was recorded during the heating and cooling stage.

An analytical scanning electron microscope (JOEL 6400) or Philips (XL30ESEM) was used to study the morphology and structure of the films. The low-angle x-ray diffraction (Siemens Diffractometer D5000 with Cu $K\alpha$ radiation) was used to confirm the phase structure of the template mixture and as primary evidence for the formation of nanostructured metal films in the 2θ range from ~0.5 to ~ 5 degrees. In addition the crystal structure of the resulting material was studied using the wide angle x-ray diffraction. The regularity of the nanostructure was investigated using a JOEL 2000FX transmission electron microscope operating at an accelerating voltage of 200 kV. The TEM metal film characterization was carried out by scratching tiny metal particles from the gold substrate into the TEM Cu grid.

Mass spectra were recorded on a Micromass Platform quadrupole mass analyser (Micromass, Altrincham, UK) with an electrospray ion source. The instrument was calibrated with a mixture of sodium and caesium iodide, the operating conditions were capillary 3.5 kV, HV lens 0.5 kV, cone voltage 20 V, source temperature 110 °C, ES (Electrospray) eluent: 100% acetonitrile at 100 µl /min, ~1-10 µg / ml solutions were made using an Hewlett Packard (Palo Alto, CA, USA) HP 1050 autosampler.

2.3 Preparation of the liquid crystal template mixtures

The liquid crystalline template mixtures were prepared in wt% ratios of water mixed with the surfactant at room temperature. The solution appeared to be very viscous. To ensure homogeneity of the mixtures the solutions were heated and stirred manually for ca. 5 min using a glass rod. After cooling the temperature the template mixture becomes gel-like.

2.4 Electrochemical deposition of nanostructured metal films

2.4.1 Deposition onto gold electrodes of 1 mm and 25 μm diameter sealed in glass

Mesoporous Pd was deposited onto the freshly polished gold surface from a solution containing 12 wt% $(NH_4)_2PdCl_4$, 47 wt% Brij® 56, 39 wt% H_2O (purified) and 2 wt% heptane. The same composition was used to prepare a mesoporous platinum, and rhodium film from the metal salt – either H_2PtCl_6 or $RhCl_3$ – Brij®56, H_2O and heptane. In place of Brij®56, $C_{16}(EO)_8$ was also used subject to the experimental requirements. The electrochemical deposition of the mesoporous metals was carried out potentiostatically at 25 °C with the deposition initiated by a potential step from +0.4 V, where no reaction occurs, to +0.1 V where Pd, -0.1V where Pt or –0.2V, the potential where Rh are deposited. The potentials are reported with respect to the saturated calomel electrode. The total amount of all metals deposited, assuming a 100% faradaic efficiency, was controlled by measuring the total charge passed. 3.5 mC was the charge passed for the deposition onto gold electrodes of 1 mm diameter and 88 μC was passed for the deposition onto gold electrodes of 25 μm diameter. After deposition the mesoporous metal films were rinsed in purified H_2O in order to remove the adhering surfactant mixture.

2.4.2 Deposition onto the gold electrode area of SRL devices

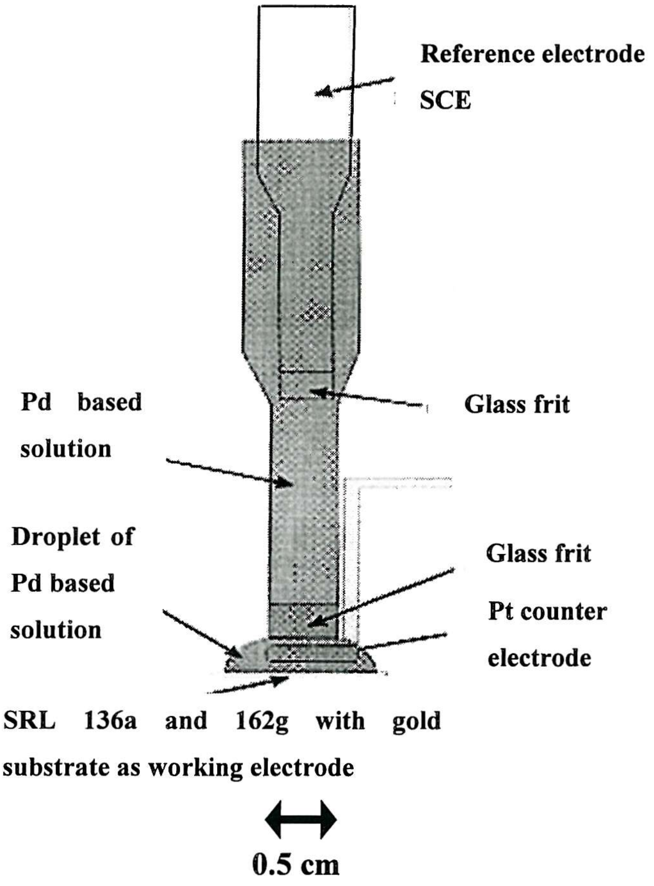

Figure 8: Schematic representation of the droplet apparatus

The electrochemical deposition of mesoporous metal films (Pd, Pt, Rh) from Brij® 56 and $C_{16}(EO)_8$ onto the SRL 162g and SRL 136a devices were carried out using the droplet apparatus shown in Figure 8. The substrates were positioned in a zero insertion force socket used as the sample holder positioned on an x,y,z microdrive. The droplet of electrolyte solution was confined to the area of the gold electrode on top of the micro-hotplate, taking care not to break down the heater membrane. To reduce the number of broken devices slight changes in the experimental procedure were made. The deposition mixture was put onto the electrode area.

The electrochemical deposition of mesoporous Pd from the hexagonal phase using 50 wt. % Brij® 56 or $C_{16}(EO)_8$ and 50 wt% 1.06 M $(NH_4)_2PdCl_4$ /heptane at 25 °C was carried out potentiostatically with the deposition initiated by a potential step from +0.4 V where no reaction occurs to +0.1 V where Pd is deposited. The potentials are reported with respect to the saturated calomel electrode.

The deposition of mesoporous Pt and Rh was carried out using $C_{16}(EO)_8$ or Brij®56, H_2PtCl_6 and $RhCl_3$ at the same composition shown above. The potential was stepped from +0.4V to –0.1V in the case of Pt and –0.2V for Rh. At these potentials the deposition of the metals occurs. The charge passed for the deposition of the metals were mostly of 20 mC.

Shortly after deposition the gold electrode area was rinsed in water (purified) for 5 minutes. The devices on which the mesoporous metals were deposited were soaked overnight in purified water unless otherwise stated.

2.5 Electrochemical measurements on nanostructured metal films

Mesoporous metal films were freshly prepared before each electrochemical measurement. Electrochemical measurements were carried out at room temperature in a glass beaker cell containing 1 M H_2SO_4 solution. A stream of highly purified argon was bubbled into the solution during the electrochemical experiments. The counter electrode was a large area platinum gauze. All potentials are reported with respect to the saturated mercurous sulfate electrode (potentials with respect to SMSE are shifted 0.45V negative of the corresponding potential vs. SCE). The reference electrode was used in conjunction with a Luggin capillary for all experiments and stored in a saturated potassium sulfate solution when not in use. The reference electrodes were rinsed in purified H_2O prior to use.

2.6 Gas-testing measurements of nanostructured metal layers deposited onto SRL devices

All the gas-testing measurements were carried out by City Technology.

To test the response of metal catalyst layers deposited onto devices to methane and volatile silicon compounds (HMDS), an entire gas testing rig was built. It consists of two major parts. The first is the gas handling part which controls the concentration of the gases as well as their flow and the second is the Wheatstone bridge with the interface electronics. This second part is in detail described in Chapter 7.

Two mass flow controllers (DMFC Tylan 2900 series), with a maximum flow of 500 sccm (standard cubic centimetre), were used to control the flow of the gases from their cylinders to the gas test chamber by controlling the total flow and therefore the total concentration of methane in air. The two gases used in this work were synthetic air and 2.5% methane in air, both supplied by BOC Special Gases. ¼" Nylon tubing was used to connect the cylinders, the mass flow controllers and the gas test chamber. A flow meter calibrated to air was put after the gas test chamber to ensure that the chamber was leak free. Exhaust of the gases was provided by a nylon tube going in a fumehood.

Chapter 3 The preparation and characterizaton of H_1-e Pd films

3.1 Introduction

In this chapter we report the deposition of nanostructured palladium by electrochemical reduction of palladium ions dissolved in aqueous domains of the hexagonal lyotropic liquid crystalline phase (H_I–e Pd).

The first part describes the phase behaviour of the plating system while the second part focuses on the characterization of the deposited nanostructured Pd film. Here we describe the surface morphology using Scanning Electron Microscopy and prove the existence for the hexagonal arrangement and regular pore distribution by Transmission Electron Microscopy and X-Ray Diffraction.

In the third part we describe the electrochemical properties of the H_I–e Pd film. The H_I-e Pd electrodes were studied over the full range of potentials including the adsorption and desorption of hydrogen and oxygen.

On the one hand our attention was drawn to potential regions where the surface oxide was formed. From the charge passed for the surface stripping reaction in the cyclic voltammetry we can calculate the electrochemical active surface area. To our knowledge, different surface oxide states can be produced on the Pd metal surface following through the cyclic voltammetry when applying periodic potential cycling to Pd electrodes. We were particular interested in the oxide states of the H_I-e Pd films when cycled to the oxide region. The use of H_I-e Pd films by Guerin [10] revealed remarkable voltammetric features in the oxide region on the anodic cycle presumable caused by different oxidation states of palladium.

On the other hand we focused our attention to more negative potentials in the voltammetry where the hydrogen adsorption/absorption on the Pd surface and into the bulk-Pd takes place. The palladium-hydrogen system has been the subject of several studies in the past [47-52]. The electrochemistry of palladium differs significantly from that of platinum. The Pd process has the special ability for hydrogen to enter and permeate rapidly through the lattice in large quantities. It is well-known that thin layers of Pd limit the amount of hydrogen absorbed into the bulk-Pd [50]. We are therefore interested to see the effect of the thin walls (2.5 nm) of our nanostructured Pd films on this process. As outlined in the literature the use of thin films of Pd as electrodes enhances the distinction between the adsorption and absorption of hydrogen

[50, 73, 74]. We focus on the separation between these two features and describe in detail the permeation of hydrogen through the metal lattice and the transition from the α- to the β hydride phase.

3.2 Phase behaviour

The nanostructure of the metals deposited from the lyotropic liquid crystalline phases of non-ionic surfactant mixtures are directly determined by the structures of the lyotropic phases used. We therefore found it necessary to characterize the phase behaviour of mixtures of non-ionic surfactant, water and palladium salt.

Two non-ionic surfactants were used in this work octaethyleneglycol monohexadecyl ether ($C_{16}EO_8$) and Brij®56. $C_{16}EO_8$ is available as highly purified, monodisperse material whereas Brij®56 is a polydisperse commercial cheaply available surfactant which is predominantly polyoxyethylene(10) cetyl ether (decaethyleneglycol monohexadecyl ether ($C_{16}EO_{10}$)) but also contains a range of other surfactants. Section 7.3.2 outlines this issue in detail showing mass spectroscopic analysis of Brij®56 and comparing three different batches of Brij®56 with each other.

Figure 9 shows the phase diagram obtained using mixtures of $C_{16}EO_8$ and ammonium tetrachloropalladate solution. The most common lyotropic liquid crystalline phases were observed: hexagonal, cubic and lamellar. The hexagonal phase, H_I, exists from 30 to 40 wt% $C_{16}EO_8$ up to 80 to 90 wt% and is stable up to 55°C for compositions around 55 wt% $C_{16}EO_8$. The cubic phase, V_I, occupies a smaller region of existence between 55 to 60 wt% and 80-90 wt% of $C_{16}EO_8$ in water at higher temperatures than the hexagonal phase with the maximum temperature point (61°C) around 60 wt%. At higher concentrations of surfactant in water the lamellar phase, L_α, predominates. The domain of existence of the lamellar phase starts between 55 and 60 wt% of surfactant in water and continues above 90 wt%.

Figure 10 shows the phase diagram of Brij®56 from which the similar phase behaviour is observed. The large region of the phase diagram is occupied by the hexagonal phase which domain of existence starts between 30-40 wt% of surfactant in water and continues to 80-90 wt%. In this case the hexagonal phase is stable to a similar value of temperature compared to the phase diagram of $C_{16}EO_8$ with the maximum point of 53°C at 55 wt% surfactant.

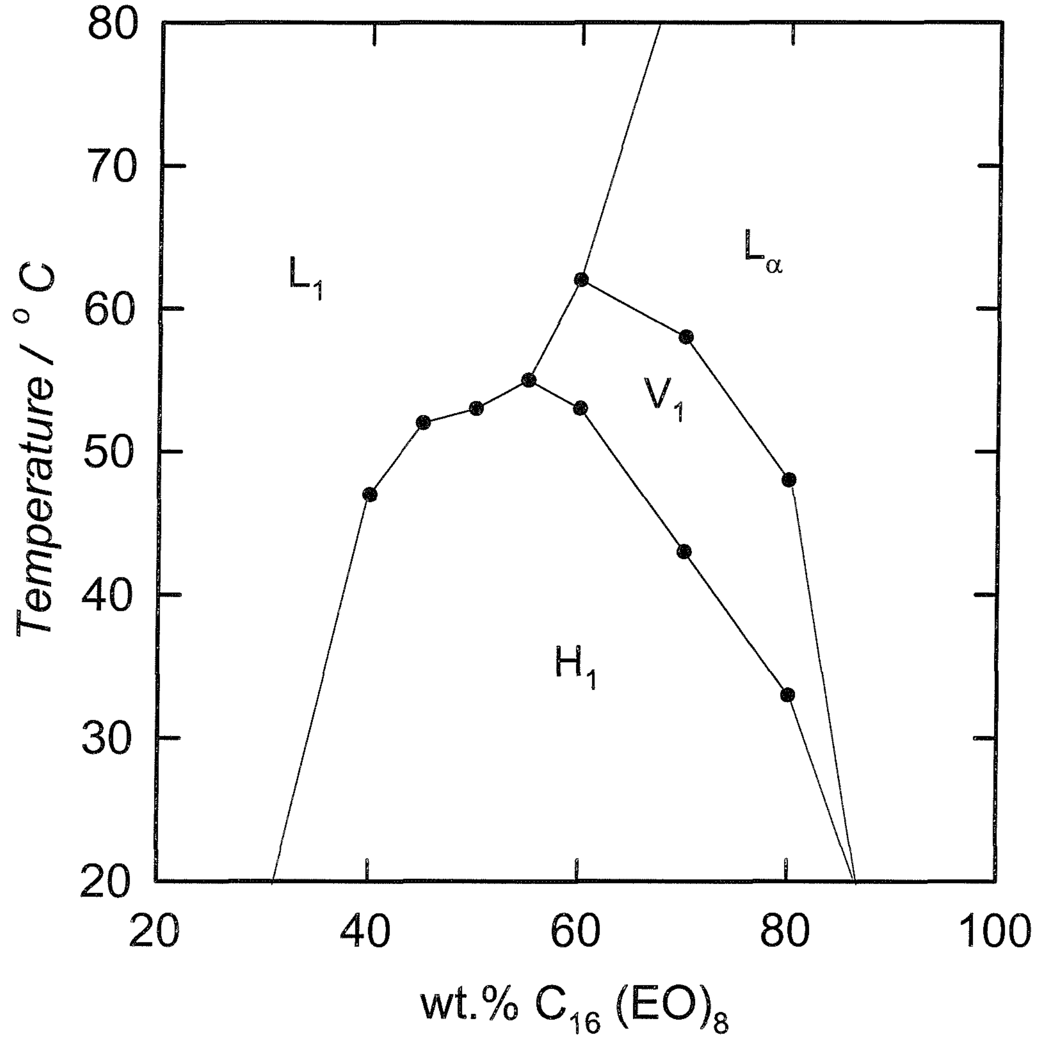

Figure 9: Phase diagram for mixtures of a 1.40 mol/l solution of $(NH_4)_2PdCl_4$ *in water and* $C_{16}EO_8$*. The concentration (by weight) of surfactant was increased from 20 to 80%.* H_1 *is the hexagonal phase,* V_1 *the cubic phase,* L_α *the lamellar phase and* L_1 *the micellar solution. The weight ratio between* $(NH_4)_2PdCl_4$ *and water was kept fixed at 0.4 and the weight ratio of surfactant to heptane was kept constant at 22.*

The cubic phase, V_1, has a slightly reduced range of stability. Although it exists in the same range of surfactant concentration as in the phase diagram for $C_{16}EO_8$ the maximum point occurs at 59°C at 60 wt% of surfactant in water.

The domain of existence of the cubic phase shown in both phase diagrams does not cover a large range of temperature and no evidence has been found for the existence of this phase at room temperature. However, the electrodeposition of mesoporous Pd from this phase can lead to a relatively high surface area which is of interest for the use of mesoporous Pd films as high surface area metal catalyst deposited on low-power micropellistors.

The domain of existence of the lamellar phase for Brij®56 looks very similar to those results reported for $C_{16}EO_8$. Comparing the phase diagram in our studies to the phase diagram of $C_{16}EO_8$ in water shown by Mitchell et al. [11] we do not note any difference. In our case we assume that the addition of ammonium tetrachloropalladate does not perturb the phase boundaries. This contrasts to the results shown in [23] where hexachloroplatinic acid added to the template mixture of $C_{16}EO_8$ + water leads to qualitative changes in the phase behaviour caused by interaction between the metal salt and the surfactant head groups.

Brij®56 is a bulk commercial surfactant and slight variations in compositions occur between the different batches. Measurements using two different batches of material showed essentially the same phase behaviour when mixed with water and ammonium tetrachloropalladate solutions except there was a variation of ±1.5 °C in the positions of the hexagonal/cubic and cubic/lamellar boundaries.

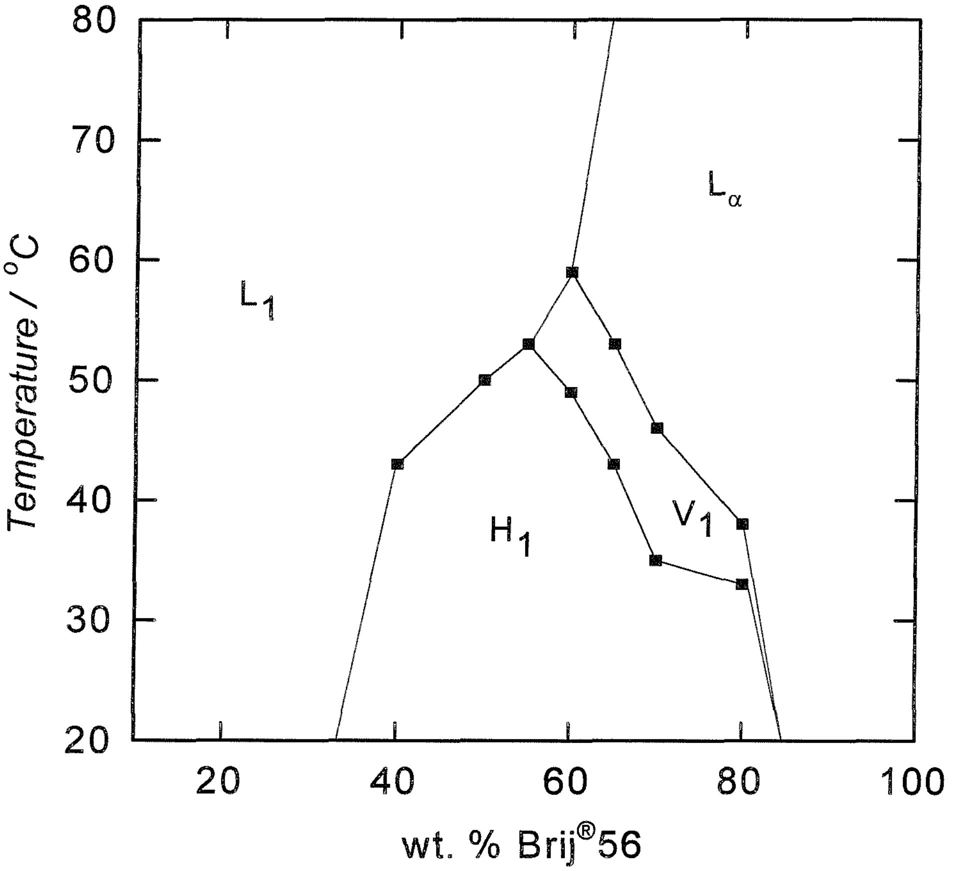

Figure 10: Phase diagram for mixtures of a 1.40 mol/l solution of $(NH_4)_2PdCl_4$ *in water, Brij®56 and heptane. The ratio between* $(NH_4)_2PdCl_4$ */ water (0.4) and surfactant / heptane (22) was kept constant. The composition (by weight) of surfactant in the aqueous solution was increased from 20 to 80%.* H_I *is the hexagonal phase,* V_I *the cubic phase,* L_α *the lamellar phase and* L_I *the micellar solution.*

This section has shown the phase behaviour of mixtures containing non-ionic surfactant, water and palladium salt. We have not found much difference of the phase behaviour when $C_{16}EO_8$ or Brij®56 was used as surfactant. Subsequent reduction of Pd salt leads to Pd hexagonally arranged on nanometer scale. In the next section we study briefly the electrodeposition of these metal films.

3.3 Electrodeposition of mesoporous Pd onto gold electrodes

This section describes the Pd deposition onto the gold electrode from the template mixture. The Pd salt was mixed with the non-ionic surfactant, water and heptane to produce the template mixture for the deposition of the mesoporous Pd films. No supporting electrolyte was added to the templating solution as this could influence the existence of the liquid crystalline phases and disrupt the pore arrangement.

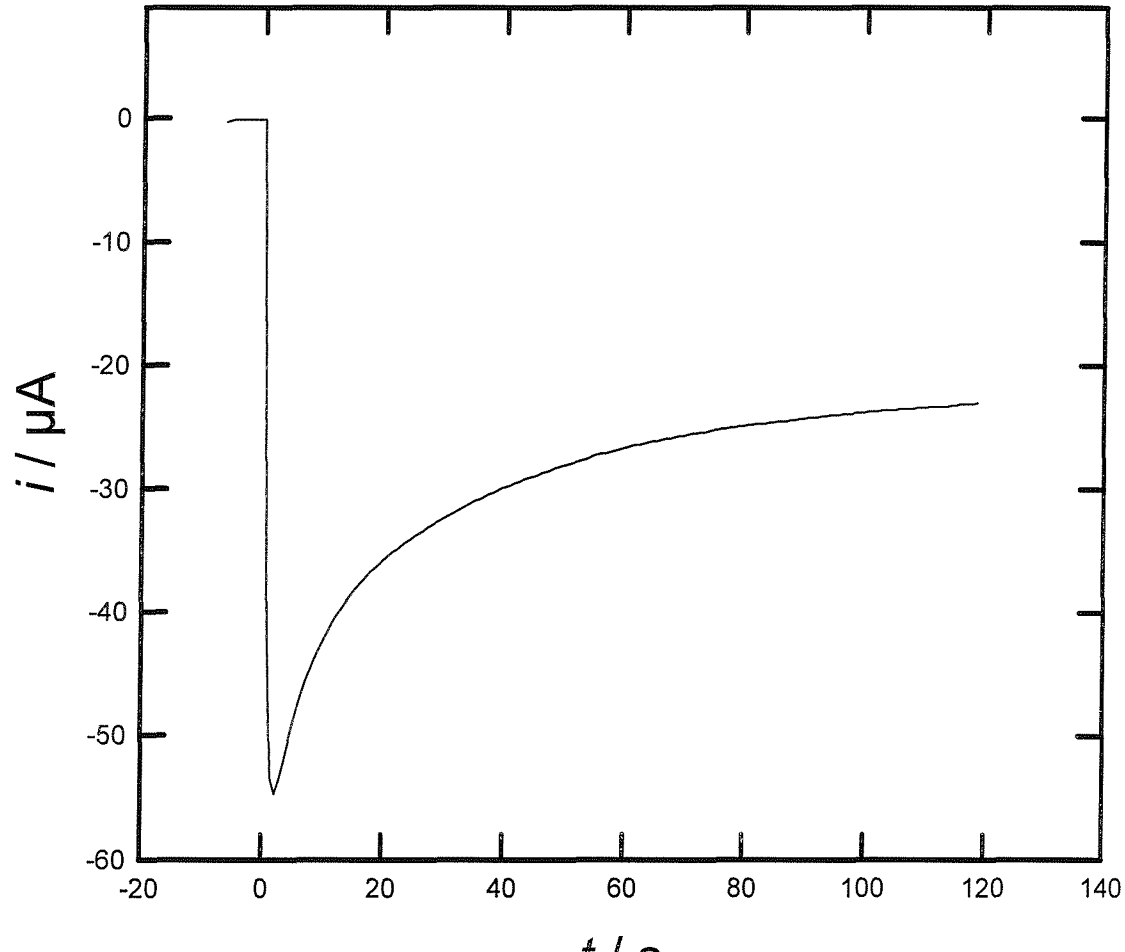

Figure 11: Current transient for the electrodeposition of mesoporous Pd from 12 wt% $(NH_4)_2PdCl_4$ + 47 wt% $C_{16}EO_8$ + 2 wt% heptane and 39 wt% water at 0.1 V vs SCE on 1 mm diameter gold disc electrode

Figure 11 shows a typical current transient obtained during the electrodeposition of Pd from the template mixture at 0.1 V vs SCE on a 1mm diameter gold disc electrode. S. Guerin [10] investigated the elctrodeposition of Pd under the same conditions and found 0.1 V as suitable potential for the deposition of Pd. From the figure we note that the reduction current rises nearly to -55 μA immediately after the potential step as a result of the double layer charging. The current decreases then to reach -24 μA after 120 s. The total amount of Pd deposited, assuming a 100% faradaic efficiency, corresponds to a charge of 3.5 mC. The current never reaches a plateau over the period of time of 120s but the decay becomes very slow thereafter.

We would not expect the current of mesoporous Pd to reach the plateau due to the fact that the mixture is too thick to allow convection. Therefore a concentration polarization may occur which would force the Pd ions to travel further to reach the electrode surface. The ions come from further away and hence the current at the electrode surface decreases towards zero. This is in contrast to the results shown for Pd deposited from the aqueous solution [10]. The current reaches a plateau presumably because of the convection in the solution.

This section has briefly shown the properties of the electrodeposition of mesoporous Pd from the template mixture. In the next section we study in detail the characterization of these metal films.

3.4 Characterization of nanostructured palladium

The H_I-e Pd films electrochemically deposited at 0.1 V vs SCE from the hexagonal phase are adhered well to the evaporated gold electrodes used for the deposition.

Figure 12 shows a scanning electron micrograph of an H_I-e Pd film. Scanning Electron Microscopy (SEM) was used to examine the surface morphology of the deposited mesoporous Pd film.

Figure 12 shows the edge of view of mesoporous Pd film at a tilt angle of 70° deposited on gold/glass. The H_I–e Pd film is starting to lift away from the substrate. The film is dense, uniform and continuous over the whole range with no evidence of nanostructure on the SEM scale.

To examine the nanostructure of the electrochemically deposited Pd films it is necessary to use Transmission Electron Microscopy (TEM). To provide clear evidence for the hexagonal arrangement of Pd films in nanometer – sized dimensions is subject to the orientation of the TEM-image. The evidence for the hexagonal array of the pores running through the Pd film can be given if the image shows a "pores end on" view. However, the experiments carried out by B. Cressey at the Southampton microscopy centre revealed that the pores end on image is rather unlikely to be obtained. This is certainly the case for Pd films prepared from the Brij®56 template mixture. Figure 13 shows an orientation of the TEM–image from which the hexagonal array of the pores cannot be seen but we can see the porous channels running through the film. Inspection of these pores shows that they are continuous and approximately straight over their whole length. The pores of the structure shown in Figure 13 have a diameter of (20 ± 2 Å) and the wall thickness has been found to be (20 ± 2 Å). The measurements were taken using the software programm "Scanimage". Figure 14 shows the TEM – image of H_I–e Pd scraped from the electrode surface. This image shows an orientation of the sample which approaches the pores end on view. From the results obtained we can conclude that clear evidence for hexagonal arranged pores cannot be given. We note slight indication of a porous structure consisting of cylindrical pores with pore size diameter of (25 ± 2) Å and wall thickness of (25 ± 2 Å).

In both figures the porous structure only appears at the edge of the TEM-image of the Pd-film scraped from the electrode surface. Most part of the image appears to be dark since the sample is too thick and therefore the electron beam cannot travel through.

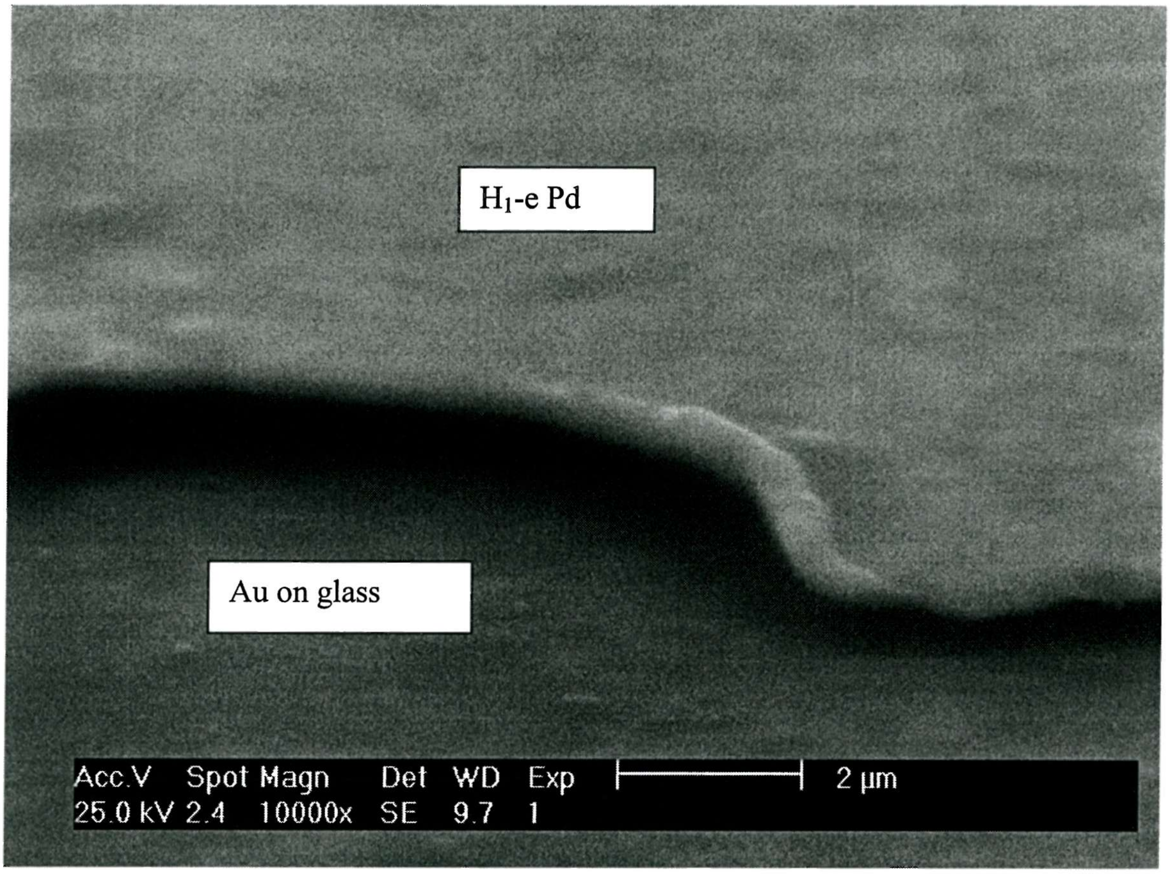

Figure 12: Scanning electron micrograph of an H_1-e Pd film deposited on an evaporated gold electrode. The film was deposited from a mixture of 12 wt% $(NH_4)_2PdCl_4$, 47 wt% $C_{16}EO_8$, 39 wt% water, 2 wt% heptane. The total charge passed was 0.53 C/cm^2 and the image was obtained at the tilt angle of 70°.

Better evidence for a regular pore distribution in H_1-e Pd films may be given by X-ray diffraction. The Pd films formed by electrochemical deposition from the template mixture were studied by low angle XRD. *Figure 15* shows the low angle XRD patterns obtained for the hexagonal phase of the Pd template mixture. The low angle x-ray reflection of the Pd film shows a diffraction peak corresponding to the (100) diffraction plane of the hexagonal structure with a d-spacing of 55 Å. This value was estimated using the Bragg equation.

$$n\lambda = 2d\sin\theta \qquad \text{Equation 1}$$

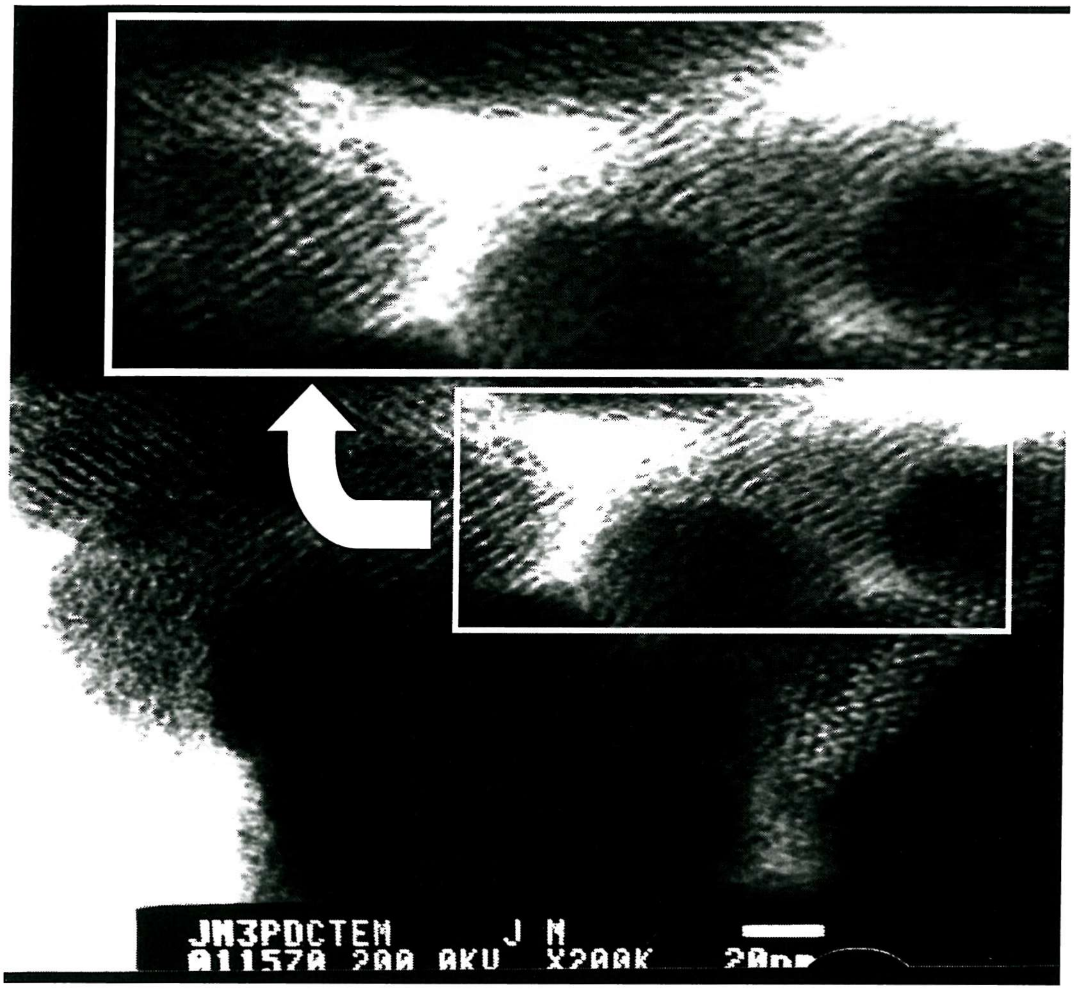

Figure 13: Transmission electron micrograph of a sample scraped from an H_1-e Pd film deposited from the template solution of 12 wt% $(NH_4)_2PdCl_4$, 47 wt% $C_{16}EO_8$, 39 wt% water, 2 wt% heptane on an evaporated gold electrode. The charge passed for deposition was 0.55 C / cm^2.

Although the peak maximum in *Figure 15* appears to be broad, the value calculated for the d-spacing is consistent with the deposition of Pd films with a nanostructure of regular pore distribution derived from the structure of the template solution. The pore to pore distance for this hexagonal array, given by $d_{100} / \cos 30^{\circ}$, was found to be 63.5 Å.

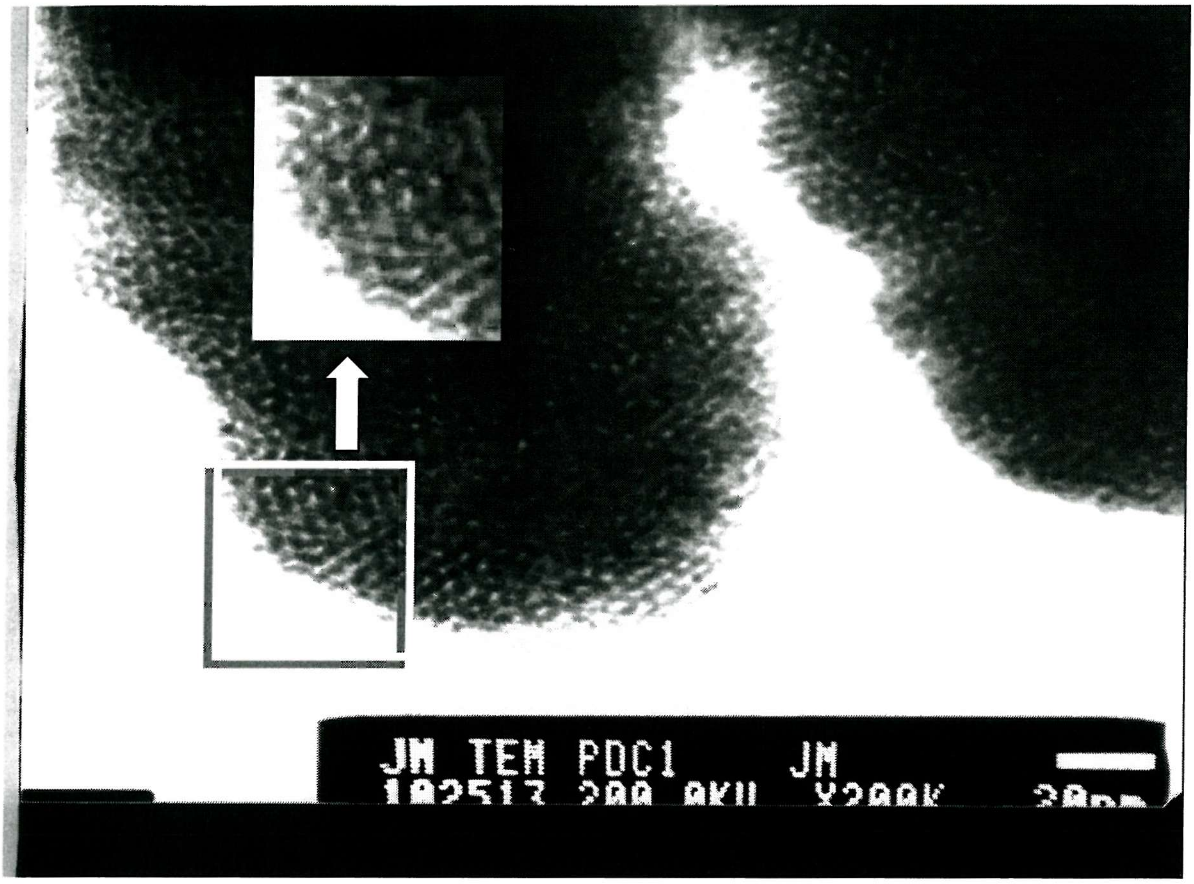

Figure 14: Transmission electron micrograph of a sample scraped from an H_I*-e Pd film deposited from the* $C_{16}(EO)_8$ *templating bath under the same conditions as in Figure 13. .*

The high angle XRD patterns for Pd films electrochemically deposited on evaporated gold from the hexagonal template phase are shown in Figure 16. The diffraction patterns show the characteristic reflection for a highly polycrystalline Pd film with a face centred cubic crystal structure [75]. The diffraction pattern for the Pd film exhibits a (111) growth orientation with a significant (200) reflection.

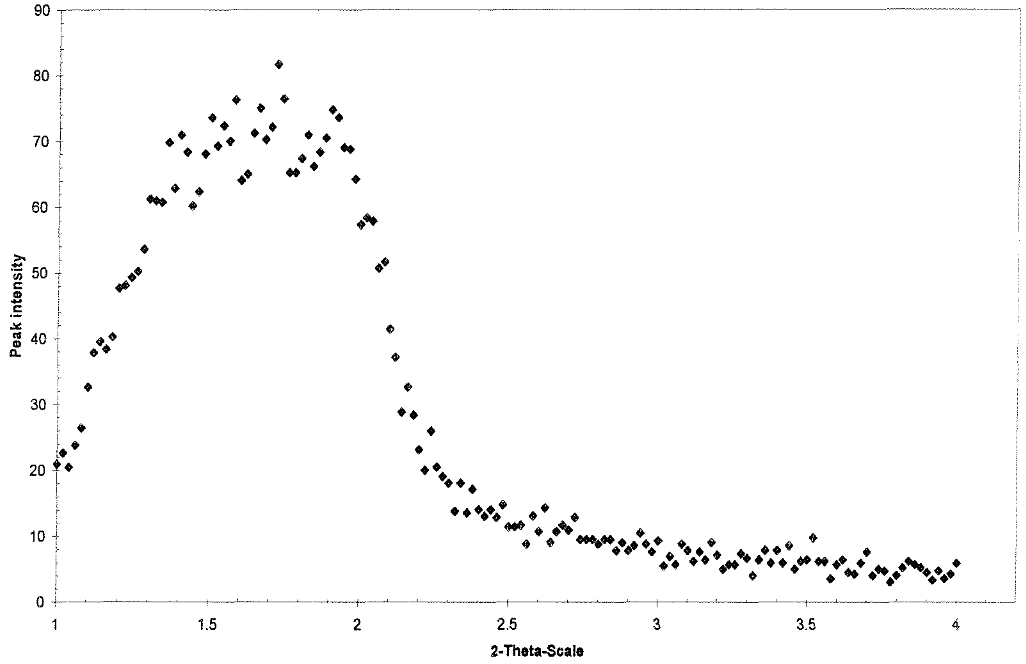

Figure 15: Low angle x-ray reflection of an H_I*-e Pd film deposited on an evaporated gold electrode from the template solution 12 wt%* $(NH_4)_2PdCl_4$*, 47 wt%* $C_{16}EO_8$*, 39 wt% water, 2 wt% heptane.*

The grain size of the Pd film was estimated from the XRD peak broadening by means of the Scherrer equation [76].

$$L = 0.9\,\lambda / \beta \cos\theta \qquad \textit{Equation 2}$$

Where L is the grain size thickness (Å), λ is the wavelength of x-ray (1.54 Å), β is the width at half height in (rad) of the 2 θ diffraction peak and θ is the diffraction angle of the peak centre.

The estimated grain size of the Pd particle was found to be 200 Å.

Mesoporous Pd films deposited onto the gold substrates were shown to be dense, uniform and continuous. By using TEM we only have slight indication for the hexagonal arrangement of the Pd film on nanoscale. Clear evidence for the regular pore distribution was given by XRD-measurements. In the next section we use cyclic voltammetry to determine the electroactive surface area of H_I-e Pd films as another tool to prove the existence of the nanostructure.

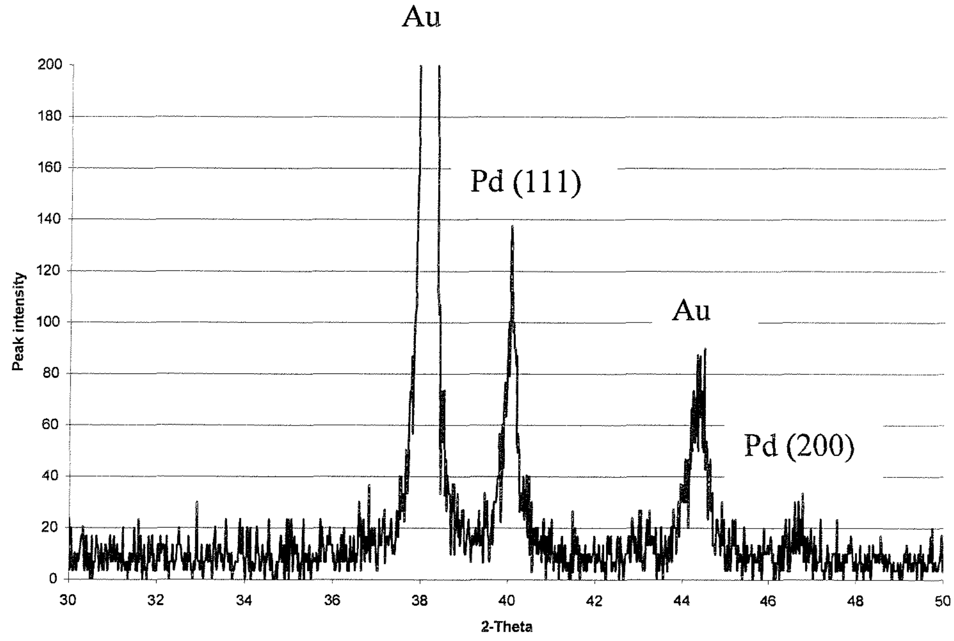

Figure 16: Wide angle x-ray reflection of an H_I-e Pd film deposited on an evaporated gold electrode. The 2-Theta scale between 30 and 50° was enlarged.

3.5 Electrochemical characterization of the electroactive surface area

Cyclic voltammetric measurements were used to characterize the electrochemically active surface area of H_I-e Pd films estimated from the charge passed for the oxide stripping peak. The H_I-e Pd films were deposited from the liquid crystalline templates containing mixtures of surfactant molecules and aqueous solutions spontaneously assembled into regular structures of nanometer-sized dimensions. After deposition the surfactant filled the pores of the H_I-e Pd films. The obtained nanostructured metal films were then washed in water to remove the surfactant. Superficial washing removed the surfactant only from the outside of the film. Comparing Figure 17 and Figure 18 it will become clear that prolonged washing was necessary to remove the surfactant out of the pores.

Figure 17 shows a set of voltammograms of H_I-e Pd film in 1 M sulfuric acid solution at 20 mV/s deposited on a gold disc electrode of 1mm diameter. The film was washed for 10 min in water after deposition. The hydrogen region, which is explained in detail in section 3.7, exhibits well-resolved peaks associated to the formation of adsorbed and absorbed hydrogen.

We focus in this part on the oxide region. On the anodic scan, from 0.1 V the formation of the surface oxide layer occurs. On the reverse scan, the cathodic sweep, the reduction of the formed surface oxide appears giving rise to a well defined peak at 0.05 V. These features are very similar to those of bulk polycrystalline Pd electrodes under the same conditions outlined in section 3.7.2.

However it has to be stressed that the charge passed for the formation and stripping of the surface oxide layer reaches smaller values than for H_I-e Pd films.

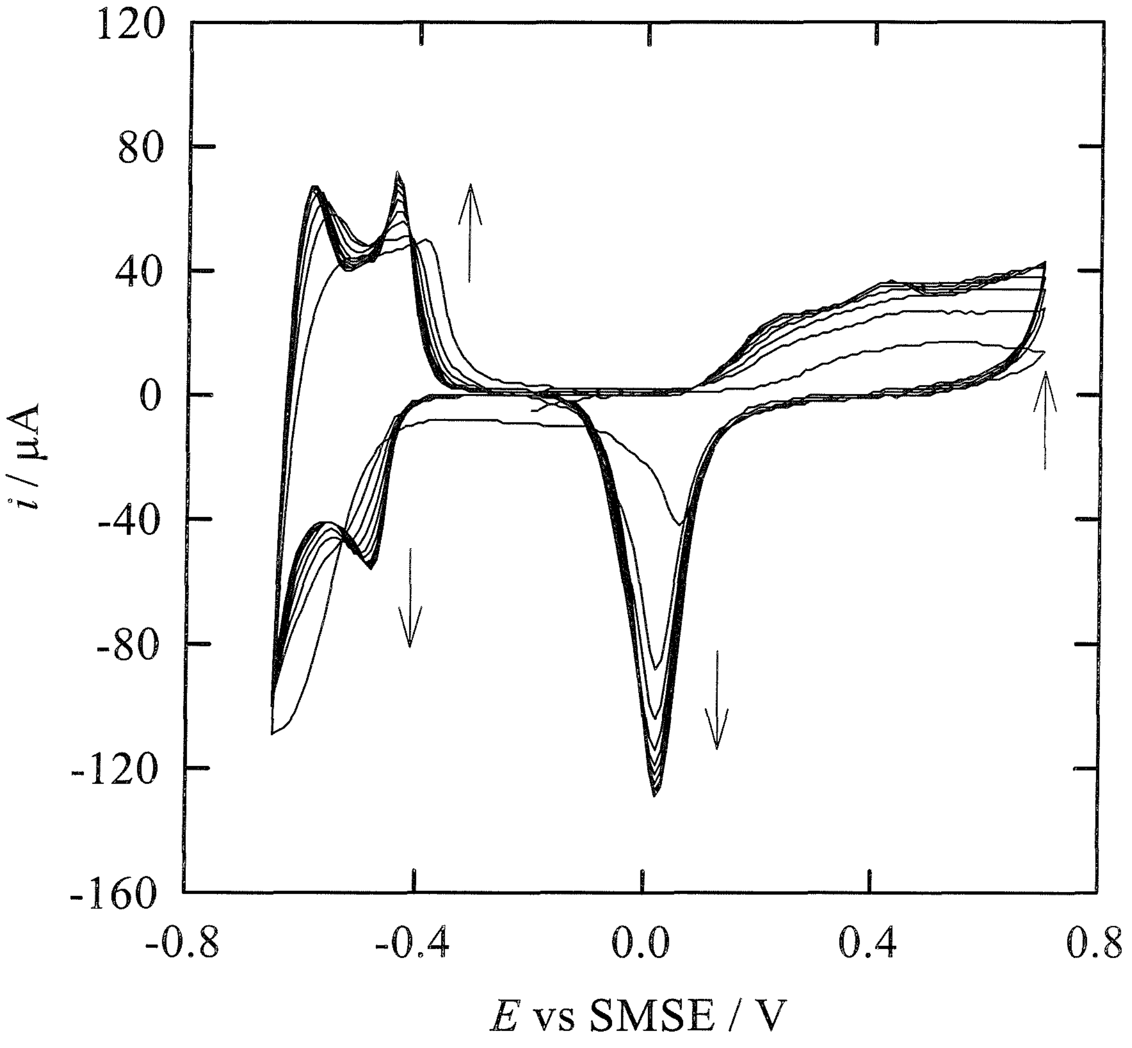

Figure 17: Cyclic voltammogram of an H_I-e Pd film (200 nm thick, deposited from the Brij®56 plating bath, total deposition charge 3.5 mC) deposited on a gold disc electrode (area 0.0079 cm^2) recorded at 20 mV/s in 1 M sulfuric acid. The film was soaked in water for 10 min immediately before the start of the voltammetry.

The peaks for the formation and reduction of the H_I-e Pd surface oxide layer increase in size with each successive cycle. This happens because the surfactant left in the pores of the H_I-e Pd after deposition diffuses out and are replaced by the 1 M sulfuric acid solution during cycling. As a consequence the electrochemically active surface area in contact with the acid solution increases which leads to the increase of the charge associated to the formation and removal of the surface oxide layer.

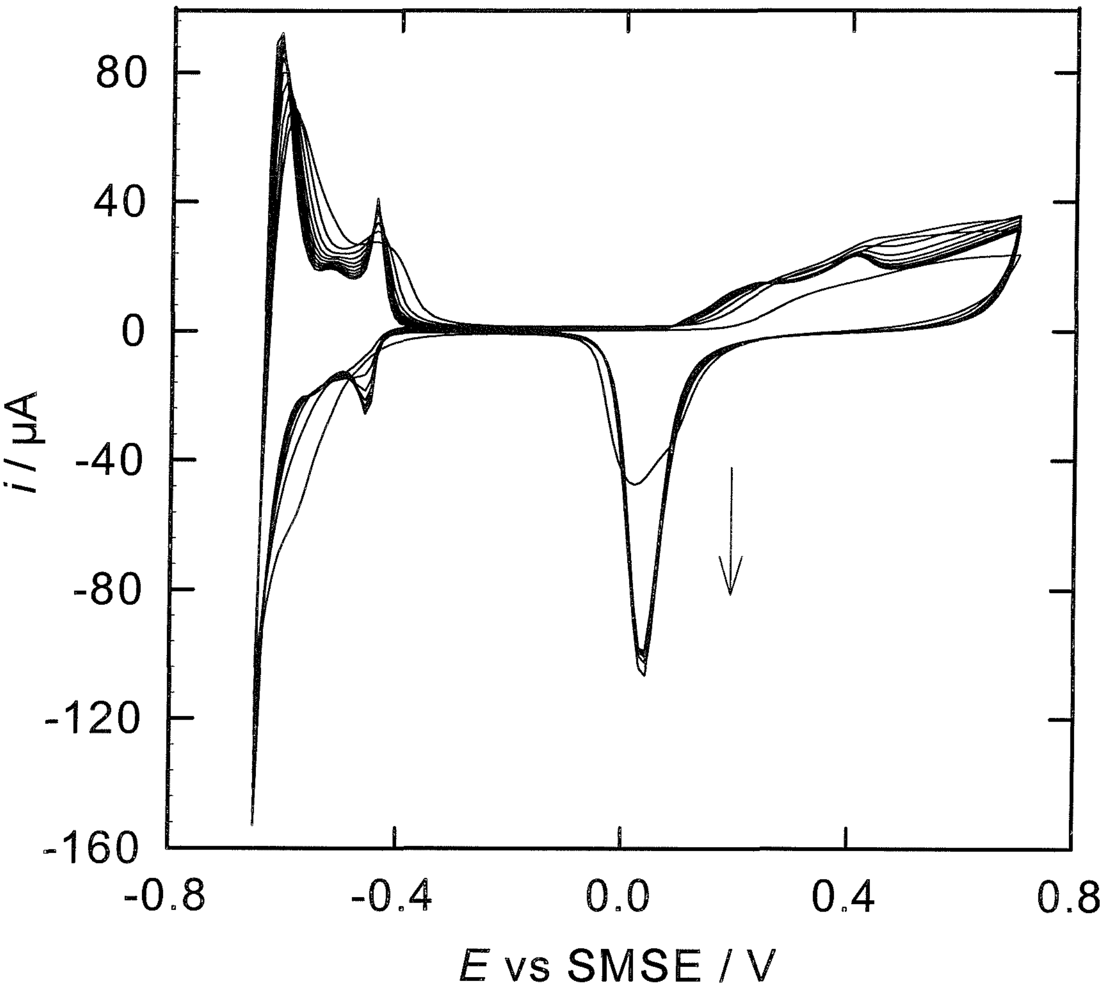

Figure 18: Cyclic voltammogram of an H_I *–e Pd film (200 nm thick, deposited from the Brij®56 plating bath, total deposition charge 3.5 mC) deposited on gold disc electrode (area 0.0079* cm^2*) recorded at 20 mV/s in 1 M sulfuric acid. The film was soaked in water for 1 hour before the start of the voltammetry.*

Figure 18 shows a set of voltammograms of H_I-e Pd in 1 M sulfuric acid at 20 mV/s deposited on the gold disc electrode of 1mm diameter. The same conditions were chosen compared to the voltammogram in Figure 17. The difference in Figure 18 is the prolonged washing to remove the surfactant from the pores (1 hour). We can see from Figure 18 that the charge associated to the removal of the surface oxide layer stabilizes after only one cycle indicating that the surfactant originally occupying the pores diffused out. This effect implies that to get a stable voltammetry after the first cycle requires a prolonged washing of H_I-e Pd in water of at least one hour to remove the surfactant from the pores. The changes in the voltammetry between the first and the subsequent cycles in Figure 18 are caused by the fact that the soak of 1 M sulfuric acid into the pores cleans the Pd surface.

As expected, it takes more time for the removal of all of the surfactant from the pores for films with increase in thickness as the pores become longer. Experiments (not presented here) showed that that to wash out the surfactant completely from the pores of a film of 1 μm thickness takes at least 4 h.

To estimate the total surface area from the charge passed the oxide stripping peak Rand and Woods [77, 78] used the conversion factor of 424 $\mu C / cm^2$. They investigated the voltammetry of polycrystalline Pd in 1 M sulfuric acid. We transferred this conversion factor to our studies, Figure 18, assuming that the surface oxide layer formed on our nanostructured Pd electrodes is the same as that formed on bulk Pd electrodes. We obtained a specific surface area of 91 m^2 / g and an area per unit volume of 1.1×10^7 cm^2 / cm^3, a value which is consistent with the nanostructure found by TEM and XRD and implies that the pores running throughout the nanostructured film are completely accessed by the electrolyte solution. Taking all prepared samples into account we found on average a variation in the estimated surface area of 20%.

Cyclic voltammetric measurements revealed the existence of high surface area Pd metal films electrochemically deposited on nanoscale. To access electrochemically the high surface area given by the nanostructure with the first cyclic voltammetric cycle it was necessary to soak the freshly prepared Pd films in acid media to replace the surfactant left in the pores of the nanostructure by the electrolyte solution. The longer the pores become due to the increase in thickness of the metal film the more time it takes to wash out the surfactant. Proceeding from the fact that we can obtain nanostructured Pd metal films by direct-templating from the liquid crystalline phases with access to the high electroactive surface area we can now focus on the oxide region given in the cyclic voltammogram of these H_I–e Pd films.

3.6 The oxide region in the voltammetry of H_1-e Pd

3.6.1 Mass loss of H_1-e Pd by repeatedly cycling into the oxide formation region

To investigate the dissolution of H_1-e Pd films, determined by the decrease of mass of Pd electrodes, during cycling in 1 M sulfuric acid voltammetric measurements were carried out with the use of the EQCM-equipment which enables us to monitor the changes of the mesoporous Pd film during the experiment.

EQCM works by using a thin quartz crystal partially loaded on both sides with metal electrodes. These two electrodes serve two purposes. They allow us to establish an alternating electrical field across the crystal, causing the crystal to vibrate around the resonant frequency and in addition one of them can be used as a working electrode for electrochemical experiments. The earliest forms of EQCM were using the Sauerbrey equation to interpret the frequency changes of the quartz crystal.

$$\Delta f = -2f_0^2\ \Delta m / A(\mu_q \rho_q)^{1/2} \qquad \textit{Equation 3}$$

where Δf is the frequency shift,

f_0 is the resonant frequency of the quartz crystal before mass changes,

Δm is the mass change,

A is the piezoelectrically active area,

μ_q is the shear modulus of the quartz crystal,

ρ_q is the density of the quartz crystal.

It can be seen from equation 3 that this model assumes that only mass changes induce frequency shifts. In fact, frequency changes will also be affected by changes in the viscoelastic properties of the layer and of the solution in contact with the electrode. Since the frequency changes have a more complex origin than a simple mass change, another equation describing the frequency changes and taking into account the mass changes and the viscoelastic properties of the overlayer at the electrode was proposed. It is known as the Sauerbrey-Kanazawa-Bruckenstein equation.

$$\Delta f_s = -(2f_s^2 / (\mu_q \rho_q)^{1/2})\ (\Delta m / A) - (f_s^{3/2} / (\pi^{1/2}\ (\rho_q \mu_q)^{1/2})\ (\rho_L \eta_L)^{1/2}) \qquad \textit{Equation 4}$$

where ρ_L and η_L are the mass density and the viscosity of the liquid,

f_s is the frequency of the quartz crystal and the overlayer [79].

However changes in frequency alone are insufficient to describe mass and viscoelastic changes. It is necessary to focus on the distinction between the contribution of rigid mass and viscoelastic properties to frequency changes. Therefore an electrochemical model based on the Butterworth-van Dyke equivalent circuit was established to separate the mass from the resistive components of the oscillating frequency. The analysis method employed in our case has been described by Calvo et al. [80] and uses a non-linear fitting analysis of the measured electroacoustic impedance of a quartz crystal to extract mass and viscous resistance of the overlayer.

We considered a viscous solution in contact with a thin and rigid gold electrode deposited on the quartz crystal. These conditions satisfy the criteria for the relative hardness of the underlayer (gold electrode) and the overlayer (template mixture) described by Calvo et al. [81]. Therefore the contribution of the overlayer to the total impedance is expressed as:

$$Z_f = R_f + j\omega L_f \quad \text{with } \omega L_f = X_{Lf} \qquad \text{Equation 5}$$

Where R_f and X_{Lf} are the real and the imaginary parts of the electroacoustic impedance.

Two limiting cases can be distinguished, the first is for a film of low viscosity. Here the imaginary part, X_{Lf}, of equation is equal to the real part R_f. The second case is for a film of high viscosity. In this case the real part R_f tends towards zero. This limit corresponds to the Sauerbrey equation and the imaginary part is given by:

$$X_{Lf} = (2\omega_0 L_q / (\pi(\mu_q \rho_q)^{1/2})(\omega_0 m_f / A) \qquad \text{Equation 6}$$

Where m_f is the mass of the overlayer and A the active area of the quartz crystal.

To explain simply the changes R_f and X_{Lf} during the experiment we conclude that for our model, R_f only depends on viscoelastic changes of the overlayer whereas X_{Lf} depends on both, the viscoelastic changes and the mass changes of the overlayer. In the case where $\Delta R = 0$ the imaginary part of the electroacoustic impedance X_{Lf} corresponds to the Sauerbrey equation and purely on mass changes. From the measurements of the electroacoustic impedance we can extract the real and imaginary part. This allows us to obtain useful information on mass and viscoelastic properties of the electrochemical reaction.

After electrodeposition of mesoporous Pd onto the quartz crystal from the hexagonal lyotropic liquid crystalline phase the mesoporous Pd film was rinsed with purified water to remove the template from the outside of the film. The mesoporous Pd film was then soaked in water overnight to remove the surfactant from the pores.

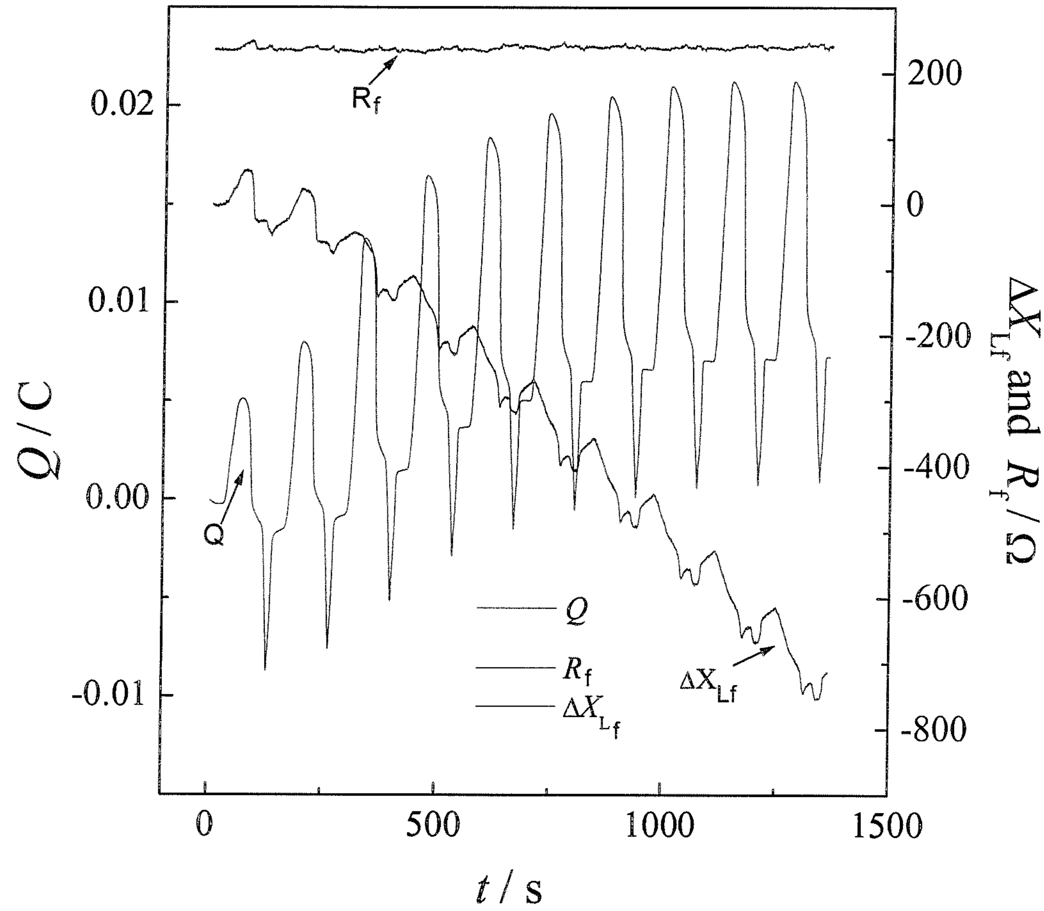

Figure 19: Cyclic voltammogram of H_I*-e Pd in 1 M* H_2SO_4 *at 20 mV/s with the simultaneous use of EQCM. It shows the changes in the real* R_f *and imaginary parts* ΔX_{Lf} *of the electroacoustic impedance and changes in the charge* Q *passed for deposition of the mesoporous Pd film when cycled between -0.65 to 0.7 V vs SMSE.*

Figure 19 shows the results of continuous cyclic voltammetry between -0.65 V to 0.7 V vs SMSE of a mesoporous Pd film at 20 mV/s in 1M sulfuric acid with simultaneous use of EQCM.

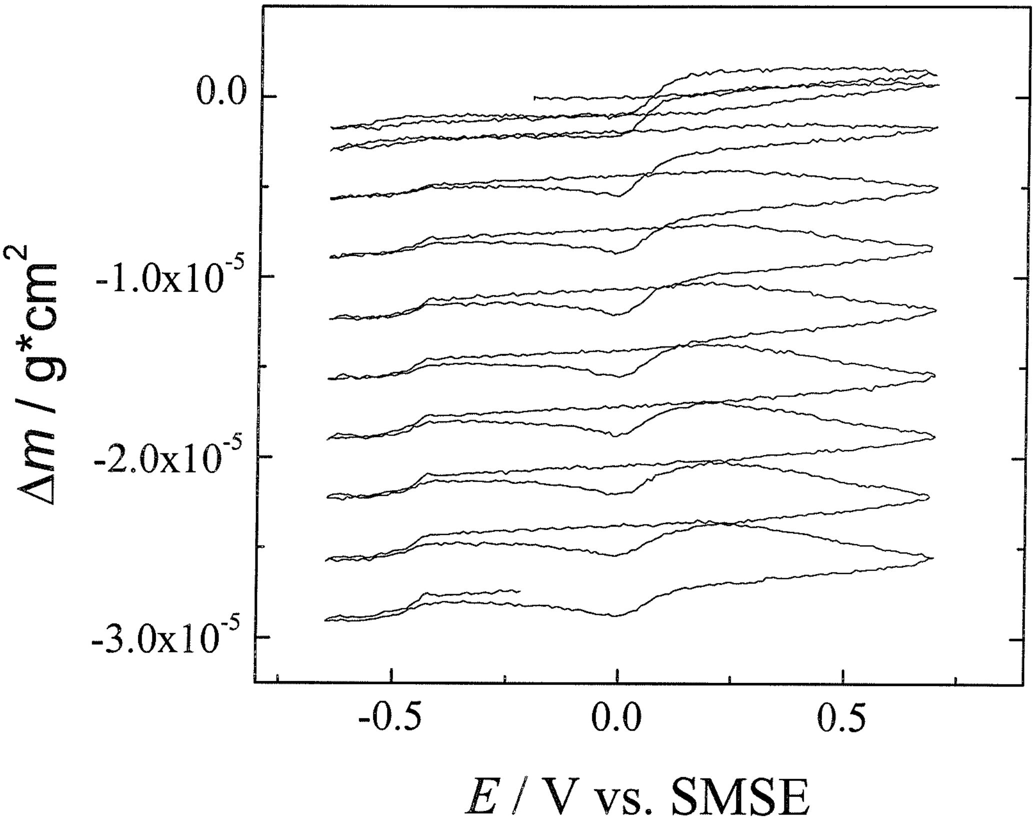

Figure 20: Mass changes of a mesoporous Pd film during cycling between -0.65 to 0.7 V at 20 mV/s in 1 M sulfuric acid. Same experimental conditions as in Figure 19.

We can see from the figure that the real part of the electroacoustic impedance, R_f, does not change at all during the process which indicates that the viscoelastic properties of the nanostructure have not been affected. It is of interest to note that the imaginary part ΔX_{Lf} decreases during the experiment. The fall in ΔX_{Lf} implies the loss of mass according to the Sauerbrey equation (equation 6).

Figure 20 focuses on the changes of mass as a function of potential. This experiment shows 10 continuous cyclic voltammtric cycles. We can see from this experiment that the quantity of Pd lost during the whole experiment is far from negligible (12%). Such a result can dramatically influence the estimation of the surface area which is based on the total mass of Pd deposited assuming a faradaic efficiency of 100%.

The EQCM-measurements on the mesoporous Pd film during cyclic voltammetry in 1 M sulfuric acid show that the loss of mass starts with the formation of the surface oxide layer at around 0.1 V vs SMSE on the anodic cycle and stops around 0.05 V on the cathodic scan, with a beginning of the mass gain, when the oxide is stripped from the electrode surface. Similarly the mass gain stops with the beginning of the mass loss in the cathodic scan at 0.1 V. Similar behaviour of mass loss is identical to that reported for bulk polycrystalline Pd [46, 78, 82]. Figure 20 shows 10 continuous cycles with the mass constantly decreasing with each cycle. In fact, during the first cycle the mass loss was approximately 1 $\mu g/cm^2$ and increased then to a value of 4 $\mu g/cm^2$ after 10 cycles. The mass gain caused by the redeposition of Pd onto gold or one Pd layer on top of another follows the same behaviour and increases cycle after cycle.

The decrease in mass implies the dissolution of the surface oxide layer formed when cycled in the oxide region. Conversely at the potential at which the oxide is stripped from the electrode the metal, reduced to the zero oxidation state, is redeposited. It can be seen from the imaginary part, ΔX_{Lf}, that the mass loss dominates over the mass gain, so more metal dissolves than is replated. This is certainly linked to the cycling in sulfuric acid. Similar results to those obtained in our studies have appeared for bulk polycrystalline Pd [77]. It shows the dissolution of Pd in the presence of sulfuric acid when cycled in the oxide region.

To investigate the effect of cyclic voltammetric cycles in 1 M sulfuric acid on the surface area 40 subsequent voltammetric cycles were carried out at 100 mV/s in 1 M sulfuric acid on mesoporous Pd deposited on a gold disc electrode. The current was related to the surface oxide stripping peak of each cycle. The resulting plot is shown in Figure 21. We can see from this figure that the current increases significantly to 6 cycles. As the current is related to the surface oxide stripping peak the electrochemically active surface area increases with each cycle; from the 6th cycle the current decreases and hence the active surface area is decreasing.

A possible explanation for the increase of the electrochemical active surface area might be given when taking the surface roughening by dissolution and replating into account. We proceed from the fact that the residue of surfactant was removed completely from the pores by soaking the H_I-e Pd layers in water. This was shown in the cyclic voltammetry of H_I-e Pd in 1 M H_2SO_4 in Figure 18 where the surface oxide stripping peak stabilizes after only one voltammetric cycle indicating that the surfactant originally occupying the pores diffused out.

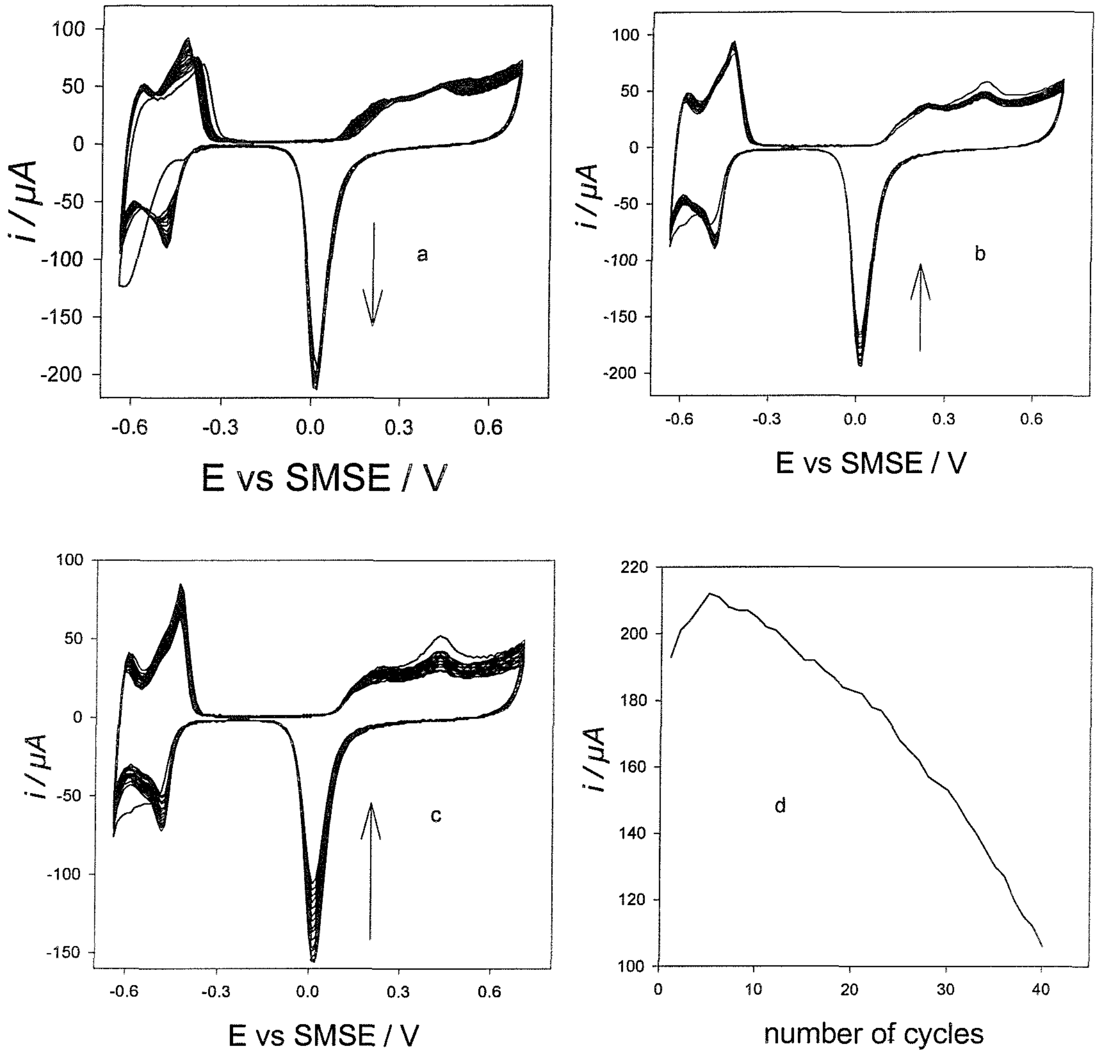

Figure 21: H_I-e Pd was deposited (total deposition charge 3.5 mC, deposited from the Brij®56 plating bath) on the gold disc electrode (area 0.0079 cm^2). The metal film was soaked in water overnight after deposition. Figure a), b) and c) show subsequent voltammetric measurements of the mesoporous metal film in 1 M sulfuric acid at 100 mV/s vs SMSE between -0.65 to 0.7 V. The current was estimated from the cyclic voltammograms and related to each cycle in figure d).

Therefore the increase in the electroactive surface area in Figure 21 is not attributable to the removal of surfactant from the pores by continuous cyclic voltammetry. The increase rather corresponds to the fact that the surface becomes rougher with more voltammetric cycles.

A possible explanation for the decrease of the electrochemical active surface area may be given by considering the dissolution of Pd during cycling in sulfuric acid which causes overall the mass loss. With more cycles the dissolution process determines the experiment. That could cause finally the damage of the nanostructure.

In this section we investigated the dissolution of H_I–e Pd films during cycling in 1 M sulfuric acid with the simultaneous use of the EQCM. We showed that the loss of mass appears when cycling the Pd electrodes in the oxide formation region and increases continuously with subsequent cycles.

3.6.2 Surface modifications of H_I-e Pd films

We noticed from the cyclic voltammogram in Figure 18 two additional peaks on the anodic scan at 0.25 V and 0.4 V vs SMSE. These features on the cyclic voltammogram have been noticed for H_I-e Pd films (3.5 mC total deposition charge). It is of particular interest to note that these peaks in the oxide region appear in our case without a great deal of potential pre-treatment. The well-pronounced pair of peaks of H_I-e Pd immersed in 1 M H_2SO_4 appears after a few voltammetric cycles when starting the scan at 0.2 V vs SMSE and continuing first to the negative direction. It has to be emphasized that we have not found any evidence of these features in the cyclic voltammograms of ordinary Pd wire electrodes in our work.

In searching the literature we found reports [77, 83-86] of investigations of electrochemical processes of oxidized films formed on the Pd metal electrode. The mentioned publications showed that to get the additional peaks in the oxide region required periodic potential cycling of Pd electrodes for more than 10 minutes. This subsequent cleaning of the prepared Pd electrodes (Pd wire of at least 0.5 mm diameter) was pointed out by Rand and Woods [77, 86] who obtained the voltammetric features on the anodic cycle in the oxide region at 0.85 and 1.1 V vs SHE which is very similar to our studies (converting the SHE to SMSE). Burke et al. [83] investigated the electrode behaviour of Pd in aqueous solution and noticed two voltammetric features in the oxide region on the anodic scan as mentioned above. The experiments of Burke et al. showed clear and well-resolved peaks associated to potentials similar to those in our studies. They claimed the clear and well-defined resolution as a result of considerably large surface area and attributed this behaviour to the potential pre-treatment causing dissolution and replating of the Pd metal.

It has been suggested by Dall'Antonia et al. [85] that the additional voltammetric peaks on the anodic scan correspond to the different oxide states of Pd when cycled in the oxide region. Using Pd electrode polarization experiments they came to the conclusion that Pd initially oxidizes with the formation of chemisorbed O followed by the development of the surface lattice of PdO. Further Pd oxidation leads to the development of multi-layers of PdO_2 on top of several multi-layers of PdO. The oxide film on Pd that has been developed in several steps can be reduced in a single negative-going sweep that reveals two voltammetric features. The first one corresponds to the reduction of PdO_2 followed by the reduction of PdO. According to Dall'Antonia et al. [85] the well-defined oxide stripping is only due to the reduction of PdO. From reviewing other publications such as Perdriel et al. [84] we noticed the voltammetric peaks in the oxide region with the PdO_2 formation occurring at 1.283 V vs SHE. They also applied periodic potential cycling to Pd electrodes immersed in 1 M H_2SO_4 which produced a series of modifications at the metal surface. These modifications imply the change in the roughness factor and therefore the increase in the surface area. Again the response of the surface pre-treatment of Pd electrodes was seen on the voltammetry in the oxide region and reflects the several additional peaks associated to the different potentials.

We can conclude that the additional voltammetric features on the anodic scan in the oxide region in our cyclic voltammetry for H_I-e Pd are consistent with the literature. We attribute this behaviour to the formation of the different Pd oxide states.

3.7 Hydrogen electrode reaction on nanostructured palladium

3.7.1 Introduction

The hydrogen electrode reaction at transition metal electrodes can take place in alkaline as well as in acid media by the multistep sequence which can be described as the Volmer-Heyrovsky-Tafel-mechanism [48, 87-89]. The hydrogen electrode reaction on the metal surface is determined in detail by three well-known steps.

The first step in this process is the formation of adsorbed hydrogen on the metal surface originated from H atoms discharged from H_2O or H_3O^+ ions (Volmer reaction).

$$H_3O^+ + e^- \rightarrow H^{\bullet}_{ads} + H_2O \qquad \textit{Equation 7}$$

$H^{\bullet}_{ads}$ presents the adsorbed hydrogen on the metal surface.

This is followed by either the electrochemical process (Heyrovsky reaction)

$$H^{\bullet}_{ads} + H_3O^+ + e^- \rightarrow H_2 + H_2O \qquad \textit{Equation 8}$$

or the chemical catalytic recombination-type desorption process (Tafel reaction).

$$H^{\bullet}_{ads} + H^{\bullet}_{ads} \rightarrow H_2 \qquad \textit{Equation 9}$$

The relative importance of the Tafel or Heyrovsky reactions depends on the electrode potential.

The hydrogen electrode reaction at palladium electrodes is further complicated by extensive permeation of atomic hydrogen into the metal lattice to form α- and β hydride. In the literature no clear consensus has been found about the mechanism by which hydrogen enters the metal and in which way the adsorbed hydrogen is an intermediate between the adsorbed and absorbed hydrogen process. It has been suggested that the transition from the adsorbed to the absorbed state occurs via an intermediate subsurface state as dissolved hydrogen [48, 49, 88]. The chemisorbed hydrogen then undergoes the diffusion from the metal surface into the bulk-metal in competition with the Tafel- and Heyrovsky reaction. According to this the relationship between the adsorption and absorption process can be represented as follows:

$$H^+ + e^- + M \rightleftharpoons MH_{ads} \rightleftharpoons MH_{diss} \rightleftharpoons MH_{abs} \qquad \textit{Equation 10}$$

This sequence indicates the formation of the subsurface layer where H occupies interstitial sites in the host lattice below the surface. Moreover, we found literature indicating the existence of the subsurface layer for hydrogen at single-crystal faces of Ni and Pt suggested by Eberhardt et al. [90].

Lynch and Flanagan [91] claimed two adsorbed states of hydrogen (weakly and strongly chemisorbed) with different Pd-H bond strengths. They suggested that weakly chemisorbed hydrogen is located in subsurface interstitial sites and thus a precursor to absorbed hydrogen. This was suggested by estimating the rate constants for the adsorption and absorption processes after recording the hydrogen take up when the palladium filaments were exposed to high temperatures under high vacuum.

3.7.2 Electrochemical measurements

Figure 22 shows the comparison between the H_I–e Pd film and the plain Pd film deposited from the aqueous solution. The total amount of charge used to deposit Pd for both films was the same. Outlining the differences between both voltammograms we can see that the charge estimated from the surface oxide stripping peak is much larger for the H_I–e Pd film than for the corresponding plain Pd film. This difference results from the greater surface area of H_I–e Pd due to the dense array of the cylindrical pores puncturing the film. However, it is notable that the oxidation and reduction processes occur at the same potential for both films.

The second striking difference which is apparent from the voltammograms is the fact that the two voltammograms differ significantly at more negative potentials. The H_I–e Pd film exhibits a very sharp pair of peaks (denoted by H_1 and H_6) around -0.45 V vs SMSE with a smaller, broader pair of peaks (H_2 and H_5) at -0.52 V vs SMSE and then a rapidly increasing reduction current at the cathodic scan which is associated with the peak in the oxidation current at -0.625 V vs SMSE (H_3 and H_4) on the return scan. We can clearly see that this voltammogram at negative potantials is very different from the voltammetry of plain Pd. For plain Pd a rather featureless and unresolved peak can be seen. Similar results were obtained for a polycrystalline Pd wire (not shown).

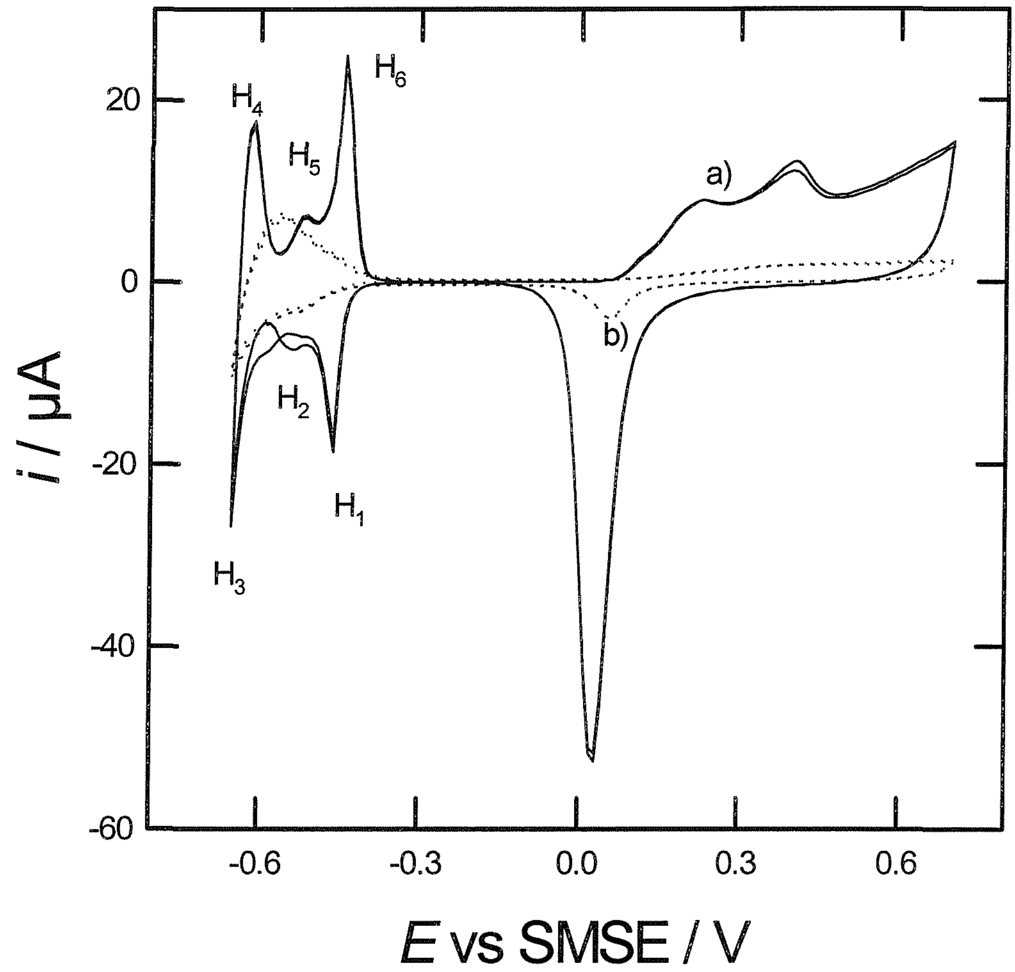

Figure 22: Cyclic voltammogram at 20 mV/s in 1 M sulphuric acid of H_I-e Pd (0.53 cm^2) a) deposited from the template mixture of 12 wt% $(NH_4)_2PdCl_4$, 47 wt% Brij®56, 39 wt% water, 2 wt% heptane and Pd (0.052 cm^2) b) deposited from the aqueous solution containing 50 mM $(NH_4)_2PdCl_4$, 1 M HCl and 1 M NH_4Cl on the gold electrode (1 mm electrode). The charge passed for deposition for both films was 3.5 mC.

This difference in the voltammetry between the H_I–e Pd film and the plain Pd film is due to the presence of the nanostructure. The well-resolved pair of peaks of the H_I–e Pd film (H_1 and H_6) corresponds to the formation and removal of adsorbed hydrogen atoms at the Pd surface. This corresponds to the Volmer-reaction (equation 7). The evidence for the attribution of the peaks H_1 and H_6 to the hydrogen adsorption is given in an experiment shown later in which crystal violet, known as inhibitor for the H-adsorption, suppresses H_1 and H_6.

Similar results have been obtained by Baldauf and Kolb [92] in studies of 1-10 monolayers Pd films deposited on gold single crystal. Tateishi et al. [73, 74] also focused on cyclic voltammetric studies of small Pd particles supported on carbon electrode surfaces. In both cases well-resolved (not as well-resolved as in our studies) peaks of adsorbed hydrogen can be obtained caused by the fact that the current for the formation of absorbed hydrogen into bulk Pd does not dominate in the voltammetry as it does for bulk Pd electrodes. The existence of the hydrogen adsorption peak in the cyclic voltammetry was proved by Baldauf and Kolb [92] in showing that the mid-peak potential for the adsorbed H-couple varied with the proton concentration. In their studies the authors measured the dependence of the current peaks on the proton and sulfate concentration and noticed that the potential of one pair of the current peaks in the hydrogen region shifts linearly with proton concentration in a solution of constant sulfate concentration (0.1 M Na_2SO_4). The slope was estimated to be 60 mV decade^{-1}. On the other hand their data did not reveal any potential shift at constant pH when the sulfate concentration was altered. This shows evidently that this pair of current peaks is caused by the hydrogen adsorption reaction.

The second possibility to confirm the assignment of hydrogen adsorption peaks was also provided by Baldauf and Kolb [92] showing the influence of an appropriate surface modification on the hydrogen adsorption peaks. The addition of crystal violet to the solution completely blocks the H-adsorption but leaves the amount of hydrogen absorbed into the bulk Pd unaltered.

We also investigated the effect of crystal violet on the voltammetry. Figure 23 shows very similar results to those reported by Baldauf and Kolb [92]. In the presence of 1 mM crystal violet the peaks H_1 and H_6 were totally suppressed confirming that they arise from the formation of the adsorbed hydrogen at the electrode surface. Based on the total charge passed for the formation of adsorbed hydrogen and comparing this to the charge of the corresponding oxide stripping peak the H to the surface Pd ratio was found to be 0.20.

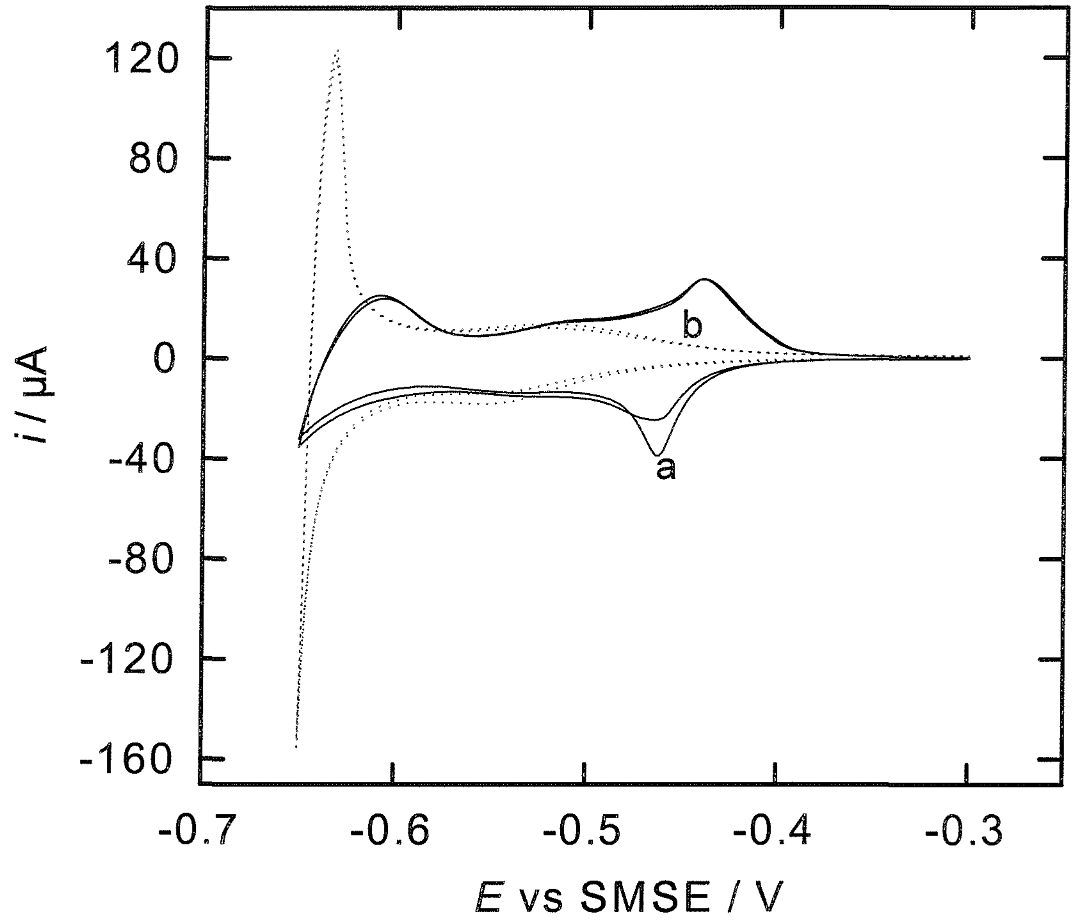

Figure 23: Cyclic voltammograms for a 200 nm thick H_I-e Pd film deposited onto a 1 mm diameter gold electrode recorded at 20 mV/s in 1 M H_2SO_4 without (curve a) and with (curve b) 1 mM crystal violet present.

For our H_I–e Pd films it was not possible to carry out voltammetric studies below 0.1 M without encountering significant distortion in the voltammetry. This was caused by the fact that significant concentration changes can be expected to occur within narrow pores in the structure during the voltammetry. If we refer for example to the charge passed in the peaks H_I and H_6 59 and 88 μC in Figure 22 and convert this to the corresponding change in the proton concentration within the pores of the nanostructure we find a change in the proton concentration of the order of several mmolar. In addition at low electrolyte concentration or at high sweep rates the voltammetry can be distorted by the IR drop occurring along the pores (Figure 24).

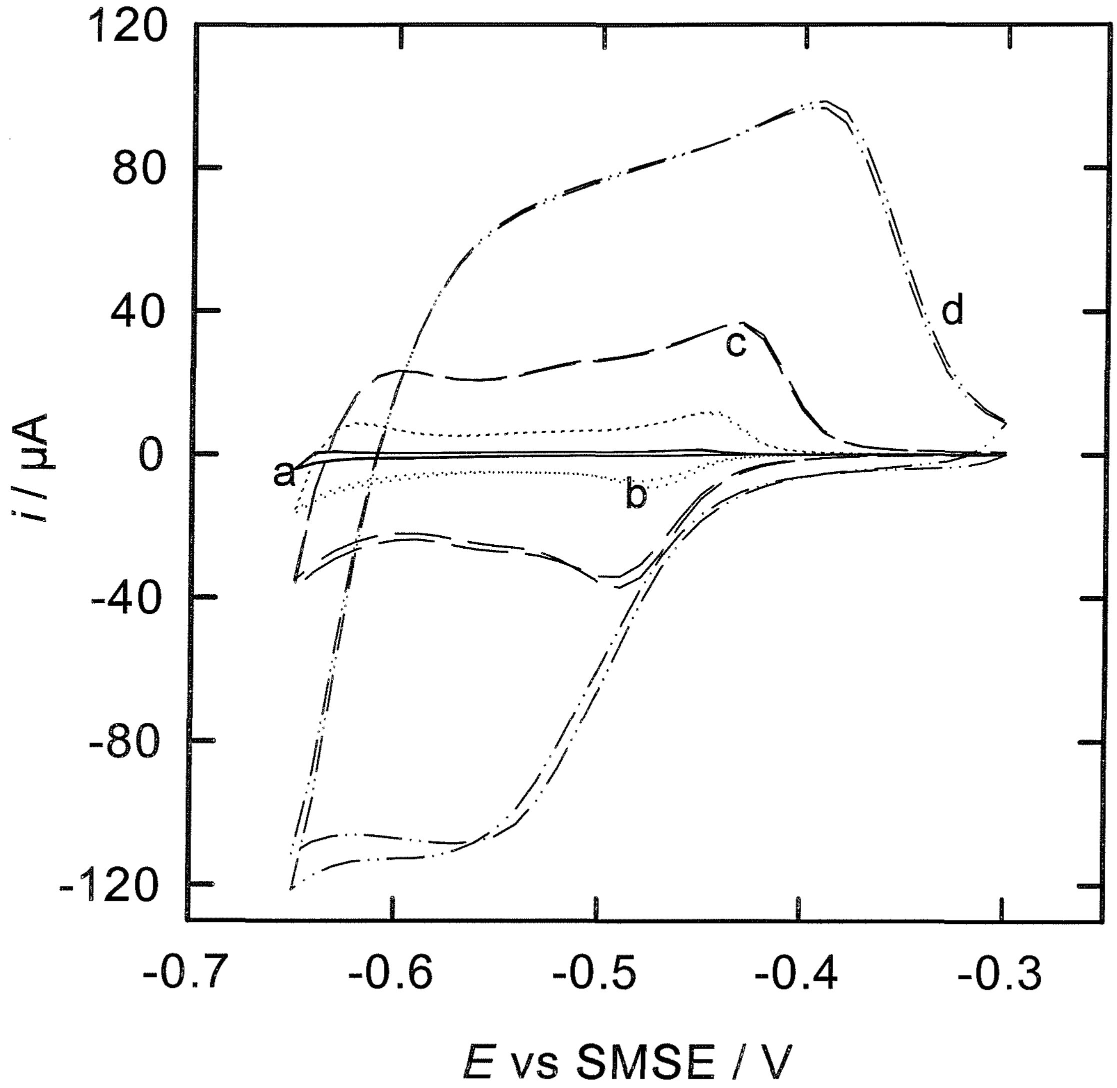

Figure 24: Cyclic voltammograms of an H_I-e Pd film (200 nm thick, deposited from the Brij®56 plating bath, deposition charge 3.5 mC) deposited on a gold disc electrode (area 0.0079 cm^2) recorded at 5 a), 20 b), 50 c) and 200 mV/s in 0.1 M H_2SO_4.

This effect has been investigated by Elliott and Owen [29]. Nevertheless, we have investigated the concentration dependence of the mid-potential for the H_I and H_6 peaks over a limited proton concentration range and find that it agrees with the results of Baldauf and Kolb [92].

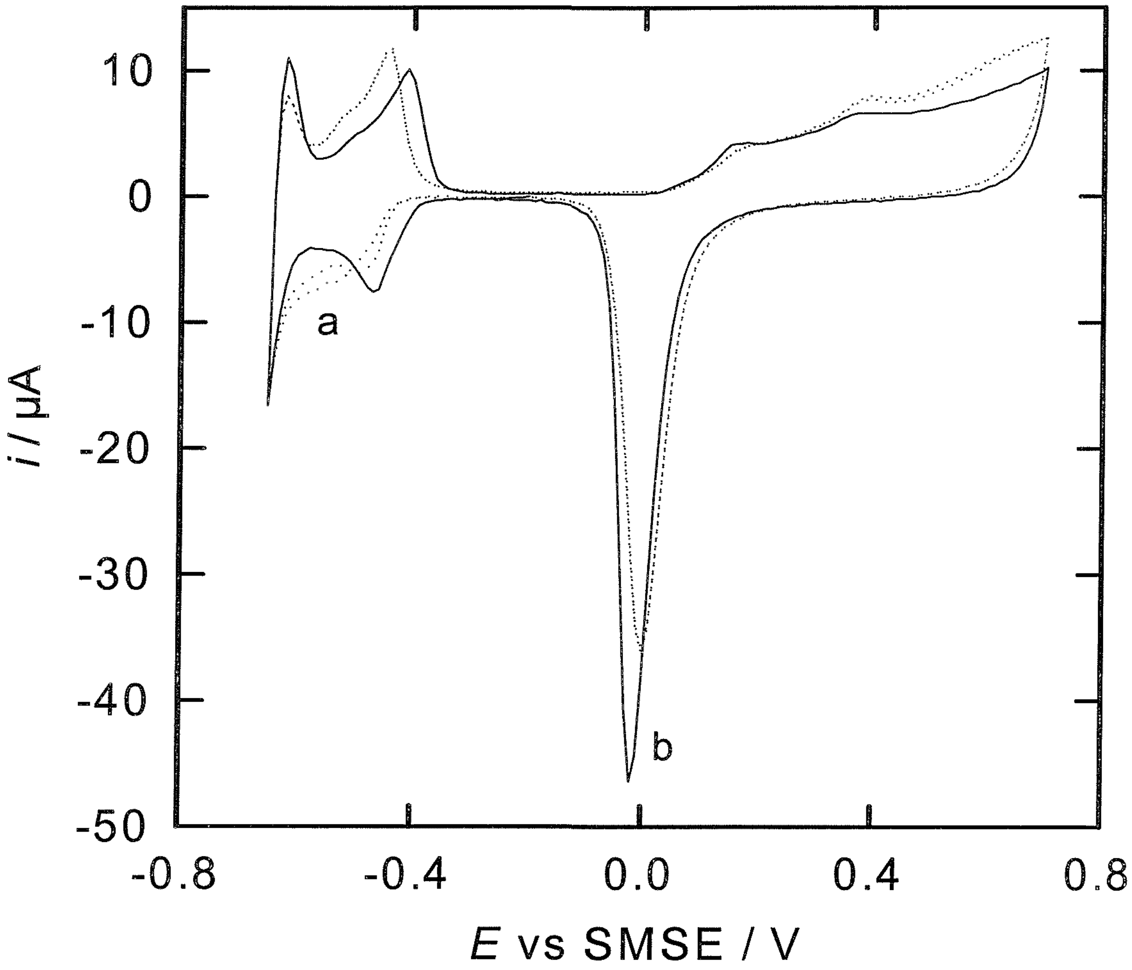

Figure 25: Cyclic voltammograms of an H_I-e Pd film (200 nm thick, deposited from the Brij®56 plating bath, deposition charge 3.5 mC) deposited on a gold disc electrode (area 0.0079 cm^2) recorded at 20 mV/s in 0.1 M H_2SO_4 a) and b) 0.1 M $HClO_4$.

Figure 25 shows a typical voltammogram for an H_I–e Pd in 0.1 M sulfuric acid and 0.1 M perchloric acid. Comparing the results to those presented in Figure 22 we notice 11 mV shift in the mid-peak potential when going from 1 M to 0.1 M sulfuric acid. In addition, changing from the sulfuric to the perchloric acid solution has only little effect on the voltammetry beyond a small shift which can be attributed to the difference of the two solutions.

The Hydrogen region of H_I-e Pd shown in the cyclic voltammogram in 1 M sulfuric acid is well-defined unlike that for a plain Pd film deposited from the aqueous solution under the same conditions. Crystal violet, known as an inhibitor for the H-adsorption on the Pd surface, was added to the solution and so it was possible to knock out the adsorption peaks (H_1, H_6) completely. We then have been left with the remaining two pairs of peaks (H_2-H_5, H_3-H_4) associated with the formation of absorbed hydrogen The H-absorption process into the bulk palladium is subject of the next section.

3.7.3 Absorption of hydrogen into H_I-e Pd

In this section we concentrate on the hydrogen-absorption behaviour with the emphasis on the α- β phase transition. When the potential is scanned further cathodic, Figure 26, we can clearly see that the peaks H_3 and H_4 of Figure 22 become the two large peaks associated with the formation and oxidation of the β-hydride phase.

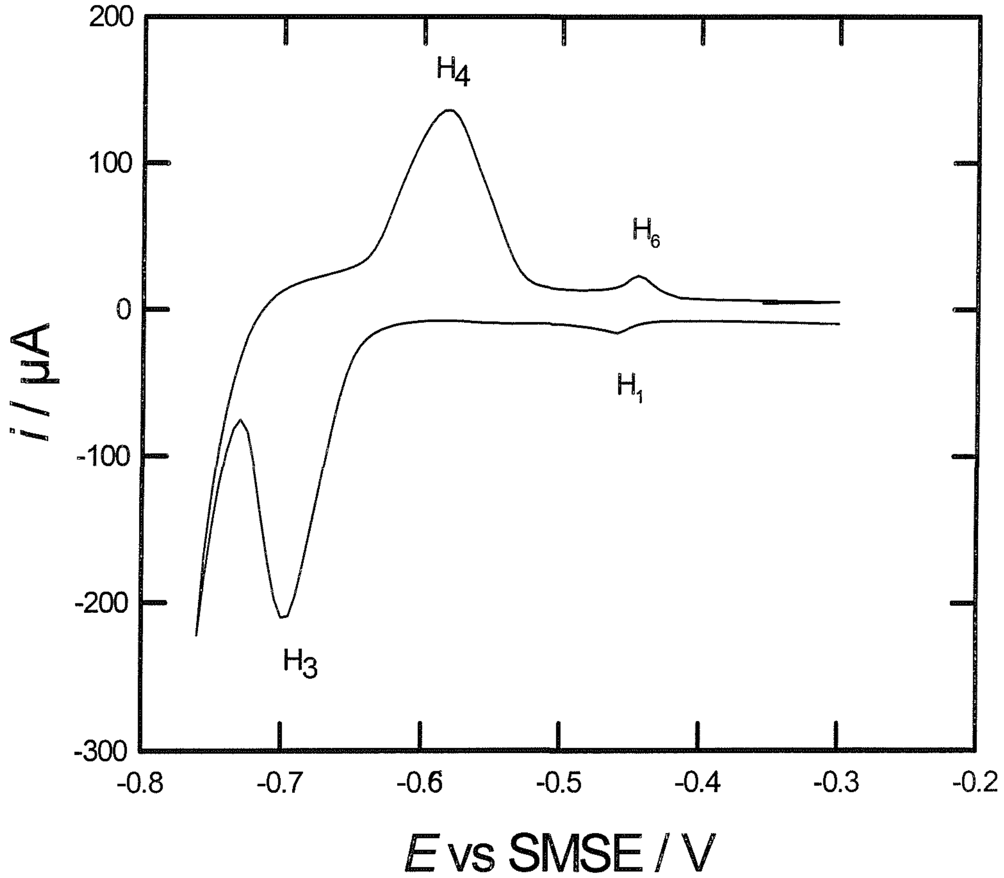

Figure 26: Cyclic voltammogram of an H_I-e Pd film deposited from the Brij®56 plating solution onto a gold disc electrode (1mm diameter, deposition charge 3.5 mC) recorded at 10 mV/s in 1 M H_2SO_4.

In order to investigate the formation of the hydride phases in more detail we carried out a series of experiments in which the potential of the electrode was stepped from -0.56 V to increasingly cathodic potentials, held at the cathodic potential for 120 s and then swept back at 10 mV/s to –0.2 V. In a separate set of experiments the length of time that the electrode was held at the cathodic potential was varied in order to ensure that sufficient time was allowed for the system to equilibrate at the cathodic potential before the anodic sweep.

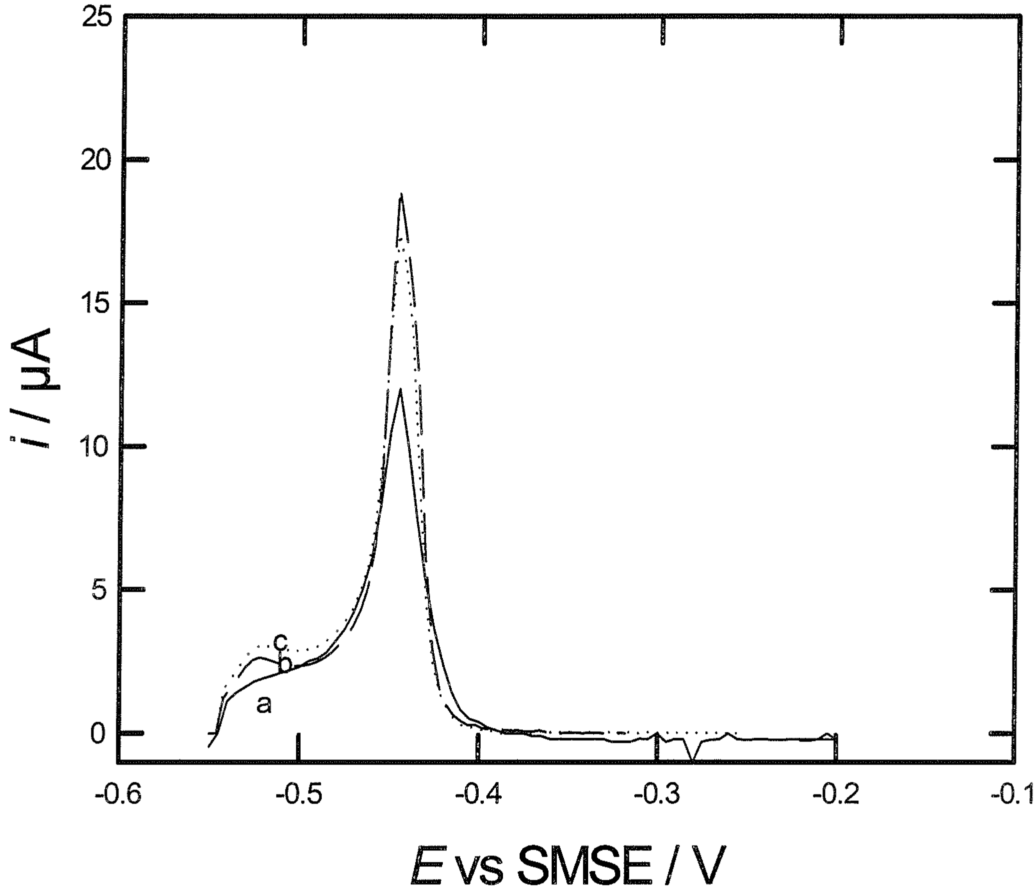

Figure 27: Cyclic voltammogram of an H_I-e Pd film deposited from the Brij®56 plating solution onto a gold disc electrode (1 mm diameter, 3.5 mC deposition charge) recorded at 10 mV/s in 1 M H_2SO_4. Before the anodic sweep hydrogen was loaded into bulk Pd for different lengths of time 5 s a), 20 s b) and 120 s c) at -0.55 V.

The peak on the anodic sweep in Figure 27 corresponds to the oxidation of absorbed hydrogen atoms in bulk Pd. We can see that the area underneath the peak increases until the length of time of 120 s is reached. We did not find any significant increase in the area underneath the peak when hydrogen was loaded into the bulk Pd for more than 120 s.

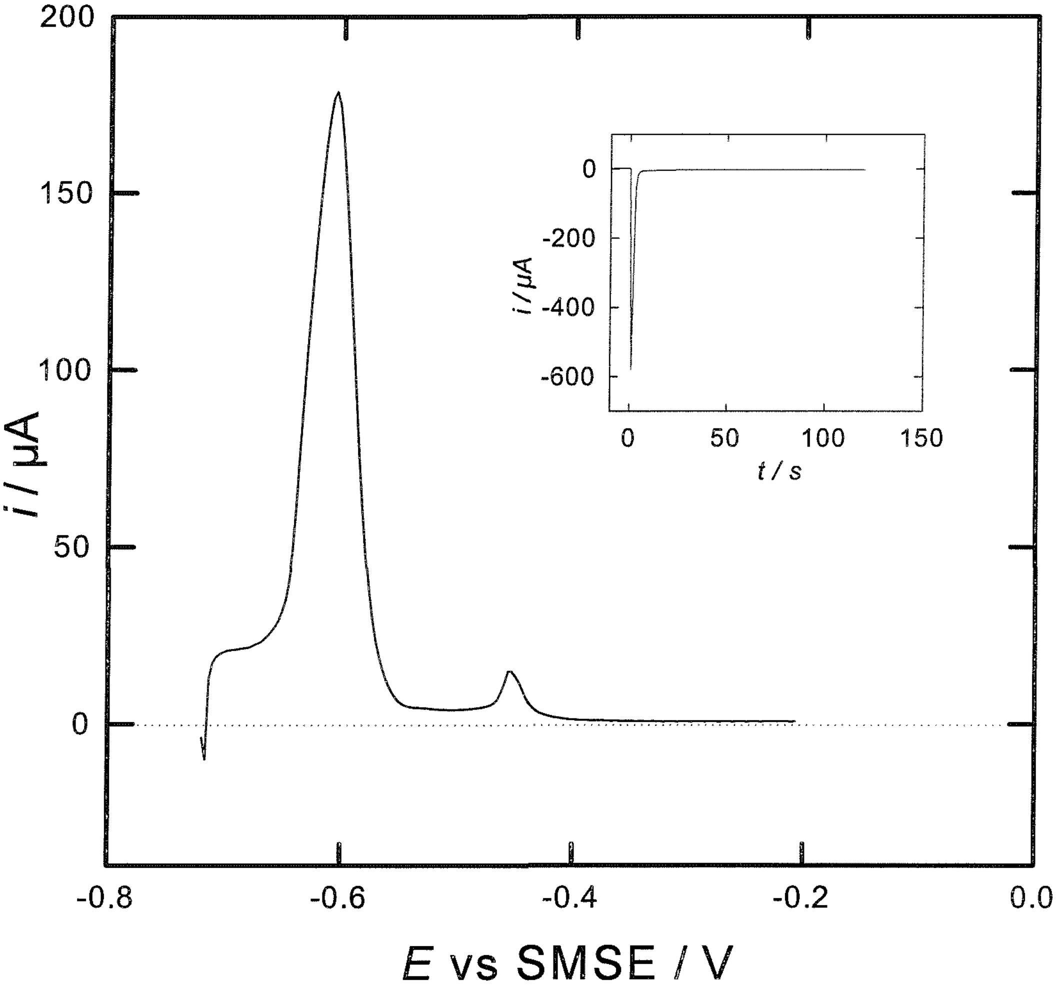

Figure 28: Example of a voltammgram for the oxidation of hydrogen absorbed and adsorbed on an H_I-e Pd film in 1 M H_2SO_4 recorded at 10 mV/s. The electrode was stepped from -0.2 to -0.72 V vs SMSE and held there for 120 s to load the electrode with hydrogen immediately before the anodic scan. The inset shows the corresponding current transient for loading the electrode with hydrogen at -0.72 V. The H_I-e Pd film was deposited (3.5 mC) from the Brij®56 plating bath onto a 1 mm diameter gold disc electrode.

This was also found to be the case when the electrode was stepped to far negative potentials (-0.76 V vs SMSE). We therefore found the length of time of 120 s to absorb hydrogen into Pd bulk of our H_I–e Pd films sufficient to equilibrate at each potential.

Figure 28 shows the reverse scan of a typical cyclic voltammogram of H_I–e Pd at 10 mV/s in 1 M sulfuric acid after stepping the potential of the electrode from -0.56 V to -0.72 V vs SMSE and held at this potential for 120 s. The corresponding potential step experiment is shown as an inset in the same figure. On the reverse voltammetric sweep there are two well-resolved peaks. The peak at -0.6 V vs SMSE corresponds to the reduction of β-hydride, while the peak at -0.453 V vs SMSE corresponds to the reduction of the adsorbed hydrogen on the Pd surface. The oxidation occurs at the same potential as shown in Figure 22 for the pair of peaks H_1 and H_6. It is also of interest to note that the peaks in the voltammetry are better resolved than the corresponding peaks reported from similar experiments on thin Pd films (300 to 500 monolayer equivalents) by Czerwinski et al. [50]. This indicates that the permeation of hydrogen into bulk-Pd and the H-adsorption on the Pd surface occurs for the H_I–e Pd films more rapidly than for thin Pd films studied by Czerwinski et al. [50].

By decreasing the potential of the electrode below -0.65 V vs SMSE we obtain the resulting anodic voltammetric sweep from which the α- and the β-hydride phase can be clearly distinguished (Figure 29).

The β-hydride phase on the anodic cycle dominating the cyclic voltammogram, Figure 28, has almost disappeared in Figure 29. Figure 29 shows the cyclic voltammogram of H_I–e Pd at 10 mV/s after stepping the potential of the electrode to -0.60 V to load up hydrogen into bulk Pd. The peak at -0.55 V can be attributed to the formation of the α-hydride phase, while the peak at -0.45 V corresponds to the hydrogen adsorption on the Pd surface. This peak again occurs at around the same potential as peak H_6 in Figure 22 and Figure 26.

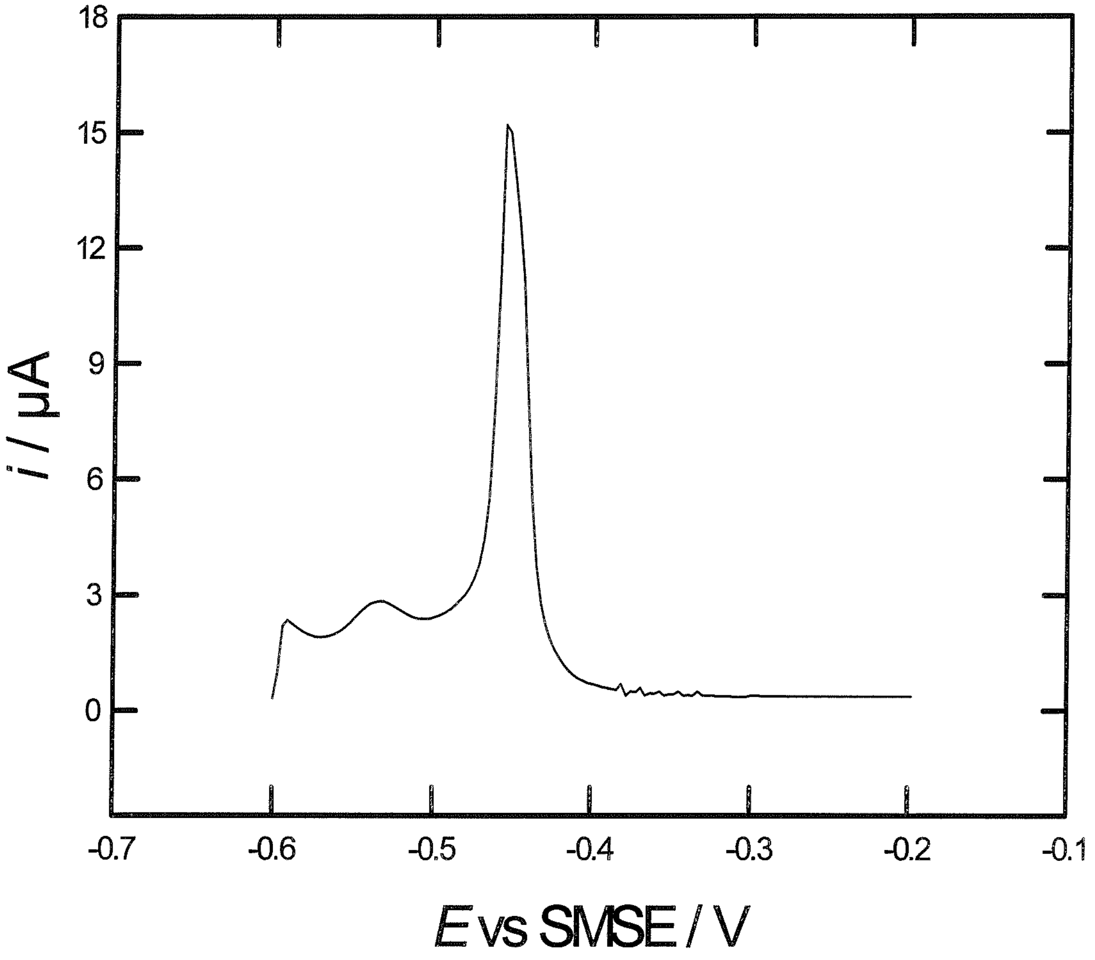

Figure 29: Cyclic voltammogram for the oxidation of hydrogen absorbed and adsorbed on an H_I-e Pd film in 1 M H_2SO_4 recorded at 10 mV/s. The electrode was stepped from -0.2 to -0.60 V vs SMSE and held there for 120 s to load the electrode with hydrogen immediately before the anodic scan. The H_I-e Pd film was deposited from the Brij®56 plating bath onto a 1 mm diameter gold disc electrode (charge passed 3.5 mC).

The proof for the existence of an H-adsorption peak can be provided by adding crystal violet to the acid solution. The potential of the electrode was stepped to -0.72 V vs SMSE and held at that potential for 120 s. Figure 30 shows the voltammetry of the reverse anodic cycle corresponding to the formation of absorbed hydrogen. Curve a) presents the voltammetry obtained after adding crystal violet to the solution. Curve b) shows the reverse sweep without crystal violet added to the solution prior to the insertion of hydrogen. We note from curve a) that crystal violet when added to the solution knocks out the peak at -0.45 V vs SMSE completely.

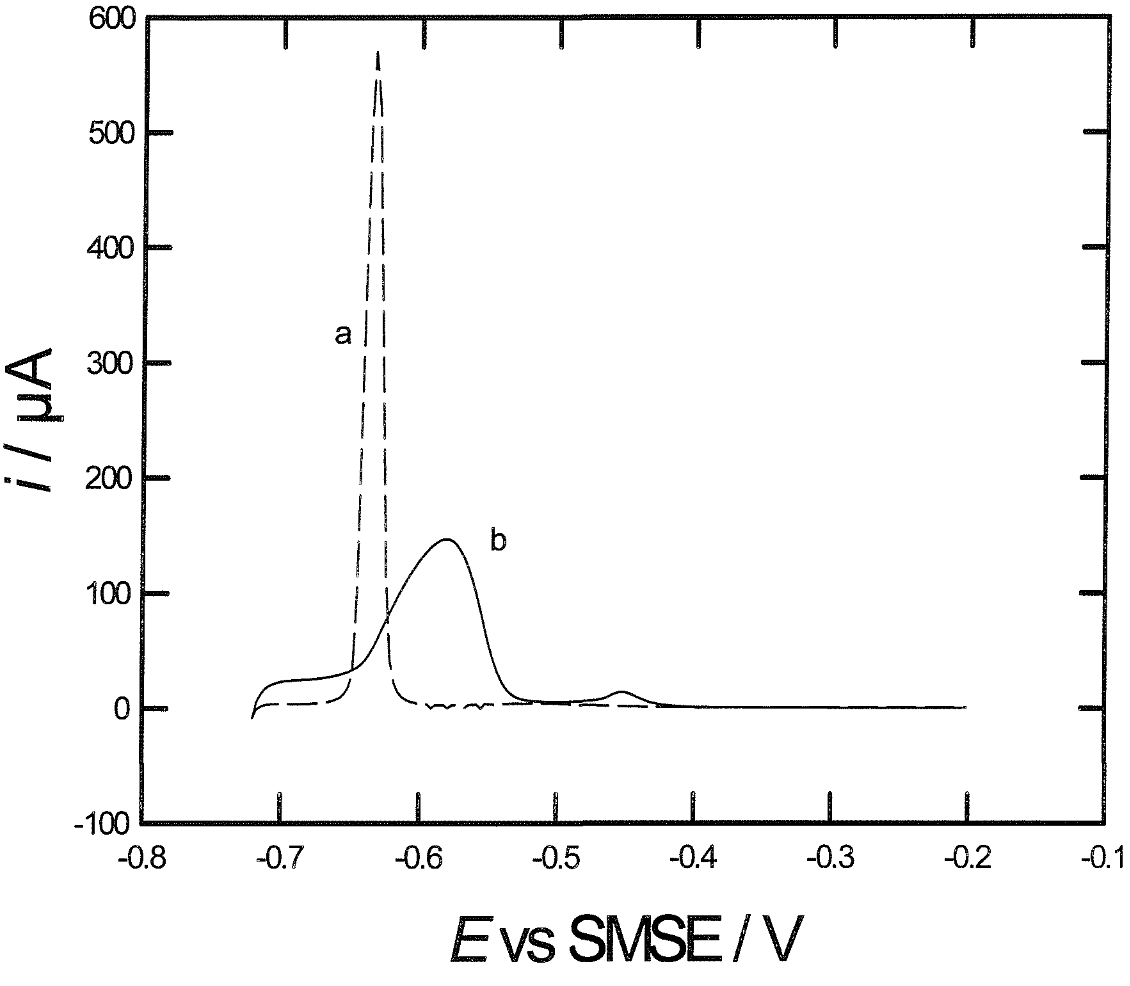

Figure 30: Cyclic voltammogram for a 200 nm thick H_I-e Pd film deposited from a Brij® 56 plating solution onto a 1 mm diameter gold disc electrode (deposition charge 3.5 mC) recorded at 20 mV/s in 1 M H_2SO_4 without (curve b) and with (curve a) 1 mM crystal violet. The electrode was stepped from -0.2 to -0.72 V vs SMSE and held there for 120 s to load the electrode with hydrogen immediately before the anodic scan.

As crystal violet inhibits the H-adsorption on to the metal surface we can conclude that the peak at -0.45 V is associated to the adsorption of hydrogen on the Pd surface. Comparing the peaks for absorption of hydrogen in curve a) with b) we note remarkable difference in peak potential and sharpness. The areas underneath the peaks are roughly the same. The potential of the hydrogen absorption peak on the anodic sweep in curve a) occurs at -0.63 V which is about 0.03 V different from the absorption peak in curve b).

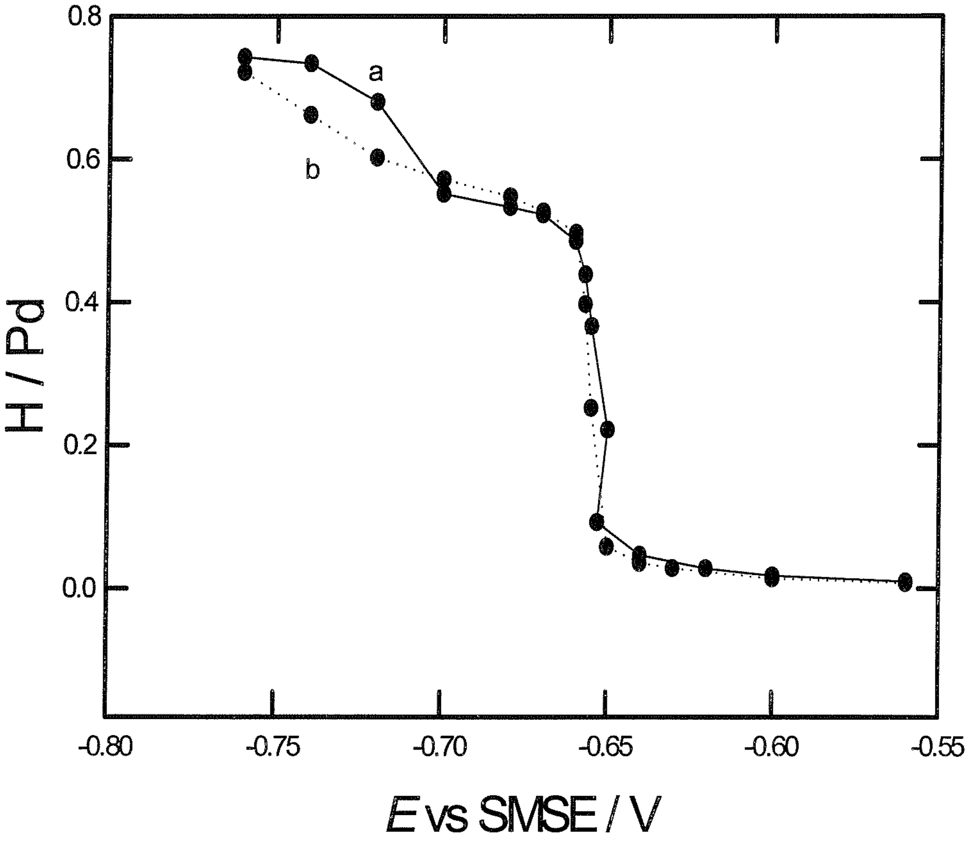

Figure 31: Plot of the H/Pd ratio as a function of potential for an H_I-e Pd film. The hydrogen loading of the electrode was determined from anodic voltammetric sweeps of the type shown in Figure 28 after stepping the electrode to different cathodic potentials. The total palladium loading was calculated from the charge passed to deposit the H_I-e Pd film (3.5 mC curve a) and 7 mC curve b) for 1 mm diameter electrode) and the measured faradaic efficiency of 95% for the deposition.

By carrying out a series of experiments in which the potential of the electrode was stepped to different cathodic values we integrate the charge passed in the reverse anodic sweep corresponding to the reduction of absorbed hydrogen and build up a plot of the charge as a function of the potential. We then converted the charge to the hydrogen/palladium ratio at each potential using the faradaic law and the total charge passed in the deposition of the Pd film. We considered the faradaic efficiency of 95%

for the deposition of H_I–e Pd calculated from EQCM-measurements [10]. The resulting plot for 3.5 mC curve a) and 7 mC curve b) as charge passed for deposition of H_I–e Pd films is shown in Figure 31. Below -0.55 V vs SMSE the H/Pd ratio increases slowly as the potential becomes more cathodic. This corresponds to the formation of α-hydride which is stable up to H/Pd less than about 0.05 [93]. The sharp rise in the H/Pd ratio at -0.653 V (equivalent to 0.046 V vs SHE) corresponds to the formation of the β-hydride phase. Within the experimental error this is consistent with Czerwinski et al. [50] who carried out similar experiments on thin Pd films (300 to 500 monolayers equivalent). The transition from the α- to the β-phase was reported to be -0.23 V vs SCE in 0.5 M H_2SO_4. It is of interest to note that the transition between both phases for an H_I–e Pd film occurs over a significantly smaller range (~20 mV as compared to ~50mV) in comparison to Czerwinski et al. [50].

Furthermore we can see from the Figure 31 that at more cathodic potentials the H/Pd ratio curve tends towards a plateau at around -0.70 V before increasing again at potentials more negative than -0.70 V vs SMSE. This significant increase in the H/Pd ratio at negative potentials more than -0.70 V is unexpected and was not reported in the literature elsewhere. From the literature [50] we would normally expect the β-hydride phase to reach a plateau. If we return to the voltammetric anodic sweep of the H_I–e Pd film in Figure 28 we can see at potentials between -0.65 V to -0.72 V an additional current as contribution to the stripping charge.

Figure 32 shows a set of cyclic voltammograms as reverse scans after stepping the electrode to different cathodic potentials and held there to load the electrode with hydrogen. It is notable that the remarkable feature on the anodic cycle occurs when stepping the electrode to cathodic potentials more negative than -0.65 V and held at that potential for 120 s before the anodic sweep. The additional current in the voltammetry appears to increase dramatically when stepping the electrode to cathodic potentials more negative than -0.70 V. This additional current appears to be capacitative and can only be explained as a result of a nanostructured Pd film used in our studies where the surface area of the Pd film is large compared to the volume of the metal. It has also to be stressed that the physical properties of our H_I–e Pd film are not to be compared with those of a plain Pd film used by Czerwinski et al. [50]. The surface area is essentially less. However, it is not clear why the double layer capacitance should be so much greater than that of the Pd metal.

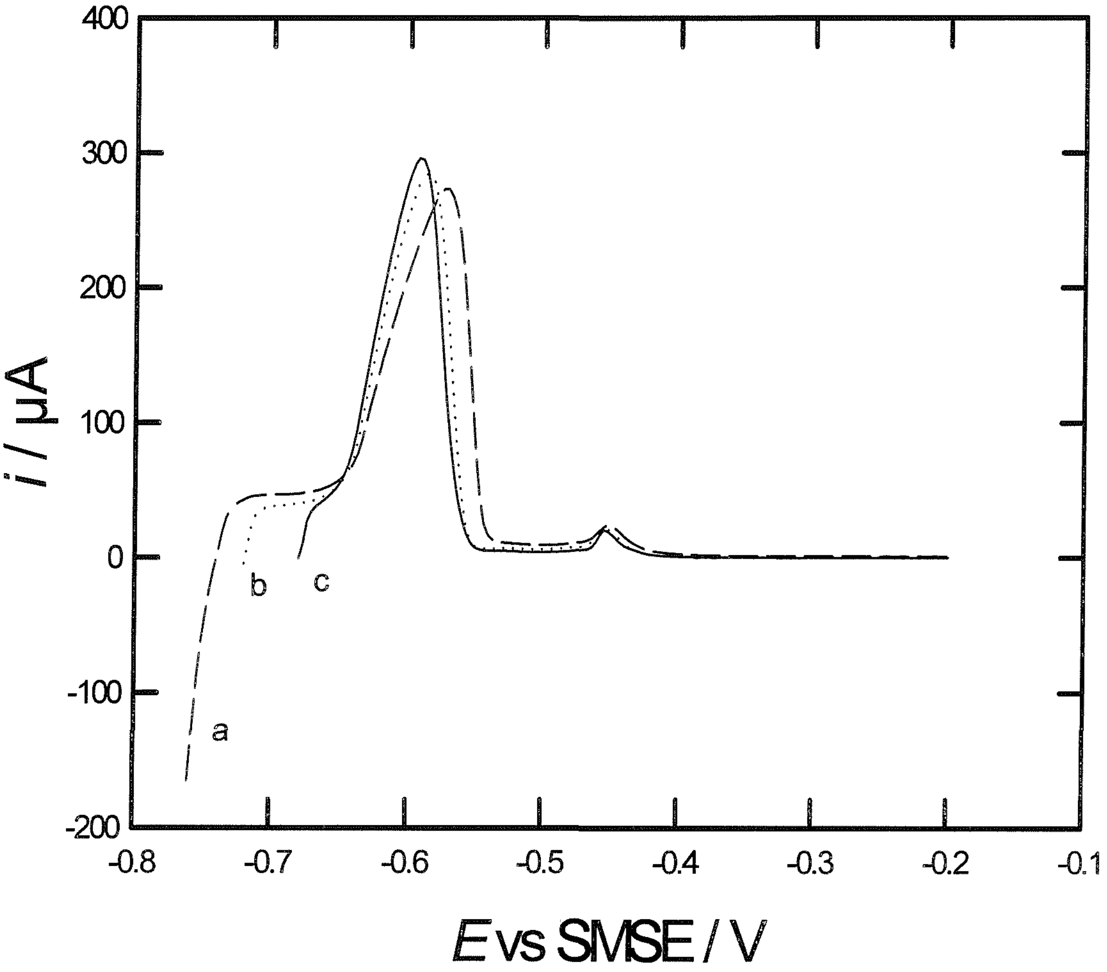

Figure 32: Set of cyclic voltammogram of an H_I-e Pd film deposited from the Brij®56 plating solution onto a gold disc electrode (1 mm diameter, 3.5 mC deposition charge) recorded at 10 mV/s in 1 M H_2SO_4. The electrode was stepped from -0.2 to different cathodic potentials -0.76 a), -0.72 b) and -0.68 V c) vs SMSE and held there for 120 s to load the electrode with hydrogen immediately before the anodic scan.

Comparing both curves a) and b) in Figure 31 we do not note any significant difference. The transition between the α- and the β-phase occurs at the same potential and in a smaller range compared to Czerwinski et al. [50]. For H_I–e Pd films with the deposition charge of 3.5 mC an even sharper rise in the H/Pd ratio is to be seen at potentials more negative than -0.70 V compared with H_I–e Pd films of 7 mC total deposition charge.

From the cyclic voltammetric studies we noticed at increasingly higher potentials more negative than -0.653 V that the formation of the β-hydride phase and its subsequent oxidation does not destroy the nanostructure of the Pd film although it has to be considered that the insertion of hydrogen into the bulk Pd to make the β-phase is accompanied by an 3% expansion in Pd lattice parameter [93]. The fact that the nanostructure has not been destroyed was shown in estimating the area underneath the surface oxide stripping peak of the H_I-e Pd film. We did not find any difference in the electroactive surface area before and after the hydrogen insertion.

From our experiments we note a sharper transition between the α- and the β phase as a function of potential and more clearly resolved peaks in the voltammetry compared to Czerwinski et al. [50] and Tateishi et al. [73, 74] who used thin Pd films for the studies. This is due to the enhanced kinetics in our electrode processes and caused by the fact that Pd atoms within the metal are not more than a few nanometers away from the surface. Hydrogen can permeate into the Pd metal walls of nanometer-sized dimensions from both sides. Thus considering the diffusion of hydrogen into the Pd lattice we do not expect the diffusion to be rate-limiting in the absorption process. The diffusion coefficient for hydrogen in the α-phase was estimated to be 2×10^{-7} cm^2/s and for the β-phase an order of magnitude higher (2×10^{-6} cm^2/s) [94]. The time taken for a hydrogen atom to diffuse right through the metal lattice would be of the order of 20 ns.

3.8 Conclusion

In this chapter we have shown that we can prepare nanostructured H_I–e Pd films by electrochemical deposition from the liquid crystalline phases of either $C_{16}EO_8$ or Brij®56. These films contain regular hexagonal arrangement of cylindrical pores with pore size diameter of 2.5 nm and wall thickness of 2.5 nm. Electrochemical studies showed that H_I–e Pd films have high electroactive surface areas of the order of 91 m^2/g (corresponding to 1×10^7 cm^2/cm^3). Cyclic voltammetry with the simultaneous use of the EQCM provided us with the fact that H_I–e Pd when cycled in the oxide region dissolves subsequently with each voltammetric cycle so that mass loss dominates over mass gain. Cyclic voltammetric measurements of Pd deposited from the aqueous solution showed that the charge passed for formation and stripping of the surface oxide layer reached smaller values than for H_I–e Pd. This is based on the obtained high surface area. We also found the hydrogen region of H_I-e Pd in the cyclic voltammetry of 1 M sulfuric acid more clearly resolved than of plain Pd. Due to the very high surface to volume ratio of H_I–e Pd films we can readily distinguish the formation of H between adsorption and absorption processes. With the use of crystal violet, as an appropriate surface modification, we were able to knock out the H-adsorption on the Pd surface completely. With the remaining peaks in the hydrogen region associated to the α- β hydride phases we studied in detail the absorption process and focused on the characteristics of the phase transition. Because of the fast kinetic for the formation of α- and β hydride phases we noticed clearly resolved peaks in the absorption region and a sharper rise in the H/Pd ratio compared to Czerwinski et al. [50].

The electrochemical deposition of Pd as high surface metal with regular, controlled nanostructure is of potential application as a catalyst for methane oxidation in gas-sensors. This will be the subject of chapter 7.

Chapter 4 The effect of poisons on promoting the H sorption into the Pd metal lattice

4.1 Introduction

It is the focus of this chapter to investigate the effect of poisons on the process of hydrogen absorption into bulk palladium. We compare the peaks associated with the formation and oxidation of the β-hydride phase of palladium with and without the addition of crystal violet to the sulfuric acid solution in a convenient range of potential. In addition, we direct our attention towards the electrochemical properties resulting from the deposition of another metal, such as H_I-e Pt and H_I-e Rh on top of H_I-e Pd. Our aim is to compare the electrochemical features obtained for both systems.

The poisoning of the palladium surface and its effect on the absorption of hydrogen into the metal lattice has been extensively studied by Conway and Jerkiewicz [48]. We include in our discussion the explanation of their results and the general interpretation outlined from reviewing the literature on this topic. We discuss the different options raised in their paper and cited therein in order to provide a reasonable explanation for the difference in the hydrogen absorption process in the voltammetry in the presence of the poison. We discuss here in detail the effect of the poison in promoting H sorption into the palladium lattice. With respect to our own results and the experimental findings in the literature it is our main concern in this chapter to find a general and consistent mechanism for the permeation of hydrogen into the palladium metal lattice in the presence of poisons which block the Pd surface sites.

4.2 The hydrogen absorption process

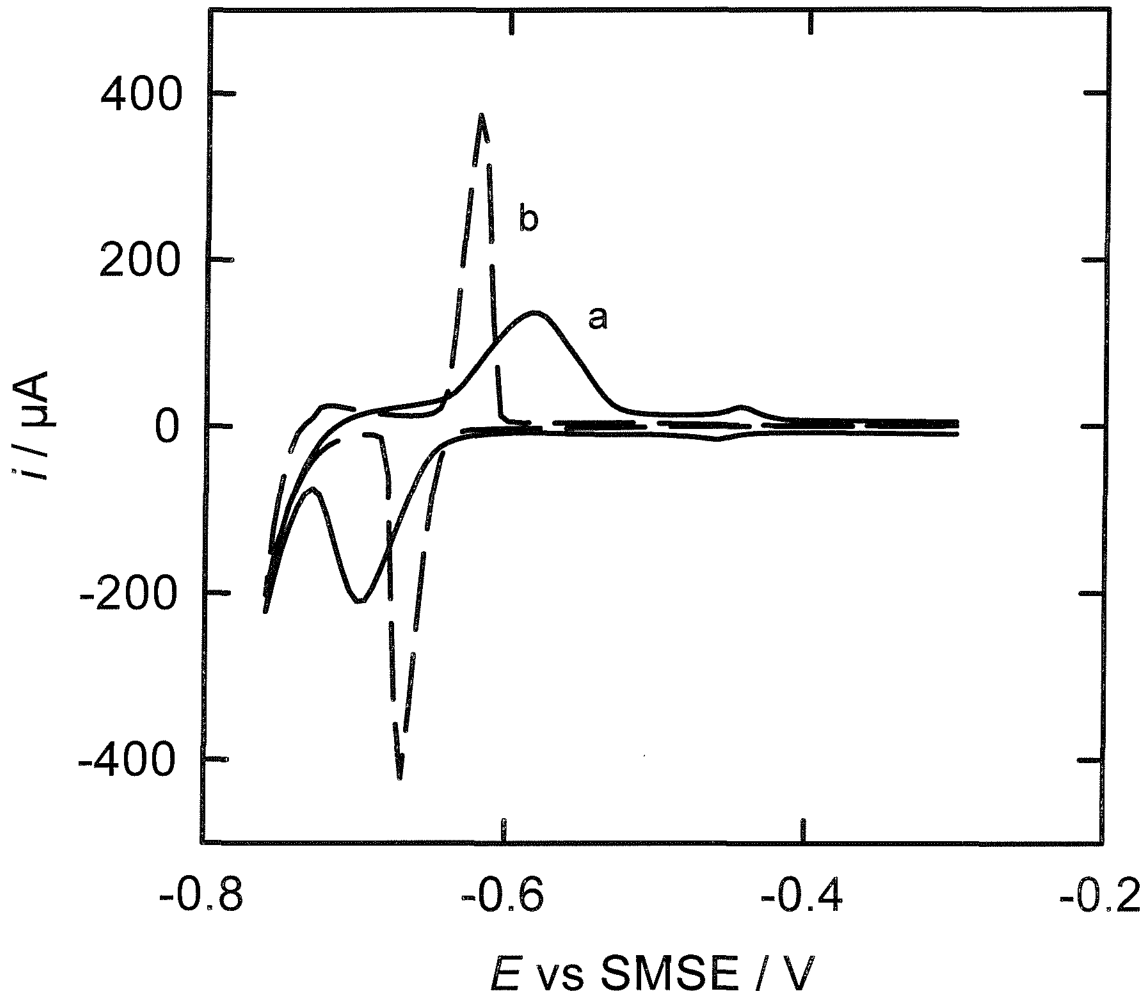

Figure 33: Set of cyclic voltammograms of H_I-e Pd (200 nm thick, deposition charge 3.5 mC, deposited from the Brij®56 plating bath) deposited on a gold disc electrode (area 0.0079 cm^2) recorded at 10 mV/s in 1M H_2SO_4 without crystal violet a) and in the presence of 1 mM crystal violet b).

Figure 33 a) shows the cyclic voltammogram of H_I-e Pd recorded in 1 M sulfuric acid at 10 mV/s without the addition of crystal violet. The voltammetry shows two voltammetric features associated to the formation of adsorbed and absorbed hydrogen.

At -0.46 V vs SMSE on the cathodic scan the peak corresponds to the formation of adsorbed hydrogen which is oxidized on the anodic scan at -0.445 V vs SMSE. The permeation of hydrogen into the metal is clearly visible at -0.7 V vs SMSE on the cathodic sweep with the oxidation occurring on the return sweep at -0.58 V vs SMSE. The voltammetry shown in curve b) in the same figure shows the return sweep of H_I-e Pd in 1 M sulfuric acid in the presence of crystal violet at 10 mV/s. The first striking difference to the voltammetry in a) is the absence of the peaks for adsorbed hydrogen onto Pd. This is not surprising since we know from previous results that the coverage of the Pd surface by crystal violet completely blocks H adsorption. It is more interesting to note that the H-absorption peak on the cathodic sweep occurs at -0.68 V vs SMSE and on the return sweep at -0.61 V which is significantly shifted of about 20 mV from the positions of the absorption peaks in the voltammetry of curve a). We have to note that the peaks for the hydrogen absorption process on nanostructured Pd in the presence of crystal violet appear to be sharper. The width at half height of the peak in the voltammetry a) was estimated to be 70 mV whereas in the voltammetry b) we found for the width at half height of the absorption peak a value of 25 mV. However, we have to emphasize that comparing both voltammograms there is no shift in the mid peak potential indicating that thermodynamic conditions have not changed whilst the experiments were carried out. We also find that the charge underneath the absorption peaks remains, within the experimental error, the same for both voltammograms.

We therefore strongly assume that the system is kinetically controlled. This indicates that the inhibition of hydrogen adsorption onto the Pd surface by the coverage of poisons affects the rate of entry of hydrogen into the Pd bulk.

To propose a mechanism by which hydrogen permeates into Pd bulk we discuss the effect of poisons on promoting the H sorption into the metal reviewing the available literature.

The hydrogen electrode reaction at transition metal electrodes can take place in alkaline as well as in acid media by the multistep sequence which can be described as the Volmer-Heyrovsky-Tafel-mechanism [48, 87-89]. The hydrogen electrode reaction on the metal surface is determined in detail by three well-known steps.

The first step in this process is the formation of adsorbed hydrogen on the metal surface originated from H atoms discharged from H_2O or H_3O^+ ions (Volmer reaction).

$$H_3O^+ + e^- \rightarrow H^\bullet_{ads} + H_2O \qquad \textit{Equation 11}$$

Where $H^\bullet_{ads}$ represents the adsorbed hydrogen on the metal surface.

This is followed by either the electrochemical process (Heyrovsky reaction)

$$H^\bullet_{ads} + H_3O^+ + e^- \rightarrow H_2 + H_2O \qquad \textit{Equation 12}$$

or the chemical catalytic recombination-type desorption process (Tafel reaction).

$$H^\bullet_{ads} + H^\bullet_{ads} \rightarrow H_2 \qquad \textit{Equation 13}$$

One of the options which we want to present here in reviewing the literature and discussing the effect on promoting the hydrogen sorption into the metal lattice is given by Shuler and Laidler [95, 96] who claimed that adsorbed hydrogen atoms are more tightly bound on the poisoned surface than on the clean surface. However, this seems rather unlikely, since poisons normally block binding sites for hydrogen at the metal surface. Therefore an increase in the M-H_{ads} bond strength is rather unreasonable. Another postulation which has been put forward is that the poisons interfere with the H atom recombination step in the cathodic H_2 evolution. According to these authors [97, 98], the number of active sites available for hydrogen atoms adsorbed on the Pd surface is reduced by the coverage of poisons. This then interferes with the cathodic H_2 recombination step reaction (equation 13) so that the activation energy for this reaction will increase. The authors suggest that while the H_2 evolution is slowed down the formation of absorbed hydrogen is favoured (equation 14) in a second order reaction for the H_{ads} coverage.

$$H_{ads} + H_{ads} \rightarrow H_{abs} \qquad \textit{Equation 14}$$

We find this conclusion rather unreasonable because it contradicts with our experimental findings. Proceeding from the assumption that the poisons present at the electrode surface interfere with the recombination step reaction so that the H_2 evolution is diminished, as the authors suggested, we would necessarily expect to see less hydrogen evolved in the hydrogen region. However, we note in comparing voltammogram a) with b) in *Figure 33* no difference in the rate of hydrogen evolved in the hydrogen region at cathodic potentials of -0.76 V vs SMSE.

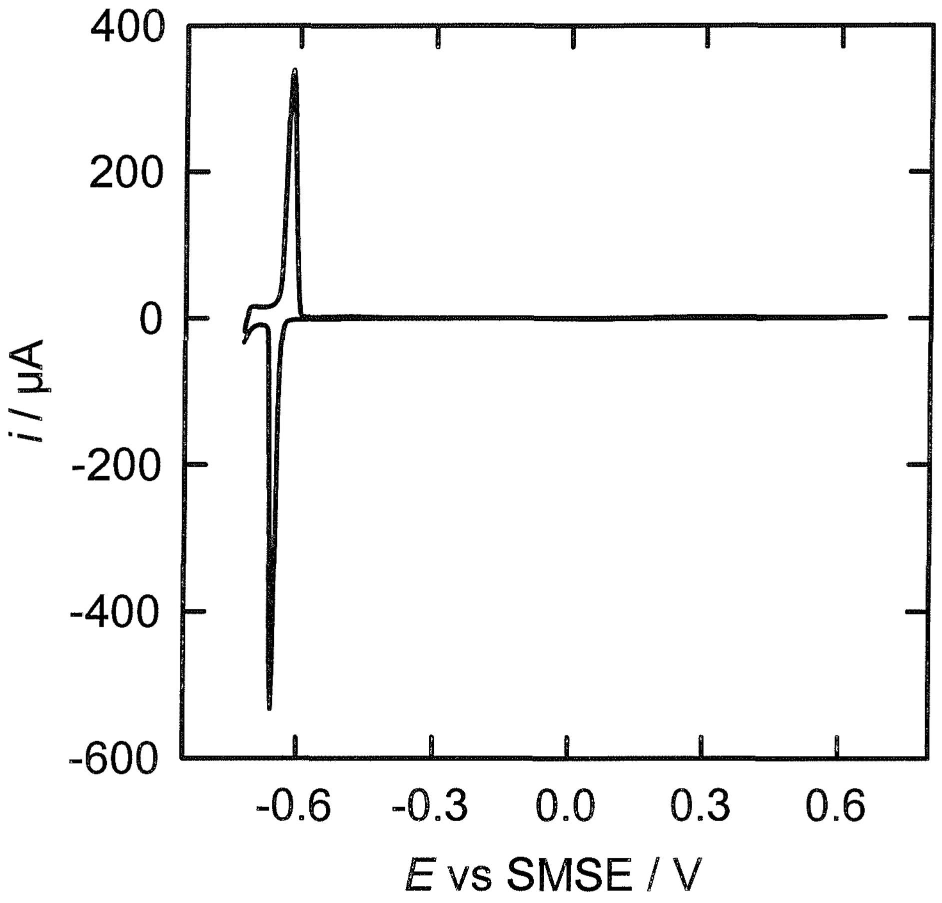

Figure 34: Cyclic voltammogram at 10 mV/s in 1 M H_2SO_4 of H_I-e Pt deposited from the template mixture of 12 wt% H_2PtCl_6, 47 wt% $C_{16}EO_8$, 39 wt% water and 2 wt% heptane at -0.1 V vs SCE on H_I-e Pd. H_I-e Pd was initially deposited on gold (0.0079 cm^2 electrode area) from the template mixture of 12 wt% $(NH_4)_2PdCl_4$, 47 wt% $C_{16}EO_8$, 39 wt% water and 2 wt% heptane at 0.1 V vs SCE (3.5 mC deposition charge).

Another model was presented by Conway and Jerkiewicz [48]. The authors considered the free energy curves of activation for adsorbed and absorbed hydrogen. They suggested that the kinetics for the transition of adsorbed to absorbed hydrogen change with the addition of poisons so that the H-entry into Pd bulk is enhanced. The authors proceeded from the assumption that the absorption process occurs via the adsorbed state as the intermediate (equation 15).

$$H_{ads} \rightarrow H_{abs} \qquad \textit{Equation 15}$$

However, no proof in the literature has been given for this. From the results presented in *Figure 33* we note that the adsorption peak for H_I-e Pd occurs at a potential which is 200 mV different from the adsorption peak. The formation of absorbed hydrogen from the adsorbed state is described by a chemical reaction and is not driven electrochemically. Since the H-adsorption and absorption process occur at very different potentials we would not assume the adsorbed hydrogen as intermediate in the H-absorption process. We would rather suggest that the H-absorption process takes place without passing through the adsorbed state (equation 16) so that hydrogen diffuses directly into Pd bulk.

$$H_3O^+ + e^- \rightarrow H_{abs} + H_2O \qquad \textit{Equation 16}$$

We then suggest that this process speeds up when the formation of adsorbed hydrogen is suppressed by the coverage of poisons. With the addition of crystal violet in the voltammogram b) in *Figure 33* we note inhibition of H-adsorption, faster kinetics in the absorption process and the same rate of evolved hydrogen compared to voltammogram a).

One could argue that the formation of adsorbed hydrogen starts on the cathodic scan at potentials of -0.65 V after which the H-absorption process immediately occurs. However, no experimental evidence has been found for this.

The striking difference to the model proposed by Conway and Jerkiewicz corresponds to the fact that we claim the hydrogen to diffuse directly into Pd bulk. This occurs with faster kinetcs when the Pd surface is poisoned by crystal violet.

Of course, we have to emphasize that with our H_I-e Pd films the distinction between the absorbed and adsorbed hydrogen peak is possible. This is due to the enhanced kinetics in our electrode processes and caused by the fact that Pd atoms within the metal are not more than a few nanometers away from the surface. Hydrogen can permeate into the metal walls of nanometer-sized dimensions from both sides and we therefore do not expect the diffusion to be rate-limiting in the absorption process. This was not the case in the experiments carried out by Conway and Jerkiewicz [48] who used ordinary Pd electrodes.

We add to this discussion results from the electrochemical deposition of Pt on top of H_I-e Pd showing similar electrochemical properties for the hydrogen absorption process as for crystal violet when added to the acid solution.

Figure 34 shows a cyclic voltammogram at 10 mV/s in 1 M sulfuric acid for H_I-e Pt deposited on top of H_I-e Pd. H_I-e Pd was initially deposited onto the gold disc electrode of 1 mm diameter (0.0079 cm^2 electrode area). Both metals were deposited from the $C_{16}EO_8$ template mixture with the total deposition charge of 3.5 mC. As we will outline in Chapter 6, the H_I-e Pt-Pd bilayer film consists of pores running continuously through the final film. The electroactive surface areas estimated for both H_I-e metal layers were found to be consistent with the nanostructure.

Focusing on the hydrogen region we note that the peak on the cathodic scan at -0.66 V vs SMSE is associated to the formation of absorbed hydrogen and gives rise to the desorption peak on the anodic sweep at -0.605 V. Comparing these results to those obtained in voltammogram a) of Figure 33 for H_I-e Pd deposited on the gold disc electrode of the same electrode area we note that the hydrogen absorption peak appears to be sharper with the significant shift in the position of the peaks of 25 mV. However, as outlined before, and to emphasize it again, no shift in the mid peak potential can be seen when comparing the voltammograms. It is noteworthy that similar behaviour between the voltammetry in Figure 34 and in Figure 33 b) was observed where crystal violet was added to the acid solution in which H_I-e Pd was electrochemically cycled.

The cyclic voltammetry in sulfuric acid in the potential limit of the hydrogen absorption region for the nanostructured Pt-Pd bilayer film reveals electrochemical properties similar to those shown for crystal violet when added to the acid solution. It is of interest to note that this behaviour appears in the presence of a dissimilar metal deposited on top of H_I-e Pd. Our experiments showed that this effect is not restricted to Pt but can also be extended to Rh. H_I-e Rh deposited onto H_I-e Pd under the same experimental conditions showed identical electrochemical behaviour in the cyclic voltammetry in acid solution.

However, from the cyclic voltammetric measurements of H_I-e Pd film electrodes we could not clearly demonstrate the absence of the hydrogen adsorption peak on the Pd surface sites when Pt and Rh were electrochemically deposited on top. In the following we want to discuss this issue in detail showing the cyclic voltammetry for Pt-Pd bilayers.

From the results presented in Figure 34 we can only assume so far that the rate of the hydrogen absorption reaction is significantly affected by the deposition of Pt onto the Pd surface. It remains an open question as to whether hydrogen permeates into Pd bulk without passing the adsorbed state with the coverage of Pt.

A couple of other questions remain unsolved. One of the problems necessary to discuss is to what extent the morphology of Pd is relevant to enhance the absorption process kinetically.

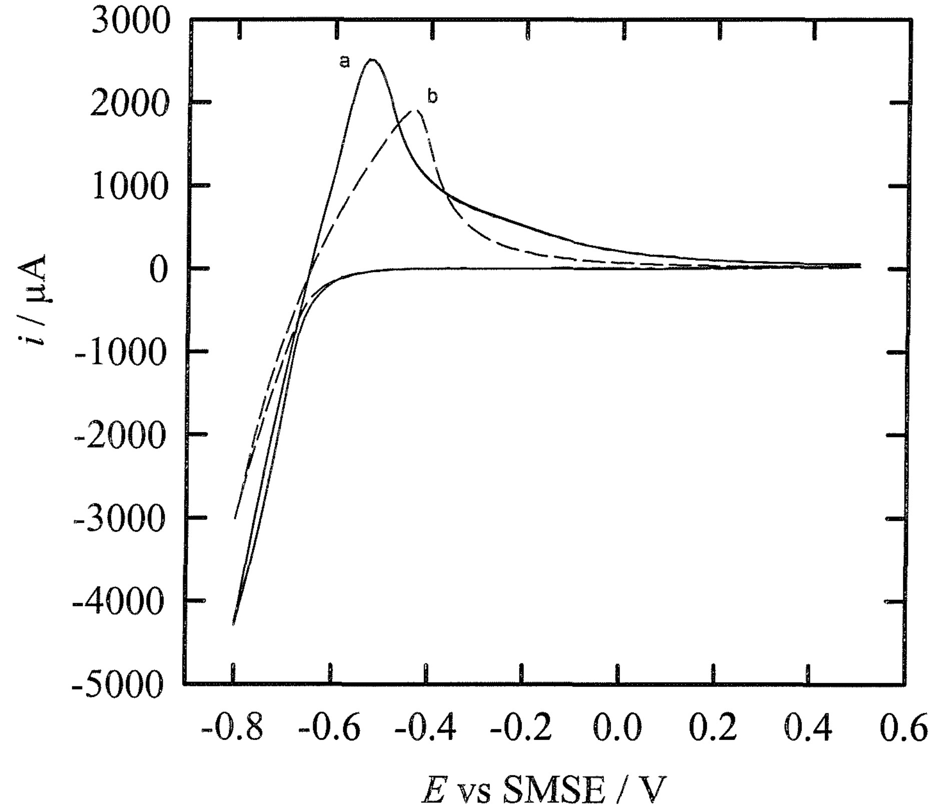

Figure 35: Cyclic voltammogram of H_I-e Pt a) (3.5 mC total deposition charge; deposited from the Brij®56 plating bath) deposited on Pd bulk (0.0045 cm^2) and cyclic voltammogram of Pd bulk electrode b) recorded at 100 mV/s in 1 M sulfuric acid.

Figure 35 shows a cyclic voltammogram for H_I-e Pt deposited on a Pd wire (polycrystalline; 0.0045 cm^2 electrode area) a) and the Pd wire alone b). For both voltammograms we notice a broad peak at -0.53 V a) and -0.43 V b) on the anodic scan and a rather non-pronounced feature on the return sweep at far negative potentials. This behaviour on the reverse cathodic voltammetric sweep is similar to that seen for polycrystalline Pd [46]. The charge underneath the peak on the anodic scan is estimated, in both cases, to be approximately 4.1 mC. It is noteworthy that with the deposition of 3.5 mC H_I-e Pt on to the Pd wire (polycrystalline Pd) a shift in the cathodic peak potential of 0.1 V vs SMSE is visible. Despite this, we can say that the electrochemical features seen in this voltammetry are quite different from those seen in Figure 33 a) and Figure 34.

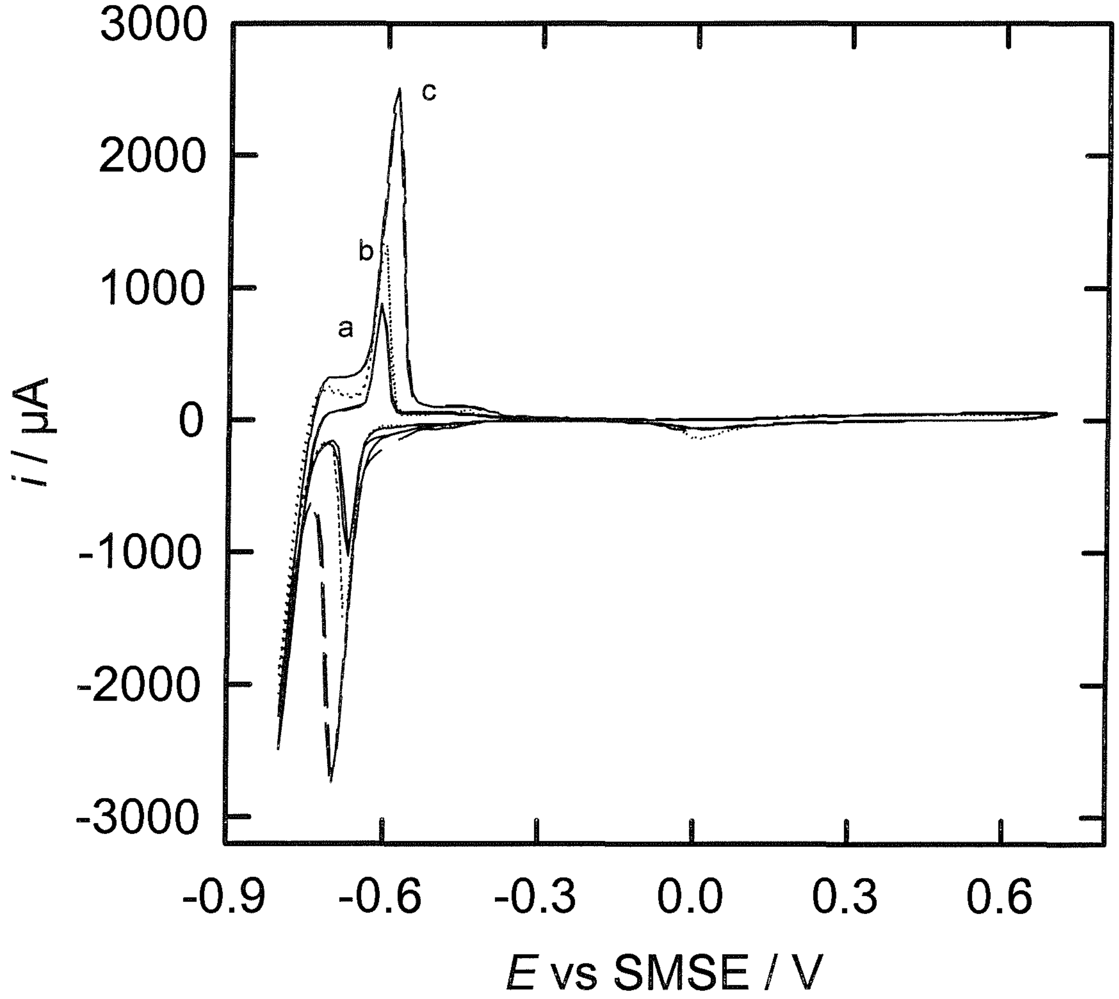

Figure 36: Set of cyclic voltammograms of H_I-e Pd deposited on a gold disc electrode (area 0.0079 cm^2) recorded at 100 mV/s in 1 M sulfuric acid with different thicknesses of Pd corresponding to the charge ranging from 1 a) 2 b) to 3.5 mC c). On top of every H_I-e Pd film the same amount of H_I –e Pt (3.5 mC) was deposited. Both metal films were deposited from the $C_{16}EO_8$ plating bath.

As already pointed out, the feature on the cathodic scan at far negative potentials is not pronounced and is very different from the well-defined peak on the cathodic response in Figure 33 a) and Figure 34. We attribute this behaviour to the absence of the nanostructure of Pd.

Figure 36 shows a set of cyclic voltammograms for different thicknesses of Pd as determined by the charge passed for their deposition. H_I-e Pd was deposited initially on the gold disc electrode. On top of every H_I-e Pd film the same amount of H_I-e Pt (3.5 mC) was electrochemically deposited. The cyclic voltammetry of these films in 1 M sulfuric acid at 100 mV/s covers the hydrogen and oxygen evolution region as potential limits. The voltammetry is determined by the H-absorption process in which the β-hydride phase dominates over the α-hydride phase as we know from earlier experiments in Chapter 3 so that we can proceed from the fact that the large peak occurring in the hydrogen region is attributable to the β-hydride phase. The charge underneath the anodic peak in each voltammogram is the same as the charge for the corresponding peak on the cathodic scan.

It is worth mentioning that with increasing Pd thickness from 1 mC to 3.5 mC remarkable differences occur in the voltammetries. First the peak potential for the H-absorption shifts on the anodic scan from -0.61 V to -0.58 V to more positive potentials and on the cathodic scan correspondingly from -0.67 V to -0.7 V to more negative potentials. As we outlined before, this might be because the system is kinetically controlled.

Another striking difference visible in the voltammetry is that with increasing Pd thickness the charge underneath the peak on the anodic scan and on the reverse voltammetric cathodic sweep increases sequentially from 0.33 to 1.5 mC. This clearly demonstrates the fact that the amount of hydrogen absorbed into bulk Pd is also dependant on the amount of Pd.

Summarizing the facts regarding the extent to which the morphology of the Pd is relevant for the H-absorption process, we can separate our results into two parts. On the one hand we found that nanostructured Pd is required to obtain a high surface / volume ratio and therefore to affect the H entry into the bulk Pd to large extent. On the other hand we showed that subsequent increase of the Pd thickness leads to the increase in the amount of hydrogen permeating into the metal lattice. These two observations are of fundamental interest in studying the H-absorption process.

To investigate the formation of the hydride phases in more detail when a dissimilar metal was deposited onto H_1-e Pd we carried out a series of experiments in which the

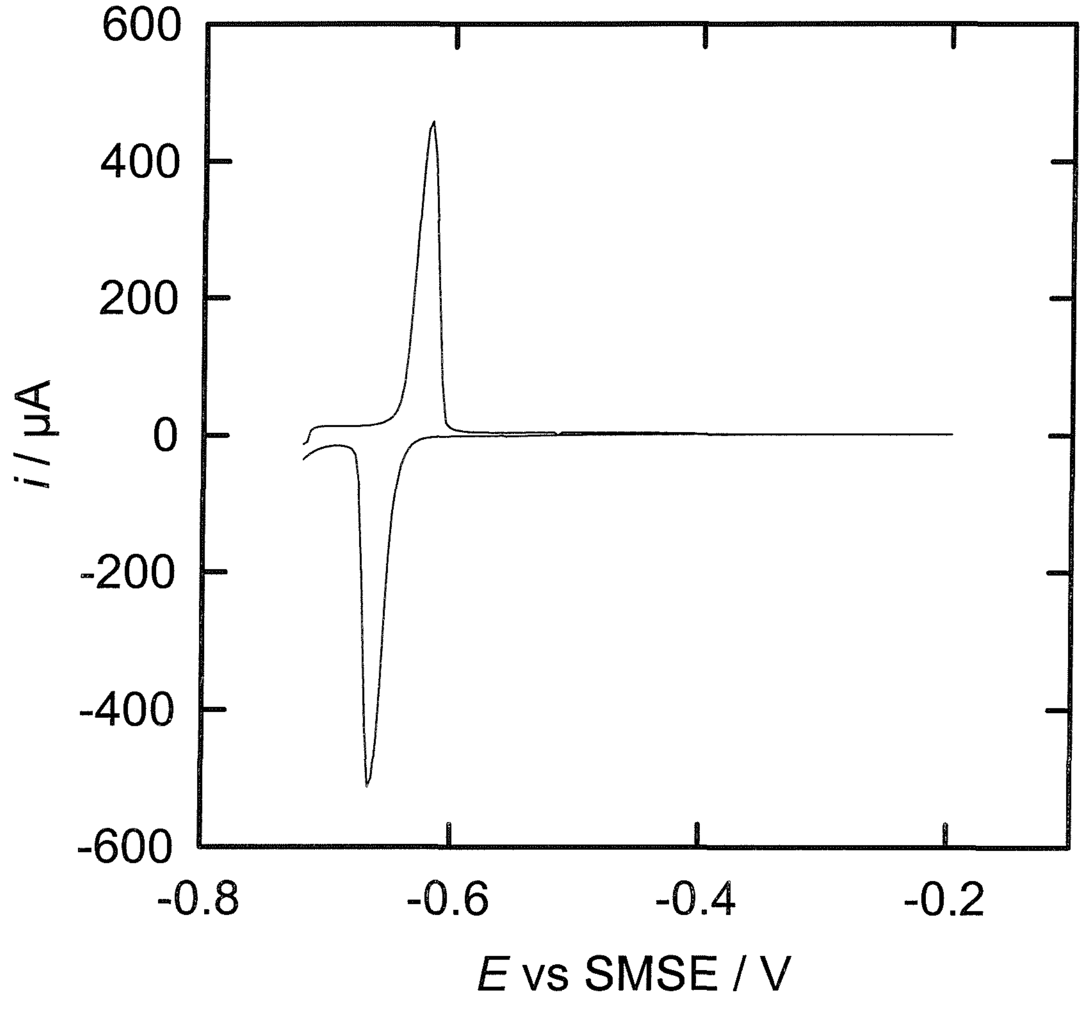

Figure 37: Example of a voltammogram for hydrogen absorbed in an H_1-e Pd film, on which H_1-e Pt was deposited, in 1 M H_2SO_4 recorded at 10 mV/s. The electrode was stepped from -0.2 V to -0.72 V vs SMSE and held there for 120s to load the electrode with hydrogen immediately before the anodic scan. Both metal films were deposited from the $C_{16}EO_8$ plating bath onto a 1 mm diameter gold disc electrode (charge passed 3.5 mC).

potential of the electrode was stepped from -0.56 V to increasingly cathodic potentials, held at the cathodic potential for 120s and then swept back at 10 mV/s to -0.2 V vs SMSE. Experiments of this type have been already carried out in Chapter 3 to get more insight into the Pd hydride phases. This time, however, we want to discuss the effect of Pt deposited on top of the H_I-e Pd. In a separate set of experiments the length of time that the electrode was held at the cathodic potential was varied in order to ensure that sufficient time was allowed for the system to equilibrate at the cathodic potential before the anodic sweep. We found that the reduction occurs rapidly and is complete after 120s. These results are similar to those observed in Chapter 3.

Figure 37 shows the reverse scan of a typical cyclic voltammogram at 10 mV/s in 1 M sulfuric acid of H_I-e Pd on which H_I-e Pt was deposited. The potential of the electrode was stepped from -0.56 V to -0.72 V vs SMSE and held at this potential for 120s. Usually we would expect to see, based on the results in Chapter 3, two well resolved peaks on the reverse voltammetric sweep. We found in Chapter 3 for the same sort of experiments, in which the electrode was stepped to different cathodic potentials, on the reverse anodic sweep a peak at -0.453 V vs SMSE corresponding to the oxidation of the adsorbed hydrogen on the Pd surface. This is not to be seen in the experiments described here when H_I-e Pt was deposited onto H_I-e Pd. It seems from this figure and the experiments shown here that the adsorbed hydrogen has completely disappeared. However, direct proof for this is given later. We also want to point out that there is a shift in the peak potential. The peak corresponding to the oxidation of the β-hydride phase in Figure 26 in Chapter 3 occurs at -0.6 V vs SMSE. This is not in accordance to the results shown here. The peak for the oxidation of the β-hydride phase occurs at -0.62 V vs SMSE. That is very similar to the experiment where crystal violet was added to the acid solution to block the Pd surface sites.

By carrying out a series of experiments of the sort shown in Figure 37 in which the potential was stepped to different cathodic values and then integrating the total charge passed in the reverse anodic sweep corresponding to the oxidation of absorbed hydrogen we can then build up a plot of the charge as a function of the potential. We then convert the charge to the H/Pd ratio at each potential using the Faraday law and the total charge passed in the deposition of the Pd film. We use a value for the faradaic efficiency of 95% for the deposition of H_I-e Pd calculated from EQCM-measurements [10]. The resulting plot for H_I-e Pd on which H_I-e Pt was deposited is shown in Figure 38 a). Below -0.55 V vs SMSE the H/Pd ratio increases slowly as the potential becomes more cathodic. This corresponds to the formation of α-hydride.

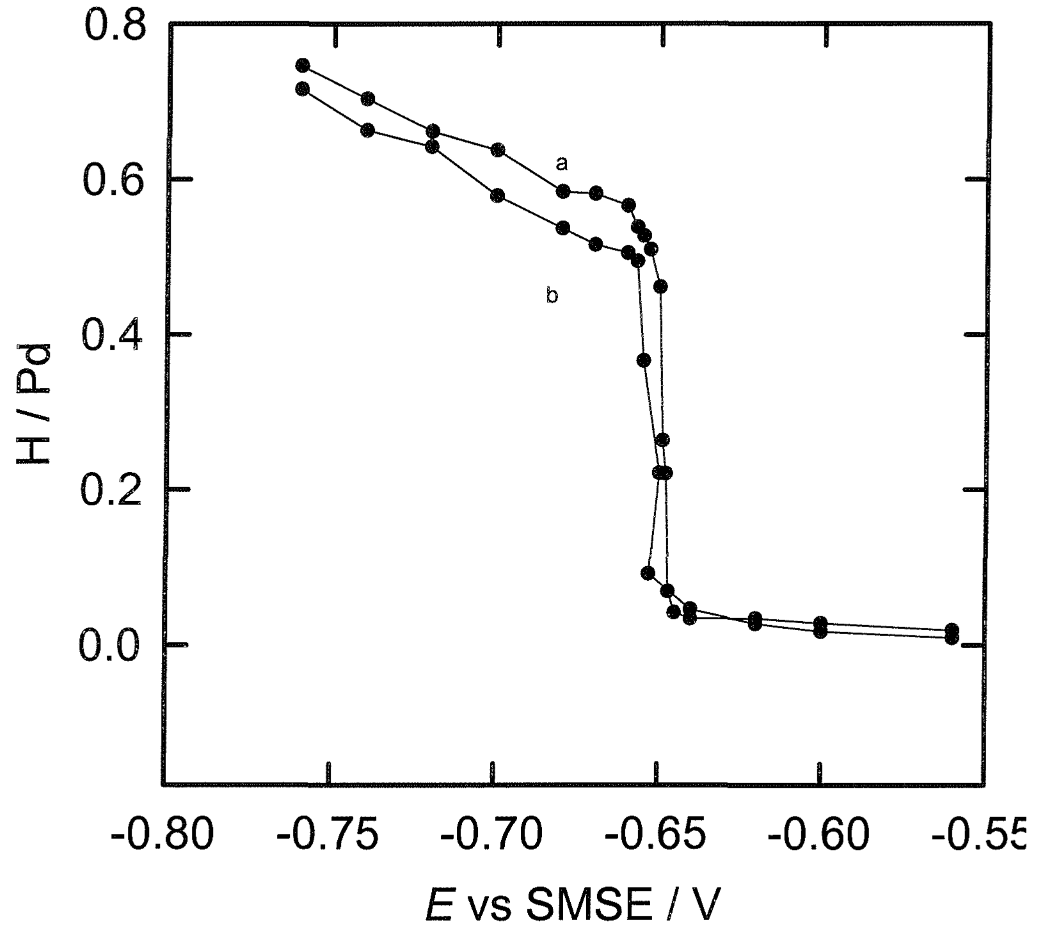

Figure 38: Plot of the H/Pd ratio as a function of potential for an H_I-e Pd film b) and H_I-e Pd on which 3.5 mC H_I-e Pt a) was deposited. The hydrogen loading of the electrode was determined from anodic voltammetric sweeps of the type shown in Figure 37 after stepping the electrode to different cathodic potentials. The total Pd loading was calculated from the charge passed to deposit the H_I-e Pd film (3.5 mC for 1mm diameter electrode) and the measured faradaic efficiency for the deposition.

We then observe a sharp rise in the H/Pd at -0.653 V corresponding to the formation of the β-hydride phase. These features are identical to those seen for the H_I-e Pd film in curve b) (without the deposition of H_I-e Pt on top). Comparing the α-β phase transition between H_I-e Pd and H_I-e Pd on which H_I-e Pt was deposited, we note that the transition between both phases for a Pt – Pd bilayer system occurs over a slightly smaller range of potential (~10 mV instead of ~20 mV).

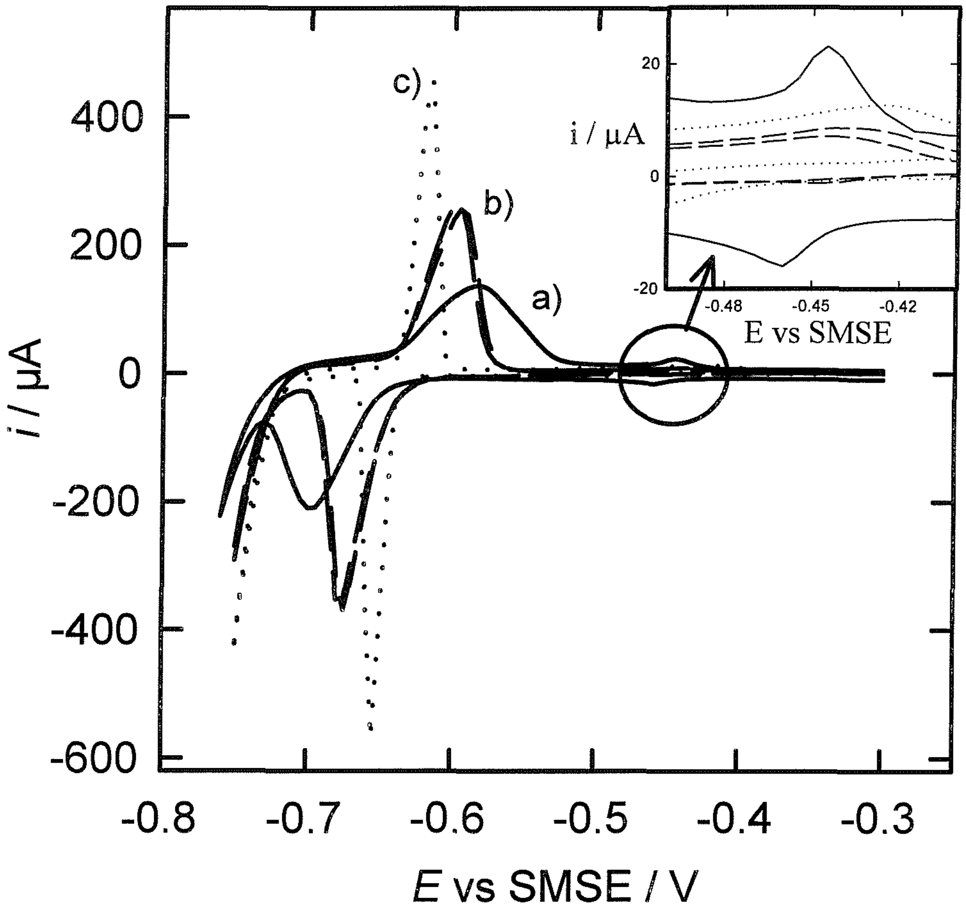

Figure 39: Set of cyclic voltammograms at 10 mV/s in 1 M sulfuric acid of Pt deposited from the aqueous solution containing 25 mM H_2PtCl_6 and 1 M HCl onto H_I-e Pd with increasing number of Pt atoms covering the Pd surface. H_I-e Pd a) was initially deposited onto a (0.0079 cm^2) gold disc electrode (3.5 mC total deposition charge). In curve b) 1 Pt atom and in curve c) 3 Pt atoms are for every 10 Pd atoms. This corresponds to a Pt coverage on the Pd surface of 0.1 and 0.3 monolayers.

Again we note, as already pointed out in Chapter 3 and in the literature [99], that at more cathodic potentials the H/Pd ratio in Figure 38 tends towards a plateau at around 0.58 for curve a) and 0.52 for curve b) before increasing again at potentials more cathodic than -0.68 V a) and -0.70 V b). The plateau values of 0.58 and 0.52 correspond to the composition of the β-hydride phase formed by the H_I-e Pd film. The further increase in the apparent H/Pd ratio in Figure 38 at more cathodic potentials as reported above has already been discussed in detail in Chapter 3.

The voltammetric features corresponding to the hydrogen absorption process seen for H_I-e Pd in the presence of crystal violet and for the Pt-Pd bilayer system are very similar and therefore it is likely that they can be accounted by a single mechanism. However, in all the experiments shown so far we cannot provide the reader with clear evidence that H-adsorption on the Pd surface disappears completely in the presence of Pt deposited on top of H_I-e Pd. In case of the absence of the H-adsorption on the Pd surface when Pt is deposited onto H_I-e Pd we would expect similar behaviour to crystal violet as inhibitor of the H-adsorption in blocking the Pd surface. This would extend the range of poisons from crystal violet to Pt promoting the H-sorption into the metal lattice in a way that hydrogen diffuses directly into the bulk Pd without passing through the adsorbed state. In the following we want to show the absence of the hydrogen adsorption peak on H_I-e Pd when Pt was deposited on top of H_I–e Pd.

Figure 39 shows a set of cyclic voltammograms at 10 mV/s in 1 M sulfuric acid of H_I-e Pt deposited from the aqueous solution containing 25 mM H_2PtCl_6 and 1 M HCl onto H_I-e Pd with increasing number of Pt atoms covering the Pd surface. H_I-e Pd a) was initially deposited onto the gold disc electrode (0.0079 cm^2 area; 3.5 mC total deposition charge). We note that with increasing number of Pt atoms deposited onto H_I-e Pd a continuous shift in peak potential of the hydrogen absorption peak on the anodic sweep from -0.58 V a), -0.595 V b) to -0.615 V c) appears. In addition, the H-absorption peak becomes increasingly sharper from 70 mV a), 40 mV b) to 20 mV c) as values for the width at half height. The H-adsorption peak, seen in voltammogram a) and enlarged in the inset in Figure 39, disappears completely with subsequent Pt coverage in curve b) and c).

To conclude, increasing the thickness of H_I-e Pt deposited onto H_I-e Pd results in the disappearance of the H-adsorption peak. The H-absorption peak shifts in potential and becomes increasingly sharper. Hence the deposition of a dissimilar metal onto H_I-e Pd causes the inhibition of the H-adsorption onto the Pd surface enhancing the direct diffusion of H into the Pd metal. These features are similar to those seen for the voltammetry of H_I-e Pd where crystal violet was added to the acid solution to block the surface sites. These results are also consistent with those shown for the H_I-e Pt-Pd bilayer system, with the total deposition charge of 3.5 mC for each metal, where small amounts of Pt get onto the Pd surface in the pores. This causes the same effect as shown in the experiment described in Figure 39.

However, to accomplish this study as conclusive and proper as we can, we thought about an experiment in which the amount of crystal violet added to the acid solution varies significantly from 0.5 to 1 mM. This is necessary to show the reader the general effect of poisons on the hydrogen absorption process.

Figure 40 shows the same sort of experiment as in Figure 39, but for crystal violet surface coverage. We can see a set of cyclic voltammograms at 10 mV/s in 1 M sulfuric acid of H_I-e Pd deposited on a gold disc electrode. Figure 40 a) shows the cyclic voltammogram of an H_I-e Pd film electrode without crystal violet whereas b) and c) presents the cyclic voltammograms of H_I-e Pd in the presence of crystal violet with increasing concentration of 0.5 mM b) and 1 mM c).

We observe similar behaviour to that seen for the Pt-Pd bilayer system. With increasing concentration of crystal violet added to the acid solution, we note a continuous shift in peak potential of the hydrogen absorption on the anodic sweep from -0.58 V a), -0.60 V b) to -0.61 V c). Again, as already seen in the previous figure, the hydrogen absorption peak becomes increasingly sharper from 70 mV a), 40 mV b) to 25 mV c) as values for the width at half height. The H-adsorption peak, present in voltammogram a), disappears completely with the addition of crystal violet.

In showing the cyclic voltammetry of H_I-e Pd electrodes, we demonstrated convincingly the effect of blocking the Pd surface sites on promoting the hydrogen sorption into the metal lattice with increasing the amount of Pt covering the Pd surface and with increasing concentration of crystal violet. Since no difference has been found in the electrochemical properties between the Pt-Pd bilayer system and crystal violet added to the acid solution, we postulate that the same mechanism of H entry into the bulk Pd occurs in both cases and suggest that this occurs without passing through the adsorbed state.

With the coverage of poisons onto the Pd surface and the inhibition of H-adsorption the H-absorption process speeds up so that faster kinetics could be seen in the voltammetries.

We might have problems to understand the fact that crystal violet diffuses into the pores of the H_1-e metal film with a pore size diameter of only 2-3 nm and fully adsorbs on the Pd surface. It is hard to believe that crystal violet with a structure given below and a relatively large molecule size of ca. 1 nm inhibits completely the H-adsorption in the porous structure. Taking the low diffusion of crystal violet into account, one could argue that the Pd surface of the bottom part of the nanostructured metal might not be blocked by crystal violet. It remains also an open question how hydrogen can diffuse directly into Pd bulk in the presence of crystal violet so that the absorption process still occurs. These issues might be in contradiction to our results. However, despite this we stress our experimental findings that we observed a disappearance of the H-adsorption and still see the absorption process with faster kinetics in the presence of crystal violet.

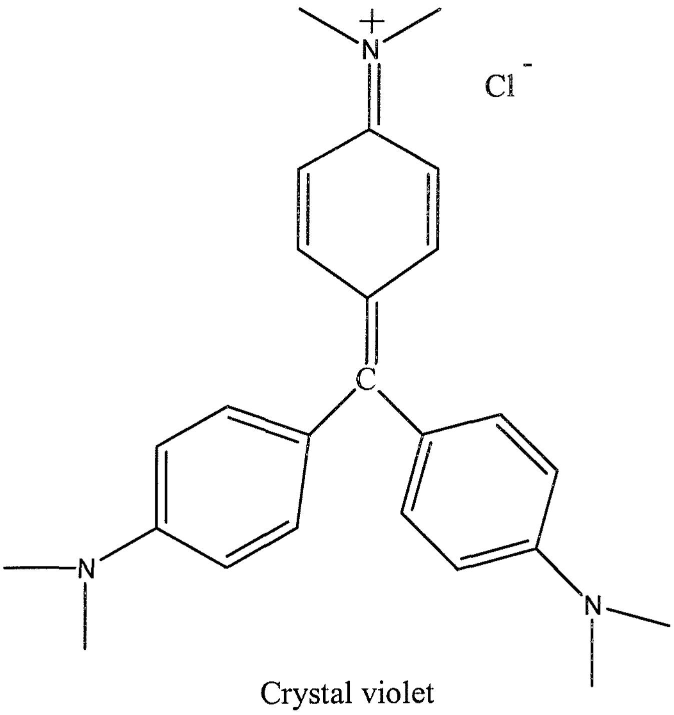

Crystal violet

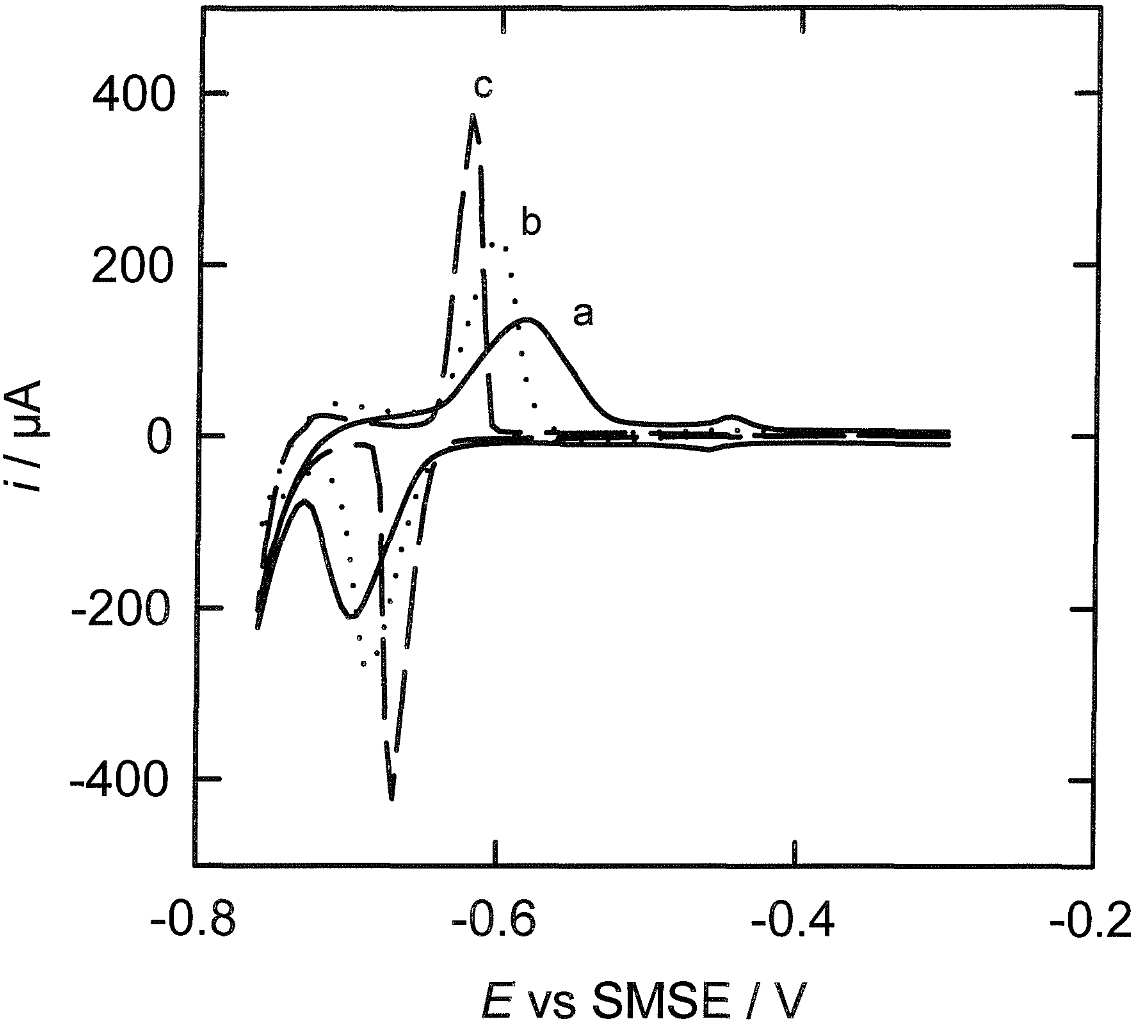

Figure 40: Set of cyclic voltammograms of H_I-e Pd (200nm thick, deposition charge 3.5 mC, deposited from the Brij®56 plating bath) deposited on a gold disc electrode (area 0.0079 cm^2) recorded at 10 mV/s in 1 M H_2SO_4 without crystal violet a) and in the presence of 0.5 mM b) and 1 mM crystal violet c).

4.3 Conclusion

In this chapter we were concerned with the poisoning of the Pd surface and the effect on the absorption of hydrogen into the metal lattice. With respect to our results and the experimental findings in the literature it has been our focus to find a general and consistent mechanism for the permeation of hydrogen into the Pd metal lattice when the surface sites are blocked by either crystal violet or Pt.

With crystal violet, as an inhibitor to block the hydrogen-adsorption on the Pd surface sites, we could clearly distinguish between the H-adsorption and the absorption peaks in the voltammetry. Herein the β-phase significantly dominates the absorption process. We noticed in the voltammetry a clear shift in the peak potential and increasingly sharper peaks in the presence of crystal violet added to the acid solution. This behaviour was also shown in the cyclic voltammetry of H_I-e Pd films on which H_I-e Pt was electrochemically deposited. The experiments showed that this was not only restricted to Pt but can also be extended to Rh.

We assumed that the H-absorption takes place without passing the adsorbed state so that hydrogen diffuses directly into Pd bulk. This process speeds up when the formation of adsorbed hydrogen is suppressed by the coverage of poisons.

To prove this as a general and consistent mechanism, we provided the reader with the evidence that the H-adsorption on the Pd surface disappears and the kinetics of the H-absorption become faster with increasing the coverage of platinum. This was also shown on H_I-e Pd electrodes in acid solutions to which a stepwise higher concentration of crystal violet was added.

These results are in accordance with the H_I-e Pt-Pd bilayer system, with the total deposition charge of 3.5 mC for each metal, where small amount of Pt get onto the Pd surface in the pores and cause the same effect as shown in Figure 39.

Chapter 5 Preparation and characterization of H_1-e Rhodium films

5.1 Introduction

We have been particularly interested in the electrochemical deposition of nanostructured materials from the lyotropic liquid crystalline phases of non-ionic surfactants. Using this approach we have electrochemically deposited Pd metal films from the hexagonal phase to produce metal films with regular arrays of nanometer-sized continuous pores arranged in a regular hexagonal array with wall thicknesses again of nanometers. We have shown that we can prepare Pd metal films with high surface area (91 m^2/g corresponding to an area per unit volume of $1.1*10^7$ cm^2/cm^3).
In this section we report the deposition of nanostructured rhodium by electrochemical reduction of rhodium ions dissolved in the aqueous domains of a hexagonal lyotropic liquid crystalline phase. The rhodium films described are denoted as H_I-e films to indicate the electrochemical deposition from the H_I hexagonal phase and as a consequence they contain a regular array of hexagonally packed pores.
In the first part of the chapter we describe the phase behaviour for the template mixture and in the second part the characterization of nanostructured Rh metal films using transmission electron microscopy, X-ray diffraction and scanning electron microscopy. In the third part we describe the electrochemical behaviour of the nanostructured Rh metal. There is no work in the literature about the preparation of nanostructured rhodium. However, a variety of publications exists reporting the electrochemical oxidation of Rh electrodes and attempting to understand the structure of the surface oxide layers formed on the rhodium electrodes [100-102]. This literature will be discussed in detail with our experimental findings below.
We also present the results of a preliminary study demonstrating electrocatalytic properties of rhodium used for the nitrate reduction process.

5.2 Phase behaviour

As shown previously the nanostructure of metals deposited from the non-ionic surfactant mixtures are directly determined by the structure of the lyotropic liquid crystalline phases employed. The studies of nanostructured Rh films therefore begin by describing the phase behaviour of mixtures containing the non-ionic surfactant and

$RhCl_3$. $C_{16}EO_8$ (octa ethylene glycol monohexadecylether) was used as a highly purified, monodisperse, commercial surfactant.

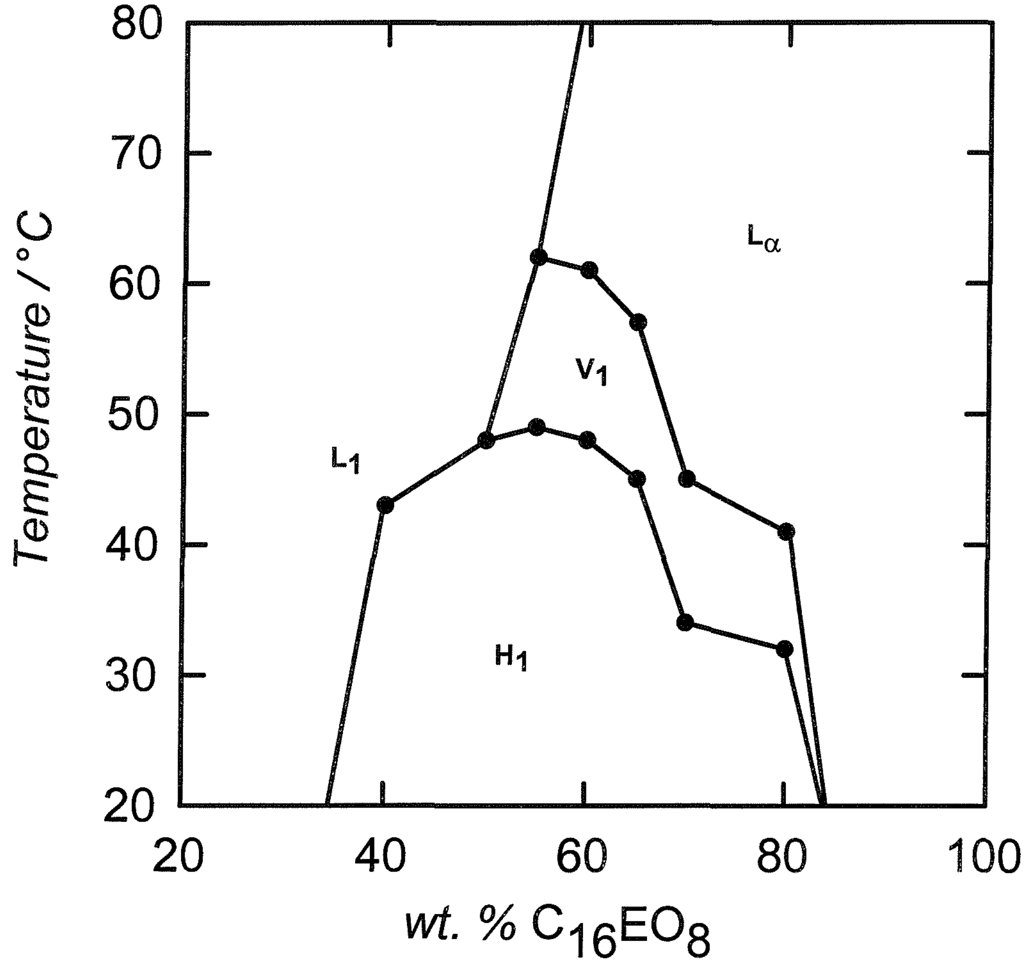

Figure 41: Pseudobinary phase diagram of $C_{16}EO_8$ and water in which the concentration of $RhCl_3$ was kept constant at 1.91 mol/l. The weight ratio of surfactant to heptane was kept fixed at 22. The solid lines which correspond to the domain boundaries are drawn as guides to the eye. H_I is the hexagonal phase, V_I the cubic phase, L_α the lamellar phase and L_I is the micellar solution.

Figure 41 shows the phase diagram for the Rh templating solution. The most common phases were obtained such as: hexagonal phase H_1, cubic phase V_1 and lamellar phase L_α. The solid lines which correspond to the domain boundaries are drawn as guides to the eye. The dotted lines drawn vertically show the compositions at which the temperature was estimated. The hexagonal domain exists from 30 to 40 wt% $C_{16}EO_8$

up to 80 to 90 wt% and is stable up to 49 °C. The cubic phase V_1 exists between 55-55 wt% up to 80-90 wt% of template with the maximum temperature around 55 wt% (62 °C). The domain of existence of the cubic phase does not cover a large range of temperature comparing with the hexagonal phase and no evidence has been found for the existence of the cubic phase at room temperature. The domain of existence of the lamellar phase starts between 50 and 55 wt% of surfactant in water and continues above 90%.

The phase behavior and location of the phase boundaries found for the rhodium chloride/$C_{16}EO_8$ systems are very similar to those reported by Mitchell [11] for the $C_{16}EO_8$ water system indicating that the presence of the rhodium salt does not significantly perturb the phase behaviour of the system. This contrasts with the findings for the corresponding platinum plating bath based on hexachloroplatinic acid where large shifts in the phase boundaries are observed [23]. This is due to strong interactions between the hexachloroplatinate anions and the elthylene oxide headgroups of the surfactant.

The phase diagram in Figure 41 shows a large composition and temperature range over which the hexagonal phase is stable. In all the subsequent experiments the H_1-e rhodium films were prepared by carrying out the deposition from this phase. In each case the presence of the hexagonal phase was confirmed by polarizing light microscopy prior to the deposition of rhodium.

In the next section we study briefly the electrodeposition of the H_1-e Rh film.

5.3 The electrodeposition of mesoporous H_I-e Rh films onto gold electrodes

This section describes the Rh deposition onto the gold electrode from the template mixture. The Rh salt was mixed with the non-ionic surfactant, water and heptane to produce the template mixture for the deposition of the mesoporous Rh films. As already pointed in Chapter 3, no supporting electrolyte was added to the template solution as this could influence the existence of the liquid crystalline phases and disrupt the pore arrangement.

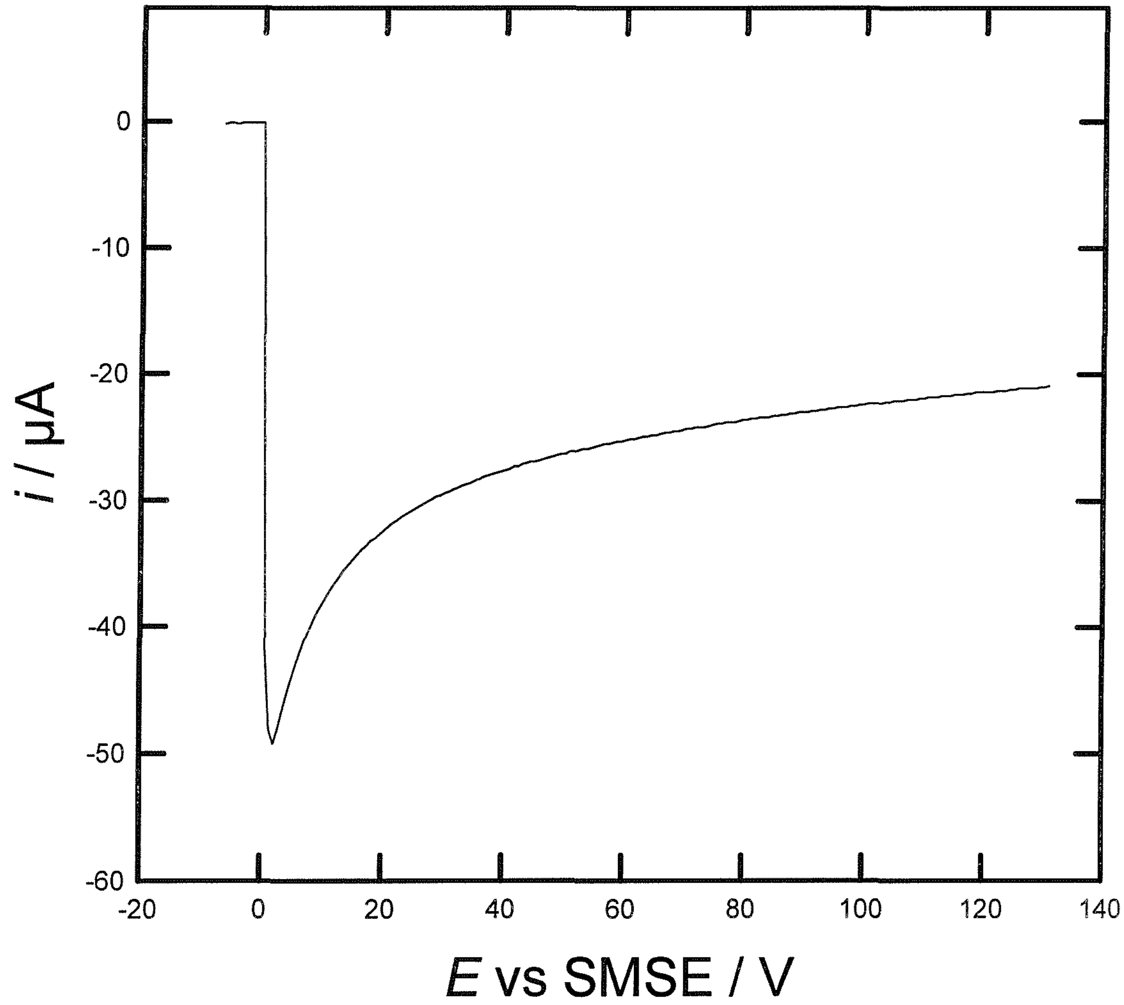

Figure 42: Current transient for the electrodeposition of mesoporous Rh from 12 wt% $RhCl_3$, 47 wt% $C_{16}EO_8$, 2 wt% heptane and 39 wt% water at -0.2 V vs SCE on 1 mm diameter gold disc electrode

Figure 42 shows a typical current transient obtained during the electrodeposition of Rh from the template mixture at -0.2 V vs SCE on a 1 mm diameter gold disc electrode. According to the literature [103] this potential was found as suitable to be applied for the deposition of Rh. Although the experimental conditions were different from those in our experiments we did not note any deviation from our experiments in this potential. From Figure 42 we note that the reduction current rises nearly to -49 μA immediately after the potential step as a result of the double layer charging. The current decreases then to reach -21 μA after 131 s.

The charge passed to deposit Rh onto the gold electrode with the geometrical area of 0.0079 cm^2 was 3.5 mC in all our experiments. Using the Faraday law and considering the porous structure of the metal film we estimated a thickness of the deposited material of 130 nm. This is based on a faradaic efficiency of 100%. This is consistent with the literature [101] and our experimental findings in the SEM-measurements.

The current never reaches a plateau over the period of time of 131 s but the decay becomes very slow thereafter. This was already shown in Chapter 3 where we compared the results for Pd deposited from the aqueous solution with the electrodeposition from the template mixture.

This section has briefly shown the properties of the electrodeposition of mesoporous Rh from the template mixture. In the next section we study in detail the characteristics of these metal films.

5.4 Characterization of H_I-e Rh films

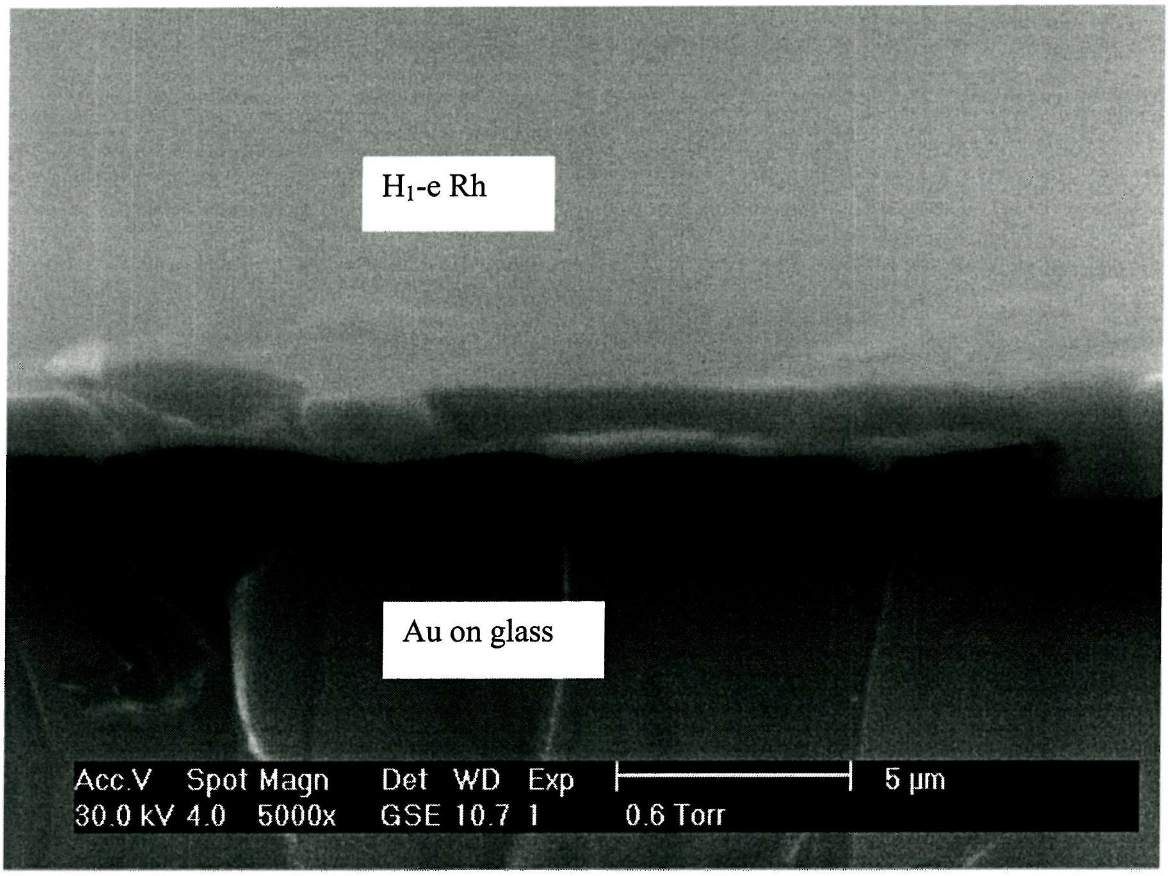

Figure 43: Scanning electron micrograph of an H_I*-e Rh film deposited on an evaporated gold electrode. The film was deposited from a mixture of 12 wt%* $RhCl_3$*, 47 wt%* $C_{16}EO_8$*, 2 wt% heptane and 39 wt% water at -0.2 V vs SCE. The total charge passed was 0.56* C / cm^2 *and the image was obtained at a tilt angle of 70°.*

The H_I-e Rh films electrochemically deposited at -0.2 V vs SCE from the hexagonal phase are adhered well to the evaporated gold electrodes used for the deposition. Figure 43 shows a scanning electron micrograph of an H_I-e Rh film. Scanning Electron Microscopy (SEM) was used to examine the surface morphology of the deposited mesoporous Rh film.

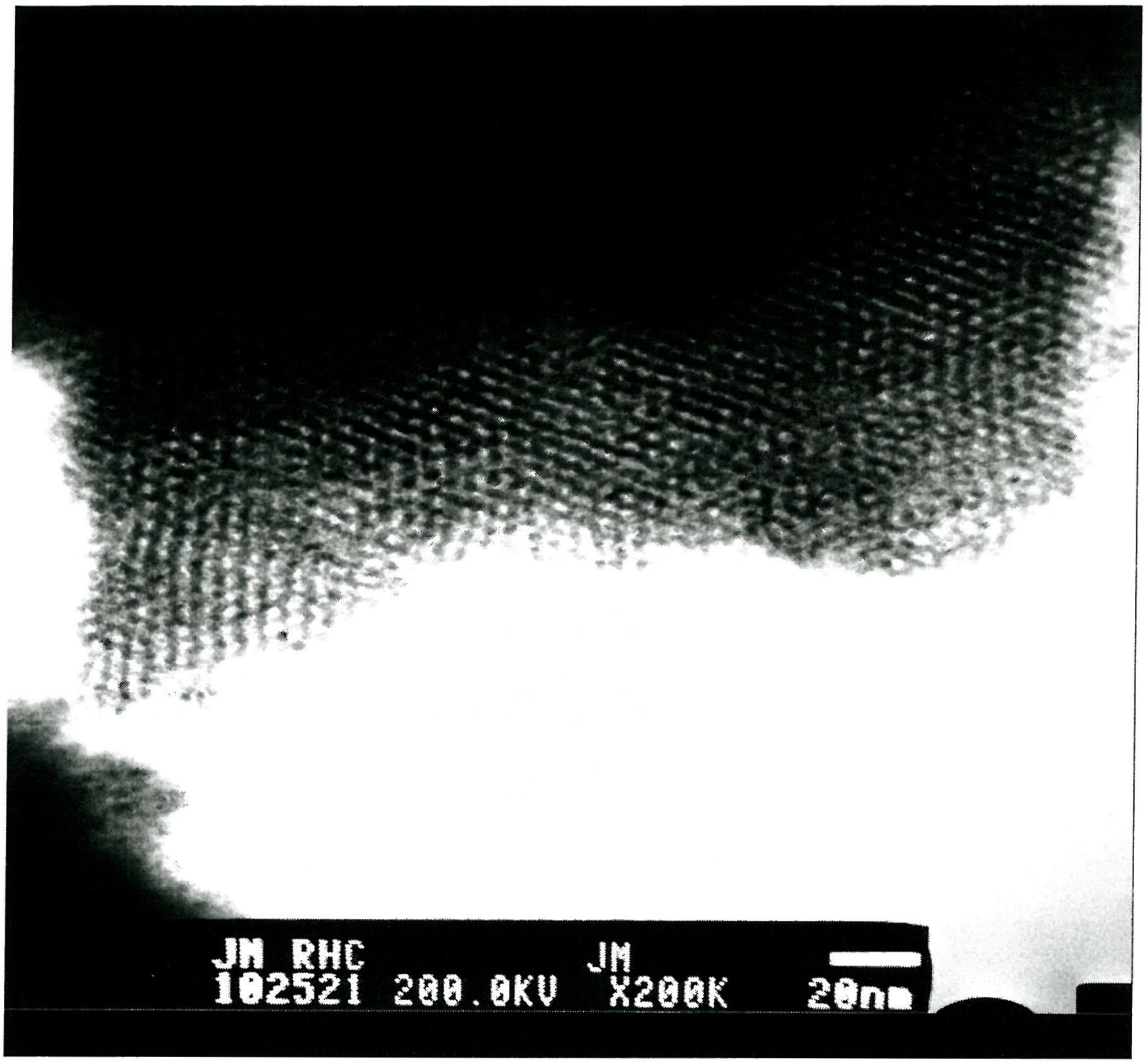

Figure 44: Transmission electron micrograph of a sample scraped from an H_I-e Rh film deposited from a mixture 12 wt% $RhCl_3$, 47 wt% $C_{16}EO_8$, 39 wt% water, 2 wt% heptane on an evaporated gold electrode at -0.2 V vs SCE. The total charge passed for deposition was 0.65 C / cm^2.

Figure 43 shows the edge of view of mesoporous Rh film at a tilt angle of 70° deposited on gold/glass. The film is dense, uniform and continuous over the whole range with no evidence of nanostructure on the SEM scale.

To examine the nanostructure of the electrochemically deposited Rh films it is necessary to use Transmission Electron Microscopy (TEM). To provide clear evidence for the hexagonal arrangement of Rh films in nanometer – sized dimensions is subject to the orientation of the TEM-image. The evidence for the hexagonal array of the pores running through the Rh film can be given if the image shows a "pores end on" view. We noticed from our experiments that to get this sort of image for H_I-e Rh films deposited from the $C_{16}EO_8$ system is of higher probability than for H_I-e Pd films. Again, as already pointed out for H_I-e Pd films, from the TEM-image of H_I-e Rh deposited from the Brij®56 system we cannot obtain sufficient information as to whether the film is of hexagonal array.

Figure 44 shows the TEM – image of H_I–e Rh deposited from the $C_{16}EO_8$ and scraped from the electrode surface. This image shows an orientation of the sample with the pores end on view. From the results obtained we can conclude that the H_I-e Rh films are punctured by pores of hexagonal arrangement. The film is determined by a porous structure consisting of cylindrical pores with pore size diameter of (35 ± 2) Å and wall thickness of (25 ± 2 Å). These values are very similar to those found for other nanoporous metals deposited under similar conditions from the hexagonal lyotropic liquid crystalline phase formed by $C_{16}EO_8$ [22, 99]

We note that the porous structure only appears at the edge of the TEM-image of the Pd-film scraped from the electrode surface. Most part of the image appears to be dark since the sample is too thick and therefore the electron beam cannot travel through.

More support for a regular pore distribution in H_I-e Rh films may be given by X-ray diffraction. The Rh films formed by electrochemical deposition from the template mixture were studied by low angle XRD. Figure 45 shows the low angle XRD patterns obtained for the hexagonal phase of the Rh template mixture. The low angle x-ray reflection of the Rh film shows a diffraction peak corresponding to the (100) diffraction plane of the hexagonal structure with a d-spacing of 49 Å. The value calculated for the d-spacing is consistent with the deposition of Rh films with a nanostructure of regular pore distribution derived from the structure of the template solution. The pore to pore distance for this hexagonal array, given by $d_{100} / \cos 30^\circ$, was found to be 56.5 Å.

Mesoporous Rh films deposited onto the gold substrates were shown to be dense, uniform and continuous. By using TEM we could provide evidence for the hexagonal arrangement of the Rh film on nanoscale. More support for the regular pore distribution was given by XRD-measurements. In the next section we use cyclic voltammetry to determine the electroactive surface area of H_I-e Rh films as another tool to prove the existence of the nanostructure.

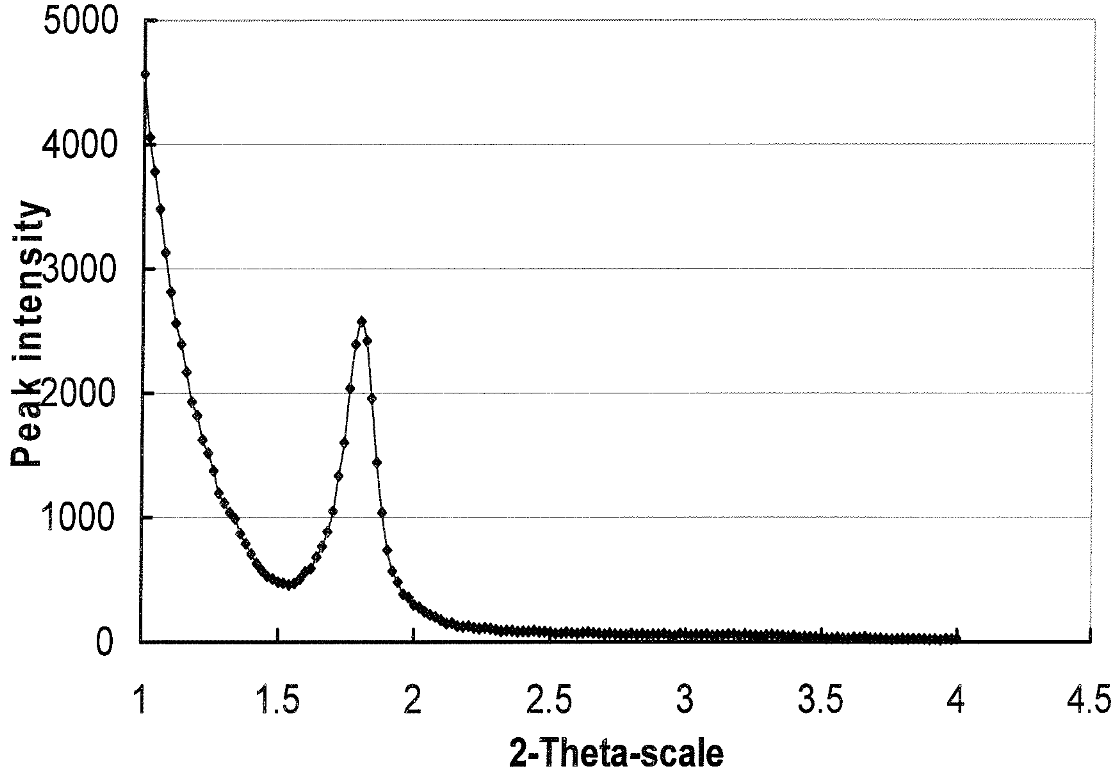

Figure 45: Low angle X-ray diffraction of H_I-e Rh film deposited on an evaporated gold electrode at -0.2 V vs SCE from a mixture of 12 wt% $RhCl_3$, 47 wt% $C_{16}EO_8$, 39 wt% water and 2 wt% heptane. The total charge passed for deposition was 0.70 C / cm^2.

5.5 Electrochemical characterization of H_I-e Rh films

Proceeding from the fact that we can make nanostructured Pd metal films by direct-templating from liquid crystalline phases with access to the high electroactive surface area we transfer this successful method to the fabrication of nanostructured Rh films.

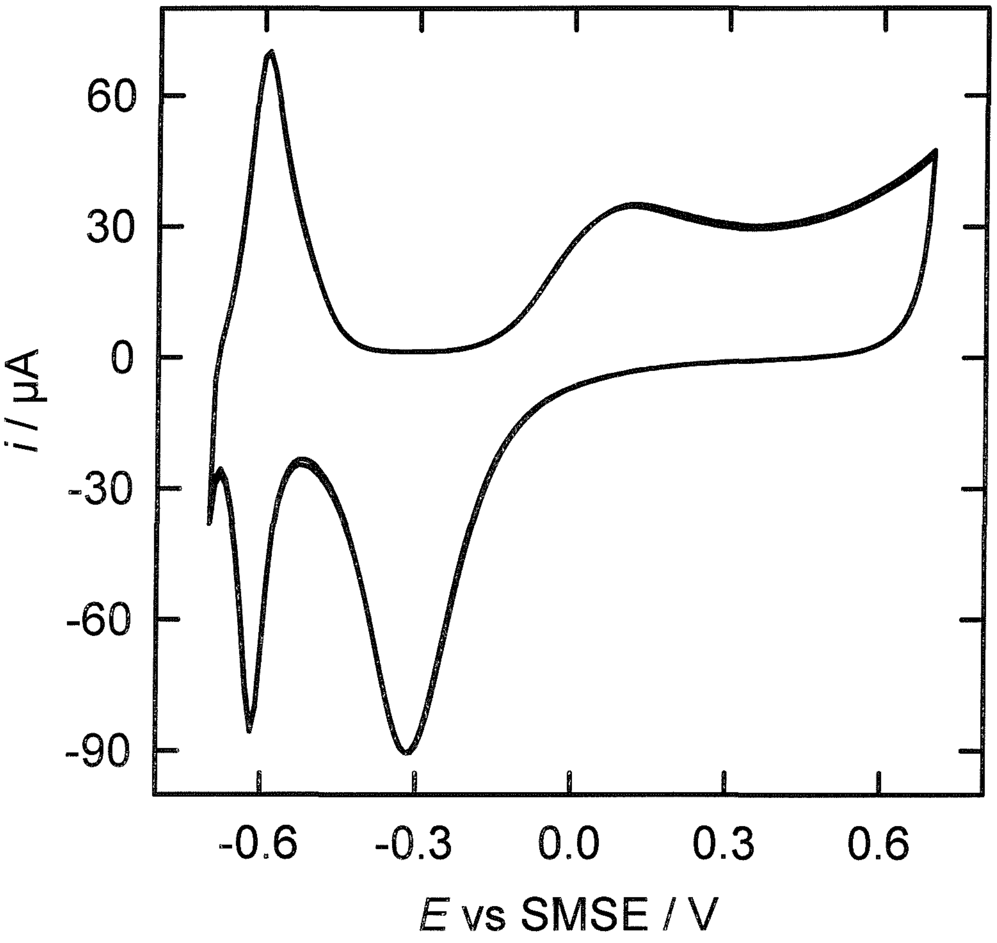

Figure 46: Cyclic voltammogram of an H_I-e Rh film (126 nm thick, total deposition charge 3.5mC) deposited at -0.2 V vs SCE from the template mixture of 12 wt% $RhCl_3$, 47 wt% $C_{16}EO_8$, 39 wt% water and 2 wt% heptane on a gold disc electrode (area 0.0079cm^2) recorded at 50 mV/s in 1 M sulfuric acid. The film was soaked in water for one hour prior to the voltammetry. The surface area of the H_I-e Rh film is 0.39 cm^2.

Attention is directed towards the surface oxides of the resulting H_I-e Rh metal electrodes from which the electroactive surface area can be estimated by calculating the charge passed in the surface oxide stripping reaction in order to prove that we obtain high surface area H_I-e Rh films. Rhodium is a noble metal that forms surface oxides upon anodic polarization. Growth of surface oxides on rhodium metal electrodes can be conveniently studied by cyclic voltammetry.

Figure 46 shows the cyclic voltammetry for a freshly prepared H_I-e Rh film electrode which was washed in water for 1 hour and then transferred to 1 M sulfuric acid. The H_I-e Rh electrode was electrochemically pre-treated by applied periodic potential-cycling in the acid solution before the start of the voltammetry. On the anodic sweep starting from -0.16 V vs SMSE we see the formation of the surface oxide. According to Jerkiewicz and Borodzinski [101] and Villiard and Jerkiewicz [102], who carried out a comprehensive study of the electrochemical formation and reduction of polycrystalline rhodium oxide layers in 0.5 M sulfuric acid solution at 298 K, Rh in the anodic region reveals different oxide states leading to the surface species Rh(OH) and at more anodic potentials $Rh(OH)_3$. The existence of these surface species were confirmed by XPS measurements [104] of the anodically-formed oxides on Rh. The electroadsorbed OH^- ions covering the metal surface subsequently lose protons and become O^{2-} surface species [105-107]. This process is followed by place exchange between the surface and the metal atom which is similar to the behaviour observed for Pt and oxygen ions [107].

It is worthwhile emphasizing that while oxide growth proceeds in two steps, oxide reduction is a one-step process as shown in Figure 46 giving rise to a well-defined stripping peak in the voltammetry at -0.31 V vs SMSE.

The voltammetry of polycrystalline Rh has been investigated by Rand and Woods [77]. Using their conversion factor of 660 $\mu C/cm^2$ [78, 101] for the surface oxide stripping peak we can estimate the electroactive surface area for our H_I-e Rh films assuming that the surface oxide on the nanostructured Rh is the same as that formed on bulk Rh. The deposited H_I-e Rh film shows the specific surface area of 32 m^2/g corresponding to an area per unit volume of 3.3×10^6 cm^2/cm^3. This value, together with the TEM and X-Ray data, is found to be consistent with the nanostructure and shows that the pores throughout the H_I-e film are accessible by the electrolyte solution.

The peaks in the voltammetry at more negative potentials are associated with the formation of adsorbed hydrogen at -0.62 V vs SMSE on the cathodic scan and with the oxidation of desorbed hydrogen at -0.59 V at the anodic scan. These features look very similar to those reported for a polycrystalline rhodium film electrode [101]. Using the conversion factor of 221 μC / cm^2 for the charge corresponding to one electron required for every Rh surface atom, we found the value of the electroactive surface of 0.38 cm^2 corresponding to the specific surface area of 31 m^2/g. According to [108] the adsorbed hydrogen on rhodium can appear in two distinguishable forms, as a weakly and as a strongly bound hydrogen. In dilute acidic solutions only weakly bound hydrogen can be seen in the voltammetry. The strongly bound form of adsorbed hydrogen becomes increasingly pronounced in more acidic solutions when increasing the concentration from 1 to 7.5 M. This was shown by Capon and Parsons [100] who then use cyclic voltammetry to provide the evidence for the different forms of adsorbed hydrogen on rhodium. In our case only one form of adsorbed hydrogen can be seen and we strongly assume, after reviewing the literature that it is the weakly bound hydrogen. Again we found no difference between the H_I-e Rh film and the plain Rh film electrode.

There is no evidence for any absorption of hydrogen into the bulk-Rh in the voltammetry. These experimental findings are consistent with the literature [101] and with calculations using the all-electron full-potential LMTO method carried out by Hennig et al. [109] who found that the dissolution energy of hydrogen in rhodium was too low to allow penetration of H into the bulk.

Electrochemical investigations of Rh [101, 102, 110-114] have shown that the oxide growth on Rh in alkaline and acidic solution under potential cycling conditions, covering the full range of potential from the hydrogen adsorption to the oxide region, depends on the solution pH, the switching potential limits, the sweep rate, the temperature and the time for which the potential was held in the oxide region. The data showed explicitly the effect of the increase of the polarization potential on the oxide charge density with the oxide reduction peak potential shifting towards less positive potentials [102]. On the other hand the authors demonstrated in their cyclic voltammetry for Rh in acid solution the effect of the increase of the polarization time on the oxide charge density with the reduction peak potential moving again towards less positive potentials. In both cases the charge determined from the oxide stripping peak remained the same despite the qualitative changes on the oxide stripping. The authors claimed that the Rh oxide layer undergoes rearrangement during the oxide growth with the potentiodynamic treatment leading to more stable forms of the oxide. The authors claimed that on potential-cycling the transformation from $Rh(OH)_3$ to Rh O(OH) appears.

Reported data from our studies will show the effect of potential-cycling on Rh electrodes, specially affecting the surface oxide growth on Rh. In the following we present data on this aspect of the H_I–e Rh electrochemistry focusing on the qualitative changes in the Rh oxide stripping peak on increasing the number of voltammetric cycles in the restricted potential range from -0.7 V to 0.7 V vs SMSE.

Figure 47 shows a set of cyclic voltammograms after the first two cycles of a H_I-e Rh film electrode at 50 mV/s in 1 M sulfuric acid. We note on the cathodic scan of the cyclic voltammogram of the H_I-e Rh film 3 peaks. The peak at more negative potentials at -0.64 V vs SMSE is associated to the hydrogen adsorption. On continuing the cathodic scan to more positive potentials we can see a well-defined peak at -0.53 V and a less pronounced peak at -0.31 V with a poorly resolved shoulder.

However, it is clear that the voltammogram shown in this figure do not reveal the voltammetric feature on the cathodic sweep for a Rh electrode presented in Figure 46 with the surface oxide stripping peak occurring at -0.31 V and with a well-defined hydrogen region.

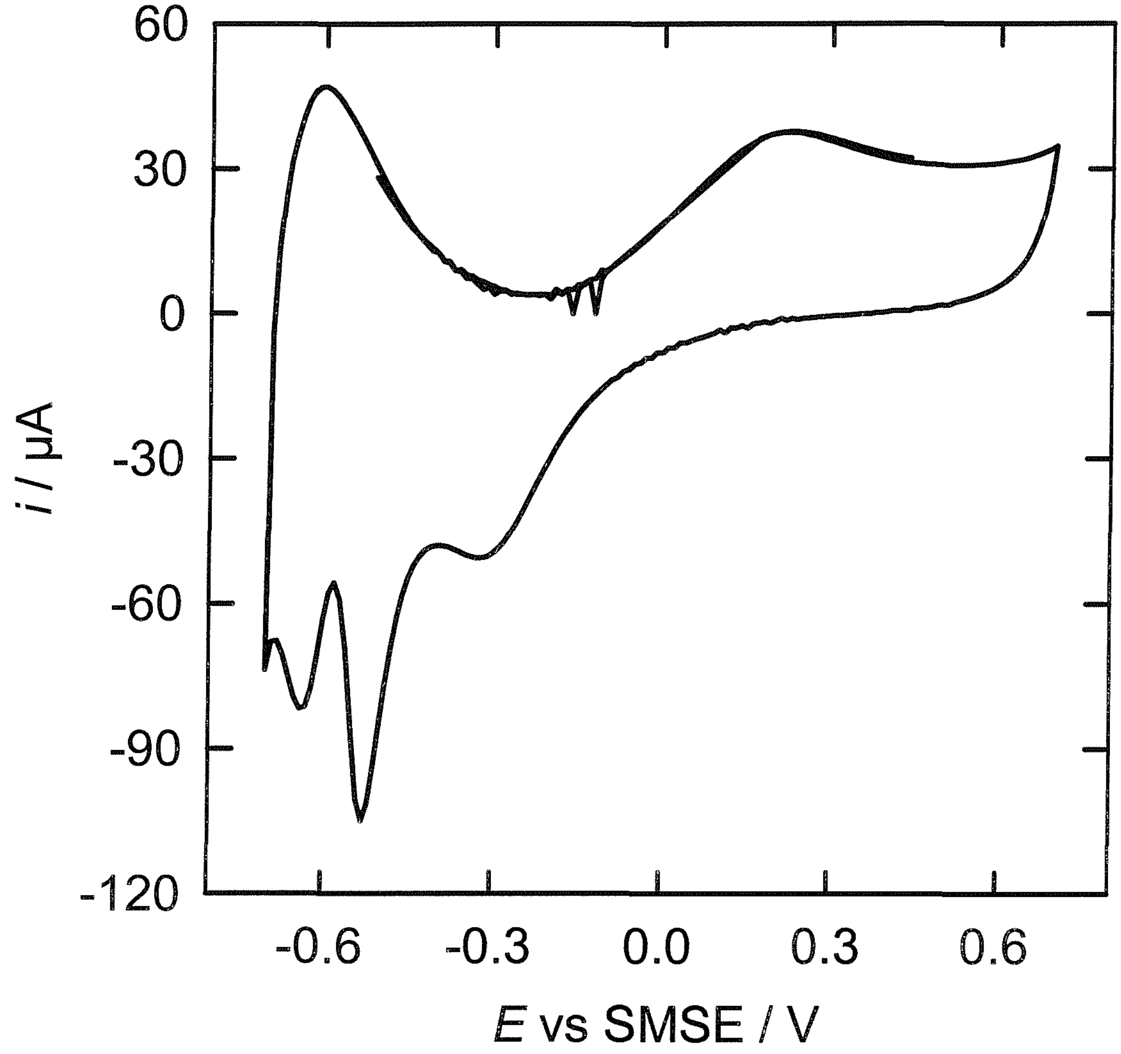

Figure 47: Cyclic voltammogram shows the first two cycles at 50 mV/s in 1 M sulphuric acid of H_I-e Rh deposited from the template mixture on a gold disc electrode of 1 mm diameter (total deposition charge 3.5 mC) at -0.2 V vs SCE.

The next figure shows how potential-cycling affects the appearance of the Rh voltammetry. Figure 48 presents a set of cyclic voltammograms showing ten subsequent cycles at 50 mV/s in 1 M sulfuric acid of the H_I-e Rh film electrode. This is the same Rh electrode used in Figure 47. We can note that on potentiodynamic treatment the peak at -0.53 V decreases in current and charge density and shifts towards positive potentials.

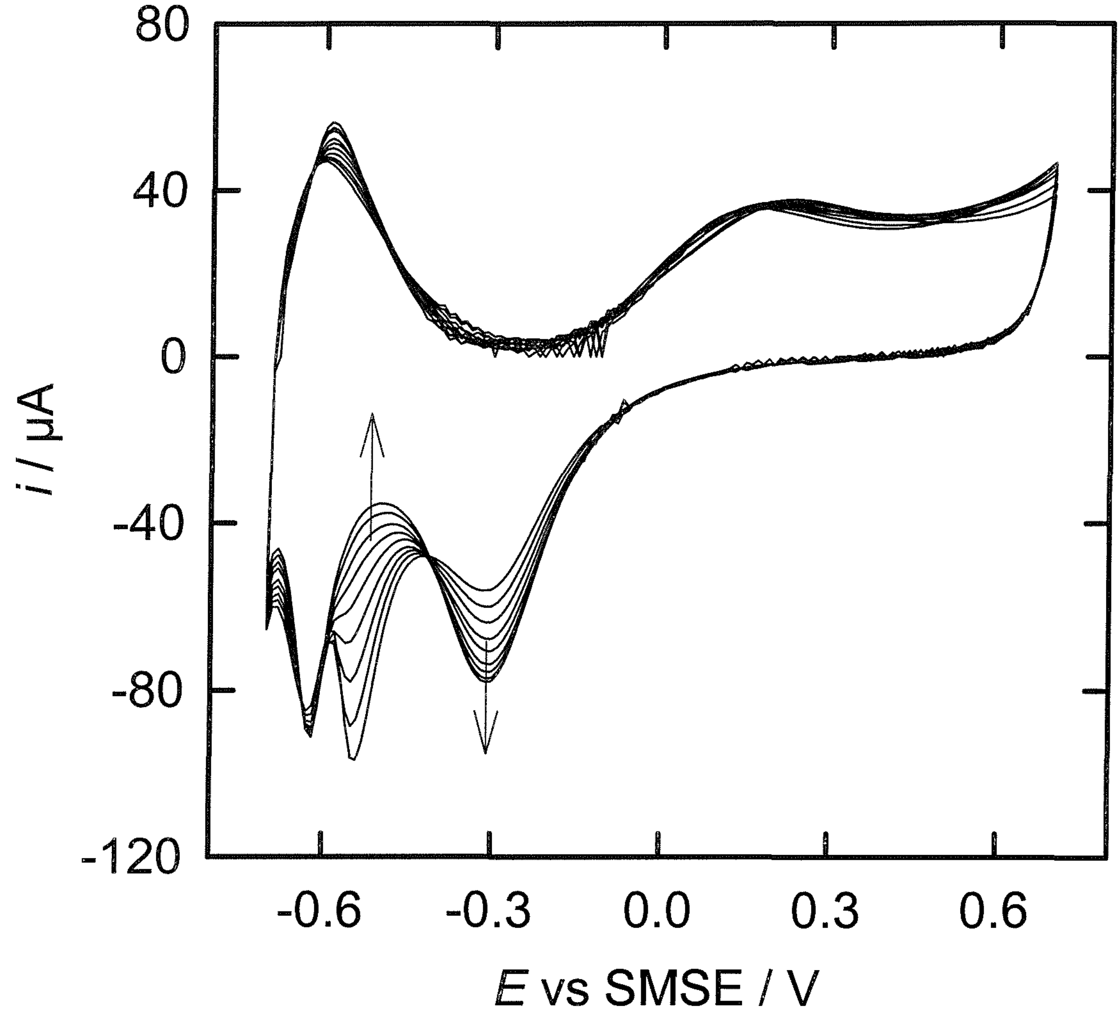

Figure 48: Set of cyclic voltammograms showing ten subsequent cycles at 50 mV/s in 1 M sulfuric acid of H_I-e Rh film electrode deposited from the $C_{16}EO_8$ template mixture on a gold disc electrode of 1 mm diameter (total deposition charge 3.5 mC).

On the other hand the peak at -0.31 V increases in current and charge density on potential-cycling. It is worth emphasizing that the summation of the charge underneath the peaks for both oxides states on the cathodic scan is similar for each voltammetric cycle. This is confirmed by the fact that we do not note any difference between each voltammetric cycle on the anodic scan. The surface area determined from the charge passed in the oxide stripping peak was estimated to be 0.34 cm^2 which corresponds to the specific surface area of 28 m^2 / g. This considers the estimation of the charge passed in both stripping peaks at -0.53 V and -0.31 V. We found this value consistent with that obtained from the oxide stripping peak in Figure 46.

Looking in the hydrogen region of the voltammetry we observe a more pronounced peak which has been shifted to -0.62 V. The fact that this peak is better resolved after potentiodynamic treatment has been also shown by Burke and O'Sullivan [112, 113] who carried out cyclic voltammetry on Rh electrodes.

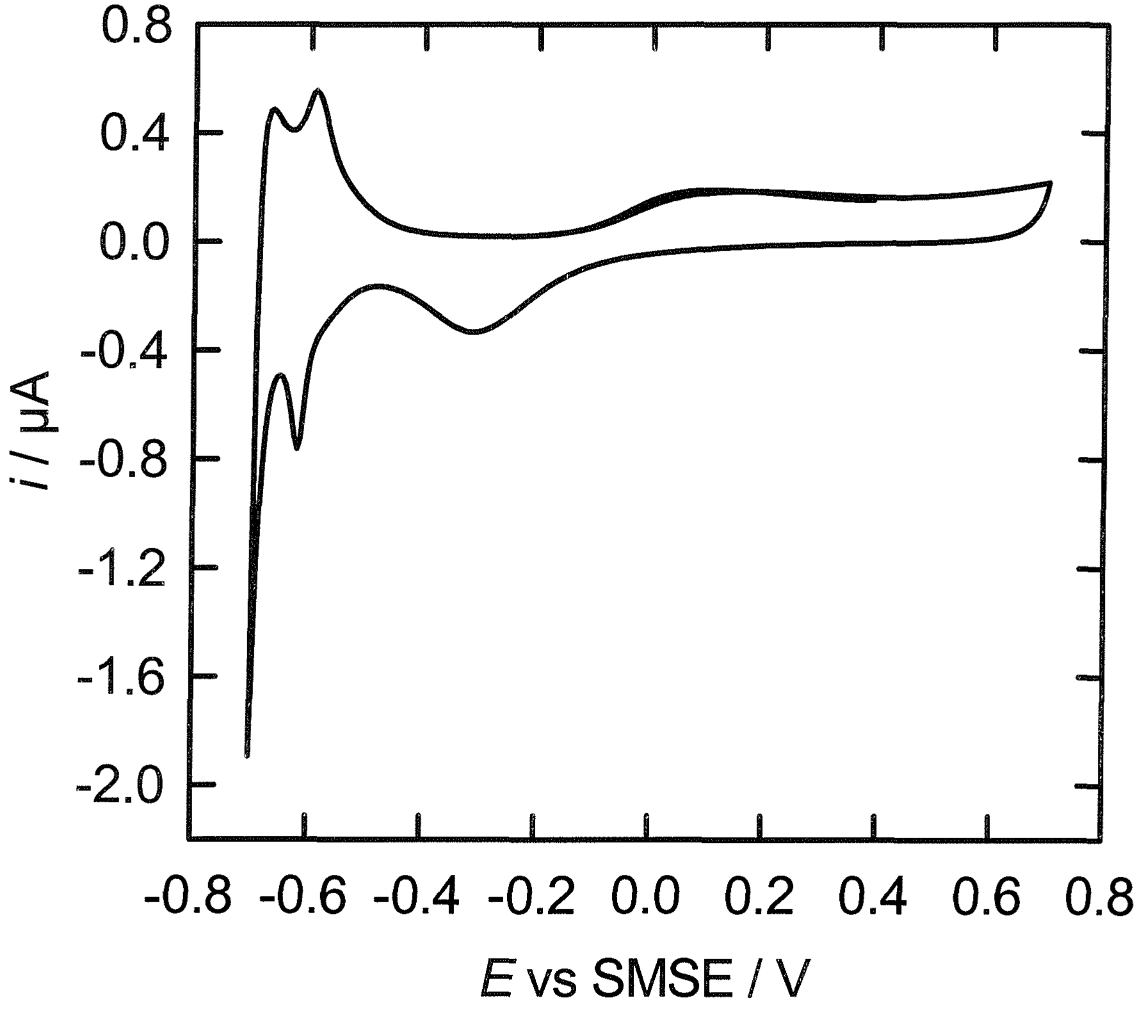

Figure 49: Cyclic voltammogram of polycrystalline Rh (0.5 mm diameter) at 50 mV / s in 1 M sulfuric acid.

We now compare the results obtained for H_I-e Rh film electrodes to those seen in the corresponding voltammogram of polycrystalline Rh. Figure 49 shows a cyclic voltammogram after the first two cycles of a polycrystalline Rh film electrode at

50 mV/s in 1 M sulfuric acid. On the anodic scan starting from -0.15 V we see the formation of the surface oxide. On the return cathodic sweep at around -0.31 V this surface oxide is removed giving rise to the well-defined stripping peak in the voltammetry.

The voltammetry of polycrystalline Rh in 1 M sulfuric acid has been investigated by Rand and Woods [78]. Using their conversion factor of 660 $\mu C / cm^2$ for the oxide stripping peak we can estimate the electroactive surface area for the Rh film and obtain surface areas of around 0.0024 cm^2 which corresponds to the specific surface area of 0.19 m^2 / g. We note that the surface oxide stripping for polycrystalline Rh occurs at the same potential as for H_1-e Rh film electrodes. The obvious difference between both electrodes can be found in the electroactive surface areas underneath the oxide stripping so that we can only attribute the high surface area to H_1-e Rh electrodes.

On continuing the cathodic scan to more negative potentials we note a well-defined peak at -0.62 V with the corresponding peak on the anodic scan at -0.59 V. From the very fact that these peaks occur at the same potential as those seen in Figure 46, we attribute this behaviour to the hydrogen adsorption. The rather featureless peak arising on the anodic scan at -0.68 V can be associated to the hydrogen evolution. Despite slight deviations in the hydrogen region with the arising of the hydrogen evolution peak for polycrystalline Rh electrodes, we can conclude that the features in the oxygen and hydrogen region of the voltammetry do not differ comparing polycrystalline Rh in Figure 49 and H_1-e Rh in Figure 46.

As seen before it is interesting to note that periodic potential-cycling in sulfuric acid has to be applied to the H_1-e Rh film electrodes in order to obtain the voltammetric behaviour in Figure 46. We note differences in the voltammetric features, specially on the cathodic scan of the oxide region, to those seen for the H_1-e electrode in Figure 47 where the potentiodynamic pre-treatment has not been carried out.

The crucial question arising now is whether the oxide stripping peak of polycrystalline Rh is qualitatively changing with the shift in the peak-potential on potential-cycling. The cyclic voltammetry of polycrystalline Rh electrodes with ten subsequent cycles under the same experimental conditions did not reveal any differences to the voltammetry shown in Figure 49. We can conclude that the oxide stripping for

LIBRARY

polycrystalline Rh remains from the first to the tenth cycle stable in peak potential after potentiodynamic pre-treatment. The very fact that on potential-cycling the oxide stripping shifts towards more positive potentials has only been observed for H_1-e Rh electrodes. It is hard at this stage to find any explanation for this. According to the literature this corresponds to the existence of two oxide states [101] and following detailed review of the published material [110, 114] we strongly assume that the Rh oxide layer undergoes rearrangements leading to a more stable configuration through periodic potential-cycling.

To conclude, the formation of the Rh oxide layers leads to oxide films having two distinguishable states, namely $R(OH)_3$ and $RO(OH)$ [101], which was confirmed by XPS measurements of anodically-formed Rh oxide [104]. The reduction of surface oxide layers gives rise to the oxide stripping which moves towards more positive potentials on potential-cycling. From the voltammetry we conclude that the summation of the charges underneath the peaks for both oxide states on the cathodic scan is similar for each voltammetric cycle. The hydrogen region, also affected, becomes better resolved with the potentiodynamic treatment with one peak which is a weakly bound species attributable to the adsorption of hydrogen on the Rh surface.

We found in our studies differences in the electrochemical properties between the H_1-e Rh and the polycrystalline Rh film electrode. One difference between both electrodes was found in the electroactive surface area underneath the oxide stripping peak so that the high surface area is only attributable to H_1-e Rh electrodes. The other significant difference lay in the fact that periodic potential-cycling had to be applied to H_1-e Rh electrodes in order to obtain voltammetric features similar to those seen for polycrystalline Rh.

5.6 The catalytic use of H_1-e Rh as high surface area metal for the electroreduction of nitrate

5.6.1 Introduction

Only a small fraction (4.9%) of the earth's surface water is suitable for human consumption. The rest (95.1%) is in oceans, seas, ice caps, glaciers or buried deep underground. Of the 4.9% of fresh water, approximately 68%, is groundwater; an important source of drinking water for many people worldwide [115]. Elevated concentration of nitrate in groundwater has raised concern over possible contamination of drinking water supplies and therefore health and environmental effects. Nitrate in groundwater is mainly due to nitrogen fertilizers, animal manure or waste, crop residue, human waste and in some cases industrial waste. A report from the World Health Organization in 1985 on health hazards from nitrate indicates that nitrate concentrations in surface waters had increased extensively over the last 30-40 years in many countries due the increased use of artificial fertilizers [116]. Association of increased cancer rate with high nitrate concentration in drinking water was observed in some places [116]. It has therefore become necessary to develop an efficient method for the reduction of nitrate to harmless products.

Different approaches have been proposed used to remove nitrate from the groundwater. These include membrane separation, ion exchange and biological denitrification [117-119]. However, these processes are expensive and generate waste which must be disposed of separately.

Several studies have examined the catalytic reduction process to remove nitrate from contaminated water using various electrode materials, such as Pt [120], platinized Pt [121], p-type diamond semiconductors [122-124], graphite modified with Co-complexes [125].

Another possibility is copper used as cathode on which nitrate can be reduced to nitrite at -1.1 V vs SCE and to ammonia with high yield at -1.4 V vs SCE [126]. Pb, Zn and Ni are also able to be used as cathodes. They can also reduce nitrate to nitrite and ammonia which is determined by the applied potential, the electrode material and other factors [127].

Hydrogen storage alloy is a new type of a functional material. It is used for the hydrogenation of nitrate to ammonia where dissolved hydrogen atoms in the alloy directly participate in the reduction [128].

Although several studies have been carried out on the reduction of nitrate using various metals and metal complex-electrodes in both acidic and alkaline solutions, relatively little has been done in neutral pH solutions. Drinking water often approaches a neutral pH of 7. It was the target of investigations by De et al. [129] who reduced nitrate electrochemically at surface of iridium-coated carbon fiber electrode in neutral pH solution. The study reveals that nitrate and nitrite can be reduced at surface modified electrodes with the formation of ammonia and nitrogen at a potential of -900 mV vs Ag/AgCl. The results obtained strongly suggest a minimal effect of pH on nitrate reduction in the pH range of 2.0 – 13.0 in $NaClO_4$ solution at the surface of iridium-coated carbon fiber electrodes.

Very few studies have examined the electroreduction of nitrate on rhodium electrodes [130-132]. Our special attention is focused on the difference in the reduction rate between mesoporous rhodium and plain rhodium film electrode. With the use of the high surface area of the mesoporous Rh film we expect to see a higher reduction rate and a detection of nitrate at much lower concentration compared to the plain Rh film. Prior to these studies we want to investigate which pH value is appropriate to obtain an efficient reduction rate. In this section we also want to provide the reader with the evidence that the Rh electrode is a much better catalyst for the nitrate reduction than Pd or Pt electrodes under the same experimental conditions.

5.6.2 Electroreduction of nitrate on rhodium electrodes

To study the electroreduction of nitrate on the rhodium surface the very first concern we are confronted with in the present work is to find the potential at which nitrate can be reduced. We therefore carried out cyclic voltammetric measurements using mesoporous Rh electrodes and varying the potential limits to look for any effect of nitrate reduction on the cathodic voltammetric response.

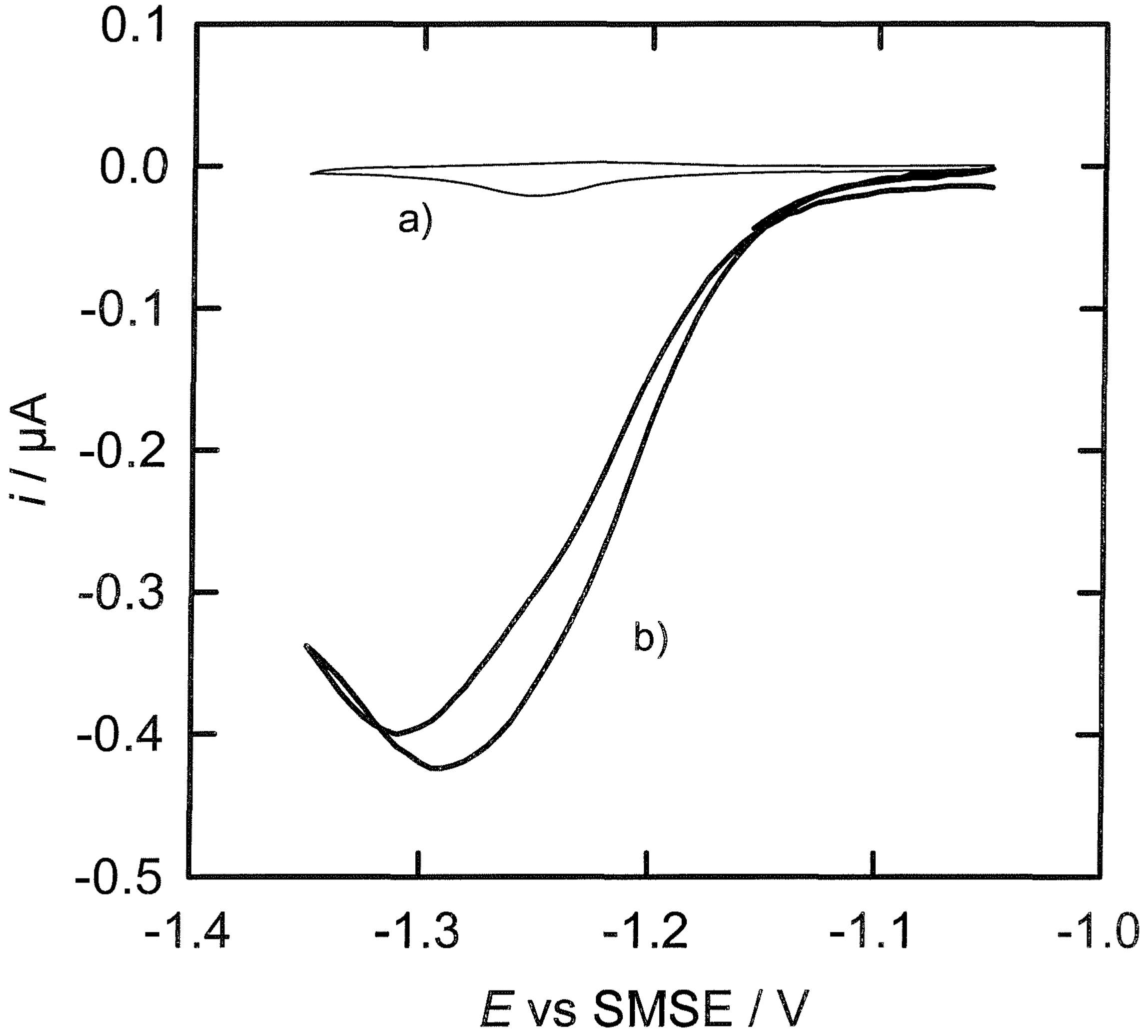

Figure 50: Cyclic voltammetry at 0.5 mV/s in 2 M NaOH a) with the addition of 30 mM $NaNO_3$ b) of H_I-e Rh deposited from the template mixture of 12 wt% $RhCl_3$, 47 wt% Brij®56, 39 wt% water and 2 wt% heptane on a gold disc electrode of 25 µm diameter (total deposition charge 87µC).

Figure 50 shows the cyclic voltammetry in a restricted potential range at 0.5 mV/s in 2 M NaOH containing 30 mM $NaNO_3$ vs SMSE at a mesoporous rhodium film electrode deposited from the template mixture of 12 wt% $RhCl_3$, 47 wt% Brij®56, 39 wt% water and 2 wt% heptane onto the gold disc electrode of 25 μm diameter.

In Figure 50 b) we can see, compared to figure a) which shows the background curve of the H_I–e Rh film in 2 M NaOH, the increase in the reduction current during the negative sweep. According to the literature [130-132] nitrate is reduced on the Rh electrode giving rise to ammonia and nitrite, and we note from our studies that the current peak increases to a limiting value of 420 nA at -1.28 V vs SMSE. This is the suitable potential at which the nitrate reduction occurs.

Remarkable in this voltammetry is the fact that the nitrate reduction scan does not remain in the steady-state after having reached the limiting current of 420 nA. We note that the current declines abruptly at potentials more negative than -1.28 V vs SMSE. This can be explained by the hydrogen covering the Rh surface [121]. To discuss this problem in detail we present Figure 51 showing the cyclic voltammogram of H_I-e Rh at 200 mV/s in 2 M NaOH deposited from a Brij®56 template mixture on a 25 μm gold disc electrode. Covering the full potential range from the oxide to the hydrogen region we want to focus our attention to the formation of hydrogen adsorbed onto the Rh surface starting at -1.20 V vs SMSE. When sweeping more cathodically to -1.38 V the hydrogen coverage increases. This behaviour competes with the nitrate reduction process onto the Rh electrode. Increasing the hydrogen adsorption then causes a reduced number of available active surface sites for nitrate. This leads to the fact that the nitrate reduction is limited and the current of this reduction process declines.

The very fact that the nitrate reduction is more efficient and therefore gives much higher reduction rate in alkaline media than in acidic solutions when using electrodes such as gold, palladium, platinum and rhodium can be provided by Ohmori et al. [133] and Petrij et al. [120]. They found that in acid solutions the reduction of nitrate to nitrite and ammonia is more hampered, whereas the yields of nitrite and ammonia increase significantly with the increase of pH in basic solutions. Hence in alkaline solutions Rh and the other metals might give the nitrate reduction process large turnover numbers.

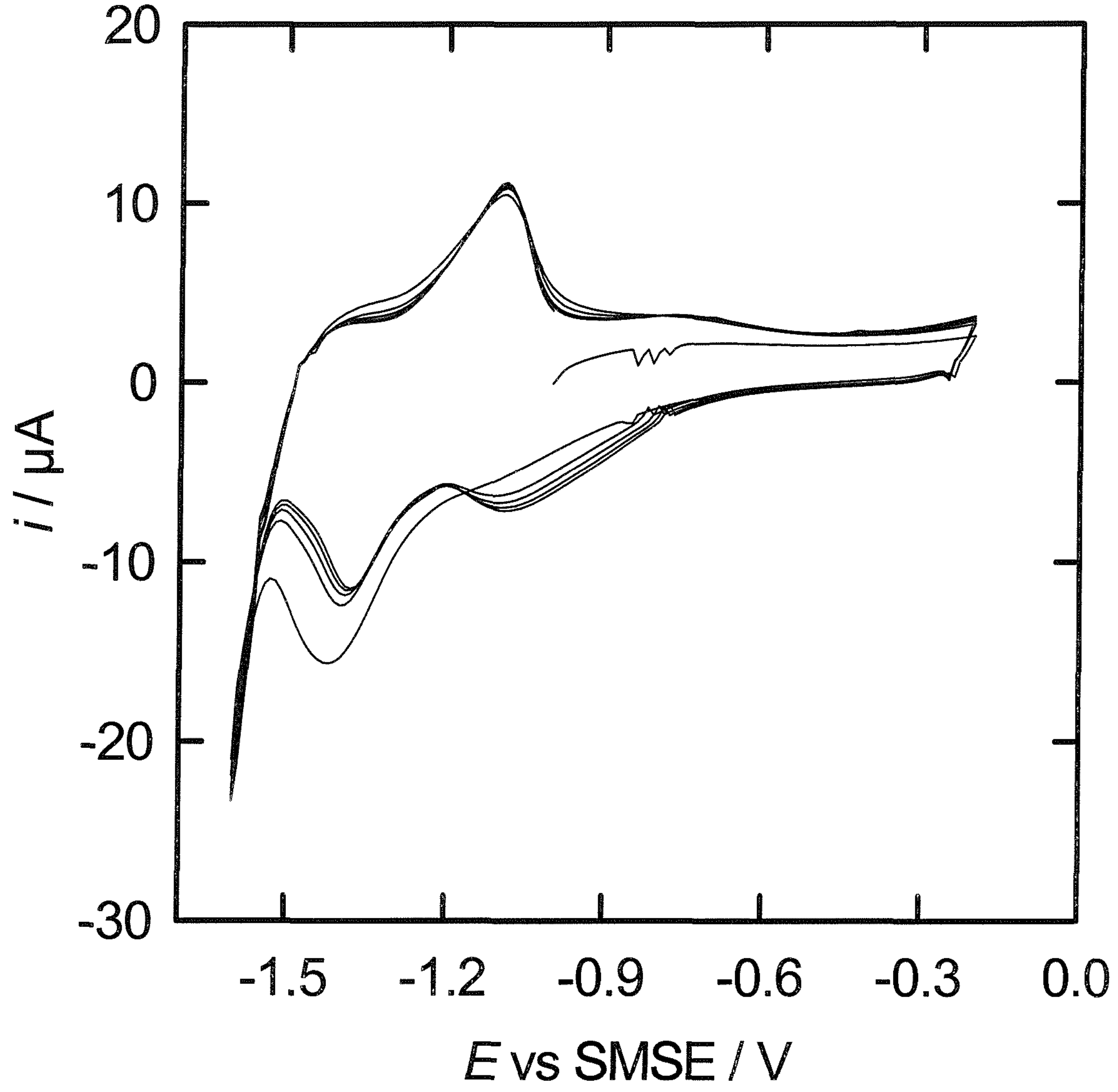

Figure 51: Cyclic voltammetry at 200 mV/s in 2 M NaOH of H_I-e Rh film deposited at -0.2 V vs SCE from the template mixture of 12 wt% $RhCl_3$, 39 wt % water, 47 wt% Brij®56 and 2 wt% heptane on a gold disc electrode of 25 µm diameter (total deposition charge 87 µC).

When reducing nitrate on the mesoporous rhodium electrode in 0.1 M TRIS buffer chosen as neutral media with the pH of 7, a significant nitrate reduction peak was not observed in our experiments. Our studies have shown that significant nitrate reduction occurs only in alkaline media. To study the electroreduction process of nitrate on the rhodium electrode with the output of a maximum current efficiency we have therefore chosen the alkaline solutions of 2 M NaOH.

We turn to Figure 52 which shows the limiting current as a function of time. Mesoporous rhodium was deposited onto the gold disc electrode (25 μm diameter). The nitrate addition to 2 M NaOH solutions was used to increase the concentration in steps from 1 mM to 570 mM. The reduction of nitrate was carried out at -1.28 V vs SMSE. It has be emphasized that to increase the nitrate concentration up to a final value of 570 mM we increased the volume of the aliquots of nitrate solution added to 2 M NaOH from 10 to 1000 μl. It can be clearly seen that with subsequent addition of nitrate the current jumps for each nitrate concentration to a different value and then decays continuously. The decay is more significant at higher nitrate concentration. This current decay proceeds while nitrate is continuously reduced on the Rh surface. We therefore assume that there are changes in the nitrate reduction process on the Rh surface and below we give three possible explanations for this.

As the first possible explanation we assume the surface to be poisoned irreversibly. This can be caused by the products resulting from the nitrate reduction. There are a limiting number of active sites on the rhodium surface converting nitrate electrochemically to products which then presumably block the available surface sites. This might hamper the nitrate reduction to large extent and finally causes the decay in current.

As a second option we assumed a soluble intermediate reversibly inhibiting the reaction. This might also have a negative impact on the reduction rate and further nitrate reduction would then be significantly hampered.

The third possible explanation might be found in the local pH shift near the electrode surface of our nanostructured Rh film apparent with the subsequent addition of nitrate electrochemically reduced onto the surface. This issue might be enhanced considering the narrow pores of the nanostructured metal film. Significant concentration changes can occur along the pores as outlined in Chapter 3 and [29, 99].

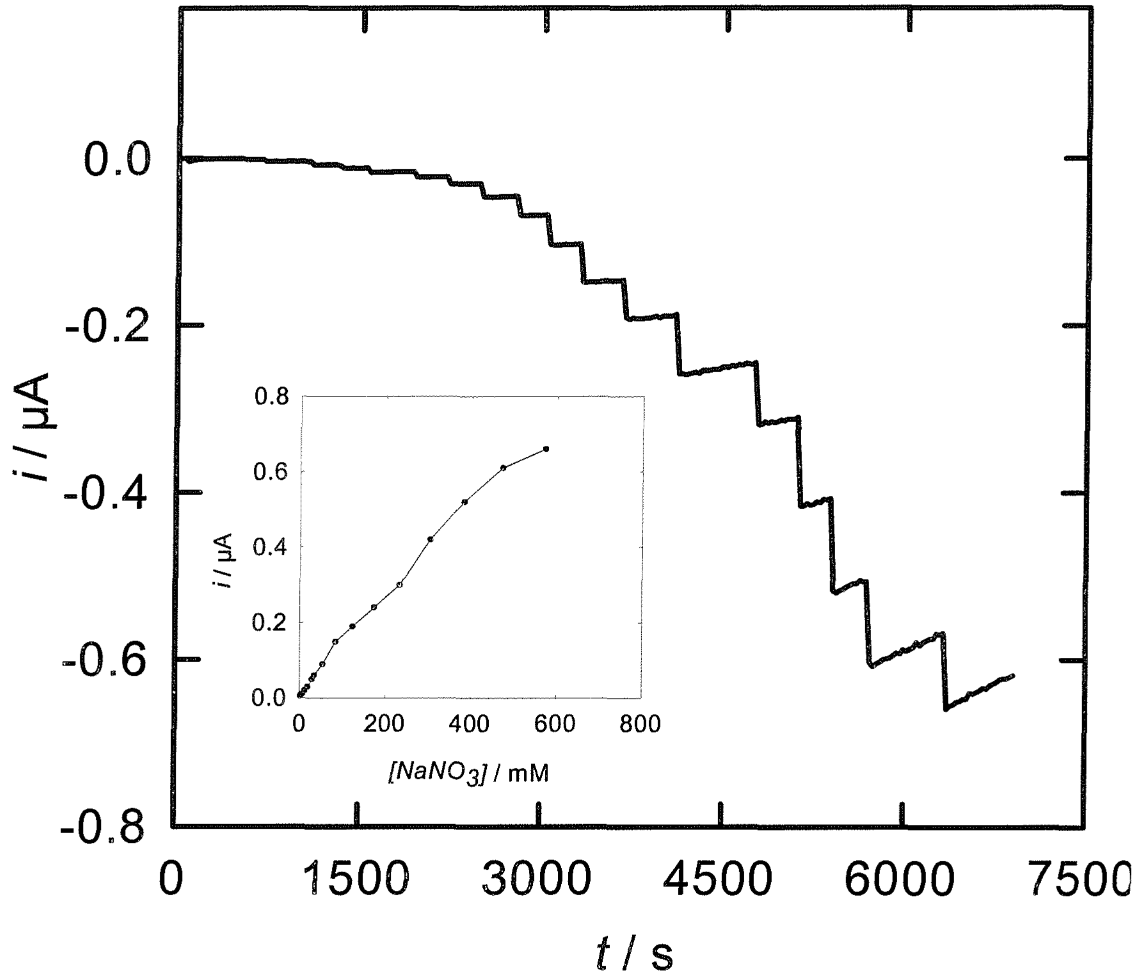

*Figure 52: Nitrate was reduced onto H_I-e Rh film at -1.28 V vs SMSE in 2 M NaOH. The concentration of nitrate was subsequently increased from 1 to 570 mM. H_I-e Rh was deposited from a template mixture of 12 wt% $RhCl_3$, 47 wt% $C_{16}EO_8$, 39 wt% water and 2 wt% heptane on a gold disc electrode (1.98*10e-4 cm^2 area). The total charge deposited was 87.5 μC for a thickness of 126 nm. The inset shows the current related to each addition of nitrate.*

To make a clear distinction between all possibilities shown in this section we carried out an experiment in which nitrate was reduced on the nanostructured Rh electrode in 2 M NaOH vs SMSE under the same conditions and using the same H_I-e Rh film, Figure 53. After the addition of 50 mM nitrate the current jumps to a value of 380 nA and then as expected continuously decays. After changing the solution, the Rh electrode was put unaltered in a fresh solution of 2 M NaOH. 50 mM nitrate was again added to the solution so that the reduction on the Rh surface occurred. We note that the current jumps to the same value.

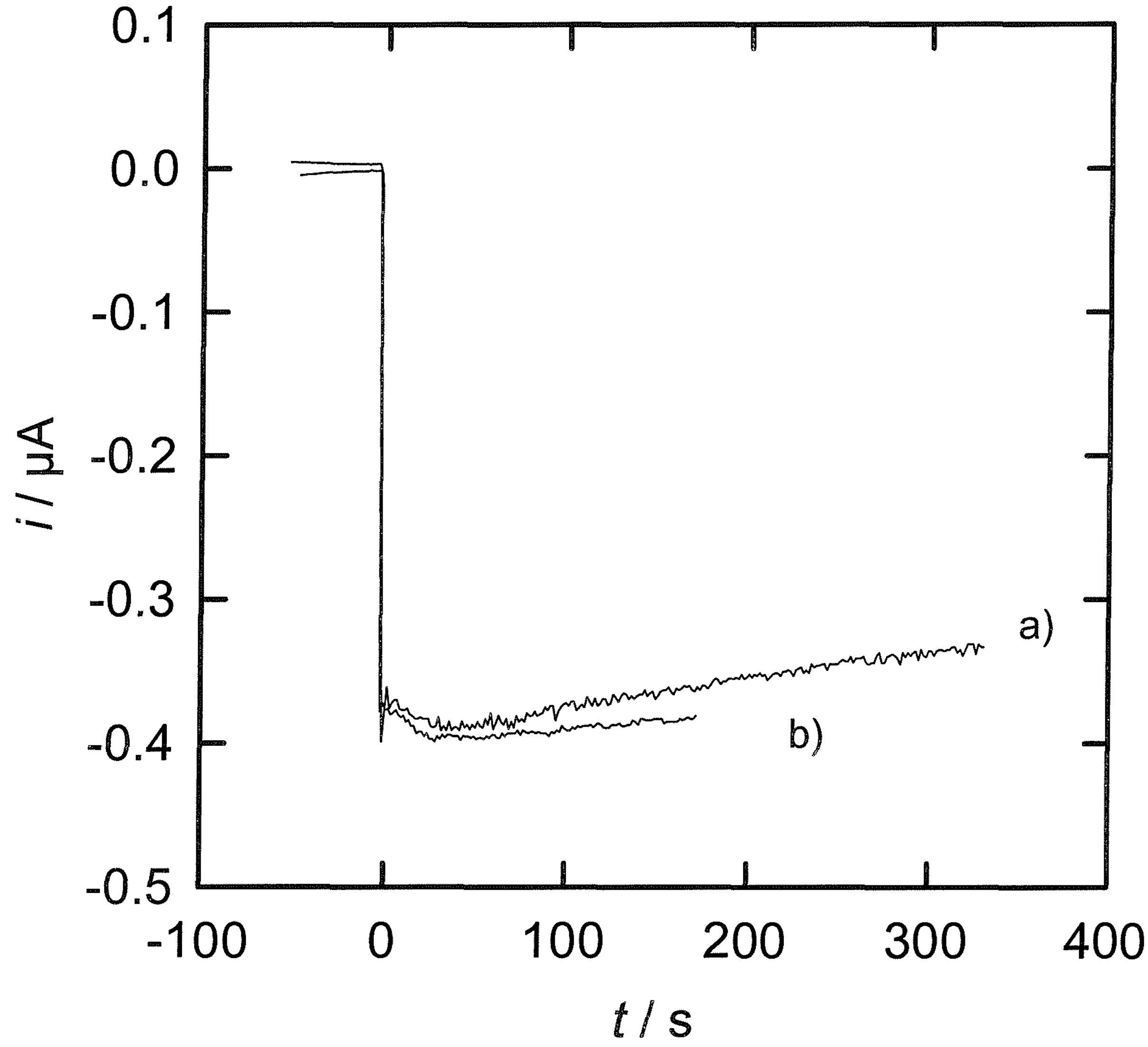

Figure 53: 50 mM Nitrate was added to 2 M NaOH solution and reduced at -1.28 V vs SMSE onto the Rh surface. H_I-e Rh was deposited onto the Au electrode ($1.98*10^{-4}$ cm^2).The charge passed for deposition was 90 µC to obtain the thickness of 126 nm. After reducing 50 mM nitrate in one step a) the mesoporous Rh electrode was put in a fresh solution. 50 mM nitrate was again added and the reduction on the Rh surface occurred b).

To draw a conclusion from this experiment, we think that the surface has not been poisoned irreversibly. From this experiment it is hard to tell whether to favour the second or the third option outlined above. At this stage we are aware of the fact how to avoid discontinuity in the nitrate reduction process. To exclude further current decay after the subsequent addition of nitrate we found it necessary to change the solution of 2 M NaOH after each addition of nitrate. The H_I-e Rh film was put unchanged in the fresh solution before start the potentiostatic measurement. We obtained then the curve for the nitrate reduction as the limiting current as a function of concentration (Figure 54).

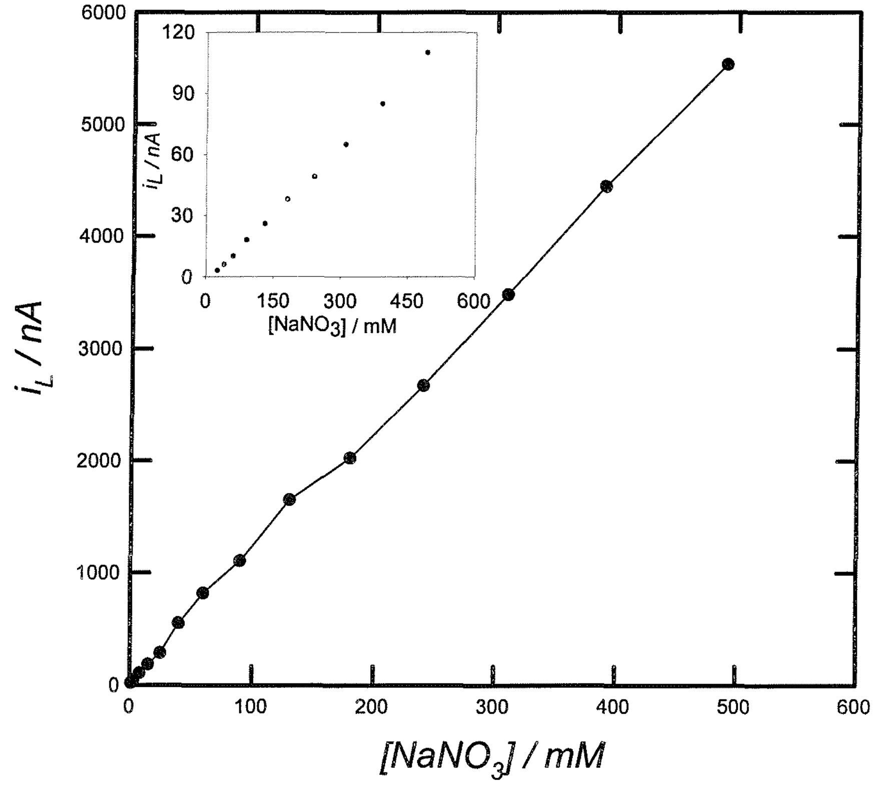

Figure 54: Nitrate was reduced at -1.28 V vs SMSE in 2 M NaOH on the H_I-e Rh surface and on the Rh film deposited from the aqueous solution containing 50 mM $RhCl_3$ and 1 M HCl (inset). H_I-e Rh was deposited from the $C_{16}EO_8$ plating bath onto a gold disc electrode (25 μm diameter, 90 μC deposition charge).

Comparing H_I-e Rh with the Rh film deposited from the aqueous solution (inset) we can see that the electroreduction of nitrate is more sensitive using H_I-e Rh films. It is also important to note that the ratio of the two slopes in Figure 54 equals the ratio of the electrode surface between these two Rh films. From this we conclude that the current is not limited by mass transport of nitrate to the electrode. The current is first order with respect to the nitrate concentration and must be determined by surface kinetics of the reaction and hence variations in the real surface area of the electrode.

Following the data obtained in Figure 54 for the electroreduction of nitrate onto the H_I-e Rh surface we use the equation I = 4nFaDc to evaluate nD obtained from the reduction process and transfer this equation to nD = i/4Fac with I = 5000 nA;

a = $20*10^{-4}$cm; c = 10^{-4} mol/cm^3; F = 96485 C/mol. We proceeded from the assumption having obtained a diffusion limited current from which then the value of nD can be estimated. The diffusion coefficient cannot be defined separately from the number of electrons transferred in the reduction process.

In addition, it has to be noted that the electrode radius of the Rh film was chosen to be 20×10^{-4} cm and not 12.5×10^{-4} cm corresponding to the radius of the gold electrode (25μm diameter) on which mesoporous Rh was deposited. This is due to the fact that after electrodeposition of the mesoporous metal films the effective diameter of the microeletrode changes. The deposit spreads over the surface and leads to an effective enlargement of the geometric area. This was shown by Birkin et al. [30] outlining two experimental methods. On the one hand the authors carried out a series of cyclic voltammetric measurements on a 25 μm Pt electrode within a solution containing $[Fe(CN)_6]^{3-}$ and demonstrated that as the eletrodeposition charge density was increased in the range of 0 to 37.5 C/cm^2 the reduction current for the redox species also increased in a way that the geometric surface area of the deposited material was found to be enlarged. This could be proved by calculating the number of electrons involved in the reduction process from the current recorded. On the other hand further evidence was given by SEM-image showing the deposit to spread over the surface of the glass insulator leading to an effective increase in the surface area.

We found the SEM-measurement on gold microelectrodes on which mesoporous Rh was deposited as appropriate to prove the overspill of the deposited material. Figure 55 shows the SEM-image of mesoporous Rh deposited onto a 25 μm gold disc electrode. We note that after electrodeposition the effective diameter of the geometric surface has increased to around 40 µm. The apparent radius of $20*10^{-4}$ cm has therefore to be considered in the equation given above.

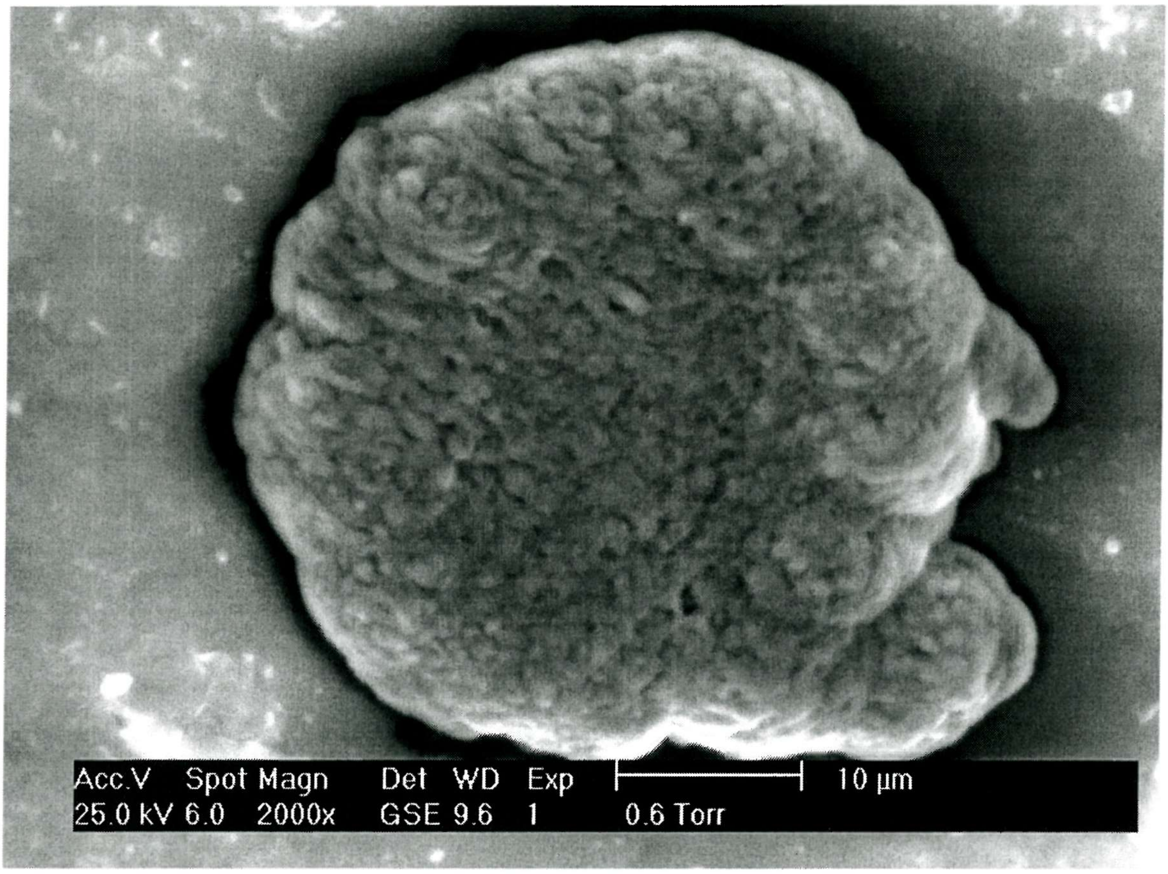

Figure 55: Scanning electron micrograph of an H_I-e Rh film deposited on a Pt microelectrode (25 µm diameter). The film was deposited from a mixture of 12 wt% $RhCl_3$, 47 wt% $C_{16}EO_8$, 2 wt% heptane and 39 wt% water. The total charge passed was 90 µC and the image was obtained on the top view.

From Figure 54 and in using 20×10^{-4} cm for the radius estimated from the SEM image we calculated a value for nD of 1.4×10^{-5} cm^2 / s. In placing a value of 1.5×10^{-5} cm^2 / s [134] for the diffusion coefficient of nitrate we evaluated n = 1 as the number of electrons. With this number for the nitrate reduction process we are in disagreement with the outlined literature [125, 126, 129] proposing in clear consensus the reduction of nitrate to ammonia and nitrite which requires 8 electrons in the reduction process. According to the literature [125, 126, 129] the reduction process of nitrate proceeds first via the 2-electron transfer step by which nitrite is produced cathodically:

$$NO_3^- + H_2O + 2e^- \Rightarrow NO_2^- + 2OH^- \quad \text{Equation 17}$$

The accumulated nitrite ion is further reduced through subsequent elementary reactions providing ammonia:

$$NO_2^- + 5\,H_2O + 6e^- \Rightarrow NH_3 + 7OH^- \quad \text{Equation 18}$$

The summation of these elementary steps is represented in one equation as follows:

$$NO_3^- + 6\,H_2O + 8e^- \Rightarrow NH_3 + 9OH^- \quad \text{Equation 19}$$

In discussing the nitrate reduction process we would rather assume a kinetically limited reaction with a rate constant k. From the nitrate reduction process on the H_I-e Rh electrode and the Rh film deposited from the aqueous solution we can conclude that in both cases the curves are linear in current and the ratio of the electrode surface equals the ratio of the slope between the two processes. We would rather suggest for both cases a kinetic limitation than a mass transfer regime.

In the course of our research we also intend to provide the reader with the evidence that the mesoporous Rh film electrode used as a catalyst for the nitrate reduction is of higher efficiency than Pd and Pt under the same experimental conditions.

We therefore focused our attention on experimental studies reducing nitrate potentiostatically on the H_I-e Pt and H_I-e Pd surface in 2 M NaOH. Each film was deposited with the total deposition charge of 90 μC on a 25 μm gold disc electrode. We found it necessary to carry out cyclic voltammeric measurements to find out the suitable potentials at which nitrate should be reduced on Pt and Pd. Figure 56 shows the potentiostatic measurement when 50 mM nitrate was reduced onto the H_I-e Pd surface a) at -1.32 V vs SMSE in 2 M NaOH and the same amount was added to the solution and reduced on H_I-e Pt b) at -1.24 V vs SMSE. We note that the current jumps in a) to a value of around 13 nA and in b) to around 8 nA. The electroactive surface areas of H_I-e Pt and H_I-e Pd were found to be a bit less compared to the surface area of H_I-e Rh. However, this is far negligible when taking into consideration that the current jumps to 380 nA in the nitrate reduction process on H_I-e Rh for the same amount of nitrate concentration. We then notice that the reduction current for both metals (Pt and Pd) is far less. We finally can conclude that H_I-e Rh gives more sensitive response to nitrate.

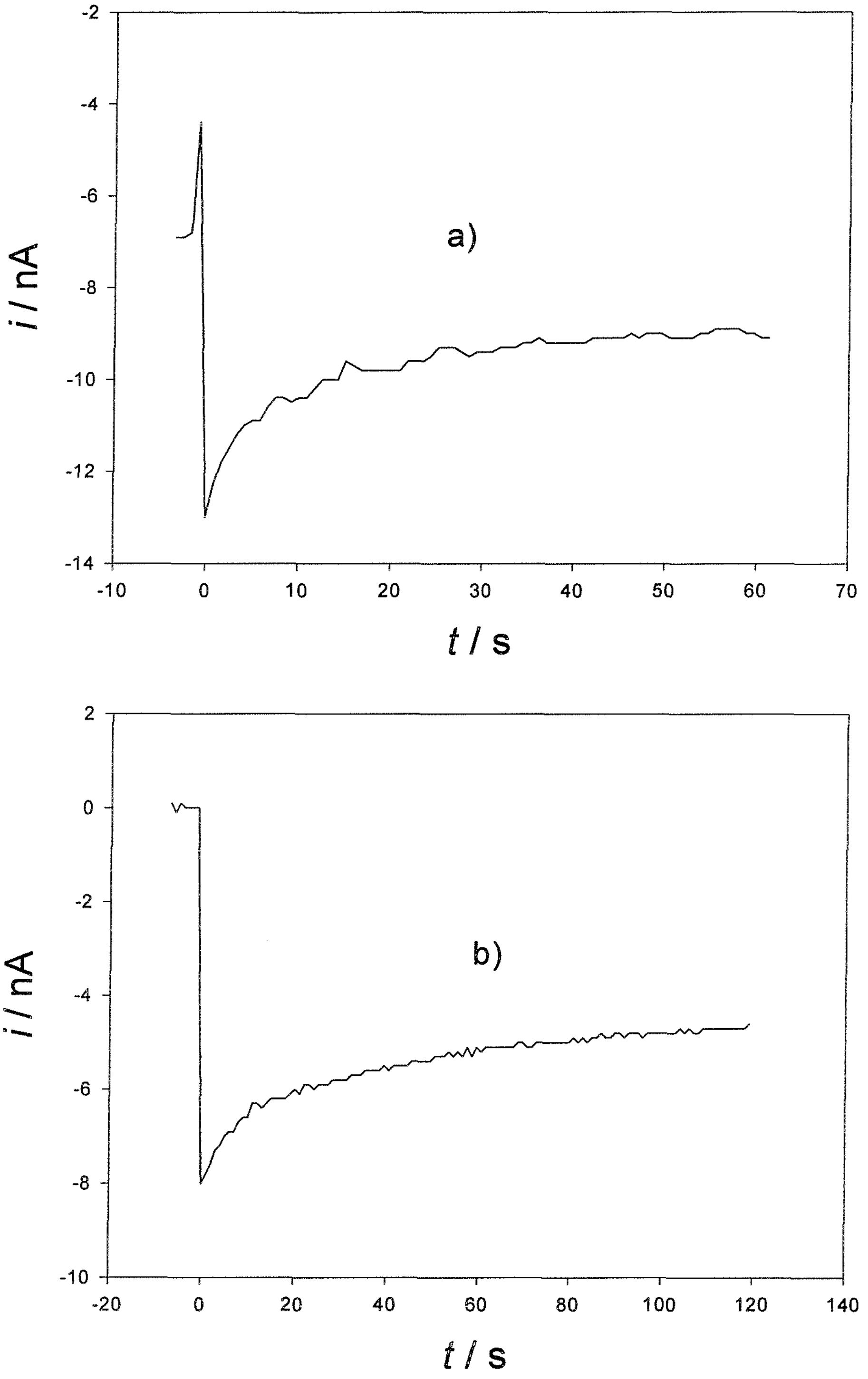

Figure 56: Nitrate was reduced on nanostructured Pd a) at -1.32 V and nanostructured Pt b) at -1.24 V vs SMSE in 2 M NaOH. The total deposition charge for both electrodes (25μm diameter) was the same (90 μC).

5.7 Conclusion

In this chapter we reported the investigation of the electrodeposition and electrochemical properties of H_I-e Rh and compared these results to those obtained for a polycrystalline Rh film electrode. First giving the evidence by TEM and X-ray that nanostructured Rh film was deposited in regular pore distribution we turned then to the cyclic voltammetric studies covering the full potential from the hydrogen to the oxide region. Our studies revealed the fact that the surface oxide layers on Rh give rise to a stripping peak on the cathodic scan moving towards positive potentials on potential-cycling. The hydrogen region was also affected so that the peaks became better resolved by increasing the number of cycles. The hydrogen region revealed one peak attributable to the adsorption of hydrogen onto the H_I-e Rh surface.

We found in our studies similarity and differences in the electrochemical properties between the H_I-e Rh and the polycrystalline Rh film electrode. One difference between both electrodes was found in the electroactive surface area underneath the oxide stripping peak so that the high surface area is only attributable to H_I-e Rh electrodes. The other significant difference lay in the fact that periodic potential-cycling had to be applied to H_I-e Rh electrodes in order to obtain voltammetric features similar to those seen for bulk polycrystalline Rh. .

We can finally conclude that the qualitative changes in the oxide region on the cathodic sweep are due to changes in the surface oxide states enhancing the existence of more stable configurations.

We used the H_I-e Rh film electrode for the electroreduction of nitrate in alkaline solutions as the pH conveniently chosen for our studies and compared the results to those obtained for a Rh electrode deposited from the aqueous solution.. We found that with the use of the H_I-e Rh electrode we obtained greater sensivity. The H_I-e Rh film was also shown to be the better catalyst comparing to Pt and Pd. It was found that evidently higher currents were obtained when reducing nitrate onto the Rh surface.

From our studies we assumed a kinetically limited reaction when reducing nitrate onto H_I-e Rh electrodes and Rh electrodes deposited from the aqueous solution.

Chapter 6 The electrochemical deposition of (H_1–e) layers of two metals in which the pores interconnect

6.1 Introduction

In this chapter we provide the reader with the evidence that we can deposit nanostructured metal films one on top of the other so that the pores within the two films interconnect. To illustrate this, we show a schematic representation, Figure 57, of the templated electrodeposition process of one layer on top of the other. The nanostructured metal film shows a hexagonal array derived from the hexagonal phase of the template solution.

Cyclic voltammetric measurements were used to characterize the electrochemically active surface area of H_I-e Pd films estimated from the charge passed in the oxide stripping peak. The H_I-e Pd films deposited from the liquid crystalline templates contain mixtures of surfactant molecules and aqueous solution spontaneously assembled into regular structures of nanometer-sized dimensions. Using cyclic voltammetry we will show that the deposition of H_I-e metals one on top of the other occurs in such a way that the pores of hexagonal array run continuously through the final metal film. We refer to this sort of deposition as epitaxial nanostructure deposition.

In Chapter 3 and Chapter 5 we described in detail the electrochemical behaviour of H_I-e Pd and Rh films in the cyclic voltammetry in acid solutions covering the full potential from the oxide to the hydrogen region. To provide evidence for the existence of the porous structure through the final H_I-e metal film, this chapter uses the well-understood cyclic voltammetry of H_I-e Pd, Rh and Pt. The cyclic voltammetry of H_I-e Pt is described in the literature [22]. It is worth emphasizing that the surface reactions corresponding to the formation and stripping of oxide films or adsorbed hydrogen occurs at potentials which are characteristic for these metals and distinguishable from those for alloys of the metals [86].

To prove the deposition of nanostructured metals one on top of the other with continuous pores through the whole film, we selected a pair of noble metals with well-separated potentials for their surface oxide stripping peaks. Intregating the charge underneath the peak for this surface reaction, we can directly measure the area of the metal film accessed by the electrolyte solution. This enables us to determine simultaneously the areas of the upper and lower metal layers. Using this approach we should see the voltammetry of the lower metal layer even in the presence of a continuous nanostructured overlayer if the pores continuously connect through the final metal film. The cyclic voltammetry of the lower metal layer should be suppressed if the pores are blocked and the porous structure is not continuous.

The TEM-technique was found to be very difficult to apply since the contrast in the image between the two metals is very poor so that the porous arrangement cannot be distinguished between the two metals.

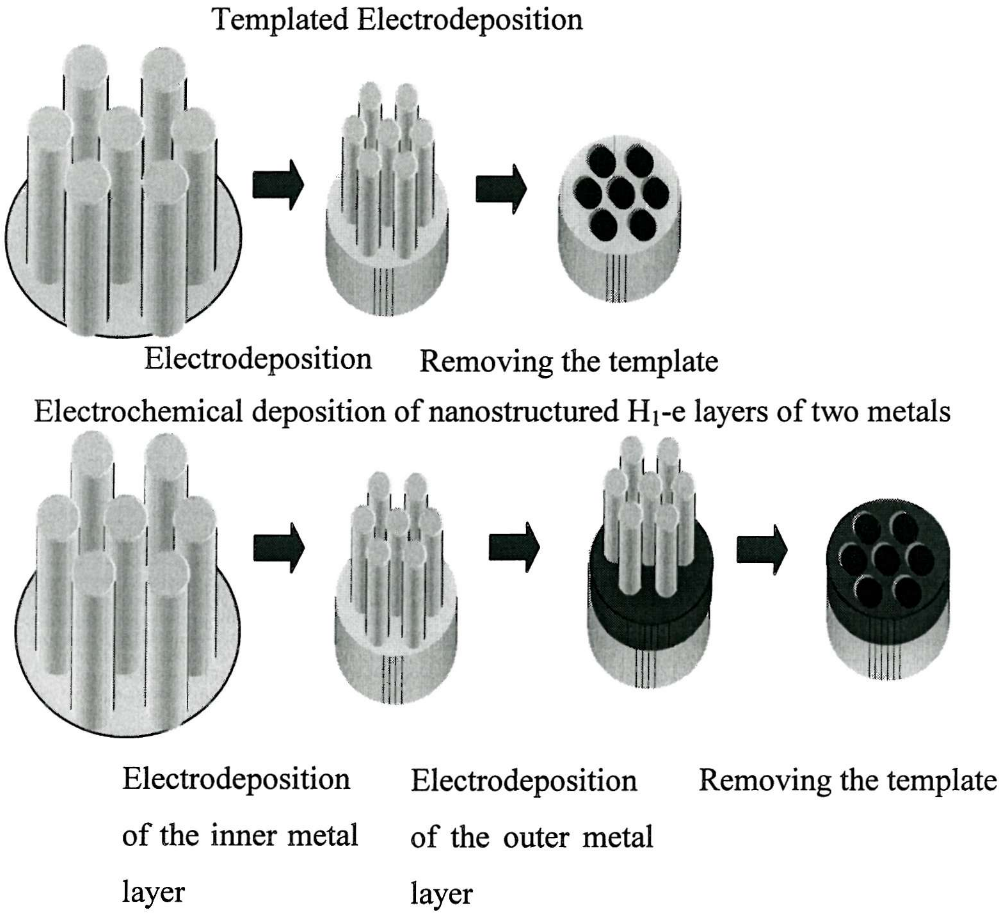

Figure 57: Schematic representation of the templated electrodeposition process of two nanostructured metals one on top of the other

6.2 Electrochemistry of noble metals

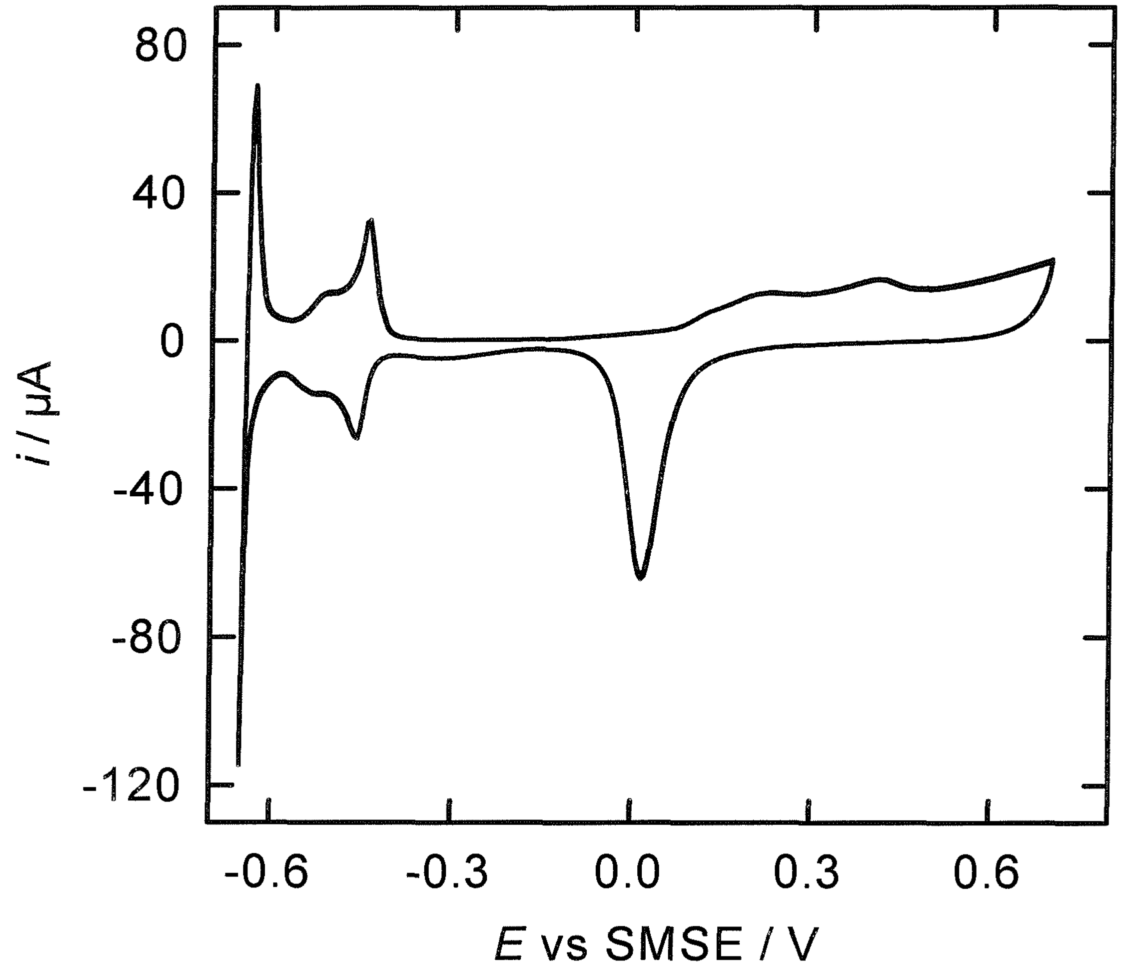

Figure 58: Cyclic voltammogram of an H_I-e Pd film (200 nm thick, deposited from the $C_{16}EO_8$ plating bath, total deposition charge 3.5 mC) deposited on a gold disc electrode (area 0.0079 cm^2) recorded at 20 mV/s in 1 M sulfuric acid. The film was soaked in water for 1 hour before the start of the voltammetry.

We have chosen for our studies palladium and rhodium as we have already characterized their voltammetry in acid solution, and we noticed that both oxide stripping peaks occur at well-separated potentials. We have shown that we can prepare Pd and Rh metal films with high surface areas and with continuous pores of regular hexagonal arrangement of nanometer-sized dimensions. In addition, mesoporous Pd and Rh films were shown to be dense, uniform, smooth and continuous over the whole SEM-image (see Chapter 3 and Chapter 5).

Figure 58 shows a typical cyclic voltammogram in 1 M H_2SO_4 at 20 mV/s for an H_I-e Pd film deposited on a gold disc electrode of 1 mm diameter from the $C_{16}EO_8$ template mixture [99]. On the anodic scan, at 0.07 V the formation of the surface oxide layers occurs. We note from the voltammogram in the oxide region on the anodic scan two peaks at 0.21 and 0.41 V attributable to the different Pd oxide states, as discussed in section 3.6.2. On the reverse scan, the cathodic sweep, the reduction of the formed surface oxide appears giving rise to a well defined peak at 0.02 V. These features are very similar to those seen for bulk polycrystalline Pd electrodes under the same experimental conditions (section 3.7.2). However, we want to emphasize that the charge passed for the formation and stripping of the surface oxide layers is much smaller for the plain Pd when compared to H_I-e Pd films.

On continuing the cathodic scan, we see the formation of adsorbed hydrogen at -0.46 V followed by the formation of α hydride around -0.55 V and the start of β hydride formation at the cathodic limit. These processes are reversed as the potential starts to scan anodic again. The voltammogram at negative potentials is very different from the voltammetry of ordinary Pd electrodes. In section 3.7.2 we noticed that this is due to the presence of the nanostructure. The high surface area metal combined with the thin walls between the pores causes well-resolved peaks corresponding to the formation and removal of adsorbed and absorbed hydrogen. In Chapter 3 we gave a full description and detailed discussion of the voltammtery of H_I-e Pd electrodes in acid solutions.

To estimate the total surface area of the H_I-e Pd film we integrate the charge passed the surface oxide stripping reaction. Using this charge together with the conversion factor for the oxide stripping on Pd of 424 $\mu C/cm^2$, we obtain 0.76 cm^2. We take into account the total charge passed to deposit the film and calculate a specific surface area for this film Pd film of 38 m^2/g. This corresponds to an area per unit volume of 4.6×10^6 cm^2/cm^3, a value which is consistent with a nanostructure and implies that the pores running throughout the nanostructured film are fully accessed by the electrolyte solution.

Figure 59 shows the cyclic voltammetry at 50 mV/s in 1 M H_2SO_4 of a H_I-e Rh film electrode. We have fully characterized the electrodeposition and electrochemical behaviour of these films in Chapter 5. On the anodic scan at -0.19 V the H_I-e Rh electrode oxide formation starts. On the return scan the oxide film is stripped from the electrode surface at -0.31 V.

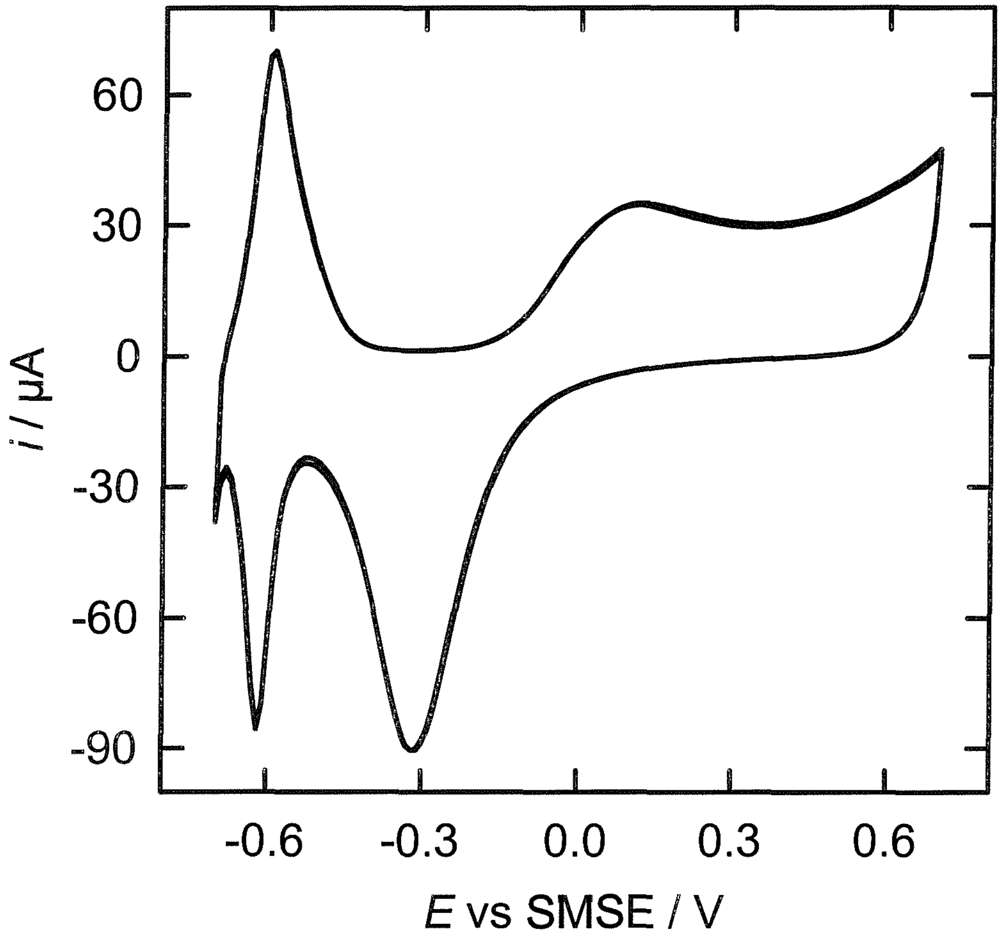

Figure 59: Cyclic voltammogram of an H_I-e Rh film (126 nm thick, total deposition charge 3.5 mC) deposited from the template mixture of 12 wt% $RhCl_3$, 47 wt% $C_{16}EO_8$, 39 wt% water and 2 wt% heptane on a gold disc electrode (area 0.0079cm^2) recorded at 50 mV/s in 1 M sulfuric acid. The film was soaked in water for one hour prior to the voltammetry. The surface area of the H_I-e Rh film is 0.39 cm^2.

The peaks in the voltammetry at cathodic potentials are associated with the formation of adsorbed hydrogen at -0.62 V on the cathodic scan and with the oxidation of adsorbed hydrogen at -0.59 V at the anodic scan. The features observed in the voltammetry for the H_I-e Rh electrode are very similar to those reported for ordinary polycrystalline Rh electrodes [101]. On integrating the charge underneath the surface oxide stripping peak in Figure 59 and using the conversion factor of 660 $\mu C/cm^2$ for oxide stripping on Rh given by Rand and Woods [78], we obtain a surface area of 0.39 cm^2. Using the known deposition charge for the film, this gives a value for the specific surface area of 32 m^2/g which corresponds to an area per unit volume of 3.3×10^6 cm^2/cm^3. This was found to be consistent with the nanostructure.

6.3 Increasing the thickness of one layer deposited on top of the other

From the results presented in Figure 58 and Figure 59 we obtain surface oxide stripping peaks for H_I-e Pd and H_I-e Rh films which are well-separated in peak potential. Thus these metal films, after deposition one on top of the other, can be easily distinguished in the voltammetry.

Figure 60 shows a set of cyclic voltammograms of H_I-e Pd deposited onto H_I-e Rh. H_I-e Rh was initially deposited onto the gold disc electrode (0.0079 cm^2 electrode area) with the charge of 3.5 mC passed to deposit the film. This amount of charge was kept constant and corresponds to a thickness of approxiametly 126 nm. The charge passed for the deposition of Pd was varied from 3.5 to 10.5 mC (voltammetric cycles 1-3), which corresponds to an increase in thickness from 200 nm to 600 nm.

To achieve the deposition of nanostructured metal films with pores running continuously through the final film, we thought about the deposition procedure. To our knowledge, using a different surfactant and changing the concentration of co-solvent in the template mixture would alter the dimensions of the nanostructure [23]. Therefore we paid attention not to change the experimental conditions required to deposit our H_I-e metal films.

Furthermore we were concerned about the treatment of the electrode between the deposition of the first and the second layer. The results in Chapter 3 showed that prolonged washing of H_I-e Pd in water of at least one hour, for a film of 200 nm thickness, was necessary to remove the surfactant from the pores. We carried out separate experiments in which the first deposited H_I-e metal film was thoroughly washed to remove all the surfactant before placing in the second template mixture.

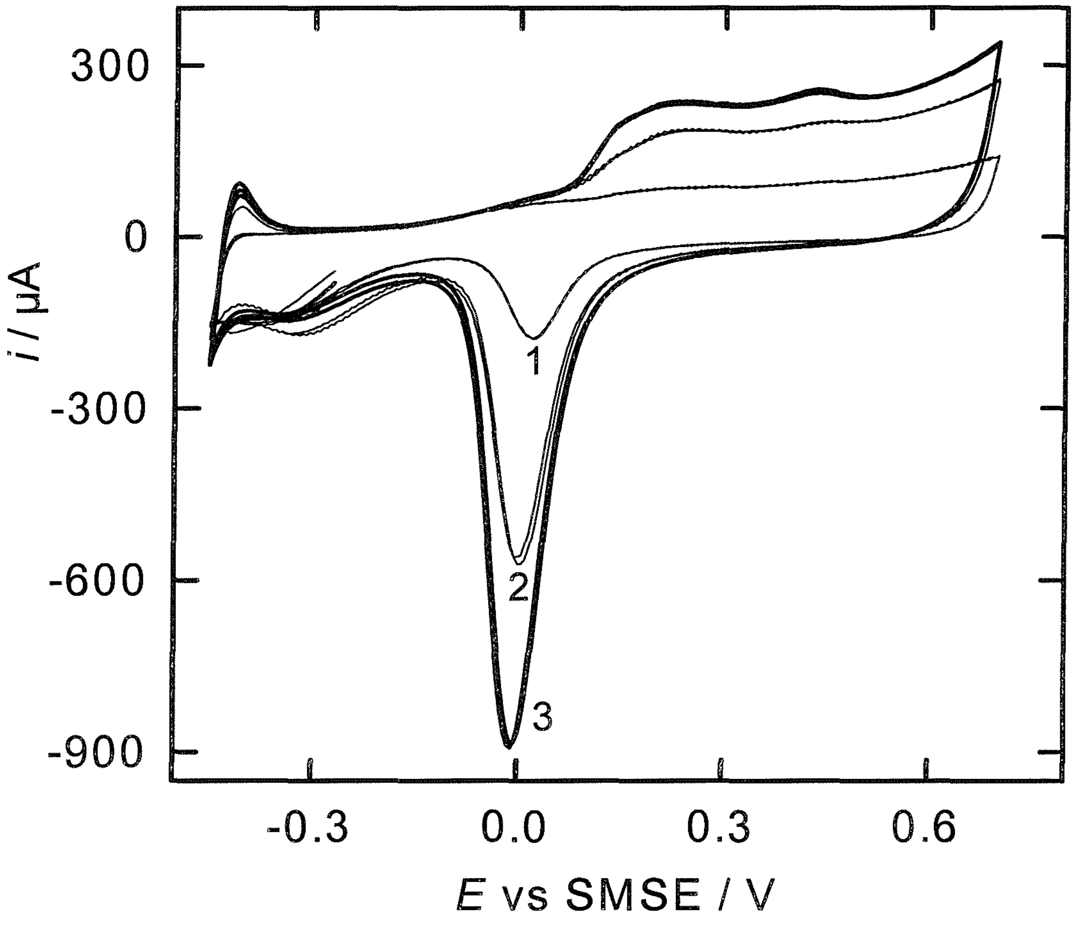

Figure 60: Set of cyclic voltammograms of H_I-e Pd deposited from the template mixture of 12 wt% $(NH_4)_2PdCl_4$, 47 wt% $C_{16}EO_8$, 39 wt% water and 2 wt% heptane at 0.1 V vs SCE on H_I-e Rh. H_I-e Rh was initially deposited on the gold disc electrode (area 0.0079cm^2) from the template mixture of 12 wt% $RhCl_3$, 47 wt% $C_{16}EO_8$, 39 wt% water and 2 wt% heptane at -0.2 V vs SCE. The amount of charge of H_I-e Pd was increased from 3.5 to 10.5 mC whereas the of H_I-e Rh was kept constant. It was cycled at 100 mV/s in 1 M H_2SO_4.

In other experiments we washed the H_I-e metal film superficially to leave the pores of the metal film filled by surfactant when it is transferred to the second plating mixture. We assume that surfactant left in the pores might then be responsible for an epitaxial alignment of the pores. However, in carrying out both experiments we did not find any difference in terms of the epitaxial deposition of the nanostructure.

We then deposited on the top the second H_I-e metal and washed the whole metal film thoroughly in water to remove all the surfactant from the pores. We then recorded the cyclic voltammetry of the bilayer in Figure 60. From this voltammetry we note the oxide formation on the anodic scan at 0.15 V with two distinguishable peaks at 0.22 and 0.43 V. On the reverse scan, the cathodic sweep, we can see two oxide stripping peaks at 0.0 and -0.33 V corresponding to the stripping of Pd and Rh respectively. We observe that the stripping peak for PdO at 0.0 V becomes larger with increasing the thickness of the outer metal layer film (H_I-e Pd) from 200 nm to 400 nm and then to 600 nm as determined by the deposition charge. From the voltammetry we can see that the charge associated with the Rh oxide stripping remains constant as the thickness of the H_I-e Pd layer increases.

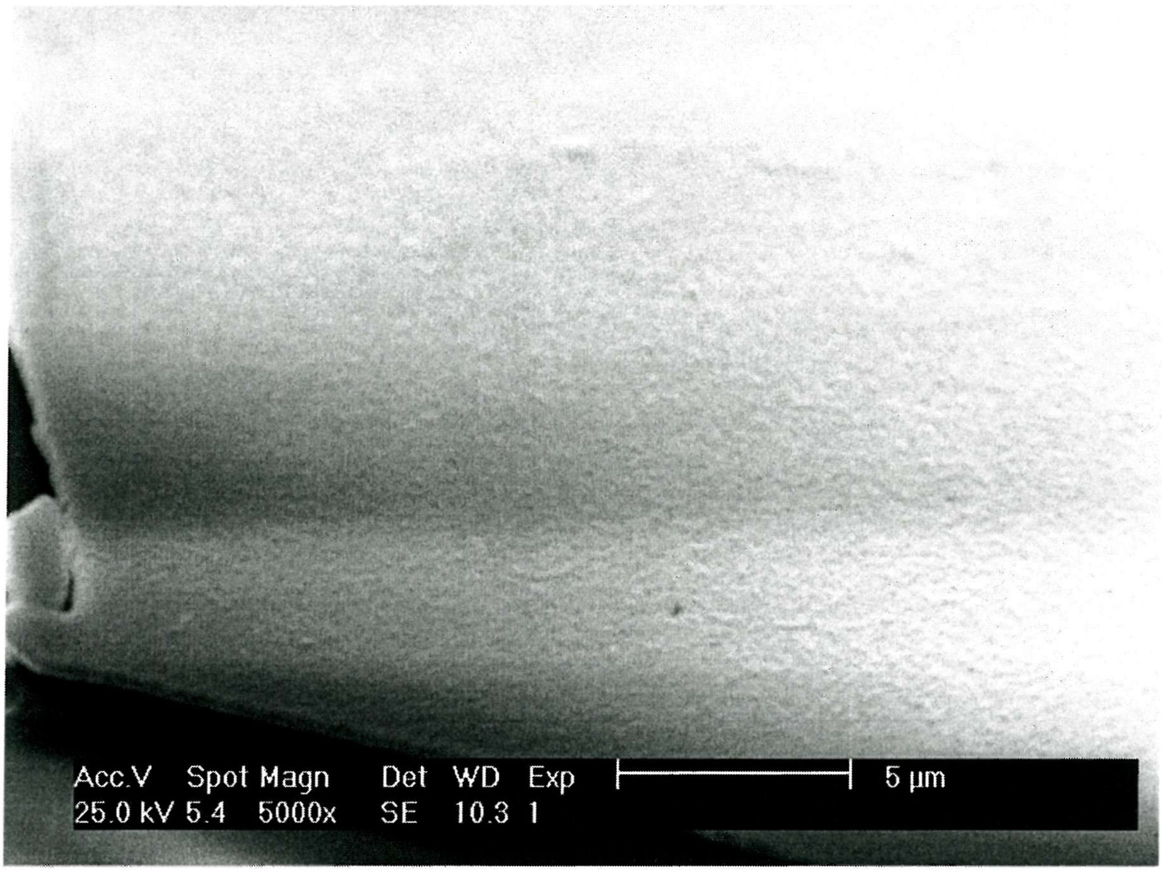

Figure 61: Scanning electron micrograph of a two-nanostructured metal film (Rh on Pd). H_I-e Pd was initially deposited on an evaporated gold electrode (1 cm^2). Both H_I-e metal films were deposited from the template mixture as outlined in Figure 60. The total charge passed for the deposition was 0.56 C/cm^2 (Pd) and 0.42 C/cm^2 (Rh). The image was obtained at a tilt angle of 70°.

This result implies that the presence of the outer layer (H_I-e Pd) directly deposited on top of the inner layer (H_I-e Rh) is not blocking the access to the Rh electrode so that the pores of the H_I-e Rh film is thoroughly accessible by the electrolyte solution.

We then integrate the charges passed in the oxide stripping processes for the rhodium and palladium films so that we can estimate the electroactive surface areas for the two layers. We obtain for the electroactive surface area of the H_I-e Rh oxide stripping peak a value of 0.30 cm^2 which corresponds to a specific surface area for the film of 24 m^2/g. This value is consistent to that shown for the bare Rh film without the H_I-e Pd layer on top. This clearly indicates that the H_I-e Pd outer layer does not block the electrolyte access to the pores in the Rh film.

We want to point out that there is no formation of an alloy between Rh and Pd since we do not observe a single oxide stripping peak at an intermediate potential for that of the two metals [86]. It has also to be stressed that SEM studies of the H_I-e bilayer film, Figure 61, show a smooth, dense overlayer, and there is no evidence of a patchy or discontinuous deposition of the metal.

Figure 62 shows a set of cyclic voltammograms of H_I-e Rh deposited on H_I-e Pd. This time, the experiments were carried out with the two layers in the reverse order. The charge passed for the deposition of Rh was increased from 3.5 mC to 10.5 mC (voltammetric cycles 1-3). This corresponds to an increase in the thickness from 126 nm to 378 nm. H_I-e Pd was initially deposited onto the gold disc electrode with the charge or 3.5 mC passed for the deposition of the film. This corresponds to a thickness of 200 nm. Again we note then the same feature for the formation and removal of the oxide layers.

However, we note that this time the Rh oxide stripping peak at -0.3 V grows in size as the thickness of the H_I-e Rh film increases. The charges associated with the formation of the H_I-e Pd oxide stripping stays constant even though the thickness of the Rh layer is increasing.

By integrating the charges underneath the oxide stripping peaks of Rh and Pd we can estimate the specific surface areas for the two layers and found values of 22 and 31 m^2/g respectively. Again these values were found to be consistent with the nanostructure.

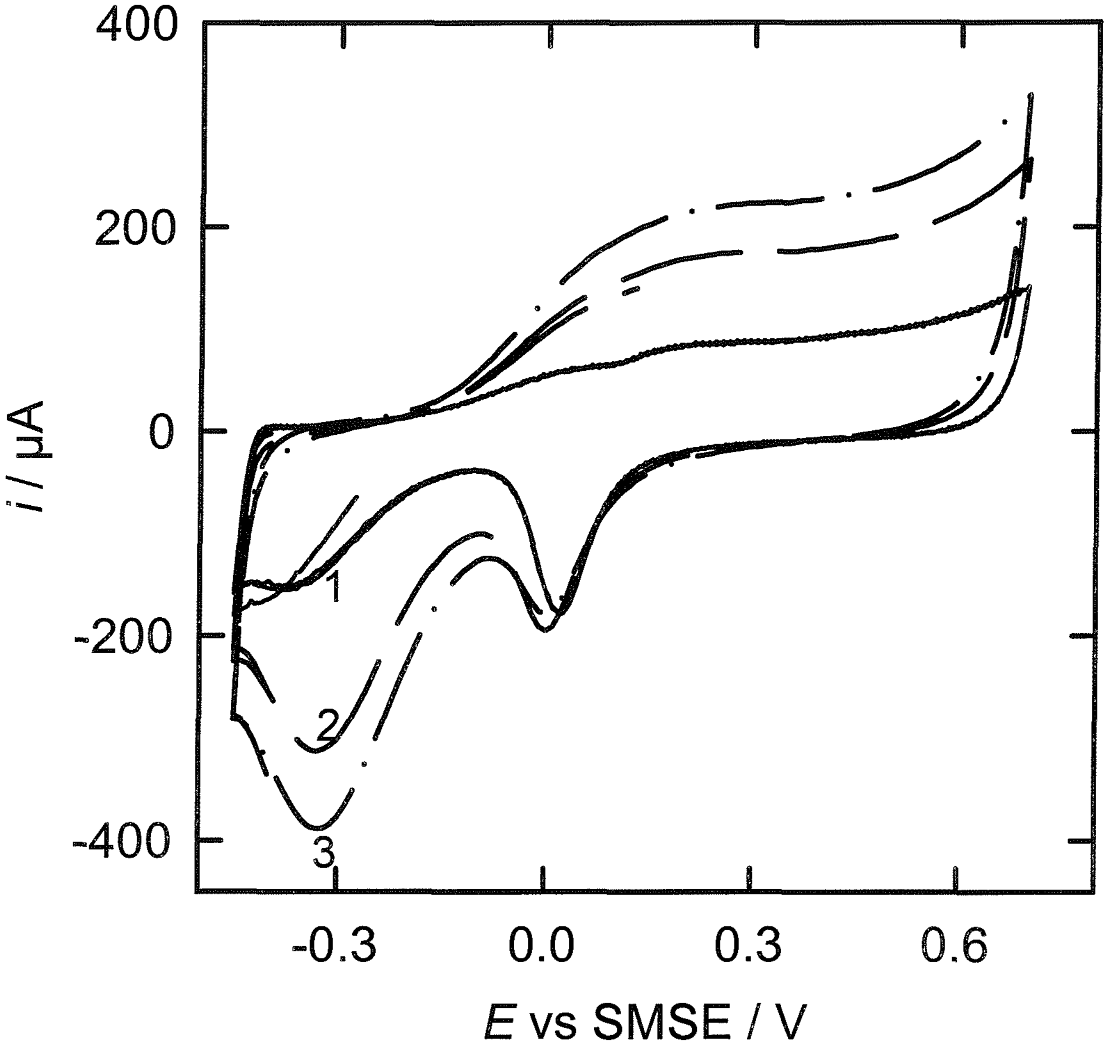

Figure 62: Set of cyclic voltammograms of H_I-e Rh deposited at -0.2 V vs SCE on H_I-e Pd. H_I-e Pd was initially deposited on a gold disc electrode (area 0.0079cm^2) at 0.1 V vs SCE. The amount of charge of H_I-e Rh was varied between 3.5 to 10.5mC (cycles 1-3). The charge of H_I-e Pd was kept constant (3.5mC). It was cycled at 100 mV/s in 1 M H_2SO_4. H_I-e Rh and H_I-e Pd were deposited from the template mixtures as outlined previously (Figure 58 and Figure 59).

6.4 Increase of the surface oxide with the removal of the surfactant

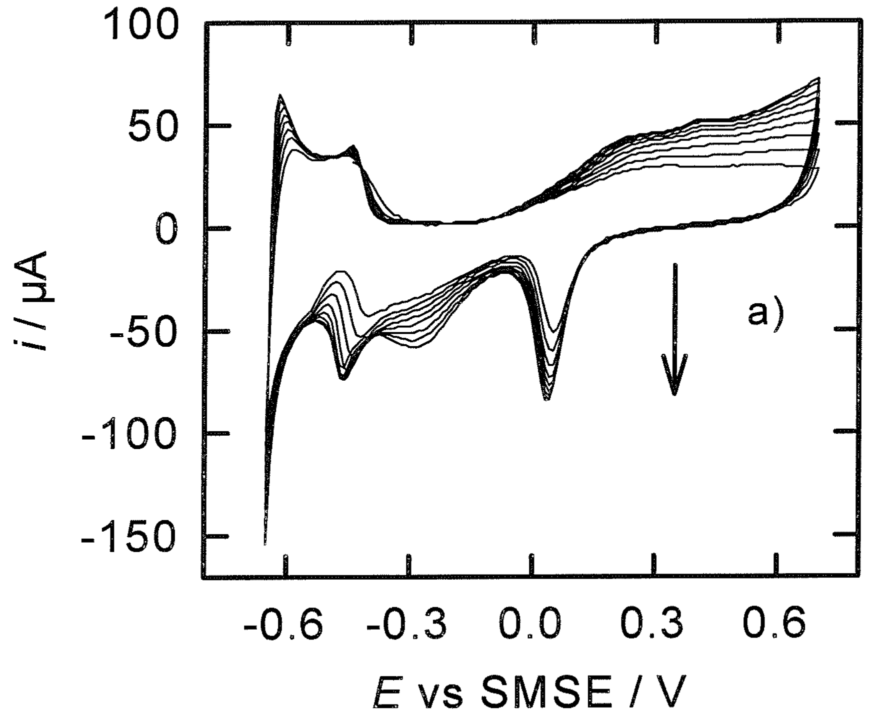

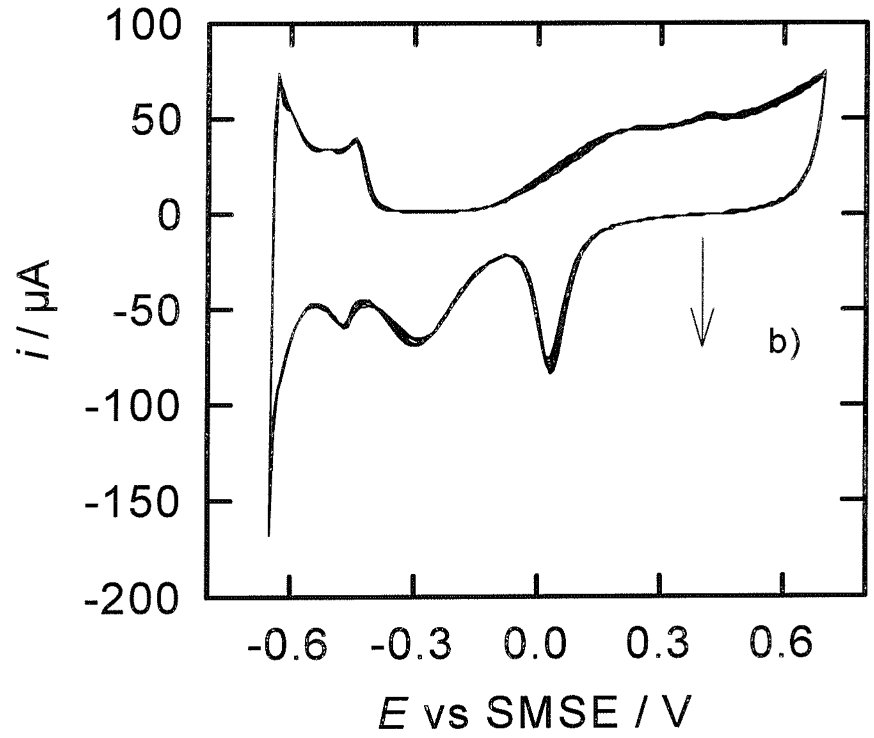

Figure 63: H_I-e Pd was deposited on H_I-e Rh at 0.1 V vs SCE. H_I-e Rh was initially deposited on a gold disc electrode (area 0.0079cm^2) at -0.2 V vs SCE. The H_I-e metal films were deposited from the template mixture outlined in Figure 60 with a total deposition charge for each H_I-e metal of 3.5mC. The H_I-e nanostructured bilayer metal film was not soaked in water. Figure a) shows the first 10 voltammetric cycles at 50 mV/s in 1 M H_2SO_4 and b) the next ten under the same conditions.

From the experiments outlined in the previous section we can conclude that no appreciable blocking of the pores occurs between both nanostructured metal films deposited one on top of the other.

However, at this stage we thought about an experiment from which we can obtain conclusive proof for the continuity of the pores through the final metal film. We therefore carried out an experiment in which the H_I-e bilayer film was only superficially washed after deposition from the template mixture. This should remove the plating mixture adhering to the outside of the film but leaves the pores filled by surfactant. We then immerse the H_I-e metal film into the acid solution after deposition and after superficial washing. By running successive voltammograms, we should see the oxide stripping peaks growing as the surfactant leaves the pores. This will cause an increase in the electroactive surface area as the pores are accessed by the electrolyte solution. Proceeding from the assumption that the pores run continuously through the final metal film, we should see the oxidation peak for the outer metal layer to appear first and increase with each voltammetric cycle. This is followed by the increase of the inner metal layer with the conclusive evidence that the pores are continuous through the final metal film.

Figure 63 shows a set cyclic voltammograms at 50 mV/s in 1 M H_2SO_4 for a 200 nm thick H_I-e Pd film deposited on top of a 126 nm thick H_I-e Rh film. H_I-e Rh was initially deposited onto the gold disc electrode. Figure a) in the cyclic voltammetry shows the first ten voltammetric cycles and b) the next under the same conditions. We can see from the voltammetry that the oxide stripping peak for Pd at around 0.0 V is clearly visible from the start and increases in size with each cycle. The oxide stripping for the Rh oxide at -0.3 V is not clearly resolved at the first few voltammetric cycles. The stripping peak becomes more pronounced with subsequent cycles.

The current of the surface oxide stripping peaks of H_I-e Rh and H_I-e Pd was related to each voltammetric cycle. In Figure 64 we can see this relationship showing a plot of peak cathodic currents at 0.0 V and -0.3 V as a function of cycle number.

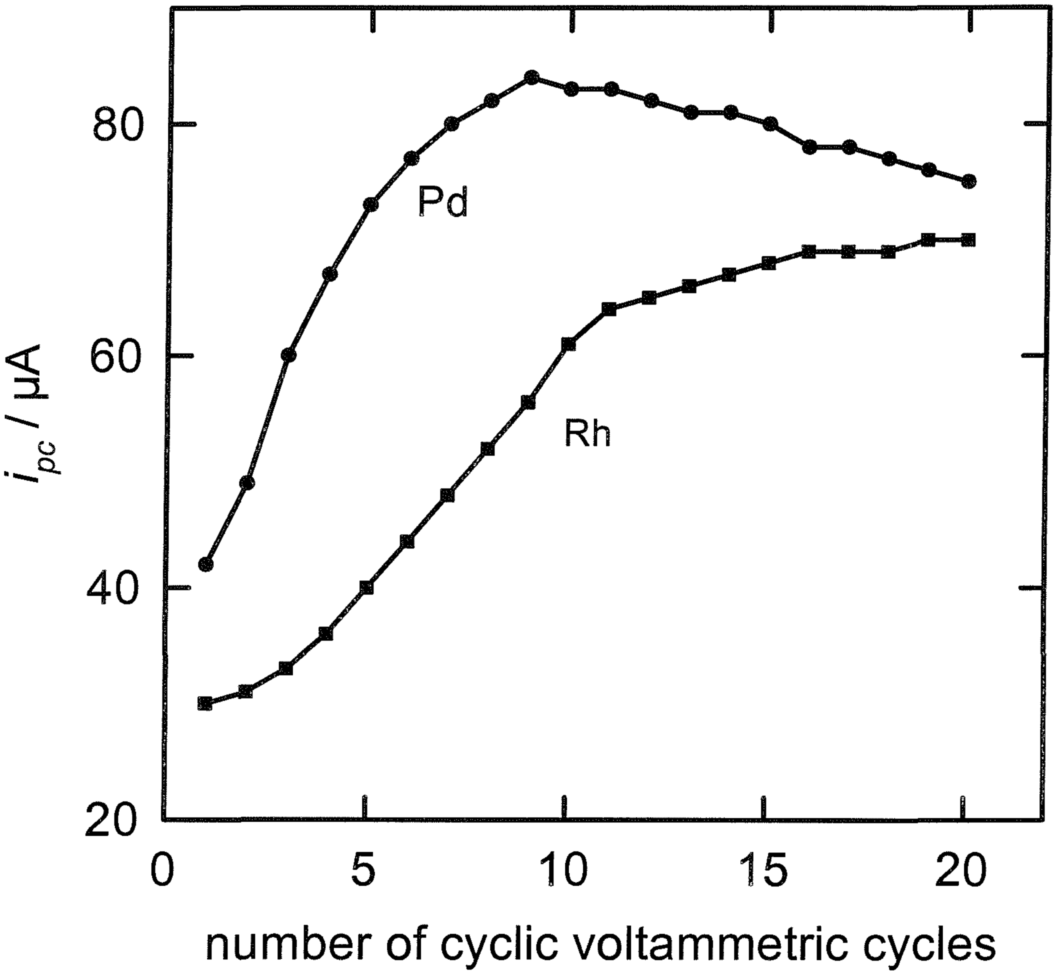

Figure 64: H_I-e Pd was deposited on H_I-e Rh which was initially deposited on a gold electrode (area 0.0079cm^2). The H_I-e metal films were deposited from the template mixtures outlined in Figure 60 with a total deposition charge for each H_I-e film of 3.5 mC. The film was not soaked in water. It was cycled in 1 M H_2SO_4 at 50 mV/s vs SMSE between -0.45 to 0.7 V. The current of the surface oxide stripping peak of H_I-e Rh and H_I-e Pd was related to each cycle

From this experiment we observe that the current related to the oxide stripping peak of the outer metal layer (H_I-e Pd) increases first followed by the increase of that for the inner metal layer (H_I-e Rh). The peak current of the surface oxide stripping of H_I-e Rh should reach a plateau when all the surfactant has been removed.

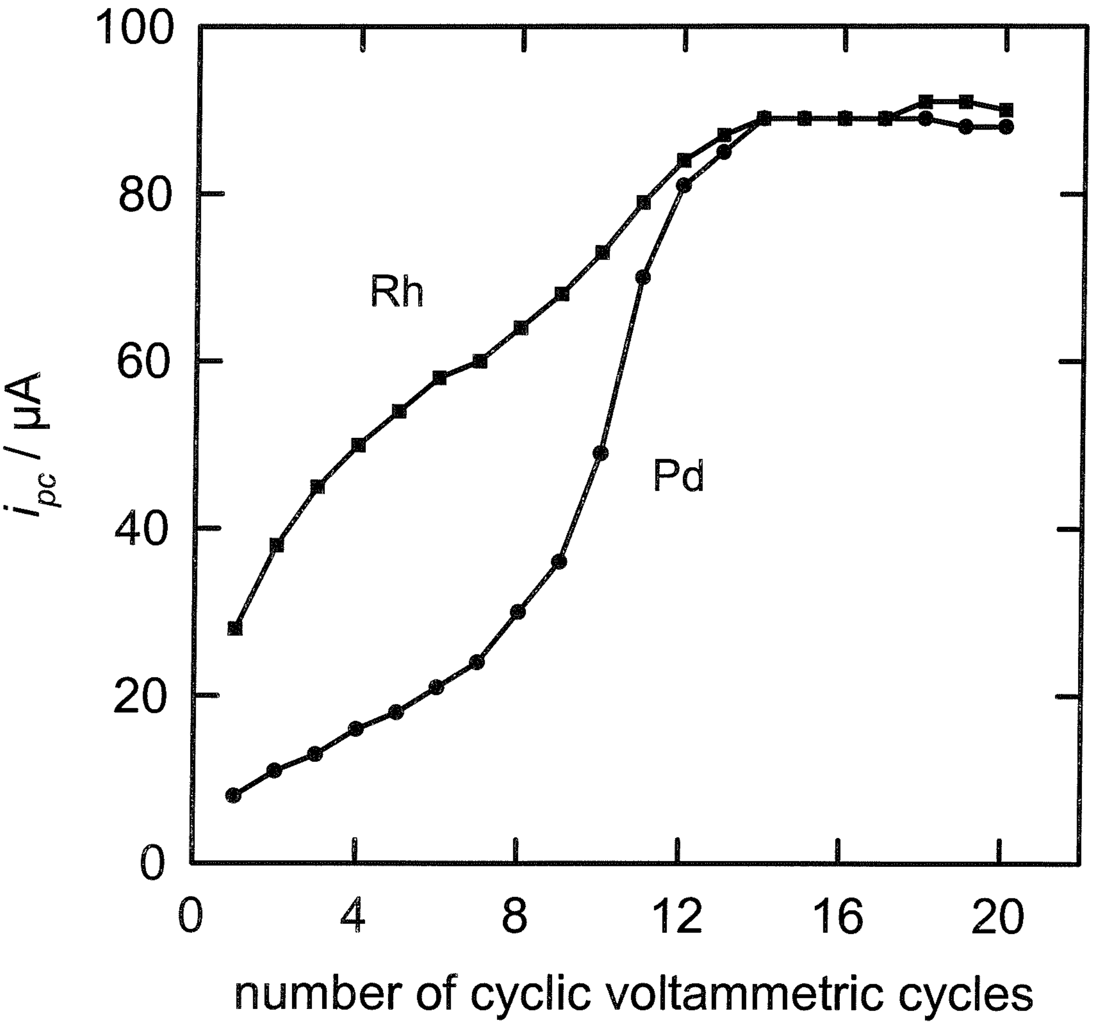

Figure 65: H_I-e Rh was deposited on H_I-e Pd which was initially deposited on gold (area 0.0079cm^2). The H_I-e metal films were deposited from the template mixtures outlined in Figure 60 with a total deposition charge for each H_I-e film of 3.5mC. The film was not soaked in water. It was cycled in 1 M H_2SO_4 at 50 mV/s vs SMSE between -0.45 to 0.7 V. The current of the surface oxide stripping of H_I-e Rh and H_I-e Pd was related to each voltammetric cycle.

It has to be stressed that the peak current for the PdO at higher cycle number decreases slightly which is attributable to the dissolution of the metal when cycled anodically in the oxide region. This was already shown in Chapter 3 with the support of EQCM measurements. By integrating the charges underneath the two oxide stripping peaks at the end of the experiment we evaluate the specific surface areas and found them consistent with the nanostructure for both metals.

We then deposited both H_I-e metals one on top of the other in a reverse order so that H_I-e Rh was directly deposited on top of the inner layer, H_I-e Pd. Comparing Figure 64 with Figure 65 we observed the same pattern for the oxide stripping peaks, but this time the other way round. From the plot in Figure 65 we can see that the oxide stripping peak for the outer metal layer, H_I-e Rh, grows first followed by that of the inner layer, H_I-e Pd. It has to be stressed that we do not note a decrease in the peak cathodic current of H_I-e Pd at higher cycle number. This is because H_I-e Pd has been deposited underneath H_I-e Rh and the overlying material might slow the dissolution of Pd species into the acid solution. We think that this is the reason why the dissolution effect of H_I-e Pd is not well-established in this case.

The continuity of the pores after deposition of two nanostructured metal films is not only restricted to the Rh and Pd bilayer films, we can extend this behaviour to a few combinations of metals. In the course of our research we studied the epitaxial deposition for Rh and Pt films and for Pd and Pt films. In case of combined Pt and Pd films we noticed that the voltammetry for the bilayer system is harder to interpret. This arises because the oxide stripping peaks for both H_I-e metals overlap. This was not the case for Rh and Pt films.

Figure 66 shows a cyclic voltammogram for a 126 nm thick H_I-e Rh film deposited on top of a 105 nm H_I-e Pt film. H_I-e Pt was initially deposited electrochemically on gold. We can see at 0.1 V on the anodic scan a shoulder corresponding to oxide formation and two stripping peaks at 0.04 V and -0.3 V assigned to stripping of Pt and Rh, respectively, on the return cathodic scan. Despite the presence of the overlying H_I-e Rh metal we note the stripping peak for Pt oxide at 0.04 V. The electroactive surface areas associated with the Pt and Rh surface oxide stripping reactions were found to be in a range of a nanostructure. Again the H_I-e Rh metal, as outer, does not block the access to the Pt electrode even through the film is directly deposited on top.

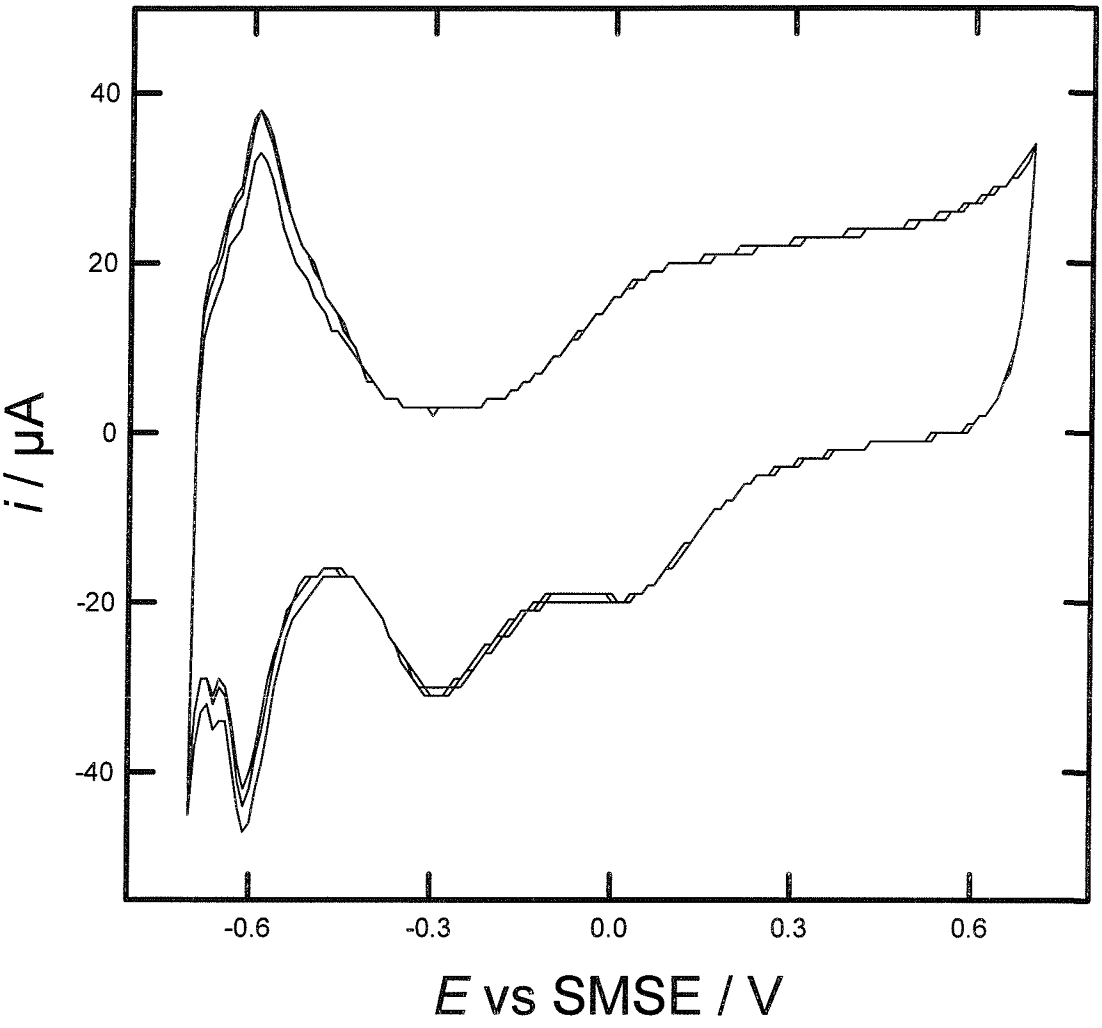

Figure 66: H_I-e Rh was deposited on H_I-e Pt at -0.2 V vs SCE from the template mixture as outlined in Figure 60. H_I-e Pt was initially deposited on a gold disc electrode (area 0.0079 cm^2) at -0.1 V vs SCE from the template of 47 wt% $C_{16}EO_8$, 39 wt% water, 12 wt% H_2PtCl_6 and 2 wt% heptane. Both H_I-e metals were deposited with the total deposition charge of 3.5 mC. Figure shows the cyclic voltammogram at 100 mV/s in 1 M H_2SO_4. The film was soaked in water for one hour prior to the voltammetry.

6.5 Conclusions

In this chapter we proved the continuity of the pores after deposition of H_I-e metal films, one deposited directly on top of the other. We selected a pair of noble metals with well-understood cyclic voltammetry and for which the surface oxide stripping peaks occur at well-separated potentials. This enabled us to determine simultaneously the areas of the upper and the lower metal layer films.

We have chosen for our studies Pd and Rh, as these H_I-e metals fulfil the necessary requirements outlined above.

In one experiment we showed that increasing the thickness of the outer layer does not block the access to the pores of the inner metal electrode. In another experiment we removed the surfactant left in the pores by running successive voltammograms. As the surfactant leaves the pores, we could see the increase in the oxide stripping of the outer metal layer first followed by that of the inner layer.

This finally was conclusive evidence that the pores are continuously accessible by the electrolyte solution through the final metal film.

SEM studies of the H_I-e bilayer film showed a smooth, dense overlayer with no evidence of a patchy discontinuous deposition.

Our results imply that the surfactant micelles in the plating mixture used to deposit the outer metal films align themselves with the surfactant micelles of the first deposited H_I-e metal film so that finally the hexagonal porous arrangement through the whole film might be given.

The deposition of H_I-e bilayers, one on top of the other, could be of advantage for the fabrication of mesoporous multilayers with interesting catalytic or other properties.

Chapter 7 Pellistors

7.1 Introduction

It has been necessary to detect the presence of various gases and to measure their concentration in air. This has become more crucial due to the industrialization. Based on the knowledge obtained during our studies on the electrochemical deposition of metal films with high surface areas, we aim to make use of their catalytic activity. When heated to around 550 °C, the high surface areas of H_I-e Pd films are converted into highly active catalyst layers (PdO) for the oxidation of methane [55, 56, 135]. Our focus in this chapter is the use of Pd films for the methane detection.

Catalytic beads operating on standard calorimetric principles have been considered as the most widely used technology for combustible gas detection in industrial application. These beads consist of a coiled platinum wire (acting as both the heater and as a resistance thermometer to sense the temperature) embedded in a porous refractory material which is loaded with an active catalyst material. Improvement in the performance of these devices is of constant interest. Although well-established in the marketplace, these devices suffer some drawbacks. These include their comparatively high power consumption and the labour intensive nature of the manufacturing process required. In addition, attention has been drawn towards the fact that the catalyst is inhibited and poisoned by certain species [69, 71, 72], in particular in the presence of volatile silicon compounds (as example hexamethyldisiloxane) as frequently found in lubricants and aerosol sprays.

To overcome these outlined problems is the main concern in terms of commercial interest. The use of silicon microfabrication and micromachined substrates is a significant advantage and offers the possibility of reduced power consumption and improved reproducibility of manufacture.

Based on the silicon microfabrication technology the silicon-microhotplate structures were made at Neuchâtel (Switzerland), *Figure 67*. The design of the substrate used to construct the planar pellistor was developed by S. M. Lee at the Sensor Research Laboratory, Department of Engineering, University of Warwick. The planar pellistor substrates were fabricated using standard silicon microfabrication techniques in a six-mask process.

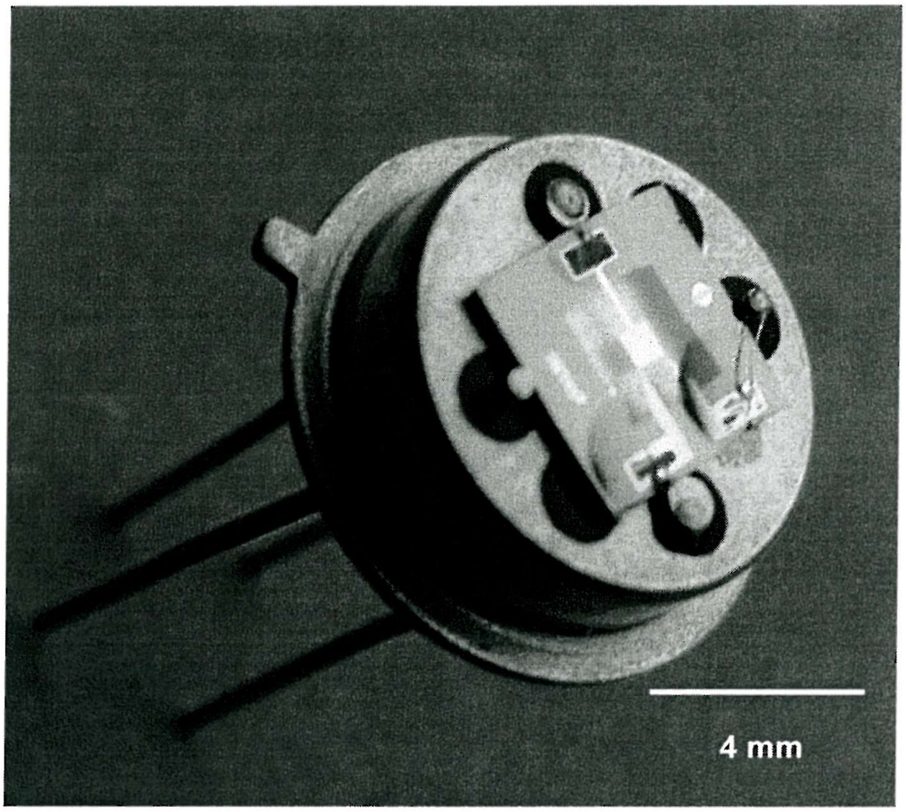

Figure 67: Micromachined substrate mounted on TO5 header for catalyst deposition and characterization

The base material is a 380 µm thick (100) silicon wafer. We want to describe briefly the construction (Figure 68). On the top side a 200 nm thick Pt heater is embedded in two 250 nm thick layers of low stress silicon rich silicon nitride (Si_3N_4). 80 nm of thermal oxide was deposited before the low pressure chemical vapour deposition of Si_3N_4 in order to help minimize any residual stress in the membrane. On the top, 300 nm thick gold electrodes were patterned by lift-off process. 10 nm layers of tantalum and titanium were used to seed the Pt and Au layers, respectively.

Silicon microfabrication can be used to produce low power microhotplate structures in large numbers with a high degree of control. The approach to the deposition of Pd films arranged into regular structures of nanometer-sized dimensions gives unique opportunity to investigate the use of the hotplate structures, when combined with a suitable catalyst, to achieve appropriate activity, robustness and ease of application.

In this chapter we present results for the deposition of H_I-e Pd films on to microfabricated silicon hotplate structures and the use of these devices to detect methane in air. We give first a brief description of the electrochemical characterization of the substrates and then outline the deposition of the H_I-e metal films onto the gold electrode of the SRL devices from two different template mixtures.

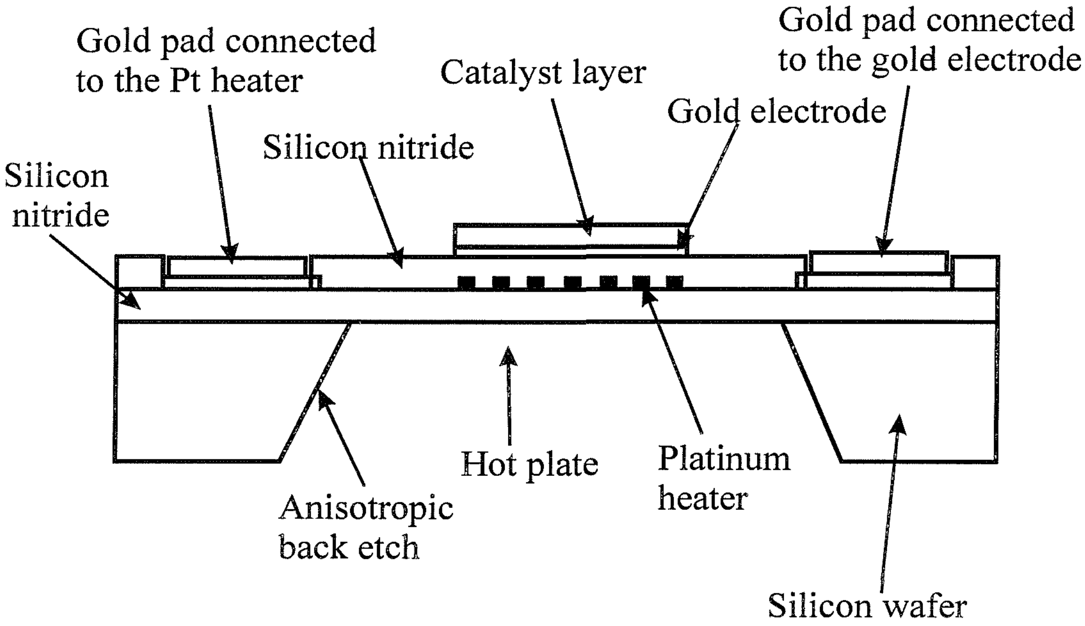

Figure 68: Cross-section of the microfabricated silicon hotplate structure

This together with the problems which we encountered during the deposition procedure and together with a description of the ways to solve them forms the foundation for the next section; the catalytic layers deposited onto SRL devices for the methane detection. In our experiments we focused on the reproducibility in the methane response. In the last section we discus the issue of how to arrange the deposition of the H_I-e metal layers on a large scale to make the results applicable in the manufacturing process.

7.2 Characterization of devices

	SRL 176 The standard Family *Membrane size: 2mm x 2mm* *Heater size: 570um x570um*	**SRL 177** The low power Family *Membrane size: 2mm x 2mm* *Heater size: 400um x400um*	**SRL 178** The small-mem /robust Family *Membrane size: 1.5mm x 1.5mm* *Heater size: 400um x400um*	**SRL 179** The robust Family *Membrane size: 1.5mm x 1.5mm* *Heater size: 570um x570um*	**SRL 180** The ultra small/robust Family *Membrane size: 1mm x 1mm* *Heater size: 400um x400um*	**SRL 181** The ultra small/ low power Family *Membrane size: 1mm x 1mm* *Heater size: 200um x200um*
a	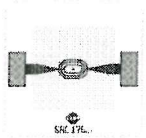 P=106mW R=3.60Ω MHR=3.51	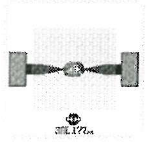 P=44mW R=3.70Ω MHR=5.00	 P=88mW R=3.7Ω MHR=3.75	 P=176mW R=3.6Ω MHR=2.63	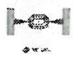 P=150mW R=4.00Ω MHR=2.37	 P=45mW R=6.00Ω MHR=4.73
b	 P=106mW R=9.00Ω MHR=3.51	 P=44mW R=12.60Ω MHR=5.00	 P=88mW R=12.60Ω MHR=3.75	 P=176mW R=9.00Ω MHR=2.63	 P=150mW R=12.60Ω MHR=2.37	 P=45mW R=12.60Ω MHR=4.73
c	 P=106mW R=26.58Ω MHR=3.51	 P=44mW R=24.00Ω MHR=5.00	 P=88mW R=24.00Ω MHR=3.75	 P=176mW R=26.58Ω MHR=2.63	 P=150mW R=24.00Ω MHR=2.37	 P=45mW R=40Ω MHR=4.73
d				 P=176mW R=235.00Ω MHR=2.63		
e				 P=220mW R=183.00Ω MHR=2.00		

Figure 69: Summary of the design of several SRL devices used during this project. Figure was provided by S. M. Lee of the University of Warwick. P= power; R = resistance; MHR = membrane size (equivalent to the gold electrode area) to heater ratio.

The Si-micro hotplate structures in combination with the metal catalyst were tested during this project towards methane and HMDS (Hexamethyldisiloxane). Figure 69 shows the design of several devices that we used in our studies. Figure 70 presents the 162g device showing the membrane and heater size. This is the device type together with 136a mostly used in our studies.

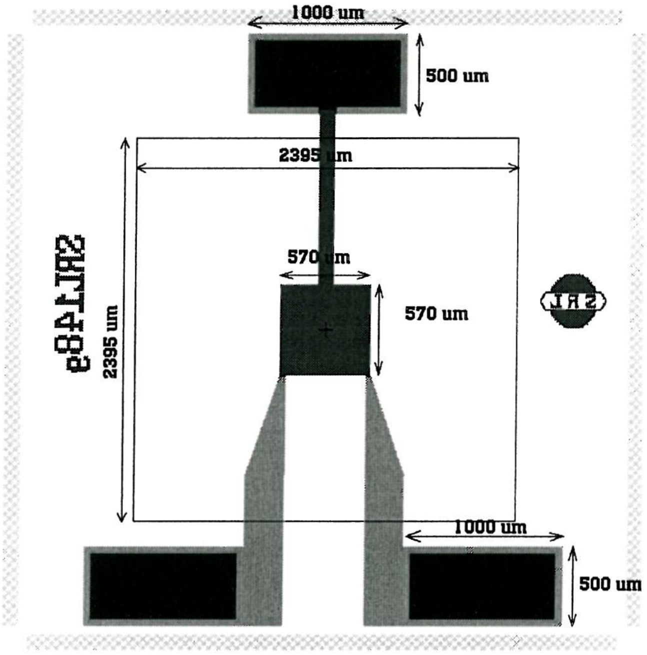

Figure 70: Micropellistor design of the device type 162g with the membrane size of 2 mm × 2 mm and the heater size of 570 μm × 570 μm

Before any metal deposition onto the gold electrode of the device occurred, the gold electrode was electrochemically characterized by using cyclic voltammetric studies. The cyclic voltammetry on gold in sulfuric acid is a non-destructive method to indicate surface defects on gold. Surface defects can be noticed by additional features in the cyclic voltammetric profile.

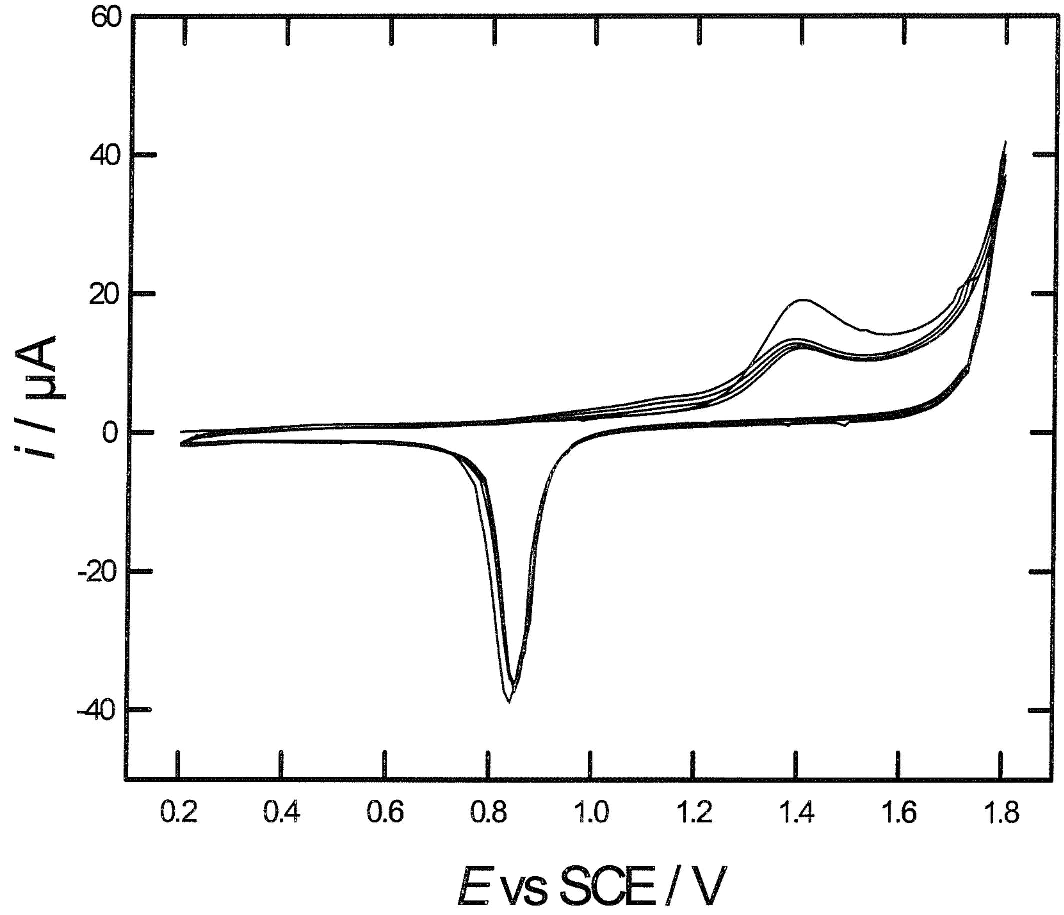

Figure 71: Cyclic voltammogram of the gold electrode of three SRL 177c devices (0.16 mm^2) at 200 mV/s in 1 M sulfuric acid before Pd deposition

Figure 71 shows the cyclic voltammogram of the gold electrode of the SRL 177c device in 1 M H_2SO_4 at 200 mV/s in the potential range from 0.2 to 1.8 V vs SCE before any deposition of palladium occurred. We can see the formation of the gold oxide on the anodic scan in the oxide region at around 1.25 V vs SCE and on the return sweep at ca. 0.85 V vs SCE which corresponds to the surface oxide stripping reaction. The voltammetric features on the profile in this figure look very similar to those reported by Hoare [136] who has investigated the voltammetry of polycrystalline gold electrodes in 1 M sulfuric acid which were in the form of small beads of 0.13 cm diameter. Using the conversion factor of 386 µC/cm^2 given by Rand and Woods [78], who studied the dissolution process of the gold electrodes in 1 M sulfuric acid, and the charge passed in the oxide stripping peak we can calculate the electroactive surface area for the gold electrode of our device which was found to be 0.036 cm^2. It is notable that the devices with the design number 136a, 162g, 177c, 180c and 181c do not show any significant difference in the voltammetric features. The peaks for the gold oxide formation and stripping reaction occur at the same potential as for the device 177c. However, we found that the electroactive surface areas underneath the oxide stripping peak differ for a few devices corresponding to the difference in the gold electrode area. We estimated the electroactive surface area and the roughness factor for each device as follows: SRL 136a (0.15 cm^2, 15), SRL 162g (0.045 cm^2, 13.9), SRL 177c (0.036 cm^2, 22.5), SRL 180c (0.034 cm^2, 21.3), 181c (0.010 cm^2, 25). These values were found to be in three replicate measurements accurate to ±0.1.

Figure 72 shows three cyclic voltammogramms of the gold electrodes of the SRL 176c devices in 1 M H_2SO_4 at 100 mV/s before the deposition of Pd occurred. The surface oxide stripping on the cathodic sweep at 0.85 V vs SCE occurs at the same potential as oultined in Figure 71 whereas on the anodic scan distortion in the oxide formation region appears. An additional peak at 1.2 V is of interest to note in the oxide region.

Changing the acid solution in which the cyclic voltammetric measurements were carried out and cleaning the gold surface by applying potential cycling pre-treatment we are likely to eliminate any contamination in the solution as possible explanation for additional peaks in the voltammetry. However, we noticed that the peak at 1.2 V is still present. We therefore might attribute this electrochemical behaviour to a manufacturing problem of the wafer giving rise to surface defects on the gold electrode of the SRL 176c device. This wafer problem might be due to contamination of the gold evaporated onto the wafer.

Summarizing the facts, we can say that cyclic voltammetry on gold electrodes of the 136a, 162g, 177c, 180c and 181c devices showed the same voltametric features occurring at the same peak potential. The electrochemical surface area estimated from the charge passed the surface oxide stripping reaction is reproducible for each device. In contrast to this the device type 176c showed in the oxide region at the anodic scan slight distortion with an additional peak at 1.2 V which is not attributable to the gold oxide formation.

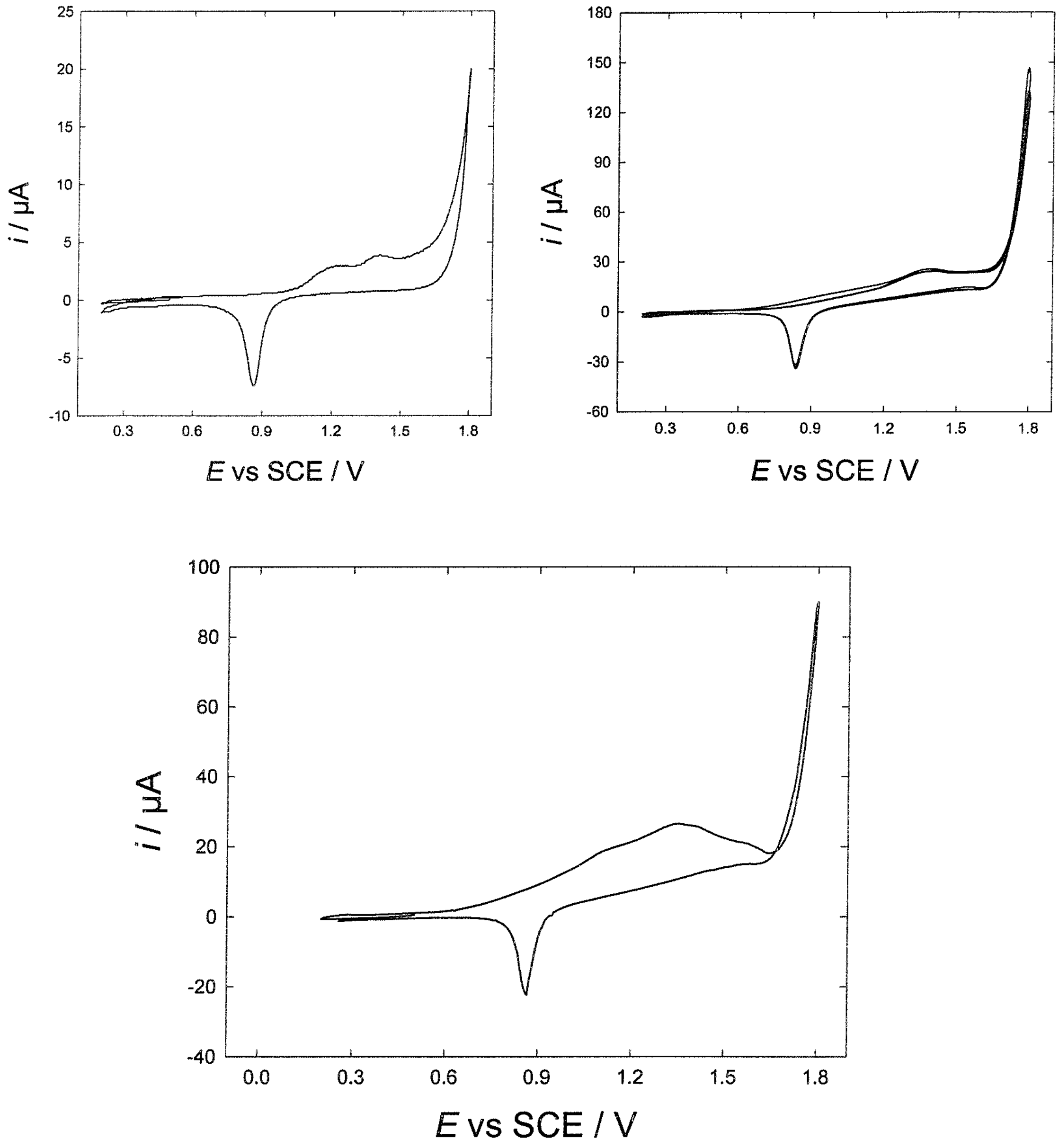

Figure 72: Cyclic voltammograms of the gold electrode of the SRL 176c device (0.32 mm^2 electrode area) in 1 M sulfuric acid at 100 mV/s before the deposition of Pd occured.

The focus of this section was the electrochemical characterization of the gold electrodes of different types of SRL devices using cyclic voltammetry as a non-destructive method to indicate surface defects on gold. During this project the next step towards the production of successful working gas-sensors used for methane detection is the deposition of metal catalyst layers onto the gold electrode of the devices. From our studies of how to arrange the metal (Pt, Pd and Rh) into regular structures of nanometer-sized dimensions we aimed to deposit H_I-e metals from the hexagonal phase onto SRL devices. This is the focus of the next section in which we compare the deposition of the metal on the one hand from the Brij®56 template mixture and on the other hand from the Pluronic F127 template mixture.

7.3 Deposition from the template mixture

7.3.1 Deposition from the Brij®56 system

To fabricate planar pellistors the deposition of Pd from the template mixture gives rise to a high surface area metal catalyst used for methane detection. To get uniform, continuous deposition of the metal catalyst layers onto the gold electrode of the devices requires more understanding of the deposition behaviour. With the aim to acquire this understanding it might be useful to look at the current transients as an indication of how reproducible the deposition appears to be.

Figure 73 and Figure 74 show the current transients when depositing Pd under the same experimental conditions from the template mixture of Brij®56 system onto the gold electrode of the SRL devices. In Figure 73 the current jumps to its maximum point of ca. 120 μA whereas in Figure 74 the maximum is only found to be 50 μA. The deposition times for each deposition on both devices (that is the time required to pass the same total charge) vary accordingly and were 180 and 430 s even though the same experimental conditions were used. In addition, we note that the current proceeds to the maximum via successive steps. Similar results were obtained for the deposition of the metal catalyst layers onto the gold electrode of SRL 136a devices. In addition, we noticed the same feature when depositing Pt and Rh from the template mixture based on the Brij®56 system (not shown). It has been also of interest to note that the deposition of the metal catalyst layers onto the gold electrode area of the SRL devices from the template mixture of the $C_{16}EO_8$ system revealed the same problem. We therefore can conclude that switching from Pd, Pt to Rh and replacing Brij®56 by

$C_{16}EO_8$ as surfactant did not show any difference in this feature of the deposition behaviour. The features in the deposition behaviour as outlined above have been observed only for the deposition onto SRL devices. We did not note this when depositing the metals from the template mixture onto the gold electrode of 1 mm diameter.

We considered as one problem a failure in the manufacturing process of the devices.

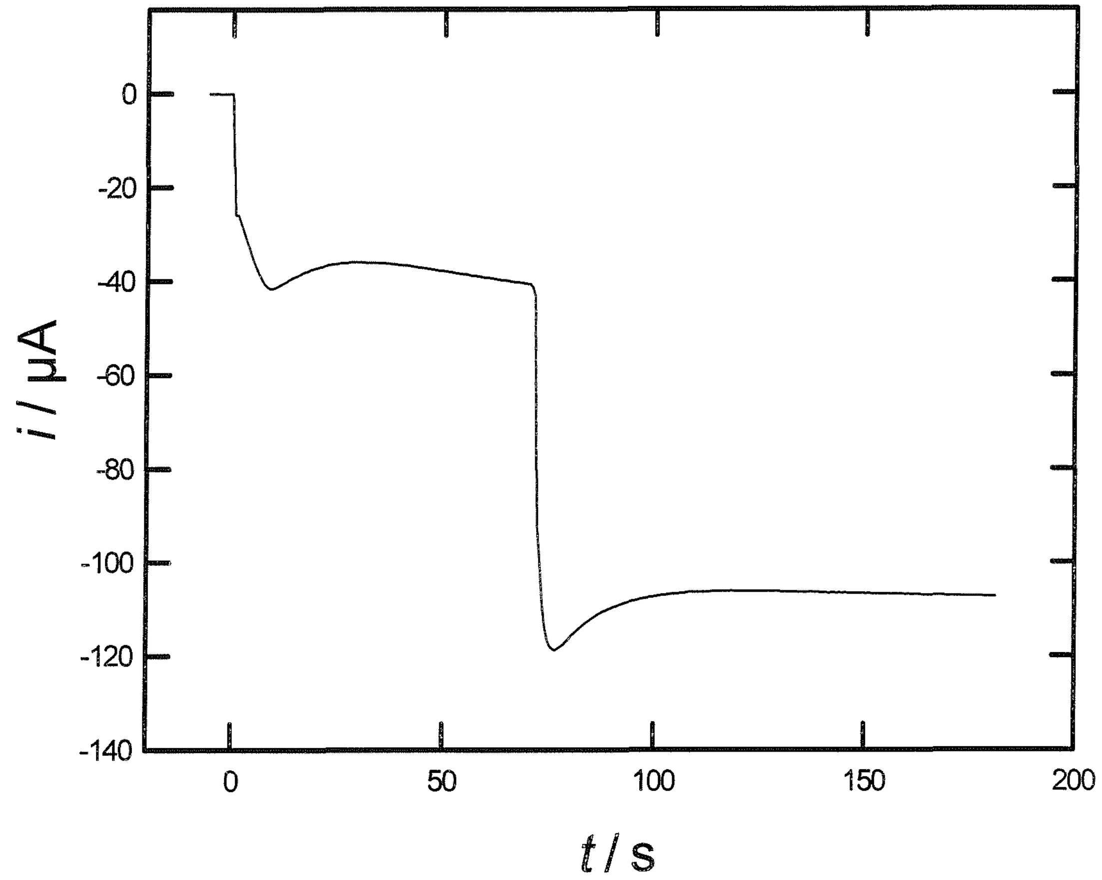

Figure 73: Current transient versus time. H_I-e Pd is deposited onto the gold electrode area of the device SRL 162g (0.32 mm^2) from the template of 12 wt% $(NH_4)_2PdCl_4$, 47 wt% Brij®56, 39 wt% water and 2 wt% heptane at 0.1 V vs SCE.

However, this is unlikely since irreproducibility in the deposition behaviour occurred for the deposition on both devices – SRL 136a and SRL 162g for each wafer.

As another approach to investigate this problem we proceed from the assumption not to get a homogeneous phase after putting the catalyst layers onto the electrode of the device. There might be air bubbles left in the viscous mixture. This might hamper the

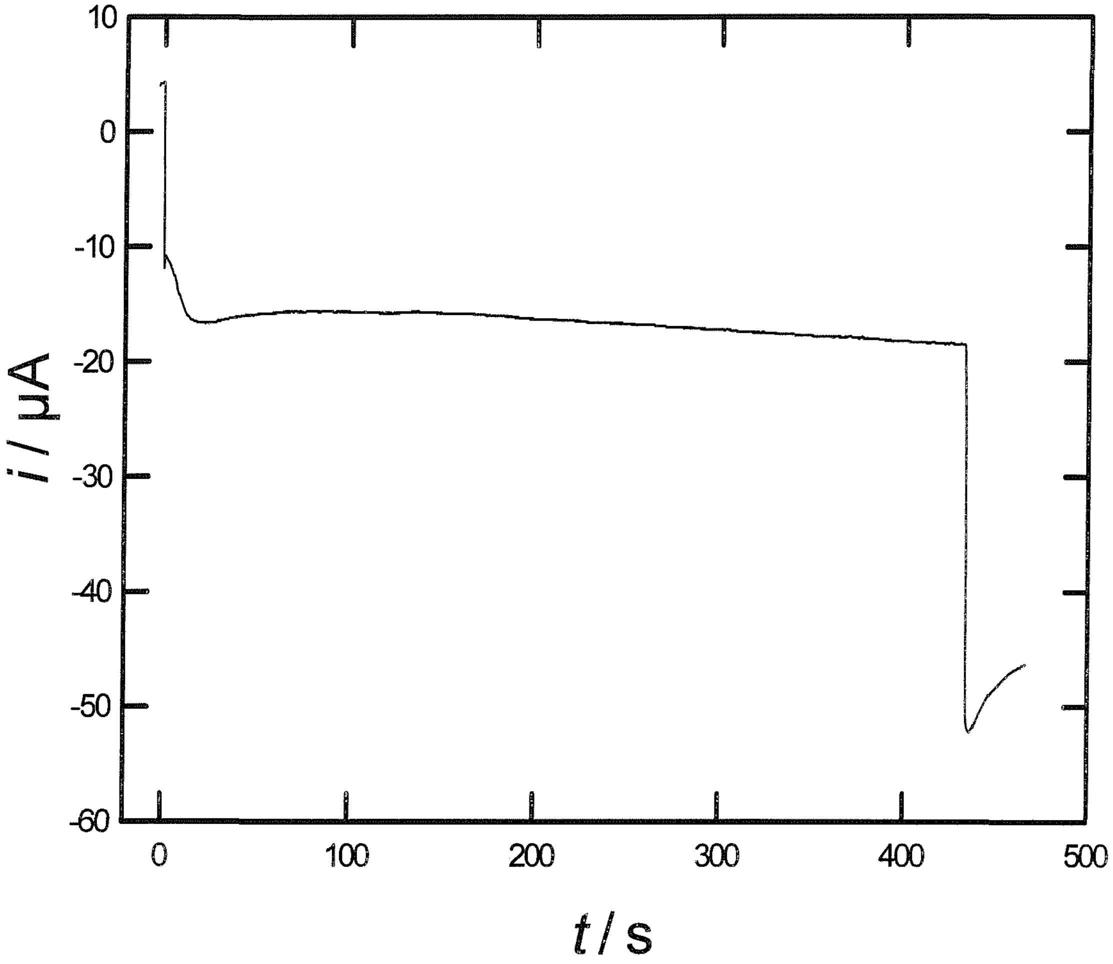

Figure 74: It shows the current transient versus time. H_I-e Pd is deposited onto the gold electrode area of SRL 162g (0.32 mm^2) from the Brij$^{®}$56 system at 0.1 V vs SCE. The template mixture is the same as used in Figure 73.

electrical contact between the gold electrode and the Pd dissolved in the aqueous solution of the hexagonal liquid crystalline structure giving rise to the jumps outlined in Figure 73 and Figure 74. Unfortunately this problem is hardly to avoid due to the fact that the membrane is very fragile and any attempt to squash the template mixture to remove the air bubbles is likely to cause the breakage of the heater membrane.

So far we tend to the opinion that air bubbles embedded in the template mixture cause the instability in the deposition behaviour. We will return to this problem later when considering the deposition from the Pluronic template mixture which is far less viscous giving rise to a uniform coverage of the gold surface after the metal deposition.

In the next section we concentrate on the surface morphology of H_1-e Pd films obtained after deposition from the Brij®56 system on evaporated gold on glass and compare these results to those reported for the deposition of H_1-e Pd from the $C_{16}EO_8$ template mixture. In finding the reasons for the difference in the apparent surface morphology we direct our attention towards the variation in composition and impurities contained in the different batches of Brij®56.

7.3.2 Mass spectroscopic measurements of Brij®56

The deposition of Pd from the hexagonal liquid crystalline phase on microhotplate structures of planar pellistors occurs from the template mixture based on the Brij®56 system. Brij®56 has been used as a cheap commercially available surfactant. The existence of Pd as a high surface area metal after deposition (3.5 mC total deposition charge) from the template mixture containing Brij®56 onto the gold electrode of 1mm diameter could be proved by cyclic voltammetric measurements giving rise to the electrochemical active surface of around 0.56 cm^2 estimated from the charge passed in the surface oxide stripping peak (Chapter 3). This high surface indicated the deposition of nanostructured Pd. However, we could better note a continuous and uniform hexagonal arrangement in the TEM-studies when using $C_{16}EO_8$ as the surfactant in the template mixture. In addition we found using SEM that using Brij®56 in the template mixture gives rough surface of H_1-ePd deposited on an evaporated gold electrode (Figure 75). This is in contrast to the results we obtained when using $C_{16}EO_8$. Smooth, continuous and uniform deposition of H_1-e Pd can be obtained under the same experimental conditions. This was already shown in Chapter 3. The deposition of H_1-e Pd from the $C_{16}EO_8$ template mixture onto the gold electrode of the SRL devices revealed the same feature. This contrasts to the deposition from the Brij®56 system. We also note identical behaviour in the deposition independently on the choice of the metal (Pd, Rh, Pt etc.). From this comparison we concluded that Brij®56 affects the electrodeposition of metal films from the hexagonal phase differently compared to $C_{16}EO_8$. We know that batches of Brij®56 obtained from

Aldrich contain traces of impurities and other surfactant. We therefore focused our attention on the components and impurities contained in one batch of Brij®56 and wanted to see the variation from batch to batch using mass spectroscopy.

$CH_3 - (CH_2)_{15} - (CH_2CH_2O)_8 - OH$

octa ethylene glycol monohexadecyl ether ($C_{16}EO_8$)

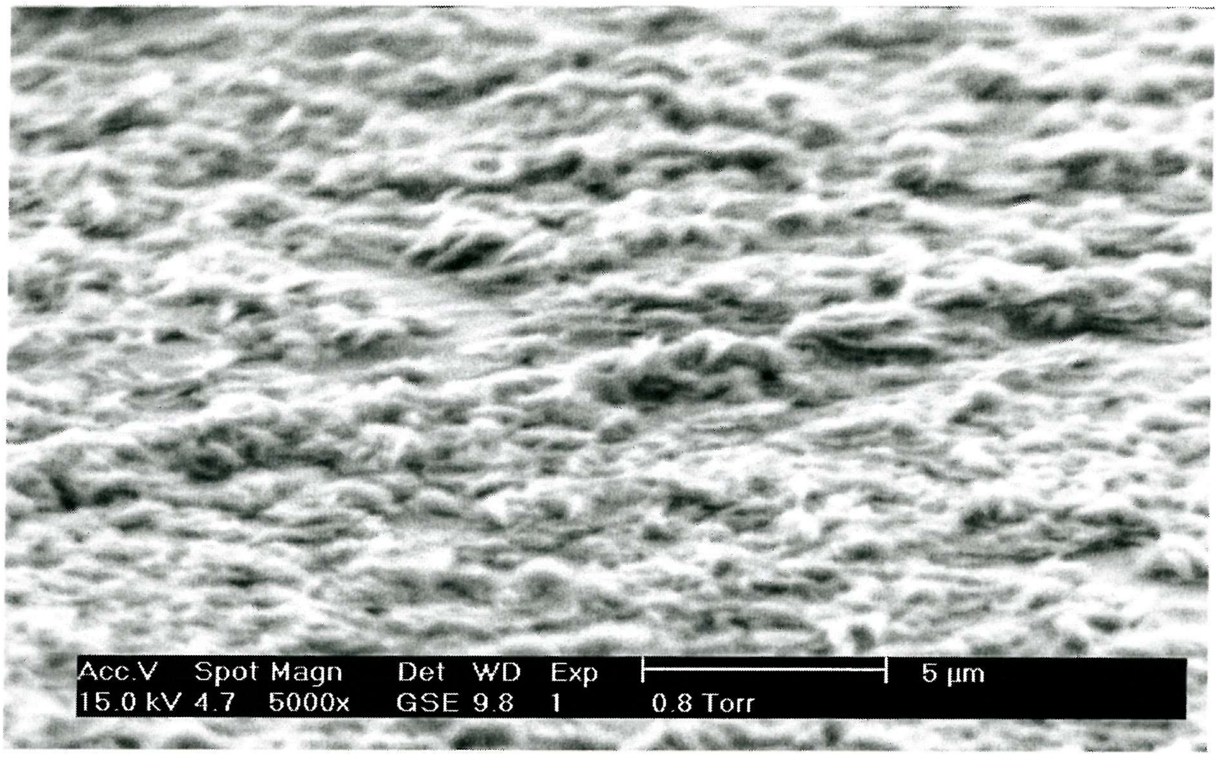

Figure 75: Scanning electron micrograph of an H_I-e Pd film deposited on an evaporated gold electrode. The film was deposited from a mixture of 12 wt% $(NH_4)_2PdCl_4$, 47 wt% Brij®56, 39 wt% water and 2 wt% heptane. The total charge passed was 0.53 C/cm^2 and the image was obtained at the tilt angle of 70 ℃.

Figure 76 a) shows the mass spectrum of $C_{16}EO_8$. Five main peaks can be seen. From the formula given above we can calculate the molecular weight which is 594.88. Considering the ions NH_4^+ and Na^+ in the solution the peak at 612.5 is attributable to ($C_{16}EO_8 + NH_4^+$) and the peak at 617.5 to ($C_{16}EO_8 + Na^+$). The peaks at 613.5; 618.5; and 619.5 can be associated to the isotopic effect. We estimated theoretically the relative intensities for the isotopic abundances of $C_{16}EO_8$ and came to the conclusion that the calculated relative intensities agree with the data. The probability for the isotopic abundances at 617.5, 618.5 and 619.5 were found to be 72%, 22% and 6% respectively.

We used here electrospray ionization generating ions by spraying a solution (aqueous or organic solvent) through a charged inlet. Once the solvent is sprayed, its droplets rapidly desolvate through the addition of heat, a stream of gas (air) or both. As the solvent evaporates, ions in the highly charged droplets get ejected. The ions are then electrostatically directed into the mass analyzer. This ion source commonly produces multiply charge ions, making it easy to detect $C_{16}EO_8$. This is accomplished by the addition of an alkali cation. Many compounds are unstable to proton addition and require alkali cation complexation in order to observe stable molecular ions. $C_{16}EO_8$ forms a stable alkali cationized molecular ion while its protonated molecular ion is often undetectable. In addition to this ammonium cation is also used.

Figure 76 b) shows the mass spectrum of Brij®56 (batch number 07727 DU) diluted to 10 μg/ml in methanol. To determine the spectrum, all the peak intensities appearing in the spectrum were added together. The peak intensity of every single peak in the spectrum could then be related to the total sum of all intensities.

In this figure we can see the main component $C_{16}EO_8$ (617.5 Da/e) with the intensity of 8% relative to all other peak intensities appearing in this spectrum. The variation of $C_{16}(EO)_n$ with $3 \leq n \leq 17$ can be seen with the highest relative intensity for $C_{16}EO_8$ (617.5 Da/e) joined by $C_{16}EO_7$ (573.5 Da/e) with 7.7% and $C_{16}EO_9$ (661.5 Da/e) with 6.4%. The $C_{16}(EO)_n$ compounds differ in the number of the ethylene oxide (EO) group (MW: 44). From the structure and the molecular weight given for $C_{16}EO_8$ we tried to work out the assignment of the other peaks appearing in the spectrum. Proceeding from $C_{16}EO_8$ we changed the alkyl chain length and the number of ethylene groups until we found agreement between the calculated MW of each proposed surfactant and the MW of the unknown surfactant shown for each peak in the spectrum.

We therefore assume the existence of other compounds in this spectrum as follows: C_9EO_7 (474.5 Da/e; 4.6%) and $C_{17}EO_5$ (496.6 Da/e; 4.8%). We found it hard and too uncertain to give any assignment for the peaks occurring at 241 Da/e (5.6%), 199.8 Da/e (1%), 261.1 Da/e (0.74%), 336 Da/e (0.7%) and 377 Da/e (1%). However, the peak intensities are relatively small. The peaks occurring at 540.6 Da/e (3.4%), 584.6 Da/e (1.8%) and 628.7 Da/e (0.9%) can be attributed to $C_{17}(EO)_n$ with n varying between $6 \leq n \leq 8$. We may suggest that the peak occurring at 474.5 Da/e (4.6%) is attributable to C_9EO_7. We then assume a variation of C_9EO_n with $7 \leq n \leq 10$ with the highest relative intensity occurring for C_9EO_7 (474.5 Da/e, 4.6%) joined by C_9EO_8 and sequentially the other compouds differing in the number of the EO groups.

a)

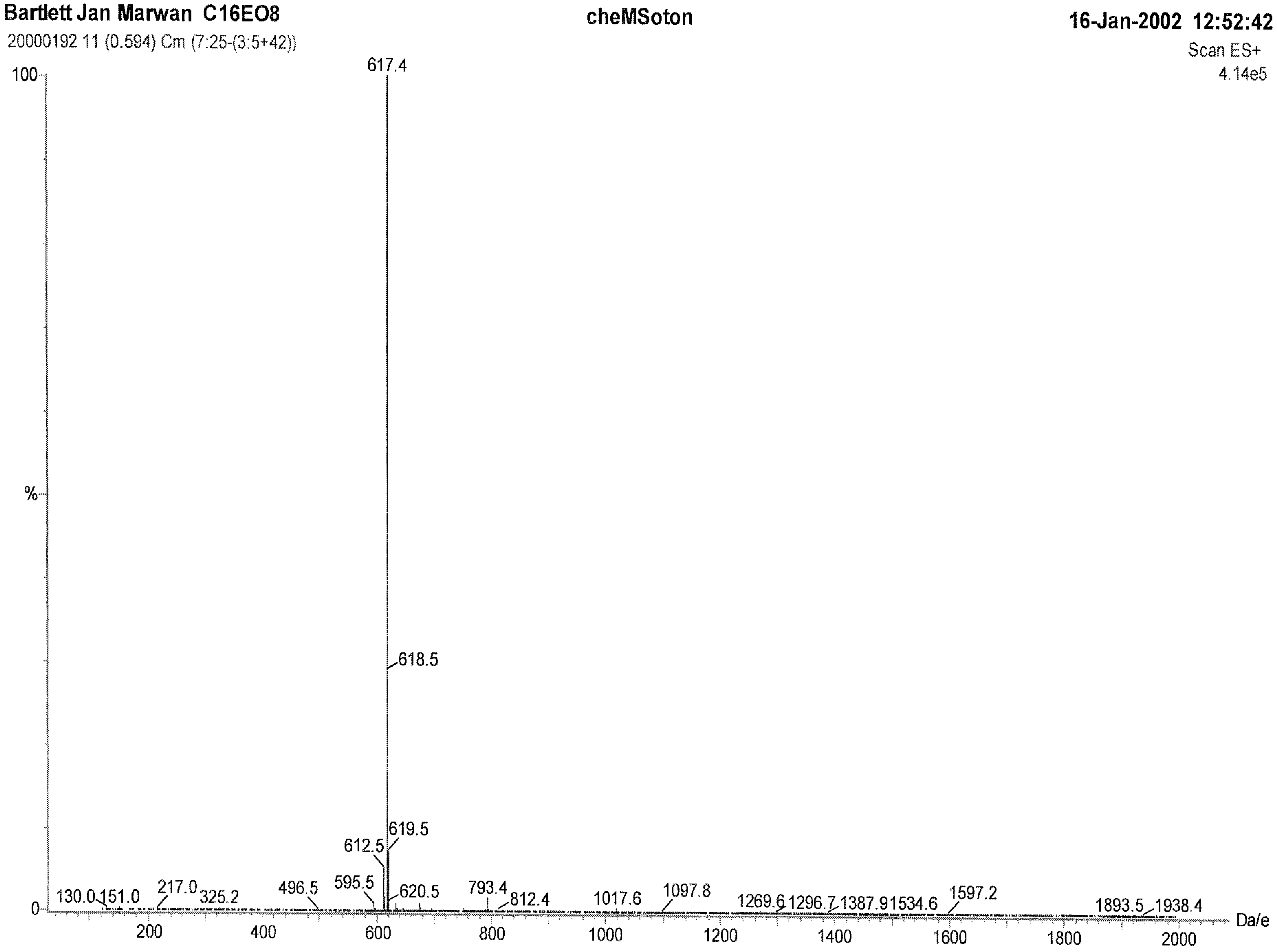
Bartlett Jan Marwan C16EO8
20000192 11 (0.594) Cm (7:25-(3:5+42))
cheMSoton
16-Jan-2002 12:52:42
Scan ES+
4.14e5
100
%
0
617.4
618.5
619.5
612.5
595.5
620.5
130.0
151.0
217.0
325.2
496.5
793.4
812.4
1017.6
1097.8
1269.6
1296.7
1387.9
1534.6
1597.2
1893.5
1938.4
200
400
600
800
1000
1200
1400
1600
1800
2000
Da/e

b)

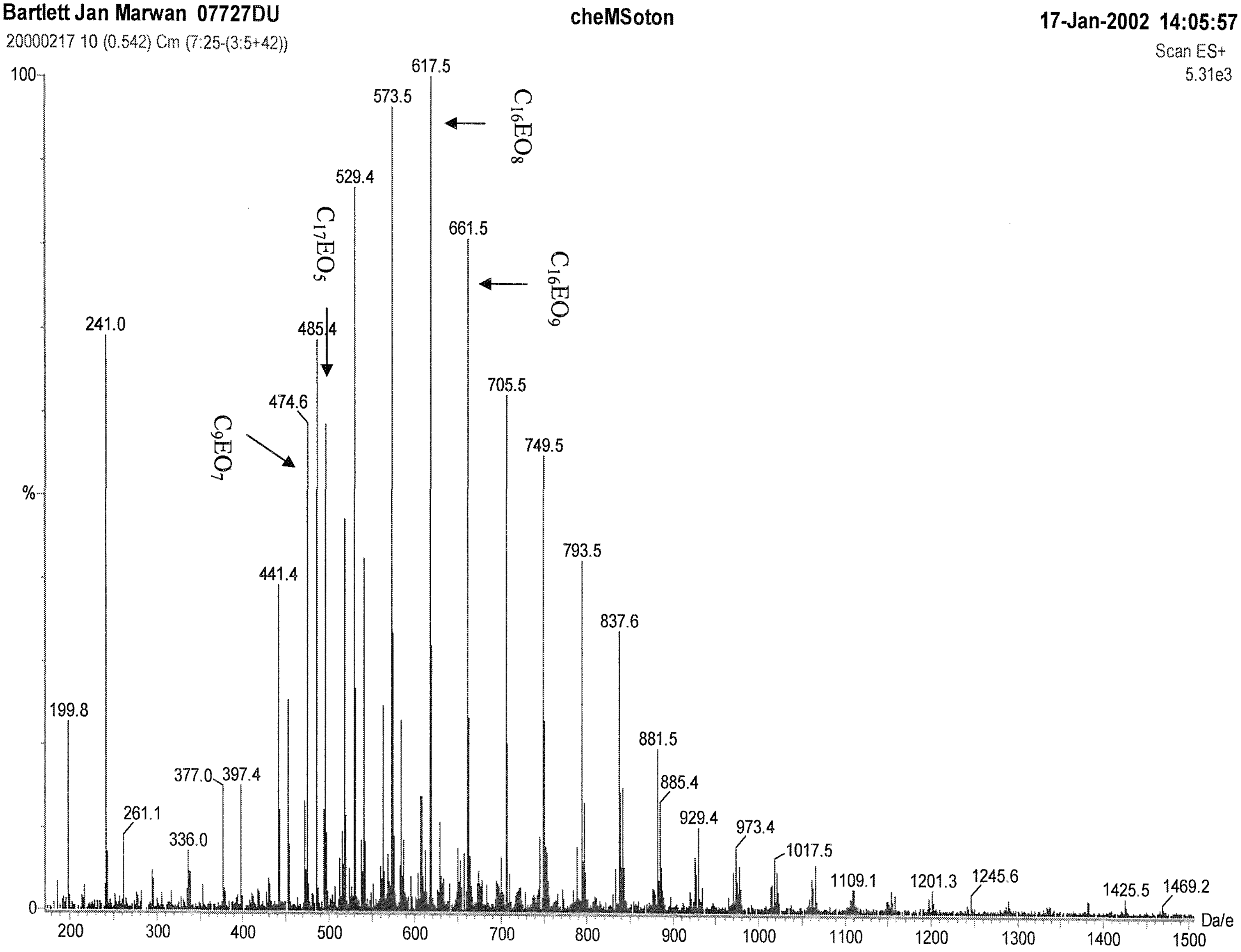
Bartlett Jan Marwan 07727DU
20000217 10 (0.542) Cm (7:25-(3:5+42))
cheMSoton
17-Jan-2002 14:05:57
Scan ES+
5.31e3
100
%
0
$C_{16}EO_8$
$C_{16}EO_9$
$C_{17}EO_5$
C_9EO_7
617.5
573.5
529.4
661.5
241.0
485.4
705.5
474.6
749.5
441.4
793.5
837.6
199.8
881.5
885.4
377.0
397.4
261.1
929.4
973.4
336.0
1017.5
1109.1
1201.3
1245.6
1425.5
1469.2
200
300
400
500
600
700
800
900
1000
1100
1200
1300
1400
1500
Da/e

c)

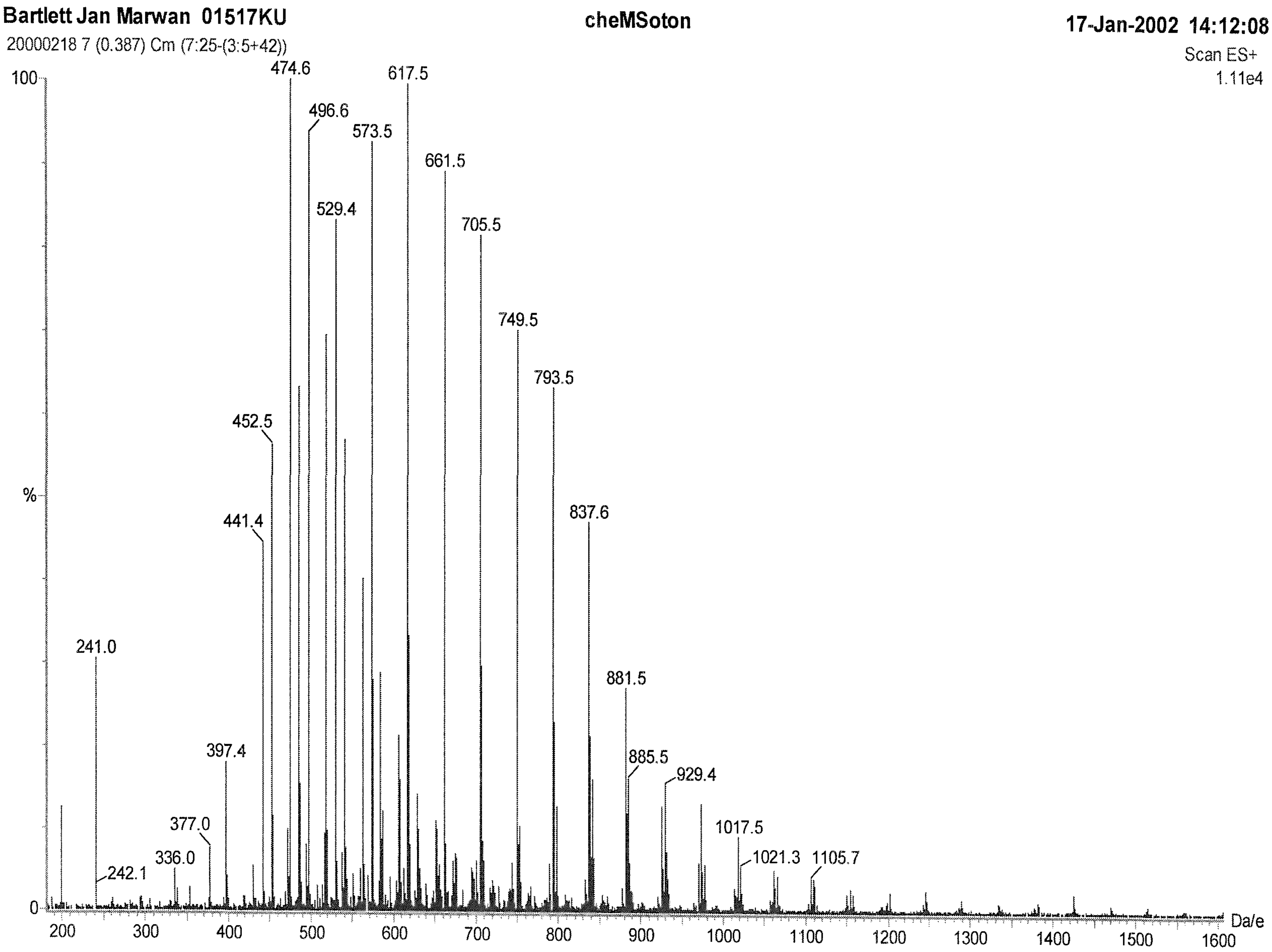
Bartlett Jan Marwan 01517KU
20000218 7 (0.387) Cm (7:25-(3:5+42))
cheMSoton
17-Jan-2002 14:12:08
Scan ES+
1.11e4
100
%
0
474.6
617.5
496.6
573.5
661.5
529.4
705.5
749.5
793.5
452.5
441.4
837.6
241.0
881.5
397.4
885.5
929.4
377.0
1017.5
336.0
1021.3
1105.7
242.1
200
300
400
500
600
700
800
900
1000
1100
1200
1300
1400
1500
1600
Da/e

d)

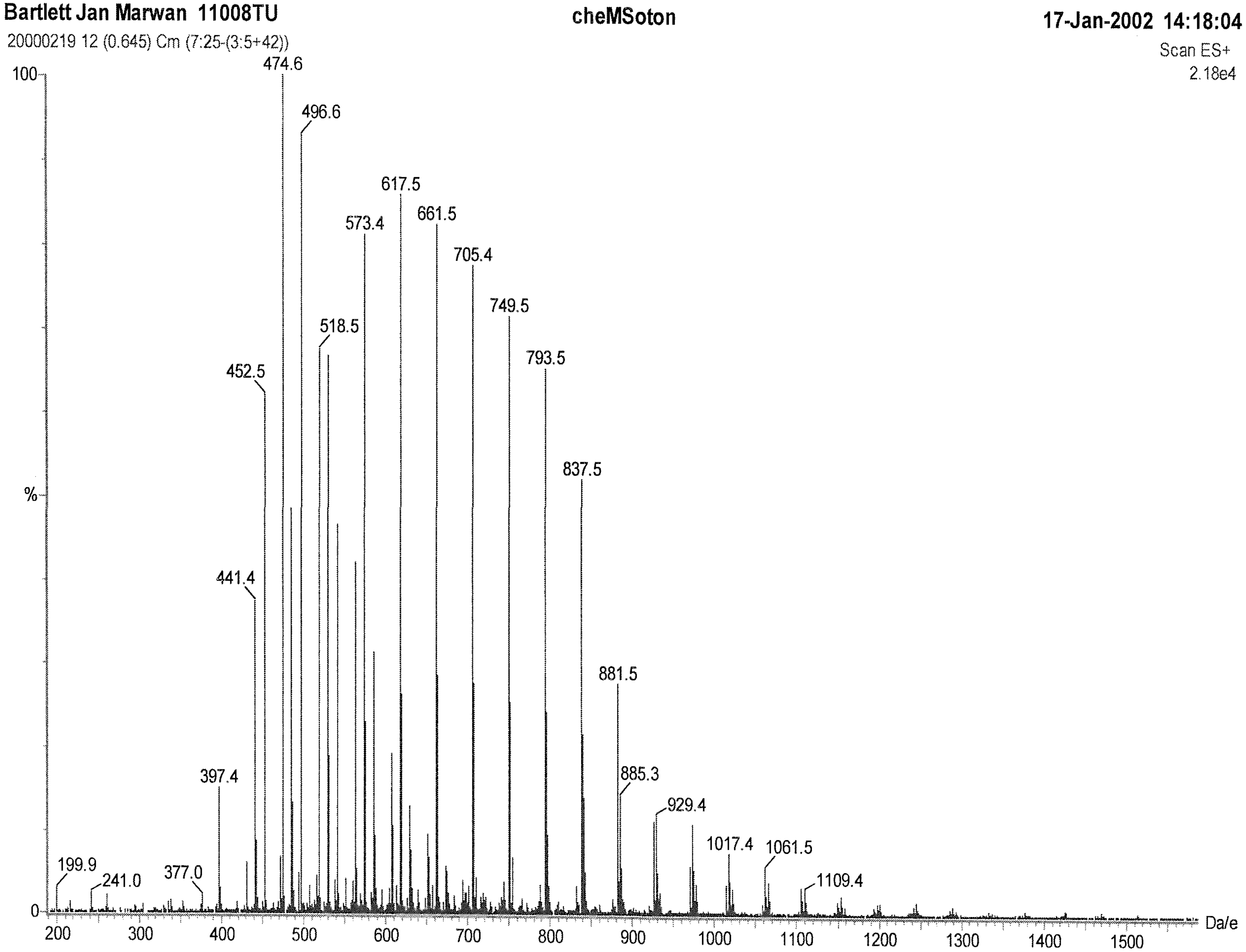
Bartlett Jan Marwan 11008TU
20000219 12 (0.645) Cm (7:25-(3:5+42))
cheMSoton
17-Jan-2002 14:18:04
Scan ES+
2.18e4
100
%
0
474.6
496.6
617.5
573.4
661.5
705.4
749.5
518.5
793.5
452.5
837.5
441.4
881.5
397.4
885.3
929.4
1017.4
1061.5
199.9
241.0
377.0
1109.4
200
300
400
500
600
700
800
900
1000
1100
1200
1300
1400
1500
Da/e

Figure 76: Mass spectrum of $C_{16}EO_8$ a) and 3 different batches of Brij®56 b), c) and d) diluted to 10 µg/ml in methanol.

surfactant	07727DU a)	01517KU b)	11008TU c)
$C_{16}EO_7$	7.7	8.5	7.4
$C_{16}EO_8$	8	9.2	7.7
$C_{16}EO_9$	6.4	8.3	7.5
C_9EO_7	4.6	9.3	9.2
$C_{17}EO_5$	4.8	8.7	8.5

Table 1: The peak intensities in % relative to the total sum of all peak intensities in the spectrum obtained for each surfactant from the mass spectroscopic studies comparing three different batches of Brij®56.

Figure 76 c) shows the mass spectrum for Brij®56 (batch number 01517KU). In comparing batch 01517KU with 07727DU we can note that there is no qualitative difference. Both batches show the same compounds. The difference can be seen quantitatively. The compounds of the highest relative intensity are now C_9EO_7 (474.6 Da/e; 9.3%), $C_{17}EO_5$ (496.6 Da/e; 8.7%), $C_{16}EO_7$ (573.5 Da/e; 8.5%), $C_{16}EO_8$ (617.5 Da/e; 9.2%) and $C_{16}EO_9$ (661.5 Da/e; 8.3%).

The last batch (Figure 76 d) on which we want to focus now is 11008TU. The relative peak intensities to which we did not find any assignment in Figure 76 b) are now too small to be detected. C_9EO_7 is of the highest intensity (9.1%) followed by $C_{17}EO_5$ (8.5%). The intensity of $C_{16}EO_8$ is of 7.7%.

Overall we can conclude that the batches of Brij®56 contain a range of surfactants. Comparing 3 different batches with each other we note quantitative and qualitative deviation. The peak at 241 Da/e, as one example, shows in the mass spectrum of the batch 07727DU a relative intensity of 5.8% which decreases to 2.8% (01517KU) and does not show any intensity in the mass spectrum of batch 11008TU. The relative intensity of C_9EO_7 and $C_{17}EO_5$ increases from 4.6% (4.8%) to 9.3% (8.7%) comparing batch 07727DU with 01517KU. The intensity of $C_{16}EO_8$ varies between 9.2 and 7.7% from batch to batch.

Mass spectroscopic analysis has shown evidently a range of surfactant contained in one batch of Brij®56 and quantitative and qualitative variation of surfactant from batch to batch. This might be responsible for slight variations in the composition between different batches. Measurements using three different batches of material showed essentially the same phase behaviour when mixed with ammonium tetra chloropalladate solutions except that there was variation of ± 2°C in the positions of the hexagonal/cubic and cubic/lamellar phase boundaries.

This behaviour is not to be seen for $C_{16}EO_8$, a highly purified but also very expensive surfactant. After 6 months we run the mass spectroscopic analysis again on the same samples originally used. Despite slight quantitative changes in the relative peak intensities for $C_{16}EO_8$, $C_{16}EO_9$ and C_9EO_7 comparing the same batch we did not find any significant difference from the results seen before.

In the next section we want to give a comprehensive study of the metal deposition from the Pluronic F127 template mixture.

7.3.3 Deposition of Pd from the Pluronic (F 127) template mixture onto the SRL 162g device

7.3.3.a The deposition behaviour

In this section we used for the deposition of palladium onto the gold electrode of the SRL 162g device Pluronic (F 127) as surfactant in the template mixture. In section 1.1.4 we introduced the approach to synthesize periodic mesoporous metals by templating with liquid crystalline phases prepared from ternary systems consisting of amphiphile triblock copolymers such as Pluronic F 127, cosurfactant such as butanol and water [24-28]. The triblock-copolymer alcohol water system exhibits a rich phase behaviour. Phases such as micellar, reverse micellar, cubic, hexagonal and lamellar lyotropic liquid crystalline phases can be obtained by varying the content of the selective solvent, water and butanol. In section 7.3.1 we outlined experiments in which palladium was deposited from the template mixture of the Brij®56 system and we noticed that for a range of devices the time taken for the deposition and the current maximum vary drastically for each deposition under the same experimental conditions.

The experiments also showed that the current did not increase to its maximum value in one step but proceeds to the maximum via successive steps.

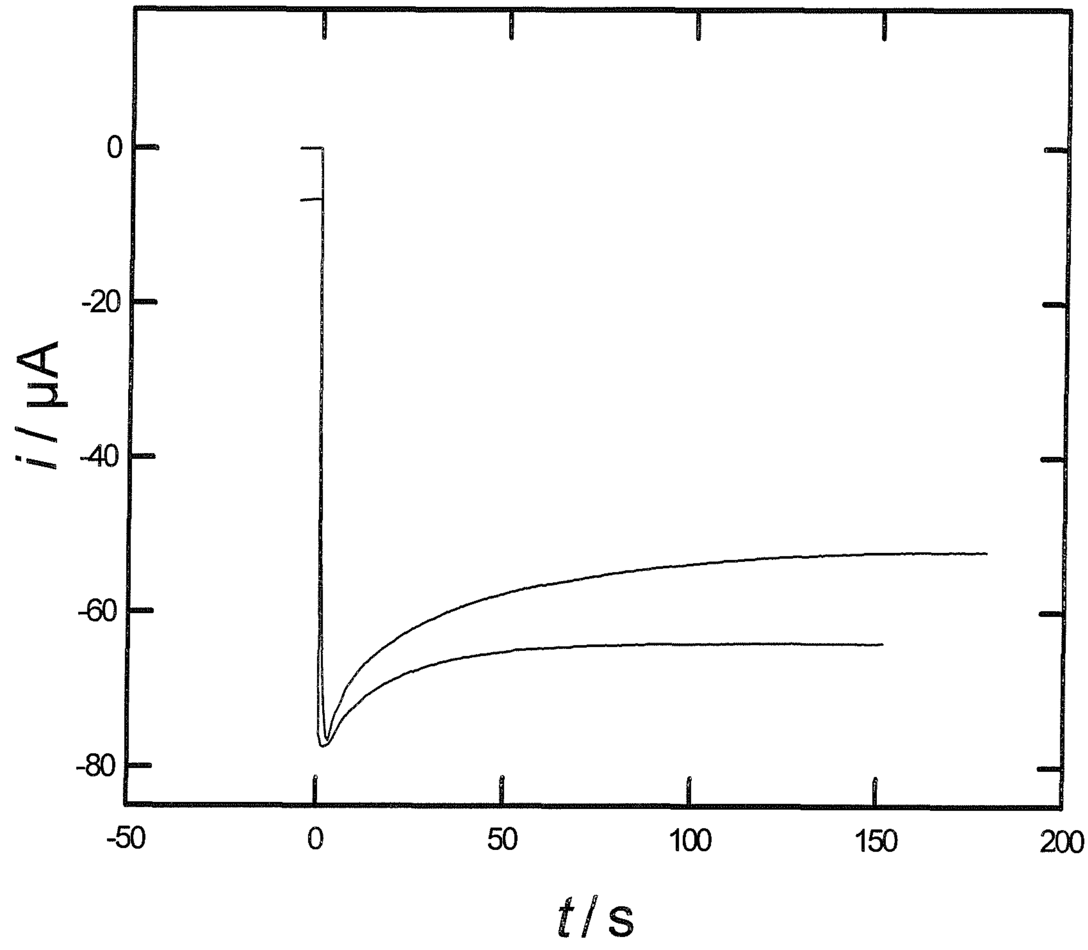

Figure 77: Two current transients vs time under the same experimental conditions for the deposition of Pd with the total deposition charge of 10 mC from the template mixture of the Pluronic F127 system on the gold electrode of the SRL 162g device.

Figure 77 shows two current transients for the deposition of Pd onto the gold electrode of the SRL 162g device from the Pluronic (F 127) template mixture system. A striking difference to the transient obtained in the section 7.3.1 is that here the current jumps straight to the maximum without any proceeding steps. It is also of interest to note that in five replicate experiments the current maxima (two shown here) are reproducible but still differ at longer times. Although with the Pluronic F 127 template mixture it is easier to remove the air bubbles when squashing the mixtures it still requires good handling to get a uniform coverage on the gold electrode of SRL devices. This might explain why there is still a slight difference between the current transients. When Brij®56 was used in the template mixture we found on average non-reproducible current transients in the deposition behaviour. The same behaviour was observed for $C_{16}EO_8$.

Pluronic (F127) and Brij®56 template mixtures differ in their viscosity; it is therefore likely that the irreproducibility in the deposition behaviour is due to the air bubbles embedded in the very high viscous phase of the Brij®56 system. This might hamper the electrical contact between the gold electrode and the Pd dissolved in the aqueous domains of the liquid crystal structure. We thought about an experiment in which the air bubbles might be removed successively by squashing the mixture using two glass slides and increasing the pressure on the glass slides. However, to deposit Pd from the template mixture we must put the mixture on the gold electrode of the device and might be left with air bubbles embedded in the viscous phase. Increasing the pressure perpendicular to the gold surface and therefore to the heater membrane it is likely to cause a breakage of the heater membrane. The replacement of Brij®56 by Pluronic (F127) as the surfactant used in the template mixture leads to a far less viscous phase and this is therefore of crucial importance in terms of the removal of the air bubbles. The template mixture of the Pluronic system only needs to be tightly compressed to remove the air bubbles with a lower probability of breaking down the heater membrane. This was shown in the experiments comparing the behaviour of Brij®56 and Pluronic.

This section showed that the template mixture of the Pluronic(F127) system gives reproducible deposition currents due its lower visosity and is in terms of the practical application a more appropriate surfactant. It has then become of more importance whether the deposition of Pd from the Pluronic mixture onto the SRL devices gives Pd films of high surface area. This will be the focus in the next section.

7.3.3.b Proof of a successful deposition of Pd on the gold electrode of the SRL device from the Pluronic(F127) template mixture with high surface area

Cyclic voltammetric studies in acid solution were used to characterize the electroactive surface area of the Pd films from the charge passed in the surface oxide stripping peak.

Figure 78 shows the cyclic voltammetry of Pd films deposited from the Pluronic template mixture onto the gold electrode of the SRL 162g device in 1 M H_2SO_4 at 200 mV/s. The voltammetry is restricted to the oxide region in the potential range between 0.2 and 1.2 V vs SCE. On the anodic scan at 0.68 V vs SCE the formation of Pd oxide starts giving rise to a well-defined stripping peak on the cathodic sweep at ca. 0.4 V vs SCE. Using the conversion factor of 424 $\mu C/cm^2$ given by Rand and Woods [77] who investigated the surface oxide stripping reaction of Pd in 1 M H_2SO_4, we estimated the specific surface area of 14.5 m^2/g which corresponds to an area per unit volume of 1.7×10^6 cm^2 / cm^3. This value gives a high surface area consistent with a nanostructure and was also found in this range when estimating the surface area after deposition of Pd from the Brij®56 system.

Preliminary studies revealed that the deposition of Pd onto the gold electrode of the low-power micro-pellistor devices from the Pluronic (F127) and the Brij®56 system do not show any significant difference in terms of the surface area determined from the charge passed the oxide stripping peak. The advantageous use of Pluronic as surfactant in the template mixture from which Pd is deposited onto the device has been outlined in the section 7.3.1. We noticed that the probability of breaking the heater membrane is far decreased due to lower viscosity.

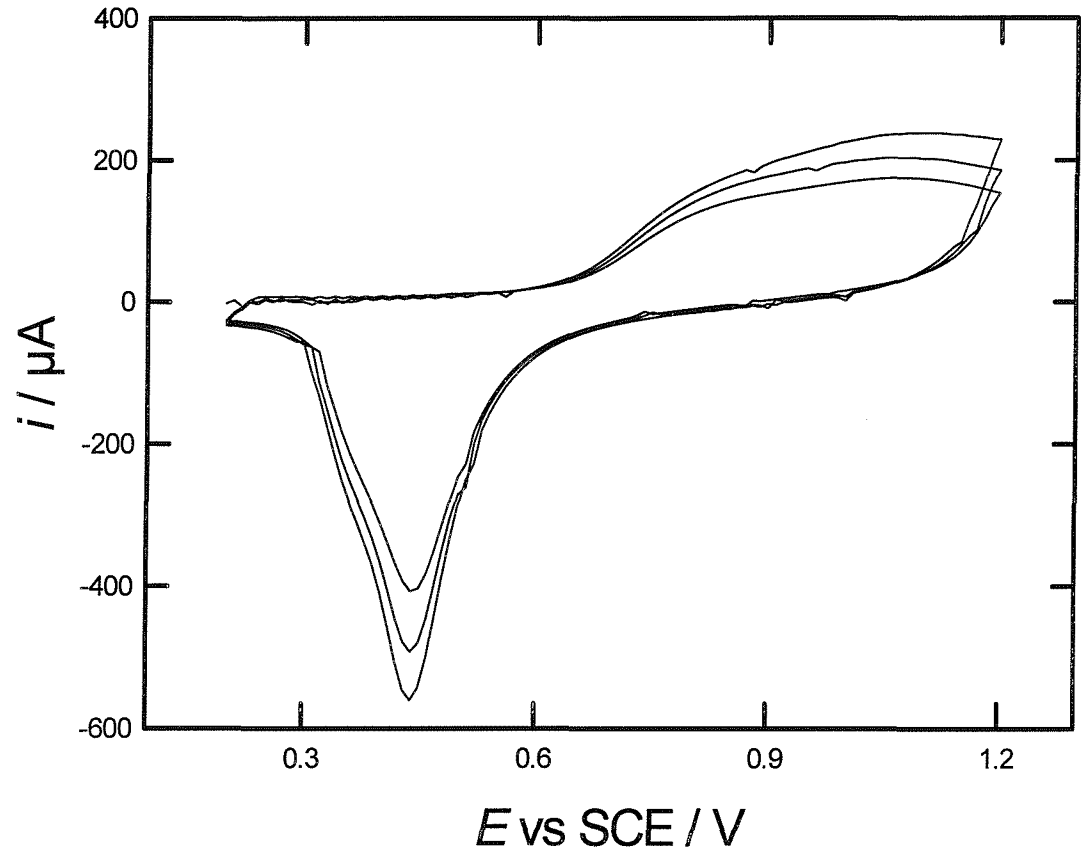

Figure 78: Cyclic voltammogram of H_I*-e Pd in 1 M sulfuric acid at 200 mV/s (total deposition charge 10 mC) deposited onto the gold electrode of the SRL 162g device (0.32* mm^2 *electrode area) from the Pluronic template mixture of 17 wt%* $(NH_4)_2PdCl_4$*, 39.9 wt% water, 29.8 wt% Pluronic F127 and 13.3 wt% 1-butanol at 0.1 V vs SCE The* H_I *-e Pd film was soaked in water overnight prior to the cyclic voltammetry.*

With the electrodeposition of H_I-e metal films (Pd, Pt and Rh) onto SRL devices and the proof of successful achieved deposition of the metal with a high electroactive surface area we have come a significant step towards the fabrication of low power micro pellistors devices in combination with deposited H_I-e metal catalyst layers. The next section describes the types of defects in the device fabrication as one of the apparent problems in our studies.

7.4 Manufacturing defects

Each type of the SRL device manufactured and delivered by Warwick is constructed to give, within the experimental error of 2%, an exact value of the cold resistance. This resistance had to be measured for all devices before and after Pd deposition onto the gold electrode to confirm the reproducibility in device fabrication and to show eventual effects of electroplating on the change in resistance.

Mainly we worked with SRL devices of the type 136a and 162g. The cold resistance is, according to the manufacturer, 180 Ω for 136a and 230 Ω for 162g. From the measurements obtained, we found the experimental error to be in a range of ± 5 Ω. We measured the cold resistance before deposition and found for a few devices (both SRL 136a and 162g) that the value was far below that expected for each type of device. This corresponds mainly to devices prepared from wafer 3. Naturally those devices showing a low cold resistance before metal deposition were not used further. The 136a and 162g devices with cold resistances in the expected range were used for further experiments. After deposition of Pd onto the gold electrode of SRL 136a and 162g devices the cold resistance was measured again. Many devices showed a cold resistance below the expected value. The cold resistance was about 30 to 70 Ω. This very serious problem also occurred in a less drastic way for wafer 4. Further experiments showed that this problem was only restricted to wafers 3 and 4 since we did not note a decrease in the cold resistance using other wafers. The low cold resistance was more pronounced after deposition of the Pd metal onto the gold electrode. This suggests that there may be faults in the processing of these substrates and that the deposition of Pd or other metals might lead to short circuits in the heater track. To investigate this effect further we carried out cyclic voltammetric studies in acid solution for 162g devices on which no catalyst was deposited. We connected the Pt heater of the SRL 162g device as the working electrode. Normally we would not expect to see any feature on the voltammogram but Figure 79 shows in the potential range from 0.3 to 1.2 V in the oxide region features similar to the cyclic voltammogram of platinum. This cyclic voltammetry was carried out prior to depositing H_I-e Pd onto the gold electrode of the SRL devices.

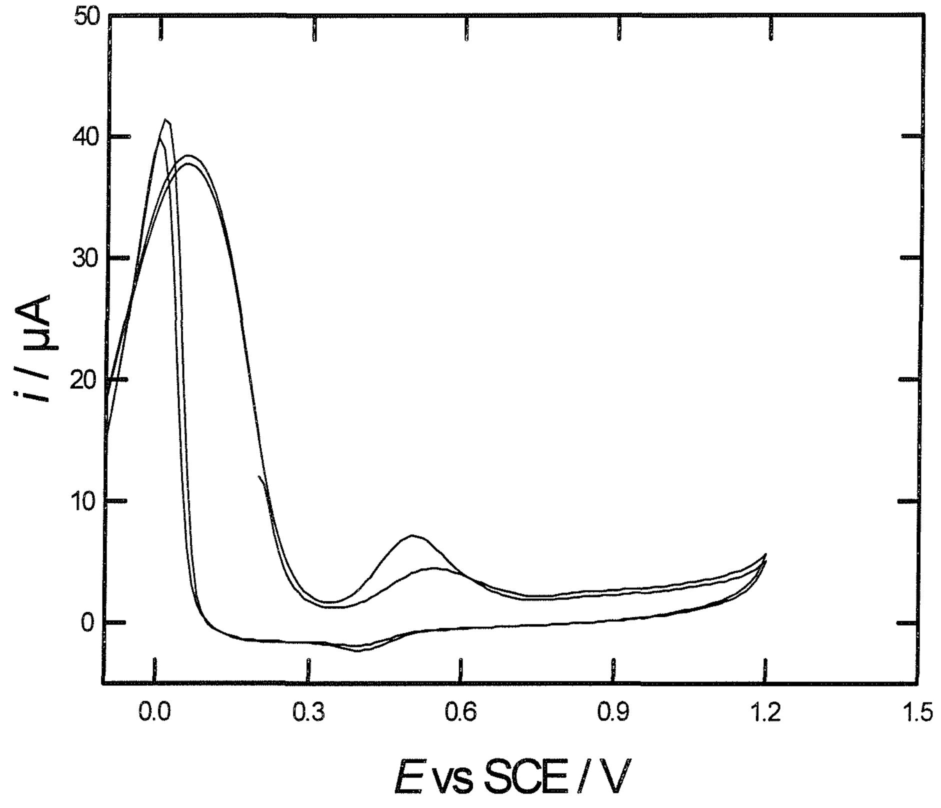

Figure 79: Cyclic voltammogram of the SRL 162g device- wafer 3 - on which no catalyst was deposited at 200 mV/s in 1 M sulfuric acid. The Pt heater has been connected as the working electrode.

We strongly assume the existence of pinholes in the heater track from which then the electrochemical features in the oxide region occur similar to those seen for Pt. The pinholes in the Pt heater track can then be filled with H_I-e Pd deposited onto the SRL device. This should cause a short circuit in the resistance of the Pt heater.

To conclude, we noticed manufacturing defects occurring for wafers 3 and 4. We have to emphasize that this problem only appeared for those wafers. From the cyclic voltammetric studies we concluded the existence of pinholes in the nitride insulation layer. The pinholes filled with deposited Pd cause then short circuit and finally the low value of the heater resistance.

7.5 Methane response on H_1-e metal catalyst layers

The aim of the larger project of which my work is a part is to fabricate planar pellistors based on high surface area metal catalysts deposited on Si micro-hotplate structures to be used for methane detection. This makes use of the nanostructure given by the deposition of Pd catalysts from liquid crystalline media. In the following we want to test the Pd catalysts layers deposited onto the gold of the SRL devices towards methane (linearity and reproducibility of response) at an operating temperature of 550 °C. This is the chosen temperature at which commercial pellistors from City Technology were tested. On heating in air palladium is converted to palladium oxide and it is generally accepted that a mixture of the metal and the oxide must be present for efficient catalysis of methane oxidation [55, 56].

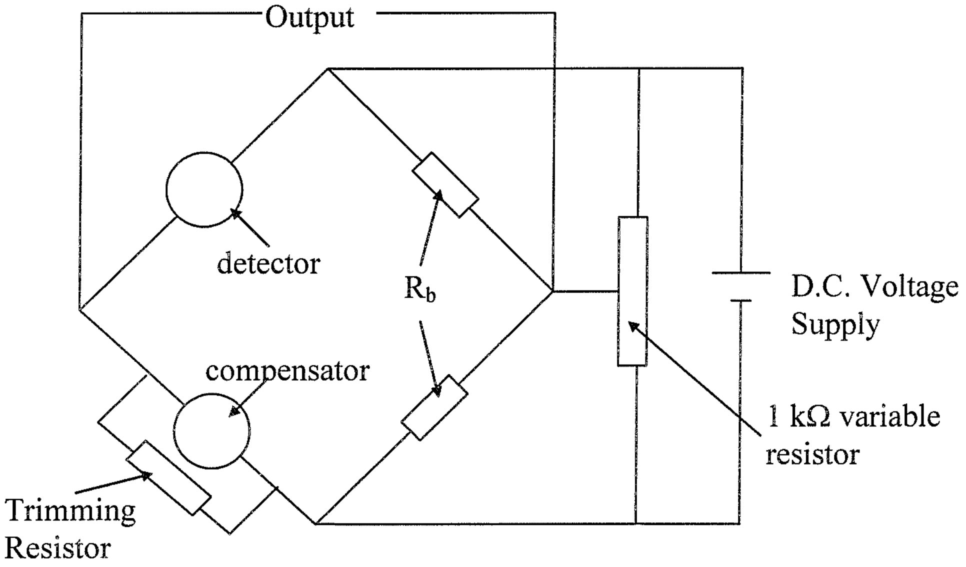

Figure 80: Wheatsone bridge used to measure the concentration of combustible gases in air with SRL devices used in our studies. R_b are resistors whose resistance is variable according to the type of pellistors. The trimming resistor is a variable resistor to set the current across the compensator.

Methane response of planar pellistors was measured in a standard wheatstone bridge circuit (Figure 80). The wheatstone bridge consists precisely of two resistors R_b, a variable resistor with a maximum value of 1 kΩ used to balance the wheatstone bridge, a compensator with a resistance value similar to the resistance of the sensor at its operating temperature and the sensor. A good wheatstone bridge should give maximum output sensitivity for minimum power consumption.

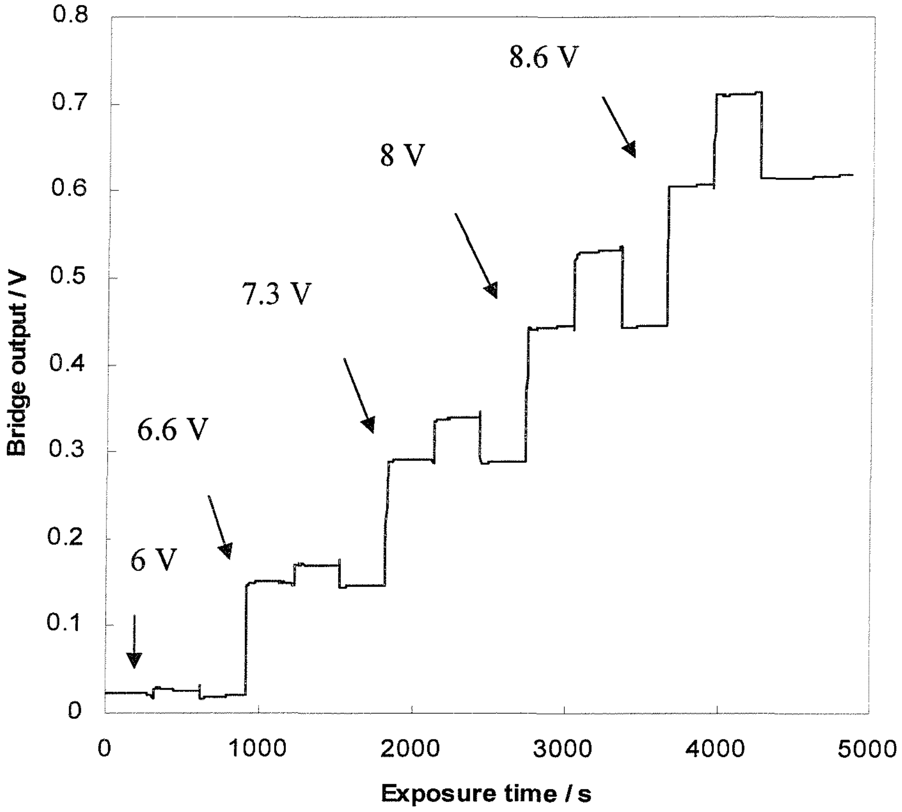

Figure 81: Response of the H_I-e Pd layers exposed to methane. H_I-e Pd was deposited onto SRL 136a device with a total deposition charge of 20 mC. H_I-e Pd was electrochemically cycled in 1 M sulfuric acid to obtain the maximum surface area. The voltage applied across the device was increased from 6; 6.6; 7.3; 8 and 8.6 V following the sequence air / 2.5% methane / air at each voltage. The measurements were carried out by S. Leclerc at City Technology.

Sensitivity of noble metals used as catalytic sensors varies with temperature. So called "volcano curves" can be obtained by recording the output sensitivity of sensors as a function of the operating temperature. To obtain the volcano curve the voltage was varied in a range between 6 and 8.6 V.

We prepared several batches of devices on which H_I-e Pd, H_I-e Rh and H_I-e Pt were deposited and delivered S. Leclerc at City Technology who carried out all the gas-testing measurements. The H_I-e metal layers deposited onto the devices were exposed to methane and in some experiments additionally poisoned by HMDS (Hexamethyldisiloxane).

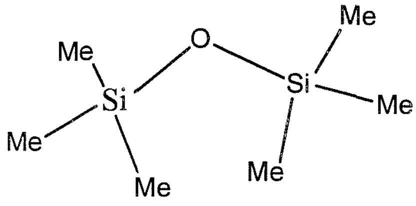

Hexamethyldisiloxane

Figure 81 shows the response of one of these devices when exposed to a sequence air/CH_4/air for 8 minutes at 6, 6.6; 7.3; 8 and 8.6 V. In increasing the voltage applied across the device we note a stepwise increase of the bridge output from 20 mV at an operating voltage of 6 V to finally 570 mV corresponding to an operating voltage of 8.6 V. From the exposure of the H_I-e Pd layers to a mixture of air/methane while increasing the voltage across the device we note at each voltage a slight increase of the response in the bridge output. This is based on the fact that heat is produced with the oxidation of methane to water and carbon dioxide on the Pd surface. As this happens the temperature and hence the resistance of the Pt track embedded in the silicon nitride layer increases as a result of the surrounding exothermic process. This then can be seen in the response behaviour with the increase of the bridge output value so that we can finally attribute this behaviour to the methane response.

We carried out another experiment of the same sort and recorded again the response of H_I-e Pd layers exposed to methane. The volcano plot was obtained by increasing the voltage applied across the device. We changed the experimental conditions in such a way that periodic potential-cycling was not applied to the Pd layers in sulfuric acid after deposition onto SRL devices. It has to be stressed that this potentiodynamic ageing covering the full range of potential from the oxide to the hydrogen region of H_I-e Pd has been carried out in the previous experiments. Figure 82 shows the response to a mixture of air/methane of a device on which H_I-e Pd was deposited with a total deposition charge of 20 mC. The device was exposed to a sequence air/methane/air for 5 minutes at 6; 7.4 and 8.6 V. We note the stepwise increase of the bridge output from 40 mV to 670 mV whilst the operating voltage was increased.

From the results obtained we can clearly see that at each voltage step the response is slightly decreasing when exposing the devices to methane.

In this respect we note a significant difference to the experiment described in Figure 81. The exposure to methane of the H_I-e Pd layers deposited onto SRL devices shows a response at each voltage in opposite directions. In the presence of methane we would expect heat production due to the exothermic reaction on the Pd surface causing an increase in the bridge output. This is not to be seen in the response in Figure 82. We note a cooling effect clearly indicating that the device is responding to methane, but not because of a catalytic combustion effect. We attributed this behaviour to the difference in the thermal conductivity between dry air and 2.5% methane in air.

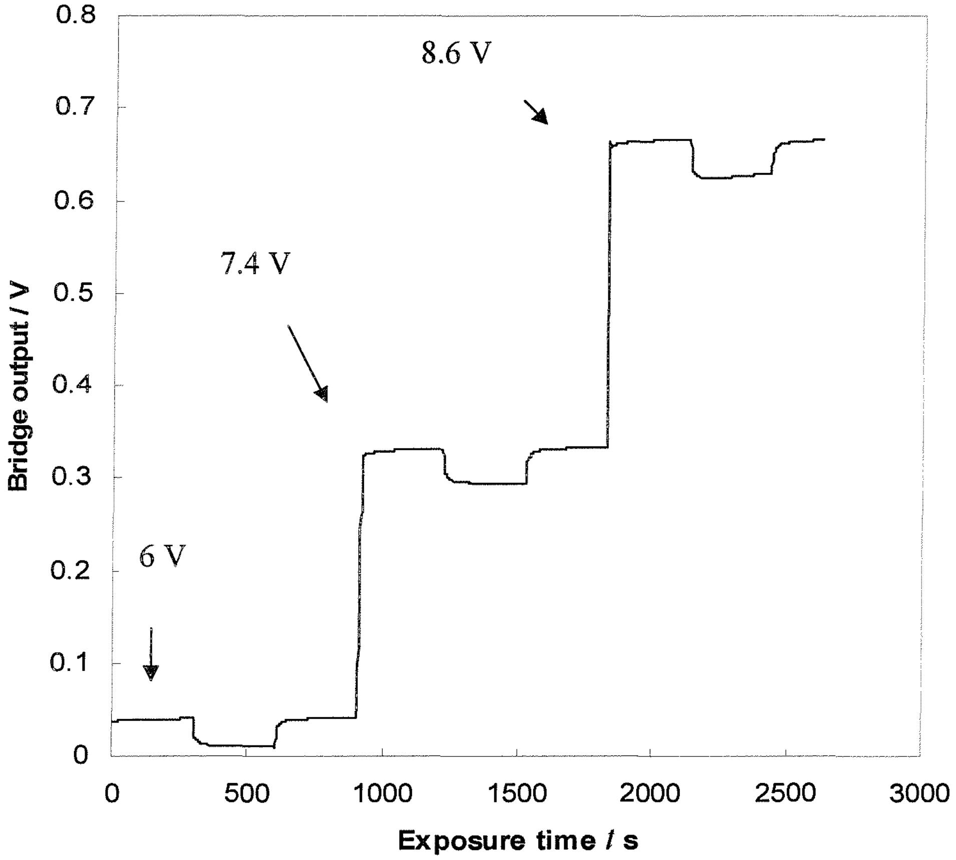

Figure 82: Responses to 2.5% CH_4 for mesoporous Pd deposited onto SRL 136a devices (20 mC total deposition charge). The devices were exposed to a sequence air/CH_4/air for 5 minutes at 6, 7.4 and 8.6V. The measurements were carried out by S. Leclerc at City Technology.

The response of H_I-e Pd to methane with the increase in the bridge output in Figure 81 leads us to believe that the catalytic active surface required to detect methane is only present for the experimental conditions chosen here.

In comparing the experimental procedure we note that the striking difference in preparing the H_I-e Pd films is based on the question whether the potentiodynamic pre treatment was applied. To prepare the H_I-e Pd layers in Figure 81 potentiodynamic pre-treatment was applied after the deposition and prior to the methane exposure. This might be of relevance to obtain the catalytic active Pd surface required for the methane detection.

However, we return to this issue later. As another possibility to approach this problem, we also considered the formation of a Pd-Au alloy when heating the H_I-e Pd layers deposited onto the gold electrode of the SRL device to the operating temperature at which the oxidation of methane occurs. The cyclic voltammetry of the proposed alloy should then convincingly show the anodic shift of the oxide stripping peak of this alloy compared to the Pd oxide stripping peak [86].

Figure 83 shows cyclic voltammograms of H_I-e Pd layers deposited onto the SRL 136a device. The layers were previously exposed to methane and poisoned to HMDS. Comparing a) [0.3 mC charge passed for the deposition of H_I-e Pd] with b) [20 mC charge passed for the deposition of H_I-e Pd] it can be clearly seen that the surface oxide stripping peak occurs for both voltammograms at the same potential; 0.4 V vs SCE. This value is consistent with the peak potential when PdO is stripped from the electrode surface on the cathodic sweep as shown in section 3.5 and outlined in literature [136].

Woods [137] has reported on the investigation of Pd-Au alloy formation. In this report he came to the conclusion that the potential of the Pd oxide stripping peak shifts to increasingly higher potentials with increase in gold content. As a matter of fact in increasing the gold content to a resulting composition of 55% / 45 % (Pd/Au) the Pd oxide stripping peak at 0.80 V vs SHE (0.56 V with respect to SCE) shifts towards the Au oxide stripping peak which occurs at 0.85 V vs SCE.

To determine whether Au-Pd alloy formation was significant in our experimental studies the thickness of the Pd layers deposited onto the gold electrode area was altered from 980 nm (20 mC charge passed for deposition) to 15 nm (0.3 mC charge).

The thickness of the Au layer (150 nm) was kept constant. In case of alloy formation this would have resulted in a dramatic change of the Pd/Au composition towards lower Pd content. However, we did not observe any effect on the position of the oxide stripping peak (Figure 83 – comparing a) with b)). We did not note any shift towards higher anodic potentials.

In case of Pd-Au alloy formation we would expect the surface oxide peak to appear at higher anodic potentials ranging from 0.4 to 0.85 V vs SCE. However, the results provided no evidence for this and we can exclude the alloy formation. We therefore can conclude that there is no alloy formation affecting the response behaviour when H_I-e Pd layers are exposed to methane.

In the next section we return to the potentiodynamic pre-treatment and discuss in detail whether this determines the catalytic activation as crucial experimental step to obtain the active surface required for the methane detection.

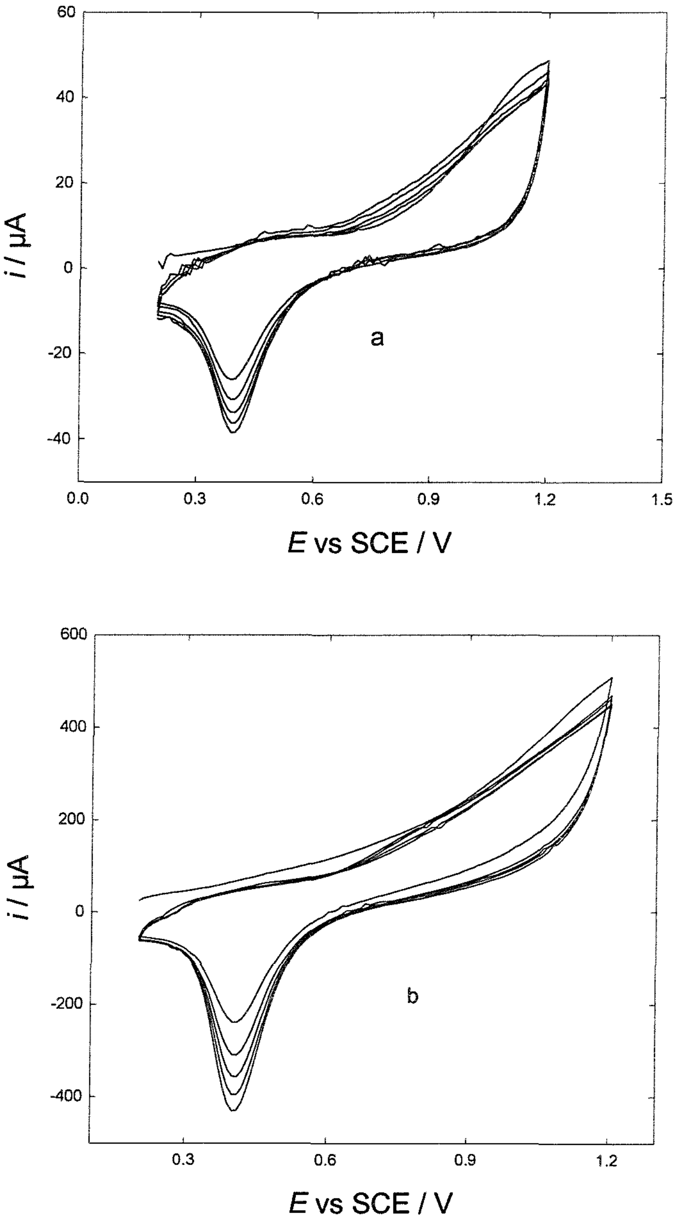

Figure 83: Cyclic voltammograms of Pd catalyst layers (0.3 mC) a) and (20 mC) b) deposited onto the device 136a. It was cycled in 1 M H_2SO_4 at 100 mV/s versus SCE. The catalyst layers were heated in air.

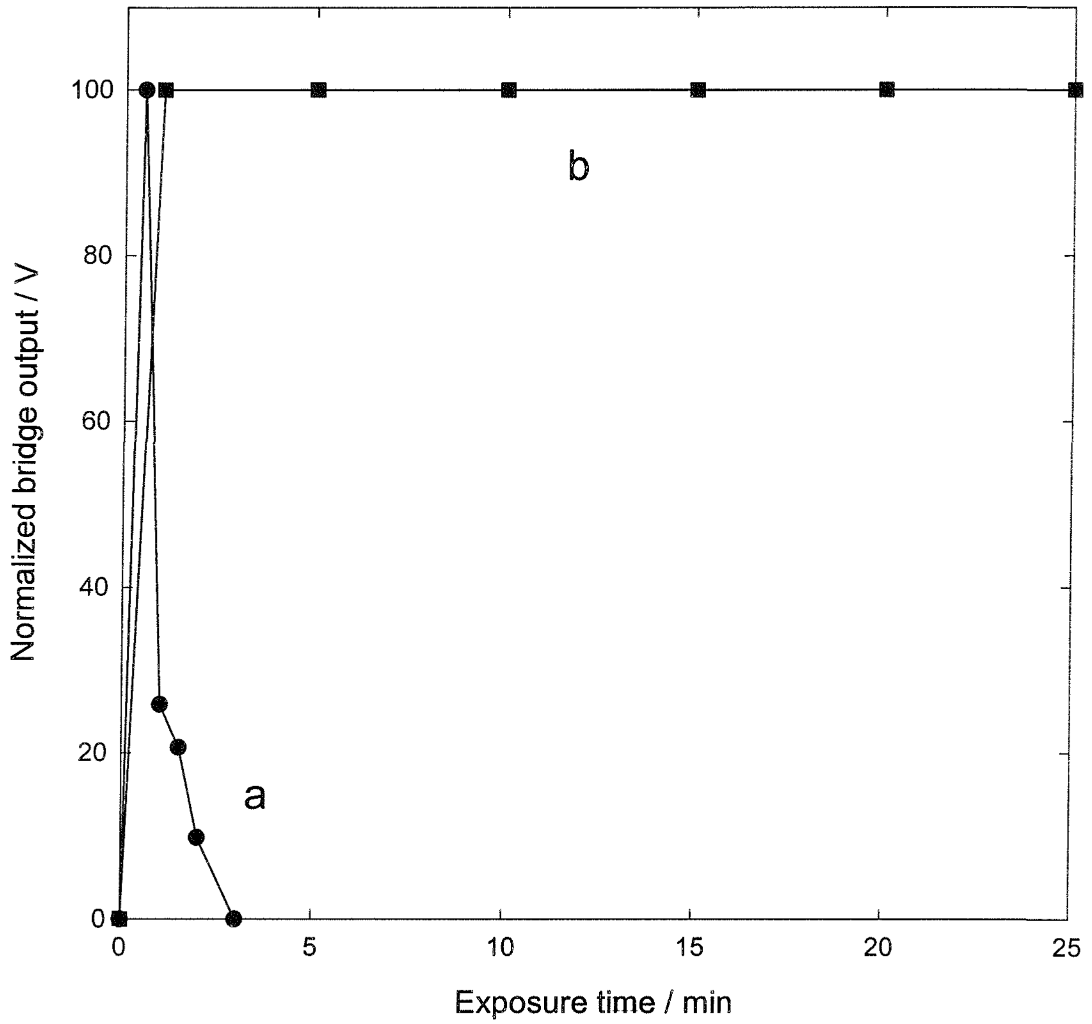

Figure 84: Response of the H_I-e Pd layers deposited onto the SRL 136a devices to 2.5% methane and 5 ppm HMDS (potentiodynamic pre-treatment on H_I-e Pd deposited onto SRL 136a devices in sulphuric acid a) and no pre-treatment b) after the deposition).

Several SRL 136a devices (with or without potentiodynamic pre-treatment in acid after metal deposition), on which H_I-e Pd was deposited, were tested towards HMDS (5 ppm). Hexamethyldisiloxane (HMDS) is the accepted standard vapour used to assess the resistance of pellistors to poisoning [69]. The catalytic active Pd surface can be poisoned by certain species [69, 72]. This is a key limitation of pellistor technology of the catalyst, once the catalytic active surface has been obtained. This fact can be taken into account to show the difference between the catalytic active surface which then can be poisoned and a device showing thermal conductivity.

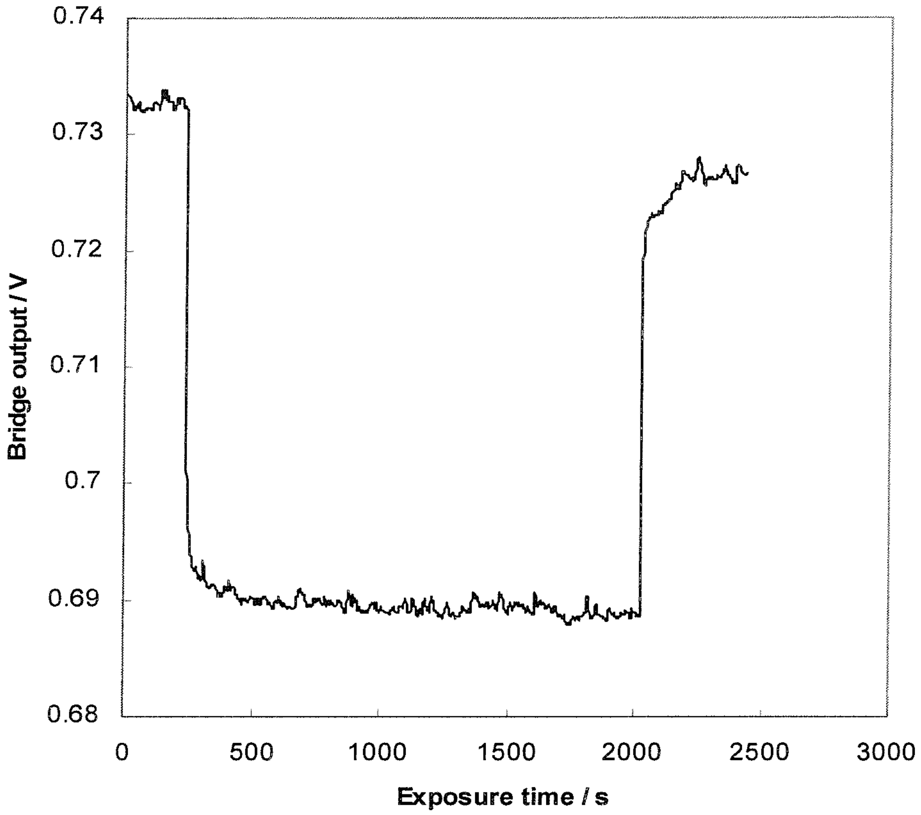

Figure 85: Response of H_I-e Pd deposited onto the SRL 162g device (20 mC total deposition charge) when exposed to 100 ppm HMDS in 2.5% CH_4 at an operating voltage of 8.6V.

Increasing the HMDS concentration further revealed no change in the response to HMDS. The same SRL device on which H_I-e Pd was deposited and previously exposed to 50 and 100 ppm HMDS was used further. Exposure to 500 ppm and 1000 ppm were carried out for the period of time of 3000s. This revealed the same behaviour as outlined before. The results were summarized in Figure 86.

The results in Figure 84 a) show that the pellistor SRL 136a on which H_I-e Pd was deposited (potentiodynamic pretreatment in acid solution after metal deposition) was poisoned very rapidly in the conditions reported. We cannot observe any response to methane of H_I-e Pd after the exposure time of 3 minutes.

On the other hand the results b) show that H_I-e Pd deposited onto the SRL 136a device were not affected by volatile silicon compounds, when the potentiodynamic pre-treatment in acid solution has not been carried out. The response does not show any decrease clearly indicating that the H_I-e Pd surface has not been catalytically activated so that then the poisoning effect cannot be observed. The response which we see for the H_I-e Pd layers not electrochemically cycled in the acid solution is attributable to the thermal conductivity of the gas sample.

Further tests were required to confirm this behaviour of mesoporous Pd deposited onto SRL devices and to show reproducibility for the conditions outlined above. In doing so, we assumed that the difference between the thermal conductivity and the catalytic activity is not affected by the size of the heater membrane so that we could use SRL devices of either type.

SRL 162g devices, on which H_I-e Pd was deposited, were exposed to HMDS as poisoning compound at an operating voltage of 8.6 V. We could not find any loss of signal in the presence of 50 ppm HMDS after an hour exposure at that voltage.

The HMDS concentration was further increased. The same device, on which H_I-e Pd was deposited and previously exposed to 50 ppm HMDS, was used again. Figure 85 shows the response of the device at 8.6V when exposed to 100 ppm HMDS in 2.5% CH_4 for 2000s. As mentioned before in previous experiments we observe for a non-catalytic Pd surface a cooling effect of the device when exposed to methane. Therefore we can not observe any loss in the response.

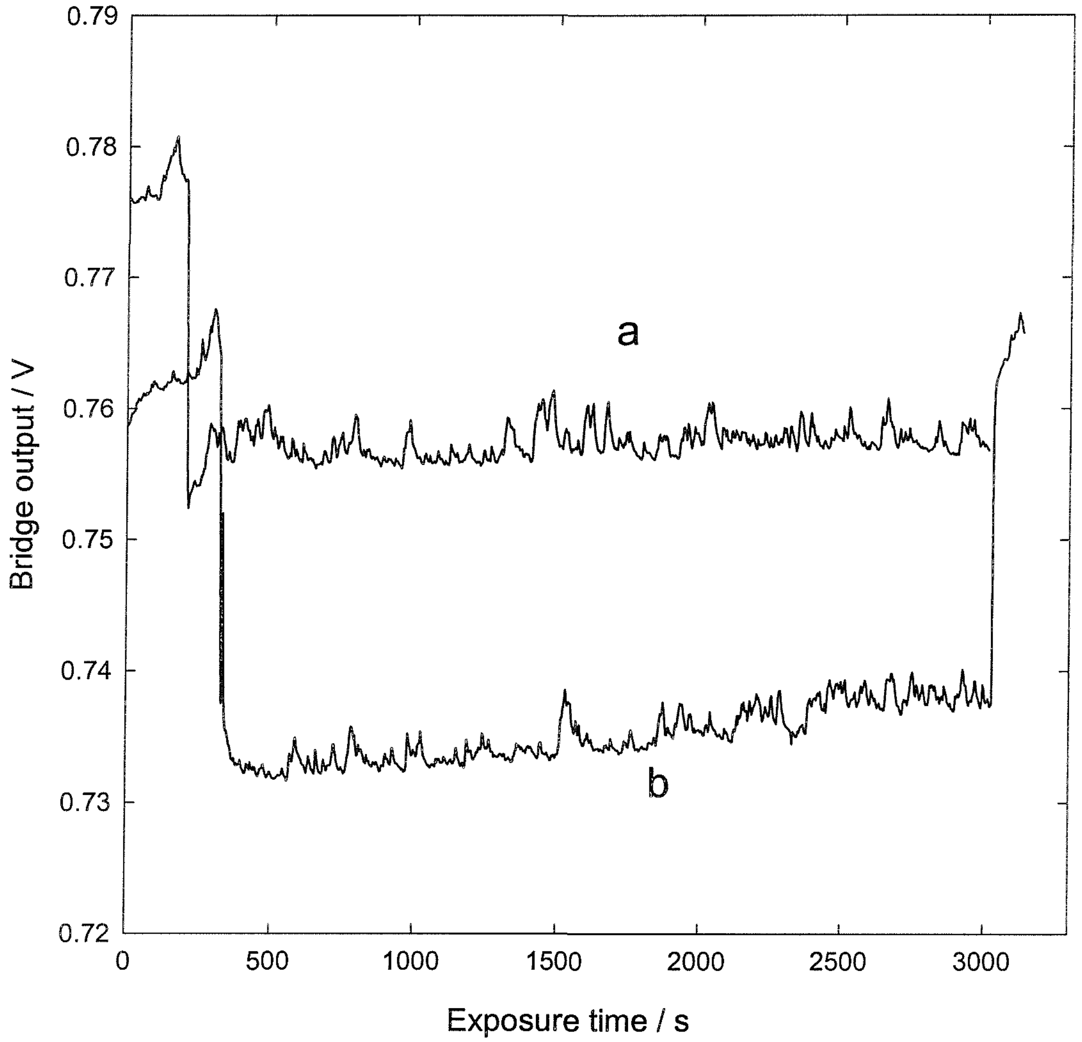

Figure 86: Response of mesoporous Pd (20 mC total deposition charge) deposited on SRL 162g when exposed to 500 ppm a) and 1000 ppm b) HMDS at an operating voltage of 8.6V.

Figure 86 shows the results of this experiment and it is apparent that H_I-e Pd layers deposited onto SRL 162g are not catalytically active in the conditions reported. Therefore the poisoning effect cannot be observed when exposing H_I-e Pd to HMDS. The potentiodynamic pre-treatment is therefore the necessary step in the experimental procedure to obtain the catalytic active surface for the methane response.

Following the results obtained by City Technology showing a response to methane for nanoporous Pd catalyst layers deposited onto SRL 136a and 162g devices after the potentiodynamic ageing in sulphuric acid we were interested to see in which way voltammetric cycling of the Pd catalyst layers in sulfuric acid has a significant impact on the catalytic activation.

One possible explanation we considered refers to the presence of sulphate in the pores of the metal film as a result of cyclic voltammetric measurements in sulphuric acid. We investigated the effect of sulphate on the catalytic activation of freshly prepared devices by carrying out one cyclic voltammetric cycle in sulphuric acid, sweeping the potential from 0.2 V to 1.2 V vs SCE at 100 mV/s. This gives sufficient time for the pores to fill with sulphuric acid. However, when tested at City Technology, we did not observe any response to methane.

Another possible explanation is the potentiodynamic pre-treatment carried out to large extent. It is unclear at this stage whether the surfactant might play an important role in this process. It has not been clarified whether the surfactant must be removed by soaking the H_I-e Pd layers in water before starting the voltammetry to activate the catalytic surface together with the periodic potential-cycling. It is also a problem to know what is causing the degradation of the methane response once the catalytic active surface has been obtained. One way to approach this problem may be given when taking the effect of anodic dissolution supported by EQCM-measurements (Chapter 3) into account. These measurements showed mass loss when nanoporous Pd was cycled anodically in the oxide region. The dissolution of the Pd nanostructure may damage the high surface area required for the detection of methane.

To conclude, H_I-e Pd after periodic potential-cycling in sulphuric acid when exposed to a mixture of air/methane showed an increase in the bridge output at each operating voltage. This response is attributable to the fact that heat production occurred with the oxidation of methane to water and carbon dioxide on the Pd surface. H_I-e Pd layers showed a cooling effect in sulphuric acid if the potentiodynamic pre-treatment had not been carried out.

The difference between the catalytic activity and the thermal conductivity was confirmed by further tests in which the catalytic active surface of H_I-e Pd was shown to be poisoned by HMDS.

7.6 Multideposition process

We showed how to deposit successively nanstructured Pd catalyst layers on Si micro hotplate structures based on high surface area metals. Our aim is to fabricate planar pellistors in large quantities by simultaneous multiple deposition onto devices. For this we would need to scale up the deposition process. To arrange the deposition on multiple devices from the template mixture it will be necessary to establish a new experimental set-up. Considering the low-cost manufacturing deposition process we might switch from Pt to glassy carbon to be used for the counter electrode since carbon is cheaply available. In the following we show the current transient for the deposition of Pd onto the SRL devices when carbon was used as the counter electrode. Our aim is to note any apparent differences to comparable experiments.

Figure 87 shows the current transient for the deposition of Pd from the Brij®56 system with the total deposition charge of 5 mC onto the SRL 162g device. Pt as the original counter electrode was replaced by carbon. The cyclic voltammetry of Pd (not shown here) at 100 mV/s in 1 M H_2SO_4 deposited on gold of the 162g device shows a well-defined peak at 0.45 V vs SCE on the cathodic scan which is consistent with the surface oxide stripping reaction of the formed PdO.

From the charge passed the stripping reaction we estimate the specific surface area of 13.7 m^2/g which corresponds to an area per unit of 1.8×10^6 cm^2/cm^3. This value is consistent with a high surface area.

To get uniform and continuous coverage of H_1-ePd onto the gold electrode surface of the SRL devices we direct our attention towards the problem how to avoid the air bubbles in the template solution which contains Brij®56 as surfactant. This problem was discussed in detail in section 7.3, however it plays an important role in the multideposition process. We consider as one possibility to heat up the template mixture. The other possibility is to replace Brij®56 by Pluronic F 127 when used as the surfactant in the template mixture which gives a less viscous hexagonal phase. Hence the template mixture for the Pluronic system needs to be only slightly squashed to remove the air bubbles after putting the mixture on to the gold electrode of the device.

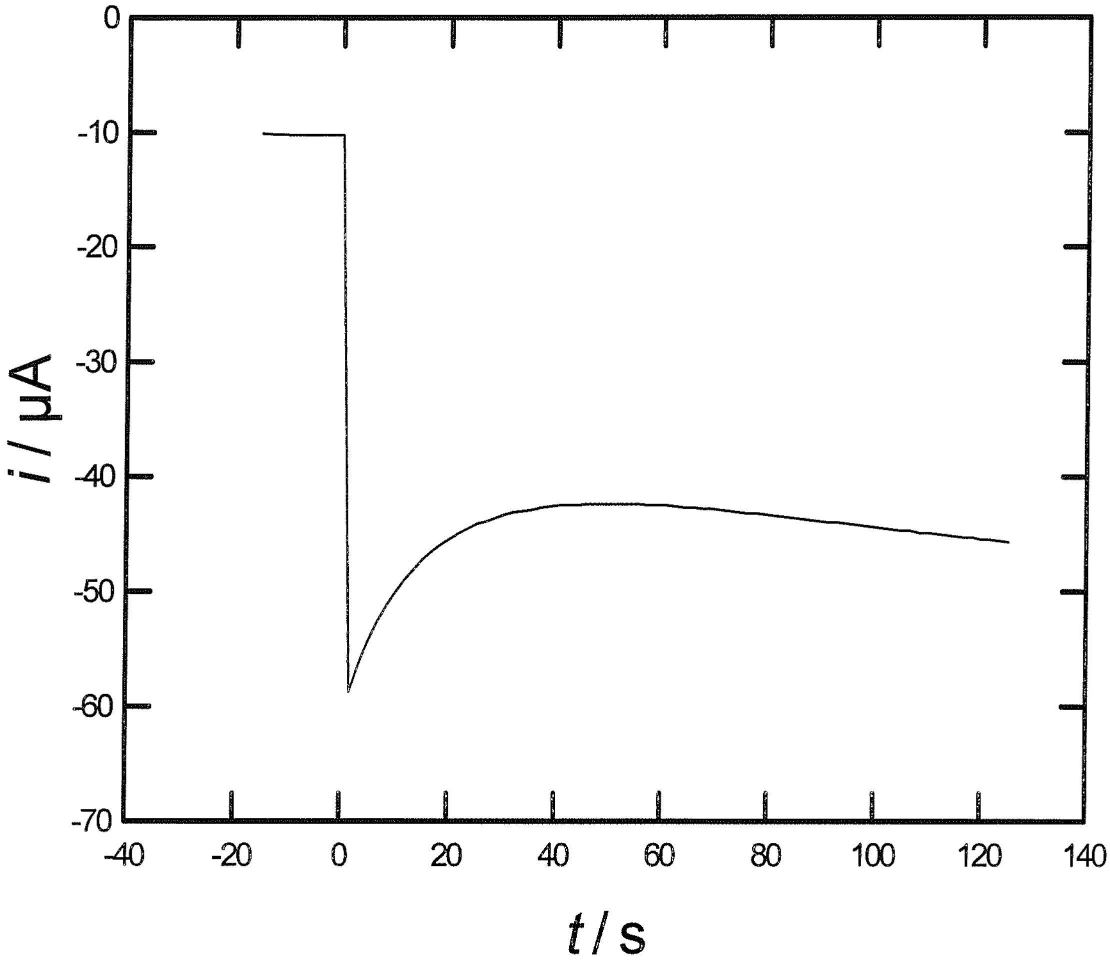

Figure 87: Current transient versus time for the deposition of Pd onto gold (1 mm diameter) with the total deposition charge of 5 mC from the template mixture of Brij$^{®}$*56 system. The Pt electrode was replaced by carbon.*

The likelihood of breaking the heater membrane is reduced. This advantage enhances the use of the Pluronic mixture in the multideposition process.

Since care has to be taken not to break the very fragile heater membrane it is more advantageous to use Pd wire as the reference electrode in contact with the template mixture. The Pd wire with the diameter of 0.5 mm is easier to be handled. This is in contrast to the calomel electrode. We measured the potential difference between the Pd wire and the calomel reference electrode when plated in the deposition mixture and found a value of 0.36 V. We found this value stable and reproducible.

Figure 88 shows the cyclic voltammetry of Pd from the template mixture of the Brij®56 system between the potential limit of -0.2 and 0.3 V at 10 mV/s. Carbon was used as counter electrode and Pd wire (0.5 mm diameter) used as reference electrode. It can be seen from the voltammetry that hardly any current is passed on the cathodic scan until 0.0 V.

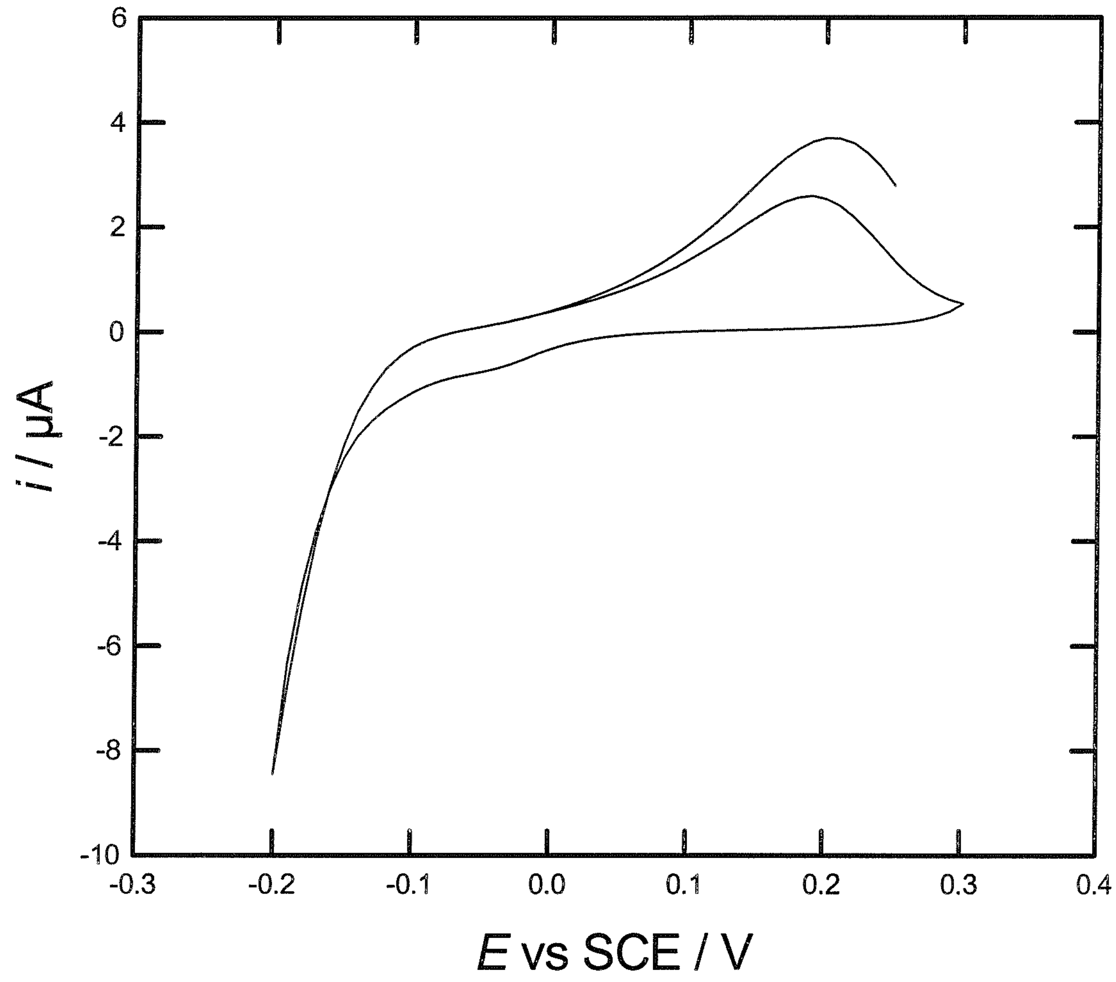

Figure 88: Cyclic voltammogram at 10 mV/s of 1.40 M Pd in the Brij®56 template mixture on the gold electrode of the SRL 162g device. Carbon was used as counter electrode and Pd wire as reference electrode.

The reduction current increases then suddenly at more cathodic potentials. A positive current peak is present in the voltammetry on the anodic scan between 0.0 to 0.3 V which corresponds to the formation of PdO. The cyclic voltammetry of Pd in 1 M sulfuric acid after deposition of Pd onto gold of 162g showed evidence for the stripping peak of PdO with the high electroactive surface area.

To conclude, replacing Pt by carbon used as counter electrode for the deposition of Pd from the template mixture did not show any significant changes in the current transient and voltammetric behaviour. The potential difference between the Pd wire and the calomel electrode was found to be 0.36 V. The cyclic voltammetry after deposition of Pd on gold of the SRL device, when Pd wire as the reference and carbon as a counter electrode were used, revealed the stripping peak with high surface area. The outlined issues will help in defining the new experimental set-up and to get low-cost producing multideposition of H_I-ePd on to microhotplate structure of the devices.

7.7 Conclusion

With the aim to fabricate planar pellistors based on high surface area metal catalysts we first paid attention to the electrochemical characterization of the devices. We found out that cyclic voltammetry of the gold electrodes of 136a, 162g, 177c, 180c and 181c devices showed voltammetric features similar to those seen in the literature [136] occurring at the same peak potential. We estimated the electroactive surface area and the roughness factor for each device: SRL 136a (0.15 cm^2, 15), SRL 162g (0.045 cm^2, 13.9), SRL 177c (0.036 cm^2, 22.5), SRL 180c (0.034 cm^2, 21.3), 181c (0.010 cm^2, 25). For the 176c device we found in the cyclic voltammetry slight distortion in the oxide region.

The next step forward to manufacture pellistors based on metal catalysts of high surface area was the deposition of H_I-e metals from the template mixture. The deposition from the Brij$^®$56 templating bath revealed irreproducible deposition current transients. In addition, we found out by SEM that using Brij$^®$56 as a component in the template mixture gives a rough surface for the H_I-e Pd which was deposited onto evaporated gold on glass. This was not the case when using $C_{16}EO_8$ as surfactant in the template mixture. The mass spectroscopic analysis of Brij®56 showed surfactants with a qualitative and quantitative variation from batch to batch. As shown in the mass spectroscopic study, this was in contrast to $C_{16}EO_8$ a highly purified but also expensive surfactant. It is of more advantage to use a commercial cheaply available surfactant such as Pluronic F127 which in addition gives as surfactant used in the template mixture a far less viscous phase and therefore diminishes the probability of breaking the heater membrane when squashing the template mixture onto the gold electrode of the SRL devices in attempting to get uniform metal deposition on the gold surface.

The change from the Brij®56 to the Pluronic templating system has become of crucial importance and it has then become of relevance to carry out preliminary studies of the deposition behaviour. We showed reproducibility in deposition current transients and the successful deposition of Pd onto the gold electrode of the SRL devices with a high electroactive surface area.

We found defects in the device fabrication occurring for devices manufactured from wafers 3 and 4. We clearly revealed the decrease in cold resistance after metal deposition. This together with cyclic voltammetric studies on the SRL device connecting the Pt heater as the working electrode indicated pinholes in the nitride insulation layer.

After deposition of the metal catalyst layers onto the gold electrode of the SRL devices we tested then these devices towards methane. From the results obtained we found that the potentiodynamic pre-treatment is a necessary step to obtain the catalytic active surface required for the methane detection. The H_I-e Pd layers were then responding to methane. If we did not apply potentiodynamic pre-treatment we observed here a cooling effect attributable to the difference in the thermal conductivity between dry air and 2.5% methane in air. The difference between the catalytic activity and thermal conductivity was confirmed by further tests in which the catalytic active surface of H_I-e Pd was shown to be poisoned by HMDS.

With the aim to fabricate the planar pellistors in a multideposition strip we focused on the problem how to scale up the deposition process. Considering the low-cost producing deposition process we discussed a few issues (change from Pt to carbon as counter electrode and from calomel to Pd wire as reference electrode) in defining the experimental set-up.

Chapter 8 Conclusions and Future work

8.1 Conclusions

In the course of our research we have shown that we can prepare nanostructured H_I-e metal films (Pd, Pt and Rh) by electrochemical deposition from the liquid crystalline phases of either $C_{16}EO_8$ or Brij®56. In order to visualize the nanoarchitecture of these films it was necessary to use TEM. TEM studies of the Pd films deposited from the template mixture of $C_{16}EO_8$ indicated the hexagonal arrangement on a nanoscale. The pores of the structure have a pore size diameter of (25 ± 2) Å and wall thickness of (25 ± 2) Å. In case of Rh films the TEM image clearly showed the regular hexagonal arrangement of uniform pores running through the metal. From the TEM we estimated the pore size diameter of about (35 ± 2) Å and the pore wall thickness of (25 ± 2) Å. Clear evidence for the regular pore distribution was given by XRD-measurements. This was shown for Pd and Rh films with a d-spacing of the porous structure of 55 Å and 49 Å respectively. By using SEM nanostructured Pd and Rh films deposited onto the gold substrates were shown to be dense, uniform and continuous.

Electrochemical studies revealed that the H_I-e metal films have a high electroactive surface area. This was shown for the H_I-e Pd films with the specific surface area of the order of 91 m^2/g and for H_I-e Rh films with 32 m^2/g. These values, together with the TEM and X-ray data, were found to be consistent with the nanostructure and showed that the pores throughout the whole film are accessible by the electrolyte solution.

We noticed from our cyclic voltammetric studies that to get stable voltammetry right from the first cycle requires a prolonged washing of the metal films in water of at least one hour to remove the surfactant from the pores, and it takes more time for the removal of all surfactant from the pores for films with increase in thickness as the pores become longer.

Cyclic voltammetric measurements of Pd metal films deposited from the aqueous solution showed that the charge passed for the formation and stripping of the surface oxide layer reached smaller values than for H_I-e Pd. We also found the hydrogen region of H_I-e Pd in the cyclic voltammetry in 1 M H_2SO_4 more clearly resolved than of plain Pd. As a result of the very high surface to volume ratio of H_I-e Pd films we could distinguish between the formation of adsorption and absorption processes. With the use of crystal violet, as an appropriate surface modification, we were able to knock out the H-adsorption on the Pd surface completely. With the remaining peaks in the hydrogen region associated to the α and β hydride phases we studied in detail the absorption process and focused on the characteristics of the phase transition. The fast kinetics for the formation of α and β hydride phases was responsible for clearly resolved peaks in the absorption region and a sharper rise in the H/Pd ratio compared to that reported by Czerwinski et al. [50].

We investigated the permeation of hydrogen into the Pd metal lattice when the surface sites were blocked by either crystal violet or Pt. We noticed in the voltammetry a clear shift in the peak potential and increasingly sharper peaks in the presence of crystal violet added to the acid solution. This behaviour was also shown in the cyclic voltammetry of H_I-e Pd metal films on which H_I-e Pt was electrochemically deposited. To explain these results we assume that the hydrogen absorption process takes place without passing through the adsorbed state so that hydrogen diffuses directly into Pd bulk. This process speeds up when the formation of adsorbed hydrogen is suppressed by the coverage of poisons. We provided the reader with evidence that the H-adsorption on the Pd surface disappears with increasing the coverage of Pt. This was also shown on H_I-e Pd electrodes in acid solution to which an increasing amount of crystal violet was added.

The electrochemical deposition of Pd as high surface area metal with regular, controlled nanostructure is of potential application as catalyst for methane oxidation in gas sensors. With the aim of fabricating planar pellistors we paid attention to the deposition of H_I-e Pd from the template mixture onto the gold electrodes of the SRL 136a and 162g devices. We found irreproducible current transients when the deposition occurred from either the Brij®56 or the $C_{16}EO_8$ template system. We attribute this behaviour to the use of the Brij®56 template mixture which gives a highly viscous phase. This contrasts to the Pluronic F127 used as surfactant in the template mixture which gives a far less viscous phase for which the probability of breaking the heater membrane is reduced when squashing the template mixture onto the gold electrode of the SRL devices. It was necessary to carry out preliminary studies of the deposition behaviour when using Pluronic F127. We showed reproducibility in deposition currents and the successful deposition of Pd onto the gold electrodes of the SRL devices with a high electroactive surface area. We then tested the devices on which H_1-e Pd was deposited towards methane and found that the potentiodynamic pre-treatment in sulfuric acid was necessary to obtain the catalytically active surface required for methane detection. If we did not apply potentiodynamic pre-treatment we observed a cooling effect attributable to the thermal conductivity between dry air and 2.5% methane in air. The difference between the response of the catalytically active surface and the thermal conductivity response was confirmed by further tests in which the catalytically active surface of H_1-e Pd was shown to be poisoned by HMDS.

Our electrochemical studies of H_1-e Rh films revealed that the surface oxide stripping peak on the cathodic scan moves towards positive potentials on periodic potential-cycling. We attribute this behaviour to changes in the surface oxide states. The hydrogen region was also found to be affected by the potentiodynamic pre-treatment so that the peaks became better resolved on increasing the number of voltammetric cycles. The hydrogen region of H_1-e Rh films revealed one peak attributable to the adsorption of hydrogen onto the H_1-e Rh surface.

We used the H_1-e Rh film electrode for the electroreduction of nitrate in alkaline media as the pH conveniently chosen for our studies and found that with the use of H_1-e Rh electrodes we obtained greater sensitivities compared to Rh deposited from the aqueous solution. The H_1-e Rh film was also found to be the better catalyst compared to H_1-e Pd and H_1-e Pt.

Using the approach to the deposition of H_1-e metal films we deposited one H_1-e metal on top of the other from a plating mixture containing the same surfactant. We have chosen here H_1-e Pd and H_1-e Rh for which the surface oxide stripping peaks occur at well-separated potentials. Cyclic voltammetric measurements showed that within the whole film even within the lower H_1-e metal film the pores remain accessible and that the electroactive surface area of the inner layer does not change as the outer layer is made thicker.

In another experiment the surfactant were removed from the pores of the bilayer structure with successive voltammetric cycles and we have shown that the surface of the outer metal layer becomes electroactive first followed by the surface of the inner layer. From the results obtained we concluded that the pores in the outer and inner layers of the H_1-e metal film are continuous through the final film.

Nanostructured H_I-e metal films offer the opportunity to produce high surface area films which can be used as catalysts.

One of the catalytic applications for H_I-e Pd was found in the methane oxidation in gas-sensors. However, in the course of our research we had to come to the conclusion that there is still some way to go for the fabrication of planar pellistors with H_I-e Pd as catalytic material used for the methane detection. The catalytic active surface required to obtain a methane response can only be achieved by periodic potential-cycling. However, on increasing the number of voltammetric cycles dissolution of PdO in acid solution occurs which could perturb the nanostructure. Further research on this issue is required.

Based on the high surface area, H_I-e Pd can also be used as catalytic material in the hydrogenation of organic molecules.

With the use of nanostructured Pd thin walls the H-absorption process is not diffusion limited so that the permeation of hydrogen into Pd bulk occurs very fast. This process speeds up in the presence of poisons blocking the Pd surface sites. This issue could be important in the application for nanostructured alloy systems to store hydrogen very quickly.

The electrochemical deposition of one nanostructured layer on top of the other offers the opportunity to produce nanostructured multilayers with a thin insulating outer metal layer on top.

References

1. G. S. Attard, J. C. Glyde, and C. G. Goeltner, Nature 378:366 (1995).
2. G. S. Attard, C. G. Goeltner, J. M. Corker, S. Henke, and R. H. Templer, Angew. Chem. Int. Ed. Engl. 36:1315 (1997).
3. G. E. Engelmann, J. C. Ziegler, and D. M. Kolb, Surf. Sci. 401:L420 (1998).
4. N. K. Raman, M. T. Anderson, and C. J. Brinker, Chem. Mater. 8:1682 (1996).
5. M. E. Davis, Nature 364:391 (1993).
6. G. E. Engelmann, J. C. Ziegler, and D. M. Kolb, J. Electrochem. Soc. 145:L33 (1998).
7. P. J. Collins, Liquid Crystals; Princeton University Press; Princeton, NJ (1990).
8. N. R. B. Coleman, PhD thesis, University of Southampton (1999).
9. M. E. Raimondi and J. M. Seddon, Liquid Crystals 26:305 (1999).
10. S. Guerin, Thesis, Southampton University, Department of Chemistry (1999).
11. D. J. Mitchell, G. J. T. Tiddy, L. Waring, T. Bostock, and M. P. M. Donald, J. Chem. Soc. Faraday Trans. I 79:975 (1983).
12. C. T. Kresge, M. E. Leonowicz, W. J. Roth, J. C. Vartuli, and J. S. Beck, Nature 359:710 (1992).
13. J. S. Beck, J. C. Vartuli, W. J. Roth, M. E. Leonowicz, C. T. Kresge, K. D. Schmitt, C. T.-W. Chu, D. H. Olson, E. W. Sheppard, S. B. McCullen, J. B. Higgins, and J. L. Schlenker, J. Am. Chem. Soc. 114:10834 (1992).
14. D. H. Park, C.-F. Cheng, and J. Klinowski, J. Mater. Chem. 7:159 (1997).
15. J. C. Vartuli, C. T. Kresge, M. E. Leonowicz, C. T.-W. Chu, S. B. McCullen, I. D. Johnson, and E. W. Sheppard, Chem. Mater. 6:2070 (1994).
16. C.-Y. Chen, S. L. Burkett, H.-X. Li, and M. E. Davis, Microporous Mater. 2:27 (1993).

17. A. Firouzi, F. Atef, A. G. Oertli, G. D. Stucky, and B. F. Chmelka, J. Am. Chem. Soc. 119:3596 (1997).
18. C.-F. Cheng, Z. Luan, and J. Klinowski, Langmuir 11:2815 (1995).
19. Q. Huo, D. I. Margolese, and G. D. Stucky, Chem. Mater. 8:1147 (1996).
20. A. Steel, S. W. Carr, and M. W. Anderson, J. Chem. Soc., Chem. Commun.:1571 (1994).
21. F. Schueth, Chem. Mater. 13:3184 (2001).
22. G. S. Attard, P. N. Bartlett, N. R. B. Coleman, J. M. Elliott, J. R. Owen, and J. H. Wang, Science 278:838 (1997).
23. G. S. Attard, P. N. Bartlett, R. B. Coleman, J. M. Elliott, and J. R. Owen, Langmuir 14:7340 (1998).
24. P. Kipkemboi, A. Fogden, V. Alfredsson, and K. Flodstroem, Langmuir 17:5398 (2001).
25. P. Holmqvist, P. Alexandridis, and B. Lindman, Langmuir 13:2471 (1997).
26. P. Feng, X. Bu, and D. J. Pine, Langmuir 16:5304 (2000).
27. B. Corp., Pluronic and Tetronic Block Copolymer Surfactants (1989).
28. R. Ivanova, B. Lindman, and A. Paschalis, Langmuir 16:9058 (2000).
29. J. M. Elliott and J. R. Owen, Phys. Chem. Chem. Phys. 2:5653 (2000).
30. P. R. Birkin, J. M. Elliott, and Y. E. Watson, Chem. Commun. 2000:1693 (2000).
31. S. A. G. Evans, J. M. Elliott, L. M. Andrews, P. N. Bartlett, P. J. Doyle, and G. Denault, Anal. Chem. 74:1322 (2002).
32. J. M. Elliott, P. R. Birkin, P. N. Bartlett, and G. S. Attard, Langmuir 15:7411 (1999).
33. P. N. Bartlett, P. R. Birkin, M. A. Ghanem, P. de Groot, and M. Sawicki, J. Electrochem. Soc. 148:C119 (2001).
34. A. H. Whitehead, J. M. Elliott, and J. R. Owen, J. Power Sources 81-82:33 (1999).
35. A. H. Whitehead, J. M. Elliott, J. R. Owen, and G. S. Attard, Chem. Commun.:331 (1999).

36. P. A. Nelson, J. M. Elliott, G. S. Attard, and J. R. Owen, Chem. Mater 14:524 (2002).
37. S. Guerin and G. S. Attard, Electrochem. Commun. 3:544 (2001).
38. G. S. Attard, S. A. A. Leclerc, S. Maniguet, A. E. Russell, I. Nandhakumar, B. R. Gollas, and P. N. Bartlett, Micro. Meso. Mat. 44-45:159 (2001).
39. I. Nandhakumar, J. M. Elliott, and G. S. Attard, Chem. Mater 13:3840 (2001).
40. J. M. Elliott, L. M. Cabuché, and P. N. Bartlett, Anal. Chem. 73:2855 (2001).
41. N. N. Greenwood and A. Earnshaw, Chemistry of the elements, 1st edition, Pergamon Press, Oxford:537 (1985).
42. T. S. Ahmadi, Z. L. Wang, A. Henglein, and M. A. El-Sayed, Chem. Mater. 8:1161 (1996).
43. L. D. Rampino and F. F. Nord, J. Am. Chem. Soc. 63:2745 (1941).
44. Kirk-Othmer, Encyclopedia of chemical technology, 3rd edition 9:494 (1980).
45. M. V. Seregina, L. M. Bronstein, O. A. Platonova, D. M. Chernyshov, and P. M. Valetsky, Chem. Mater. 9:923 (1997).
46. L. D. Burke and J. K. Casey, J. Electrochem. Soc. 140:1284 (1993).
47. J.-P. Chevillot, J. Farcy, C. Hinnen, and A. Rousseau, J. Electroanal. Chem. 64:39 (1975).
48. B. E. Conway and G. Jerkiewicz, J. Electroanal. Chem. 357:47 (1993).
49. A. Czerwinski, I. Kiersztyn, M. Grden, and J. Czapla, J. Electroanal. Chem. 471:190 (1999).
50. A. Czerwinski, R. Marassi, and S. Zamponi, J. Electroanal. Chem. 316:211 (1991).
51. F. A. Lewis, The palladium-hydrogen system; Academic Press, New York, NY. (1967).
52. A. Czerwinski and R. Marassi, J. Electroanal. Chem. 322:373 (1992).
53. N. Cioffi, L. Torsi, L. Sabbatini, P. G. Zambonin, and T. Bleve-Zacheo, J. Electroanal. Chem. 488:42 (2000).

54. P. T. Moseley, Meas. Sci. Technol. 8:223 (1997).
55. C. F. Cullis and B. M. Willatt, J. Catal. 83:267 (1983).
56. C. F. Cullis, D. E. Keene, and D. L. Trimm, J. Catal. 19:378 (1970).
57. F. Ménil, C. Lucat, and H. Debéda, Sens. Actuators B 24-25:415 (1995).
58. D.-D. Lee, W.-Y. Chung, and B.-K. Sohn, Sens. Actuators B 13-14:252 (1993).
59. P. Dutronc, C. Lucat, F. Menil, M. Loesch, and L. Combes, Sens. Actuators B 15-16:24 (1993).
60. P. Dutronc, C. Lucat, F. Menil, M. Loesch, M. C. Horillo, I. Sayago, J. Gutierrez, and J. A. de Agapito, Sens. Actuators B 15-16:384 (1993).
61. H. Debéda, L. Dulau, P. Dondon, F. Menil, C. Lucat, and P. Massok, Sens. Actuators B 44:248 (1997).
62. G. Rose and I. Zdanevitch, Sens. Actuators B 24-25:426 (1995).
63. V. Sommer, R. Rongen, P. Tobias, and D. Kohl, Sens. Actuators B 6:262 (1992).
64. V. Sommer, P. Tobias, and D. Kohl, Sens. Actuators B 12:147 (1993).
65. H. Debéda, D. Rebiere, J. Pistre, and F. Menil, Sens. Actuators B 26-27:297 (1995).
66. G. A. Samorjai and S. M. Davis, Platinum Metals Rev. 27:54 (1983).
67. E. E. Wolf and F. Alfani, Catal. Rev. Sci. Eng. 24:329 (1982).
68. A. D. Langeveld, J. P. F. M. v. Hertrooy, J. B. W. P. Loos, and J. W. Niemantsverdriet, Vacuum 38:393 (1988).
69. J. J. Ehrhardt, L. Colin, and D. Jamois, Sens. Actuators B 40:117 (1997).
70. L. Colin, A. Cassuto, J. J. Ehrhardt, M. F. Ruiz-Lopez, and D. Jamois, Appl. Surf. Sci. 99:245 (1996).
71. C. F. Cullis and B. M. Willatt, J. Catal. 86:187 (1984).
72. S. J. Gentry and A. Jones, J. Appl. Chem. Biotechnol. 28:727 (1978).
73. N. Tateishi, K. Yahikozawa, K. Nishimura, M. Suzuki, Y. Iwanaga, M. Watanabe, E. Enami, Y. Matsuda, and Y. Takasu, Electrochim. Acta 36:1235 (1990).

74. N. Tateishi, K. Yahikozawa, K. Nishimura, and Y. Takasu, Electrochim. Acta 37:2427 (1992).
75. G. Bredig and R. Allolio, Z. Phys. Chem. 41:126 (1927).
76. C. Hammond, The Basic of Crystallography and Diffraction; Oxford University Press Inc., Oxford (1997).
77. D. A. J. Rand and R. Woods, J. Electroanal. Chem. 35:209 (1972).
78. D. A. J. Rand and R. Woods, J. Electroanal. Chem. 31:29 (1970).
79. D. A. Buttry and M. D. Ward, Chem. Rev. 92:1355 (1992).
80. E. J. Calvo, C. Danilowicz, and R. Etchenique, J. Chem. Soc. Faraday Trans. 91:4083 (1995).
81. E. J. Calvo, R. Etechenique, P. N. Bartlett, K. Singhal, and C. Santamaria, Faraday Discuss. 107:141 (1997).
82. R. Woods, Chemisorption at electrodes, in Electroanalytical Chemistry, A. J. Bard, Editor; Marcel Dekker Inc.: New York-Basel:109 (1976).
83. L. D. Burke and L. C. Nagle, J. Electroanal. Chem. 461:52 (1999).
84. C. L. Perdriel, E. Custidiano, and A. J. Arvia, J. Electroanal. Chem. 246:165 (1988).
85. L. H. Dall'Antonia, G. Tremiliosi-Filho, and G. Jerkiewicz, J. Electroanal. Chem. 502:72 (2001).
86. D. A. J. Rand and R. Woods, J. Electroanal. Chem. 36:57 (1972).
87. C. Lim and S.-I. Pyun, Electrochim. Acta 39:363 (1994).
88. G. Mengoli, M. Bernardini, M. Fabrizio, C. Manduchi, and G. Zannoni, J. Electroanal. Chem. 403:143 (1996).
89. W. S. Zhang, X. W. Zhang, and H. Q. Li, J. Electroanal. Chem. 434:31 (1997).
90. W. Eberhardt, F. Greuter, and E. W. Plummer, Phys. Rev. Lett. 46:1085 (1981).
91. J. F. Lynch and T. B. Flanagan, J. Phys. Chem. 77:2628 (1973).
92. M. Baldauf and D. M. Kolb, Electrochim.Acta 38:2145 (1993).
93. H. A. Rafizadeh, Phys. Rev. B 23:1628 (1981).

94. V. Breger and F. Gileadi, Electrochim. Acta 16:177 (1971).
95. K. E. Shuler and K. J. Laidler, J. Chem. Phys. 17:1212 (1949).
96. H. S. Taylor, J. Phys. Chem. 30:145 (1926).
97. W. Beck, A. L. Glass, and E. Taylor, J. Electrochem. Soc. 11:53 (1965).
98. C.-C. Chien, D. Hodko, Z. Minevski, and J. O. M. Bockris, J. Electroanal. Chem. 338:189 (1992).
99. P. N. Bartlett, B. Gollas, S. Guerin, and J. Marwan, Phys. Chem. Chem. Phys. 4:3835 (2002).
100. A. Capon and R. Parsons, J. Electroanal. Chem. 39:275 (1972).
101. G. Jerkiewicz and J. J. Borodzinski, Langmuir 9:2202 (1993).
102. F. Villiard and G. Jerkiewicz, Can. J. Chem. 75:1656 (1997).
103. L. A. Kibler, M. Kleinert, and D. M. Kolb, J. Electroanal. Chem. 467:249 (1999).
104. M. Peuckert, Surf. Sci. 141:500 (1984).
105. B. E. Conway, B. Barnett, H. Angerstein-Kozlowska, and B. V. Tilak, J. Chem. Phys. 93:8361 (1990).
106. H. Angerstein-Kozlowska, B. E. Conway, and W. B. A. Sharp, J. Electroanal. Chem. 43:9 (1973).
107. K. J. Vetter and J. W. Schultze, J. Electroanal. Chem. 34:131 (1971).
108. A. Bewick and J. W. Russell, J. Electroanal. Chem. 142:337 (1982).
109. D. Hennig, S. Wilke, and R. Loeber, Surf. Sci. 287:89 (1993).
110. Z. Cataldi, R. O. Lezna, M. C. Giordano, and A. J. Arvia, J. Electroanal. Chem. 261:61 (1988).
111. L. D. Burke and M. B. C. Roche, J. Electroanal. Chem. 159:89 (1983).
112. L. D. Burke and E. J. M. O'Sullivan, J. Electroanal. Chem. 93:11 (1978).
113. L. D. Burke and E. J. M. O'Sullivan, J. Electroanal. Chem. 112:247 (1980).

114. C. Pallotta, N. R. De Tacconi, and A. J. Arvia, Electrochim. Acta 26:261 (1981).
115. Y. Bachmat, Ground water Contamination and Control ed. U. Zoller, Marcel Dekker, Inc, New York (1994).
116. WHO, Health Hazards from Nitrates in Drinking Water, WHO; Geneva, Switzerland (1985).
117. J. C. Kruithof and H. M. M. Koppers, Aqua 38:207 (1989).
118. F. Rogalla, G. D. E. Lurminat, J. Coutelle, and H. Godart, Proceedings of NATO Advanced Research Workshop, University of Nebraska, Lincoln, Nebraska (1990).
119. M. Green and G. Shelef, Ground water Contamination and Control Marcel Dekker, Inc, New York (1994).
120. O. A. Petrii and T. Y. Safonova, J. Electroanal. Chem. 331:897 (1992).
121. G. Horanyi and E. M. Rizmayer, J. Electroanal. Chem. 188:265 (1985).
122. R. Tenne, K. Patel, K. Hashimoto, and A. Fujishima, J. Electroanal. Chem. 347:409 (1993).
123. F. Bouamrane, A. Tadjeddine, J. E. Butler, R. Tenne, and C. Lévy-Clément, J. Electroanal. Chem. 405:95 (1996).
124. C. Reuben, E. Galun, H. Cohen, R. Tenne, R. Kalish, Y. Muraki, K. Hashimoto, A. Fujishima, J. M. Butler, and C. Lévy-Clément, J. Electroanal. Chem. 396:233 (1995).
125. Y. Xiang, D. L. Zhou, and J. F. Rusling, J. Electroanal. Chem. 424:1 (1997).
126. S. Cattarin, J. Appl. Electrochem. 22:1077 (1992).
127. H.-L. Li, J. Q. Chambers, and D. T. Hobbs, J. Appl. Electrochem. 18:454 (1988).
128. C. Lu, S. Lu, W. Qiu, and Q. Liu, Electrochim. Acta 44:2193 (1999).
129. D. De, J. Engelhardt, and E. E. Kalu, J. Electrochem. Soc. 147:4224 (2000).
130. G. Horanyi and M. Wasberg, Electrochim. Acta 42:261 (1997).

131. M. Wasberg and G. Horanyi, Electrochim. Acta 40:615 (1995).
132. K. J. Reddy and J. Lin, Wat. Res. 34:995 (2000).
133. T. Ohmori, M. S. El-Deab, and M. Osawa, J. Electroanal. Chem. 470:46 (1999).
134. Handbook of Chemistry and Physics, Elsevier; D. R. Lide, 73rd Edition (1992).
135. J. N. Carstens, S. C. Su, and A. T. Bell, J. Catal. 176:136 (1998).
136. J. P. Hoare, J. Electrochem. Soc. 131:1809 (1984).
137. R. Woods, Electrochim. Acta 14:632 (1969).